The 13th Japan-China-Korea Joint Conference on MEMS/NEMS

JCK MEMS/NEMS 2022

16-19 October, 2022, Kagoshima, Japan, Hybrid

https://www.jckmemsnems2022.com/

Conference Proceedings

actuators
an Open Access Journal by MDPI

MDPI

Organized by:

- **Keio University**
- **JCK MEMS/NEMS Executive Committee**
- **Kagoshima University**
- **Technical Committee for MEMS Commercialization, The Japan**
- **International Joint Laboratory for Micro/Nano Manufacturing and Measurement Technology**
- **Shaanxi Province Mechanical Engineering Society**
- **Mico/Nano Manufacturing Technology Institution of Chinese Mechanical Engineering Society**
- **Micro-nano Manufacturing and Equipment Institution of Chinese Society of Micro-Nano Technology**

Sponsored by:

- **Heidelberg Instruments KK**
- **Kyodo International, Inc.**
- **SIJTechnology, Inc.**
- **Sumitomo Precision Products Co., Ltd.**
- **TDC Corporation**
- **SANMEI CO,LTD**

Welcome to JCK MEMS/NEMS 2022

The JCK MEMS/NEMS Conference is organized to provide an annual East Asian forum for the recent progress in Green & Life Innovation by MEMS/NEMS technology with a special emphasis laid on international collaboration to solve environmental and social issues among East Asian Economies.

Now this year, the torch has been relayed to Japan once again, and on behalf of the Conference Committees, I would like to welcome you to the 13th Japan-China-Korea Joint Conference on MEMS/NEMS (JCK MEMS/NEMS 2022), which will be held in Kagoshima, Japan ,16-19 October, 2022. We are looking forward to an exciting and high-level scientific and strategic program that will give the opportunity to all delegates for networking and sharing ideas, while enjoying the wonderful experience in Kagoshima.

Conference Chair
Prof. Norihisa Miki
Keio University, Japan

Conference Info

There were two series of 2-side Joint Seminars on MEMS/NEMS held in north-east Asia region, including the Japan-China Joint Seminars (1st, Beijing, 2006; 2nd, Tokyo, 2007; 3rd, Wuxi, 2009) and Korea-Japan Joint Seminar (1st, 2008, Pusan). Though these seminars were successfully held with many participants, our colleagues decided to initiate a new 3-side platform, i.e., the Japan-China-Korea Joint Conference on MEMS/NEMS, aiming to share the research achievements and plan strategic collaboration more effectively in a wider scale.

Thus the 1st JCK MEMS/NEMS Conference was held at Sapporo, Japan, 2010, chaired by Prof. Renshi Sawada from Kyushu University and followed by the followings;

2011 at Jeju Island, Korea, chaired by Dr. Nak-Kyu Lee from Korea Institute of Industrial Technology (KITECH);

2012 at Shanghai, China, chaired by Dr. Xinxin Li from CAS;

2013 at Sendai, Japan, chaired by Prof. Eiji Higurashi from The university of Tokyo;

2014 at Seoul, Korea, chaired by Dr. Eung-sug Lee from KIMM;

2015 at Xi'an, China, chaired by Prof. Zhuangde Jiang from Xi'an Jiaoton University;

2016 at Sapporo, chaired by Prof. Toshihiro Itoh from The University of Tokyo;

2017 at Seoul, Korea, chaired by Dr. Eung-sug Lee from KIMM;

2018 at Dalian, China, chaired by Prof. Dongfang Wang from Jilin University;

2019 at Asahikawa, Japan, chaired by Prof. Prof. Sang-Seok Lee from Tottori University;

2020 at Seoul, Tokyo, Xi'an,Online, chaired by Dr. Sung-ho Lee from KITECH;

2021 at Xi'an, China, Hybrid, chaired by Prof. Libo Zhao from Xi'an Jiaoton University.

Conference Committee

Honorary Chair

Renshi SAWADA (Kyushu University, Japan)

Conference General Chair

Norihisa MIKI (Keio University, Japan)

Conference Co-Chairs

Sung-Ho LEE (KITECH, Korea)

Libo ZHAO (Xi'An Jiaotong University, China)

Advisory Committee

Renshi SAWADA (Kyushu University, Japan)

Nak Kyu LEE (KITECH, Korea)

Xinxin LI (SIMIT, CAS, China)

Eiji HIGURASHI (AIST, Japan)

Eung-Sug LEE (KIMM, Korea)

Zhuangde JIANG (Xi'An Jiaotong University, China)

Toshihiro ITOH (The University of Tokyo, Japan)

Eung-Sug LEE (KIMM, Korea)

Dongfang WANG (Jilin University, China)

Sang-Seok LEE (Tottori University, Japan)

Sung-Ho LEE (KITECH, Korea)

Libo ZHAO (Xi'An Jiaotong University, China)

Program Committee

Japan side

Isao SHIMOYAMA (Toyama Prefectural University, Japan)

Ryuji YOKOKAWA (Kyoto University, Japan)

Junji NISHII (Hokkaido University, Japan)

Sang-Seok LEE (Tottori University, Japan)

Toshihiro ITOH (The University of Tokyo, Japan)

Masanori MUROYAMA (Tohoku University, Japan)

Norihisa MIKI (Keio University, Japan)

Yuichi UTSUMI (University of Hyogo, Japan)

Masaya MIYAZAKI (Kyushu Institute of Technology, Japan)

Takashi KASAHARA (Hosei University, Japan)

Hirofumi NOGAMI (Kyushu University, Japan)

Ryo TAKIGAWA (Kyushu University, Japan)

Munehisa TAKEDA (MMC, Japan)

Sunao MURAKAMI (Kyushu Institute of Technology, Japan)

China side

Shanhong XIA (IECAS, China)

Xiongying YE (Tsinghua University, China)

Zhihong LI (Peking University, China)

Haixia (Alice) ZHANG (Peking University, China)

Hairong ZHENG (Shenzhen Institute of Advanced Technology,CAS, China)

Yihui WU (SKLAO, CAS, China)

Dongfang WANG (Jilin University, China)

Yuelin WANG (SIMIT, CAS, China)

Jingquan LIU (Shanghai Jiaotong University, China)

Zhuoqing YANG (Shanghai Jiaotong University, China)

Yulong ZHAO (Xi'An Jiaotong University, China)

Weizheng YUAN (Northwestern Polytechnical University ,China)

Feng CHEN (Xi'An Jiaotong University, China)

Hongzhong LIU (Xi'An Jiaotong University, China)

Lining SUN (Soochow University, China)

Daoheng SUN (Xiamen University, China)

Korea side

Young-Kweon KIM (Seoul National University, Korea)

Dong-Weon LEE (Chonnam National University, Korea)

Hye-Jin LEE (KITECH, Korea)

Jeongdai JO (KIMM, Korea)

Doosun CHOI (KIMM, Korea)

Hak-Joo LEE (KIMM, Korea)

Jae-Jong LEE (KIMM, Korea)

Jun-Ho JEONG (KIMM, Korea)

Ki-Hong KIM (KIMM, Korea)

Geunbae LIM (POSTECH, Korea)

Joonwon KIM (POSTECH, Korea)

JongSoo KO (Pusan National University, Korea)

Sang-Mae LEE (Busan Techno Park, Korea)

Gyuman KIM (Kyungpook National University, Korea)

Jongbaeg KIM (Yonsei University, Korea)

Best Paper Award Committee

Chair

Norihisa MIKI (Keio University, Japan)

Member

Sung-Ho LEE (KITECH, Korea)

Jian LU (AIST, Japan)

Libo ZHAO (Xi'An Jiaotong University, China)

Local Organizing Committee

Chair

Hirofumi NOGAMI (Kyushu University, Japan)

Member

Ryutaro MAEDA (AIST, Japan, XJTU, China)

Jian LU (AIST, Japan)

Yuko AKABANE (TDC Co. Ltd, Japan)

Ryo TAKIGAWA (Kyushu University, Japan)

Sang-Seok LEE (Tottori University, Japan)

Sung-Won YOUN (AIST, Japan)

Nao TSURUYA (Kagoshima University, Japan)

Registration fee

The registration fee includes all sessions, conference proceeding and Banquet.

In-Person (Oral / Poster / Others)			
	Normal	Student	Extra Banquet Ticket
By 30-SEPT-2022	30,000yen	10,000yen	5,000yen
After 30-SEPT-2022	35,000yen	15,000yen	5,000yen

Virtual (Oral / Poster / Others)		
	Normal	Student
By 30-SEPT-2022	30,000yen	10,000yen
After 30-SEPT-2022	35,000yen	15,000yen

Payment

On-Site

The registration fee will be charged on-site at the conference with receipt. Cash payment is encouraged.

Online Payment

Please pay through the website: https://form.jotform.me/91560927181460

Bank transfer

The registration fee can pay through Domestic Remittance as follows;

銀行名：常陽銀行

支店名：つくば並木支店

支店番号： 168

口座番号： 1411217（普通）

口座名： JCKMEMSNEMS 実行委員会 伊藤寿浩

（ジエーシーケーメムス ネムスジツコウイインカイ）

住所：〒305-8564 茨城県つくば市並木 1-2-1

Note: Transfer fees shall be borne by the Participants.

Venue

Kagoshima University Student Community Plaza

鹿児島大学（郡元）学習交流プラザ

<u>The main venue & Registration</u>

Kagoshima University Student Community Plaza 2F Student Community Hall

鹿児島大学（郡元）学習交流プラザ２階 学習交流ホール

<u>Exhibition Hall & Poster Venue</u>

Kagoshima University Student Community Plaza 2F Student Lounge 2

鹿児島大学（郡元）学習交流プラザ２階 学習ラウンジ２

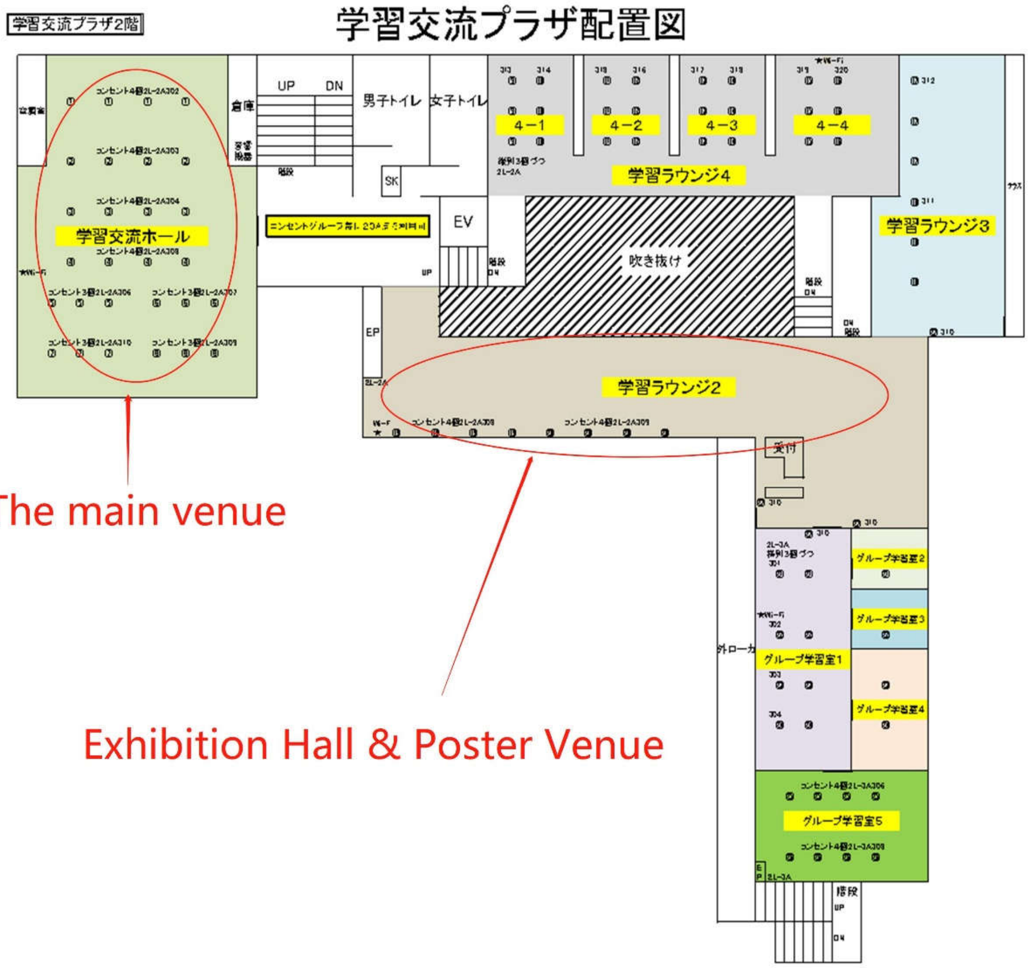

<u>Reception</u>

Kagoshima University Inamori Auditorium 2F Vege Marche'19

鹿児島大学稲盛記念館 2F「ヴェジマルシェ’19」

<u>Banquet</u>

SHIROYAMA HOTEL kagoshima 4F Rainbow

城山ホテル鹿児島 ４階「レインボー」

Technical tour

October 19th

- ➢ 09:00 departure from Kagoshima Chuo Station
- ✧ Visit Sakura-jima for geological monitoring
- ✧ Visit Science and Technological promotion of Shimadu-reginal Samurai
- ✧ Visit food factory production line
- ➢ 17:00 Kagoshima Chuo station or airport

Program At A Glance		
Time and date shows here refers to Japan Standard Time (UTC+9).		
16 October (Sunday)		
16:00-17:45	Registration	Kagoshima University Student Community Plaza 2F Student Community Hall
17:00-17:30	Special Memorial Talk	
18:00-20:00	Reception	Kagoshima University Inamori Auditorium 2F Vege Marche'19
17 October (Monday)		
08:30-17:00	Registration	Kagoshima University Student Community Plaza 2F Student Community Hall
09:00-10:10	Opening Session, Plenary and Invited Session	
10:10-10:40	Coffee Break	Group Photo & Poster Session & Exhibition
10:40-12:00	Invited Session	
12:00-13:00	Lunch Time	Poster Session & Exhibition
13:00-14:50	Oral Session	
14:50-15:20	Coffee Break	Poster Session & Exhibition
15:20-16:00	Oral Session	
16:00-17:15	Industry Oral Session	
18:00	Banquet	SHIROYAMA HOTEL Kagoshima 4F Rainbow
18 October(Tuesday)		
08:30-16:00	Registration	Kagoshima University Student Community Plaza 2F Student Community Hall
09:00-10:30	Plenary and Invited Session	
10:30-11:00	Coffee Break	Exhibition
11:00-11:50	Oral Session	
11:50-13:00	Lunch Time	Exhibition
13:00-14:40	Oral Session	
14:40-15:10	Coffee Break	Exhibition
15:10-15:20	Poster Session (Virtual)	
15:20-16:30	Plenary and Invited Session	
16:30-16:35	Announcement of JCK MEMS/NEMS 2023	
16:35-16:40	Closing Message	
19 October(Wednesday)		
Technical Tour(Option) 9:00 departure from Kagoshima Chuo Station ~Visit Sakura-jima for geological monitoring ~Visit Science and Technological promotion of Shimadu -reginal Samurai ~Visit food factory production line 17:00 Kagoshima Chuo station or airport		

Time of Talk / Presentation	
Plenary Talk	**Speech: 25 minutes** **Question: 5 minutes**
Invited Talk	**Speech: 17 minutes** **Question: 3 minutes**
Industry Oral Presentation	**Presentation: 13 minutes** **Question: 2 minutes**
Oral Presentation (Normal)	**Presentation: 13 minutes** **Question: 2 minutes**
Oral Presentation (Student)	**Presentation: 8 minutes** **Question: 2 minutes**
Poster Presentation (Virtual)	**Presentation: 3 minutes** **Question: 2 minutes**
Poster Presentation (In-Person)	**Depending on the situation on-site**

Time and date shows here refers to Japan Standard Time (UTC+9).		
16 October (Sunday)		
16:00-17:45	Registration	Kagoshima University Student Community Plaza 2F Student Community Hall
17:00-17:30	Special Memorial Talk	Micro/Nano Manufacturing and Its Applications- Under One Roof Report - Part VIIII Dong F. Wang (Virtual) , Jilin University, CHINA
18:00-20:00	Reception	Kagoshima University Inamori Auditorium 2F Vege Marche'19
17 October (Monday)		
08:30-17:00	Registration	Kagoshima University Student Community Plaza 2F Student Community Hall
Opening, Plenary and Invited Session Chair: Prof. Ryutaro Maeda & Prof. Sung-Ho LEE		
09:00-09:05	Opening Address	Prof. Norihisa Miki, Keio University, JAPAN
09:05-09:10	Address from China	Prof. Libo ZHAO, Xi'an Jiaotong University, CHINA
09:10-09:15	Address from Japan	Prof. Toshihiro ITOH, The University of Tokyo, JAPAN
09:15-09:20	Address from Korea	Dr. EungSug LEE, KIMM, KOREA
09:20-09:50	Plenary 1	3D artificial cell membrane structure arrays fabricated on Si substrate in a microfluidic channel Prof. Tae Song Kim (Virtual) , Korea Institute of Science and Technology, KOREA
09:50-10:10	Invited 1	An example of applying blockchain technology to semiconductor fabrication SVP Myoung Soo Choi, SK Hynix, South KOREA;Tottori University, JAPAN
10:10-10:40	Coffee Break	Group Photo & Poster Session & Exhibition
Invited Session Chair:Dr. Jian Lu		
10:40-11:00	Invited 2	Fabrication of Flexible Li ion Battery Dr. Seungmin Hyun (Virtual) , Korea Institute of Machinery and Materials, KOREA
11:00-11:20	Invited 3	MEMS foundry Service in Sony Semiconductor Manufacturing Corp. and Development of advanced process technology in collaboration with Tohoku University Dr. Hidetoshi Miyashita, Sony Semiconductor Manufacturing Corporation, JAPAN
11:20-11:40	Invited 4	IoD (Iternet of Disaster)-Feasibility Study of Debris Flow Detection in Sakurajima- Dr. Yuichi Kurashima, National Institute of Advanced Industrial Science and Technology (AIST), JAPAN
11:40-12:00	Invited 5	Laser Manufacturing of Multifunctional Flexible Sensors & System Integration Prof. Kaichen Xu (Virtual) , Zhejiang University, CHINA
12:00-13:00	Lunch Time	Poster Session & Exhibition

Oral Session **Chair: Prof. Toshihiro ITOH**		
13:00-13:15	Oral 1	Introduction of the development on vibration-resistant physics package for chip-scale atomic clocks Dr. Munehisa Takeda, Micromachine Center, JAPAN
13:15-13:30	Oral 2	Development of Inter-electrode Thin Gaps Filled by Nanofluids for the Investigation of Direct Electrification Mechanism Dr. Jian Lu, National Institute of Advanced Industrial Science and Technology (AIST), JAPAN
13:30-13:45	Oral 3	High-throughput and label-free cancer stem-like cell assay at a single cell level by microfluidic devices Prof. Noritada Kaji, Kyushu University, JAPAN
13:45-14:00	Oral 4	Grating-Based Surface Plasmon Resonance Sensor for Visible Light Employing a Metal/Semiconductor Junction for Electrical Readout Prof. Tetsuo Kan, The University of Electro-Communications, JAPAN
14:00-14:10	Oral 5	Development of a picoliter-sized incubator array for the cultivation of microorganisms Yuma Tanaka, Tsukuba University, JAPAN
14:10-14:20	Oral 6	Cantilever Type Pyroelectric Device Structure for Compact Non-Contact Temperature Sensor Yudai Chida, The University of Tokyo, JAPAN
14:20-14:30	Oral 7	Planar spring-supported force plate with an eddy current displacement sensor Yuta Kawasaki, Keio university, JAPAN
14:30-14:40	Oral 8	Cone-Shaped Air Chamber for the Wearable Scratching-Sound Sensing Device Shun Muramatsu, The University of Tokyo, JAPAN
14:40-14:50	Oral 9	A Basic Study of Texture Classification by Active Sensing Using a MEMS-LSI Integrated Tactile Sensor Takao Saitou,Tohoku Institute of Technology, JAPAN
14:50-15:20	Coffee Break	Poster Session & Exhibition
Oral Session & Industry Oral Session **Chair: Prof. Norihisa Miki & Dr. Yuichi Kurashima**		
15:20-15:30	Oral 10	Optimization of Electrode Structure for Rumen Bacteria Fuel Cell Yusuke Yashiro, The University of Tokyo, JAPAN
15:30-15:40	Oral 11	A Passive Wireless Vibration Sensing Method in Harsh Environment Ziqi Zhao, The University of Tokyo, JAPAN
15:40-15:50	Oral 12	On chip organic synthesis by microwave heating in a microchannel coupled with post-wall waveguide Kaito Fujitani (Virtual) , University of Hyogo, JAPAN
15:50-16:00	Oral 13	Characterization of Polyether Sulfone Membranes for Renal Replacement Therapy Devices Rei Kono, Keio university, JAPAN
16:00-16:15	Industry Oral 1	Introduction to Micro/Nano fabrication services Kenshin Ikeda, Kyodo International, Inc. JAPAN
16:15-16:30	Industry Oral 2	Development of efficient polishing technology for large size diamond substrates Yuko Akabane, TDC Corporation, JAPAN
16:30-16:45	Industry Oral 3	PZT thin film lineups and MEMS foundry in Sumitomo Precision Group Hideo Hashimoto, Sumitomo Precision Products Co., Ltd., JAPAN

16:45-17:00	Industry Oral 4	Introducing Super Inkjet Technology Naoki Tashiro, SIJTechnology, Inc., JAPAN
17:00-17:15	Industry Oral 5	Power of Direct Writing / Heidelberg Instruments System Line Up Mitsunori Saito, Heidelberg Instruments KK, JAPAN
18:00	Banquet	SHIROYAMA HOTEL Kagoshima 4F Rainbow
18 October(Tuesday)		
08:30-16:00	Registration	Kagoshima University Student Community Plaza 2F Student Community Hall
Plenary and Invited Session Chair: Prof. Xudong Fang & Dr. Munehisa Takeda		
09:00-09:30	Plenary 2	Recent Progress of thin films thermocouples by MEMS Technologies Prof. Bian Tian (Virtual) , Xi'an Jiaotong University, CHINA
09:30-09:50	Invited 6	Microchannel cantilevers beyond mass sensing applications Prof. Jungchul Lee (Virtual) , Korea Advanced Institute of Science and Technology, KOREA
09:50-10:10	Invited 7	Flexible Sensing Electronics for Smart Prosthetic Hand Prof. Ting Zhang (Virtual) , Suzhou Institute of Nano-tech and Nano-bionics, Chinese Academy of Sciences, CHINA
10:10-10:30	Invited 8	Ultrabright Fluorescent Silicon Nanomaterials for pH Sensing and Bio-Medical Imaging Applications Prof. Yufei Liu (Virtual) , Chongqing University, CHINA
10:30-11:00	Coffee Break	Exhibition
Oral Session Chair: Prof. TADAO MATSUNAGA & Prof. Yuichi Utsumi		
11:00-11:10	Oral 14	NEMS Force Sensors Based on Suspended Graphene Membranes Xiaoya Liang (Virtual) , Xi'an Jiaotong University, CHINA
11:10-11:20	Oral 15	Internal Resonance in Coupled Oscillators and Its Sensing Applications Cao Xia (Virtual) , Jilin University, CHINA
11:20-11:30	Oral 16	Flexible strain sensor based on magnetron-sputtered MoS2 film Xing Pang (Virtual) , Xi'an Jiaotong University, CHINA
11:30-11:40	Oral 17	Sky-blue microfluidic electrogenerated chemiluminescence device with host-guest solutions Emiri Kato (Virtual) , Hosei University, JAPAN
11:40-11:50	Oral 18	Operation of 4H-SiC Piezoresistive Pressure Sensor for extreme environments Lukang Wang (Virtual) , Xi'an Jiaotong University, CHINA
11:50-13:00	Lunch Time	Exhibition
Oral Session Chair: President. Yuko Akabane		
13:00-13:10	Oral 19	A microbial fuel cell using microbes in the mud YUKI SANO, Tottori University, JAPAN
13:10-13:20	Oral 20	Flow Control in Paper Channels Using Thermo-responsive Valve MASAYA NAGANO, Kumamoto University, JAPAN

13:20-13:30	Oral 21	Optofluidic device with Gold- nanofève -based-SERS active nanostructure Shunya Saegusa,University of Hyogo, JAPAN
13:30-13:40	Oral 22	Development of a Sensor for Simultaneous Measurement of Heart Rate and Contact Load during Husbandry Training Takumi Hiejima, Kyushu University, JAPAN
13:40-13:50	Interval	
13:50-14:00	Oral 23	Design and process optimization of multi frequency piezoelectric vibration energy harvester in power grid Qian Wang (Virtual) , Xi'an Jiaotong University, CHINA
14:00-14:10	Oral 24	Bidirectional Vibration Energy Harvesting of L-shaped Mass Piezoelectric Beams Adapting to Multiple Scenarios Congsheng Duan (Virtual) , Xi'an Jiaotong University, CHINA
14:10-14:20	Oral 25	Triboelectric Nanogenerator Based on Solid-Liquid electrification Interface and Top Electrode Structure Yahui Li (Virtual) , Shanghai Jiao Tong University CHINA
14:20-14:30	Oral 26	Research on output performance of different PVDF thicknesses and adhesives Zhenxuan Fei (Virtual) , Xi'an Jiaotong University, CHINA
14:30-14:40	Oral 27	Design, Fabrication, and Test of 4H-SiC Accelerometer Yu Yang (Virtual) , Xi'an Jiaotong University, CHINA
14:40-15:10	Coffee Break	Exhibition
Invited, Plenary and Poster (Virtual) Session Chair: Prof. Hirofumi NOGAMI & Dr.Masaya Miyazaki		
15:10-15:15	Poster (Virtual) 1	Development of a Quality Prediction Model for High Pressure Die Casting Process Using Load Cell Sensor Seung Jin Kong (Virtual) , Korea Institute of Industrial Technology, KOREA
15:15-15:20	Poster (Virtual) 2	Mechanical-electrical stimulation integrated culture platform for promoting actuation performance of engineered skeletal muscle Jianfeng Chen (Virtual) , Nanchang University, CHINA
15:20-15:40	Invited 9	A MODIFIED LUMPED PARAMETER MODEL FOR MEMS MICROPHONE DEVELOPMENT Dr. Kumjae Shin (Virtual) , KITECH (Korea Institute of Industrial Technology), KOREA
15:40-16:00	Invited 10	Ultra-precision Measurement for Some Tumor Markers Prof. Lei Liu (Virtual) , Southeast University, CHINA
16:00-16:30	Plenary 3	Emergent Functions of Electrically-induced Bubbles Prof. Yoko Yamanishi, Kyushu University, JAPAN
16:30-16:35	Announcement of JCK MEMS/NEMS 2023 Prof. Dr. Jeong-Dai Jo, KIMM(Korea Institute of Machinery & Materials)	
16:35-16:40	Closing Message	Prof. Ryutaro Maeda, Xi'an Jiaotong University, CHINA

Time and date shows here refers to Japan Standard Time (UTC+9).	
Poster Session	
17 October (Monday) 10:10-10:40 & 12:00-13:00 & 14:50-15:20 Kagoshima University Student Community Plaza 2F Student Lounge 2	
Poster 1	Evaluation of humidity-sensing electrode based on conductive carbon resin Lan Zhang, National Institute of Advanced Industrial Science and Technology (AIST), JAPAN
Poster 2	Key Technologies of Silicon Carbide High Temperature Sensing Devices Chen Wu, Xi'an Jiaotong University, CHINA
Poster 3	Capsuled edible wireless sensor for gut bacterial monitoring Hiroaki Onoe, Keio universityy, JAPAN
Poster 4	Cationic lipid nanoparticles encapsulating positively charged DNA/polyethyleneimine complexes for effective long-chain plasmid DNAs transfection Shuya Uno, Hokkaido University, JAPAN
Poster 5	Grasping Force Evaluation of Minimally Invasive Surgical Robotic Forceps TADAO MATSUNAGA, Tottori University, JAPAN
Poster 6	Development of shock wave focusing device for needle-free electrically induced microbubbles injector Yibo MA, Kyushu University, JAPAN
Poster 7	Development of gel micromachining technique for tissue formation with multiple types of cells Keito Sonoda, Kumamoto University, JAPAN
Poster 8	Fundamental evaluation of biosensing microdevice based on immune response Yusuke Ide, Kumamoto University, JAPAN
Poster 9	Microfabrication of Surface Acoustic Wave Devices with Micro-Patterned AlN Thin films Sunao MURAKAMI, Kyushu Institute of Technology, JAPAN
Poster 10	Degradation Evaluation by Viscosity Measurement of Low Volume Oil Samples Kenji Sakamoto, Kyushu Institute of Technology, JAPAN
Poster 11	Facile detection of CD9 based on a non-competitive fluorescence polarization immunoassay using a peptide as a tracer Shunsuke Chida, Hokkaido University, JAPAN
Poster 12	Development of early lameness detection system for zoo giraffes Kenjiro Nakai, Kyushu University, JAPAN
Poster 13	Fabrication of LiTaO3/SiC hybrid wafer using surface activated bonding method Seigo Murakami, Kyushu University, JAPAN
Poster 14	Fabrication of LNOI/Si optical modulator using room temperature wafer bonding method Kaname Watanabe, Kyushu University, JAPAN
Poster 15	Design and Fabrication of pH-ISFET Sensor Using MEMS Technology Hoang Ba Cuong, SHTPLAB, Vietnema

Plenary Talk

- Prof. Bian Tian
  Xi'an Jiaotong University, CHINA
  Title: Recent Progress of thin films thermocouples by MEMS Technologies
- Prof. Tae Song Kim
  Korea Institute of Science and Technology, KOREA
  Title: 3D artificial cell membrane structure arrays fabricated on Si substrate in a microfluidic channel
- Prof. Yoko Yamanishi
  Kyushu University, JAPAN
  Title: Emergent Functions of Electrically-induced Bubbles

Prof. Tae Song Kim

Korea Institute of Science and Technology, KOREA

Title:

3D artificial cell membrane structure arrays fabricated on Si substrate in a microfluidic channel

Abstract:

In nature, 3-dimensional (3D) lipid bilayer structures as an array form are frequently observed. Examples can be found in human organs that chemoreceptors to sense various smells or tastes are widely distributed around 3D lipid structures like cilia in olfactory organ or microvilli in a tongue for maximizing the efficiency of a sensing capability, which is closely related to the increase of the number of binding receptors with the increase of surface area as well as an increased probability to meet and bind target molecules as compared with 2D structures. For the last several decades, however, due to the stability limitations of synthetic lipid membranes, the focus has been on the formation of the 2D lipid layer supported on solid substrates in the form of (1) lipid bilayers or monolayers directly deposited on the substrate; (2) tethered bilayer membranes on solid surfaces; and (3) suspended lipid bilayers over micro or nanoapertures. In this talk, the fabrication of artificial 3D lipid structure arrays to mimic sensory organs by using silicon or polymer microwells array in the microfluidic channel will be presented. An improved stability of 3D lipid membrane structure and sealing characteristics as well as pore formation of pore-forming protein in membranes will be discussed for the application to artificial sensory systems or high throughput screening platforms.

Biography:

Tae Song Kim, Ph.D

Principal researcher

Brain science creative research center, BSI

Korea Institute of Science and Technology (KIST)

Professional & Academic Activities

1994-2000 Senior Research Scientist, KIST

1997-1998 Post-doctoral associate, Dept of Electrical Eng and Computer Sci, Univ. of Minnesota, USA

2000- Principal Research Scientist, KIST

2000-2004 Head of Microsystem Research Center, KIST

2004-2010 Director, Intelligent Microsystem Center, 21st Century Frontier Program, Ministry of CIE, Korea

2004- Professor, University of Science and Technology (UST), Korea

2005 Plenary Talk in Transducers 2005, COEX, Seoul

2007 Plenary Talk in MicroTAS 2007, Paris

2007-2010 Director, Korean MEMS Technology Association

2009 Chairman, MicroTAS 2009 at Jeju, Korea

2010- Board Member of Chemical and Biological Microsystem Society

2011-2013 President, Steering Committee of International Symposium of Microchemistry and Microsystem (ISMM)

2011 President, Korean BioChip Society

2012 President, Micro and Nano System Society, Korea

2013-2016 Director, Open Research Program, KIST

2015-2019 Chief Delegate of Korea, World Micromachine Summit

2015-2020 Micro and Nano Fab Center, Director

Prof. Bian Tian
Xi'an Jiaotong University, CHINA

Title:

Recent Progress of thin films thermocouples by MEMS Technologies

Abstract:

Temperature is one of the most important physical parameters for measurement in many fields. In the decision-making of covid-19 response in 2020, the human body temperature is tested accurately and conveniently in public places by the temperature measuring gun and thermal imager.

In the industrial field, accurate control of smelting temperature in the steel smelting process can significantly improve product quality. In the medical field, for pathological observation requires accurate measurement of human body temperature in real time. In the use of some therapeutic methods such as magnetic resonance imaging, thermal hysteresis therapy, the physical parameters of the equipment used need to be adjusted by temperature indicators. In the electromechanical field, for auxiliary facilities such as power generation mainframe equipment, engine propellers, and hydraulic oil, accurate temperature measurements are required to monitor the operation of the system and thus ensure the proper operation of the project.

The thermocouple is a passive device used for temperature measurement. Compared with traditional bulk thermocouples, thin film thermocouples (TFTCs) have typical two-dimensional characteristics and possess the advantages of small heat capacity and fast response speed. With the development of technology intelligence, integration and miniaturization, thin-film thermocouples based on Micro-Nano manufacturing technology are gradually taking the dominant position with the advantages of small size, light weight, low power consumption, high reliability, high sensitivity, easy integration and resistance to harsh working environment.

Biography:

Bian Tian was born in Xi'an, Shaanxi Province, China, on January 22, 1981. He received his B.S. and M.S. degrees from Xi'an Jiaotong University in 2003 and 2007, respectively.

In 2011, he received his PhD degree from Xi'an Jiaotong University under the supervision of Professor Zhuangde Jiang, a member of the Chinese Academy of Engineering. In the same year, he joined the School of Mechanical Engineering of Xi'an Jiaotong University as a lecturer and went to the University of California, Berkeley as a visiting scholar from 2017 to 2018. He became a professor in the School of Mechanical Engineering of Xi'an Jiaotong University in October 2020.

He has been working on ultra-high temperature and piezoresistive MEMS sensors for a long time and has been awarded the national talent program. He has published 49 SCI papers, granted 16 invention patents, won the second prize of National Technical Invention (2017), the first prize of Science and Technology of Shaanxi Province (2012), and won the Youth Science and Technology Award of Shaanxi Province (2020). He is the director of the Collaborative Innovation Platform of Advanced Sensing Technology and System Integration of the Ministry of Education and the vice president of the Institute of Intelligent Sensing Technology and System of Xi'an Jiaotong University (Yantai, China).

Currently, his research interests include high temperature sensing technology, flexible temperature sensor and MEMS micro-pressure sensing technology.

Prof. Yoko Yamanishi

Kyushu University, JAPAN

Title:

Emergent Functions of Electrically-induced Bubbles

Abstract:

The presentation is about the mechanism and structure of our developed electrically-induced bubble knife and its wide applications. The novelties is that simultaneous local reagent injection and perforation to the materials of variety of hardness using bubble cavitation and plasma cavitation. Cavitation and plasma discharge were generated by pulse discharge of microelectrode having special tip structure. Injection to soft material such as animal cell was performed only by cavitation of bubble, and pore formation to hard materials such as seeds of plants or metals were achieved by synergistic effect of cavitation of bubble and plasma ablation. The novelty of the technique enable to process not only conductive material but also non-conductive material such as polymer, CFRP and silicon wafer, which is unlike conventional wire electric discharge machine. Also, the directional transportation of bubbles provides positioning accuracy of micro-processing. Moreover, we focused on the reducing power of hydrogen radical by plasma discharge and the micro-jet caused by collapse of microbubble, and aim at developing a metallization method which does not need a complicated process such as surface treatment. It was confirmed that the nanoparticle synthesis and implanting of them using a bubble injector. This simultaneous etching and deposition methods provide novel printing method of electrical circuit on wide range of material.

Biography:

Yoko Yamanishi has received the Ph.D. degree from Imperial College London (Thermofluids Section in Mechanical Engineering Department) in 2003 by the work of simultaneous optical measurement of size, temperature and velocity of a single coal particles with a combination of pyrometric and diffraction light techniques. She has joined department of mechanical engineering of Shibaura Institute of Technology, Japan in 2004-2005 as a lecturer. Then, she became a postdoctoral fellow of Department of Bioengineering and Robotics, Tohoku University in 2006 and Assistant Professor in 2008-2009, mainly have engaged in the research fields of BioMEMS and micro multiphase flow which apply to the Bio-medical Science and Engineering. She became Associate Professor of Department of Micro-Nano Systems Engineering, and Department of Mechanical Science & Engineering of Nagoya University and also a member of PRESTO JST during 2010-2012, and have started her work of electrically-induced bubble (needle-free bubble injector). She was Associate Professor of Department of Mechanical Engineering of Shibaura Institute of Technology during 2013-2015, and her work has been expanded to plasma-induced bubble and its biomedical applications. She moved to Kyushu University on April, 2016 and she became Professor of department of Mechanical Engineering, Kyushu University and leading biomedical fluid engineering laboratory. She is currently a member of CREST JST(delivery of long-chain DNA by the novel bubble injector and microstructures) and PM of moonshot (Interdisciplinary Frontier of Bio-order Extended by Nano- and Micro-bio Avatars). She is a member of IEEE, JSME, RSJ and so on.

Invited Talk

- Prof. Kaichen Xu

  Zhejiang University, CHINA

  Title: Laser Manufacturing of Multifunctional Flexible Sensors & System Integration
- Dr. Hidetoshi Miyashita

  Sony Semiconductor Manufacturing Corporation (SCK), JAPAN

  Title: MEMS foundry Service in Sony Semiconductor Manufacturing Corp. and Development of advanced process technology in collaboration with Tohoku University
- Dr. Kumjae Shin

  KITECH (Korea Institute of Industrial Technology), KOREA

  Title: A MODIFIED LUMPED PARAMETER MODEL FOR MEMS MICROPHONE DEVELOPMENT
- Prof. Jungchul Lee

  Korea Advanced Institute of Science and Technology, KOREA

  Title: Microchannel cantilevers beyond mass sensing applications
- Prof. Ting Zhang

  Suzhou Institute of Nano-tech and Nano-bionics, Chinese Academy of Sciences, CHINA

  Title: Flexible Sensing Electronics for Smart Prosthetic Hand
- Prof. Lei Liu

  Southeast University, CHINA

  Title: Ultra-precision Measurement for Some Tumor Markers
- Dr. Yuichi Kurashima

  National Institute of Advanced Industrial Science and Technology (AIST), JAPAN

  Title: IoD (Iternet of Disaster)-Feasibility Study of Debris Flow Detection in Sakurajima-
- Dr. Seungmin Hyun

  Korea Institute of Machinery and Materials, KOREA

  Title: Fabrication of Flexible Li ion Battery
- Prof. Yufei Liu

  Chongqing University, CHINA

  Title: Ultrabright Fluorescent Silicon Nanomaterials for pH Sensing and Bio-Medical Imaging Applications
- SVP Myoung Soo Choi

  SK Hynix, South KOREA;Tottori University, JAPAN

  Title:An example of applying blockchain technology to semiconductor fabrication

Prof. Kaichen Xu
Zhejiang University, CHINA

Title:

Laser Manufacturing of Multifunctional Flexible Sensors & System Integration

Abstract:

Sensors play crucial roles in the Internet of Things, artificial intelligence, and big data etc. In recent years, the development of flexible electronic manufacturing technologies has significantly extended the applications of smart sensors, which can be conformally attached onto the irregular surfaces. High-performance flexible sensors usually rely on judiciously engineering micro/nano-structures and active materials. Advanced laser manufacturing is endowed with versatile functionalities for flexible electronics. Based on the principles of laser-matter interactions, various novel flexible/soft sensors have been developed to dynamically track pressure, temperature, humidity, flow, slanting angles etc. Coupled with hybrid manufacturing technologies, this talk will also present a couple of integrated flexible sensing systems and their multifunctional applications.

Biography:

Kaichen XU is currently a ZJU-100 Professor at the School of Mechanical Engineering, Zhejiang University (ZJU). He received the PhD degree from National University of Singapore (NUS) in 2018 and then moved to Osaka Prefecture University (OPU) as a JSPS Postdoctoral Fellow in Japan. His research mainly includes hybrid laser manufacturing of multifunctional flexible electronics. Over 30 papers have been published in Adv. Mater., Adv. Funct. Mater., Adv. Sci., ACS Nano etc. He was invited to serve as a Corresponding Expert of Engineering, a journal launched by the Chinese Academy of Engineering, Youth Editor of International Journal of Extreme Manufacturing, and Editorial Board of Opto-Electronic Engineering. He is independent reviewers for over 40 journals (over 160 times).

SVP Myoung Soo Choi

SK Hynix, South Korea;Tottori University, Japan

Title:

An example of applying blockchain technology to semiconductor fabrication.

Abstract:

This talk presents an example of applying blockchain technology to semiconductor fabrication. Fabrication engineers typically modify the set values of control parameters to alter behavior properties of fabrication equipment. If the set value happens to be assigned incorrect value, the equipment could show an unexpected behavior, causing a painful recovery. Unfortunately, this erroneous case can occur in a semiconductor fabrication factory embellished with state-of-the-art systems. Surprisingly, it is very simple to draw idea that prevents the set value error as follows: (1) Prepare ledgers specifying correct values of the control parameters (2) Check the set value with the ledgers. However, it requires sophisticated protocols to implement the idea as an executable system. We are strongly inspired to make the system with blockchain technology featuring decentralized and tamper-resistant digital ledger. This presentation shows how to adopt blockchain technology for building the system that detects the set value error.

Biography:

Myoung Soo Choi was born in Incheon, South Korea. He received a Master's degree in Graduate School of Department of Electrical & Computer Engineering, Hanyang University, South Korea, 2005. From Mar 2003 to Nov 2011, he was a Principal Engineer at Mechatronics & Manufacturing Technology Center in Samsung Electronics, South Korea. After that from Dec 2011 to Dec 2018, he was a Vice President (VP) at Mechatronics R&D Center of Samsung Electronics, South Korea. In 2019, he was an Invited Researcher of Tottori University, Japan. Since Apr 2020, he has been a Ph.D. student in Tottori University, and he began working as a Senior Vice President (SVP) of SK Hynix, South Korea from Oct 2020. His research interests are smart software and equipment for semiconductor manufacturing.

Dr. Hidetoshi Miyashita
Sony Semiconductor Manufacturing Corporation (SCK), JAPAN

Title:

MEMS foundry Service in Sony Semiconductor Manufacturing Corp. and development of advanced process technology in collaboration with Tohoku University

Abstract:

Currently, Sony Semiconductor Manufacturing (SCK) provides MEMS foundry services and has experience in prototype development and mass production of various MEMS devices such as acoustic devices, gyroscope, optical MEMS, switches, mirror devices and so on. In order to continue to provide high value-added processes for customer devices, we are constantly striving to introduce new technologies. One example is the introduction of high vacuum encapsulation technology, which is currently being conducted in collaboration with Tohoku University with support from NEDO.

This presentation will also introduce this joint development.

Biography:

Hidetoshi Miyashita received his Ph.D. degree (2005), majoring in mechanical and electrical engineering, from the Tohoku University. Currently, Dr. Miyashita is an engineer of Device Engineering Department in SCK. He leads novel process introduction project in SCK. He also leads a project for mems tactile sensor with Sony R&D team. Before moving to SCK in 2016, he worked as an assistant professor at Tottori University. His research focused on chemical MEMS device with nanomaterials.

Dr. Seungmin Hyun
Korea Institute of Machinery and Materials, KOREA

Title:

Fabrication of Flexible Li ion Battery

Abstract:

Advance of flexible electronics technology led to convenience of human life due to many applications including sensor, mobile device, and health care. As a proper power source for flexible electronics, the development of flexible battery with high capacity and reliability is critical. In this study, we propose a novel geometric structure for stretchable battery, created by folding well-defined two-dimensional patterns with cutouts to produce an extremely stretchable structure with superior reliability and bi-axial deformability. The performance of the battery is maintained under dynamic deformation with a stretching ratio of 90% and a 10-mm-radius bending curvature, guaranteeing a long-lasting cycle life. Finally, the geometrically designed structure-based battery is applied to movable robots, crawling and slithering, with dynamic bi-axial deformations and can be pivotal role in the development of flexible electronics including human-friendly wearable electronics and soft robots.

Biography:

Seungmin Hyun was born in Seoul, Korea, 1969. He received his B.S. and M.S. degrees from Korea University in 1992 and 1995, respectively. In 2002, he received his PhD degree in Materials Science and Engineering from Lehigh University, PA, U.S. He served as a post-doctoral research associate in the Department of Materials Science and Engineering at Lehigh University from September 2002 to April 2006. He is a Principal Researcher at Korea Institute of Machinery and Materials in Korea since May 2006.

His current research interests are fabrication and characterization of nano scaled structures for energy storage devices. For last 26 years, he has attended many international conferences and published extensively in scientific journals including Nature Communications, Advanced Materials, Advanced Energy Materials etc.

Dr. Yuichi Kurashima
National Institute of Advanced Industrial Science and Technology (AIST), JAPAN

Title:

IoD (Internet of Disaster)-Feasibility Study of Debris Flow Detection in Sakurajima-

Abstract:

We develop a detecting system for debris flow disaster. Our final goal is realizing a low-cost debris flow detection system with a high degree of accuracy by AI technique. This talk presents establishing of a wireless MEMS vibration sensor network for AI analysis toward the realizing a debris flow detection system. First of all, we talk about wireless MEMS vibration sensor with stand-alone power system by solar power electric generation. These our developed sensors were installed at multi points around sediment control dam in Sakurajima to capture the vibration signal from debris flow. As a result, we succeed in capturing vibration signals from a real debris flow. And also, we succeed in extracting the typical feature signal of a debris flow using these vibration signals.

Biography:

Yuichi Kurashima received his Ph.D. degree (2005), majoring in applied electronic engineering, from Tokyo University of Science. He has been working at the National Institute of Advanced Industrial Science and Technology (AIST) since 2012 after having academic positions at universities. He has worked on a wide variety of semiconductor microfabrication, mechanical polishing, and grinding technologies and so on. Since working AIST, he has been actively engaged in research on bonding for packaging of MEMS. Currently, Dr, Kurashima is the Group Leader of Integrated MEMS Research Group at AIST, where he has been active in Packaging and Integration of MEMS. He also is interested in sensing for mountains and other natural environments. As part of this effort, he developed a sensor for debris flow on Sakurajima Island several years ago.

Dr. Kumjae Shin

KITECH (Korea Institute of Industrial Technology), KOREA

Title:

A MODIFIED LUMPED PARAMETER MODEL FOR MEMS MICROPHONE DEVELOPMENT

Abstract:

In this study, modified lumped parameter model (LPM) study for MEMS microphone (MM) is described. For analyzing MM's performance especially on SNR (signal to noise ratio), electro- mechano-acoustic coupling system was modeled by LPM and was matched with measurement data. By analyzing mutual dependencies of the different energy domain and calibrating model parameters, electrical, mechanical and acoustical domain components are concentrated on lumped terms. These lumped terms are analytic equations with modification factors. Analytic model for components are not always matched with real values because the real values are easily distorted by parasitic components. Therefore, we corrected the analytic components by modification factor. The modification factors of each component in LPM are calibrated by adapting measured data (frequency response and noise). We call it modified LPM. By this method, the design parameters for mechanical, electrical, acoustic lumped terms are close to the real values. Modified model shows high fidelity for measurement data. In order to increase SNR, we consider acoustic resistance of BPL hole. The acoustic resistance resulted by acoustic holes affects thermal noise of microphone directly. Instead of circle hole, diamond-shaped perforation structure on back-plate (BPL) was designed and its SNR performance was measured. The predicted SNR shows good agreement with measured SNR.

Biography:

Kumjae shin, Principal researcher, KITECH (Korea Institute of Industrial Technology)

Career

2016.3~2016.12, POSTECH, Vibration and acoustic transducer Lab.,Post Doc.

2016.12~2017.12, DB Hitek, Specialized Process department part, Senior researcher (MEMS microphone development, transducer modeling)

2017.12 ~now, KITECH, Principal researcher

Research interest

✧ MEMS microphone & hydrophone (Modeling, MEMS process, experiemnts)
✧ Vibration and acoustic transducer (Sensor & Actuator)
✧ MEMS (Micro-electromechanical system)
✧ Sensor applied monitoring system (Sensor system)
✧ Electro-mechano-acoustic transduction modeling & Multi-physics modeling
✧ FET based transduction (Scanning Probe Microscopy, Acoustic sensor. Etc.,)

Prof. Jungchul Lee

Korea Advanced Institute of Science and Technology, KOREA

Title:

Microchannel cantilevers beyond mass sensing applications

Abstract:

Microchannel cantilevers, one of promising physical microelectromechanical systems (MEMS) devices that have embedded microchannels, have been widely used in gravimetric sensing applications of liquids and particles introduced into the channel or dispensing/patterning applications with liquid phase materials when a dispensing nozzle is additionally configured near their free ends. Although there are numerous potential applications at elevated temperatures such as material synthesis, calorimetric measurements, and phase change mediated manipulation or control, to name a few, microchannel cantilevers are mostly used at or near room temperature mainly due to the absence of integrated active heating elements. Towards various applications under fast and quantitative temperature modulation, we have developed fluidic resonators with integrated heating capability. Heater-integrated microchannel cantilevers with or without a dispensing nozzle were batch-fabricated via sacrificial process, ion implantation, and other typical microfabrication processes. Fabricated heater-integrated microchannel cantilevers were thoroughly calibrated and characterized in a variety of coupled physical domains. Upon pulsed operations, electrothermomechanical time constants extracted from the transient resonance frequency provided a new measurement modality for thermophysical properties of the fluid contained in the microchannel. When a glycerol-water binary mixture was pulsed heated above its boiling point, atomized droplets could be spray-ejected out of the integrated nozzle.

Biography:

JUNGCHUL LEE, Ph.D.
Associate Professor
Manufacturing and Instrumentation Laboratory (MNIL)
Center for Extreme Thermal Physics and Manufacturing Department of Mechanical Engineering
Korea Advanced Institute of Science and Technology

--RESEARCH INTERESTS

Large scale batch fabrication of nanostructures based on silicon self-assembly, Hydrogel based micro-/nanoelectromechanical systems, Materials and processing for flexible, stretchable, and wearable devices, Nanoscale 3D printing of organic and inorganic hybrids, 3D printing for biomedical applications, Multifunctional atomic force microscopy, Single molecule force/mass spectroscopy, High-precision Laser based manufacturing and metrology, Additive manufacturing

--PROFESSIONAL APPOINTMENTS

- ✧ Edmonton, Canada
  University of Alberta 2016–2019
  Adjunct Professor; Chemical and Materials Engineering
- ✧ Daejeon, Korea
  Korea Advanced Institute of Science and Technology 2018–present
  Associate Professor; Mechanical Engineering
- ✧ Seoul, Korea
  Sogang University 2014–2018
  Associate Professor; Mechanical Engineering
- ✧ Seoul, Korea
  Sogang University 2010–2014
  Assistant Professor; Mechanical Engineering

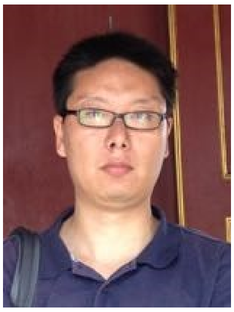

Prof. Lei Liu
Southeast University, CHINA

Title:

Ultra-precision Measurement for Some Tumor Markers

Abstract:

Sensors are equipment that can acquire physical, chemical or biological information parameters and convert them into output signals according to certain laws. It is widely used in aerospace, military engineering ocean exploration, medical diagnosis, environmental monitoring and many other fields related to national security, people's health, and social production. Nowadays, ultra-high precision, in-situ online, real-time feedback, no damage are some important features of the development of modern sensing measurement. At the same time, the latest development achievements in cutting-edge fields such as nanotechnology biomedicine, quantum theory and material engineering are also promoting new breakthroughs in measurement technology and equipment.

In view of the major demand in the field of biomedical testing equipment and the major challenge of breaking through the sensing limit, we have developed new methods and new equipment for cross-se d micro-nano manufacturing of controllable thin films based on ALD with the innovation of thin film manufacturing equipment as the breakthrough point. According to the innovation of manufacturing process, we have used the multifunctional ALD to realize the cross-scale manufacturing and performance regulation of various ultra-sensitive micro-nano thin film structures. Meanwhile, taking the innovation of measurement principle as a breakthrough, we have developed many new sensors and realized the ultra- sensitive sensing measurement of a variety of major disease markers (such as miRNA).

On this basis, we are currently working to expand our work into the field of quantum precision measurement. Combining the multiple functions of atomic force microscopy (AFM) and the quantum sensing properties of diamond NV color centers, ultra-sensitive detection of various disease markers will be achieved and further broader and

wider application will be realized in the future.

Biography:

Liu Lei is a professor of Southeast University. From 1998 to 2007, he completed his undergraduate and doctoral studies at University of Science and technology of China, then entered Southeast University and engaged in the studies on micro-nano manufacturing and ultra-sensitive measurement.

Prof. Ting Zhang

Suzhou Institute of Nano-tech and Nano-bionics, Chinese Academy of Sciences, CHINA

Title:

Flexible Sensing Electronics for Smart Prosthetic Hand

Abstract:

Smart prosthetic hand is of great significance in the field of rehabilitation, while flexible sensing electronics are the core devices for smart prosthetic hands to acquire front-end sensory signals for subsequent signal encoding, transmission, and neural interfacing to reconstruct the sense of touch. Presently, the application of smart prosthetic hand is still not popular, and one key reason is that the absence of exquisite sensing information significantly limits the accuracy and scope of in-hand manipulation. Therefore, it is essential to develop bionic flexible sensing electronics that can accurately perceive versatile information.

This talk is aimed at overviewing our recent progress of flexible sensing electronics for prosthetic hand. The design strategy of bionic flexible sensing electronics is firstly discussed. Then, the design and fabrication of several multifunctional biomimetic sensors for detecting friction force, viscoelasticity, texture, and thermal conductivity of materials are introduced. The integration of multifunctional tactile systems based on these biomimetic sensors, the read-out circuits and machine learning modules, as well as their applications in prosthetic hands for slippage perception, material classification, objects recognition, etc. are also introduced.

Biography:

Ting Zhang received his B.S. and M.S. degrees in chemical engineering in 1999 and 2002, respectively, from Nankai University, China, and his Ph.D from the University of California, Riverside, America, in 2007. In 2009, he joined Suzhou Institute of Nano-tech and Nano-bionics, Chinese Academy of Sciences, Suzhou, China, as a full Professor. He has been the director of i-Lab department and the Nano-X Vacuum Interconnected Nanotech Workstation, and deputy director of Academic Committee at Suzhou Institute of Nano-Tech and Nano-Bionics, Chinese Academy of Sciences since 2020.

He got the Distinguished Young Scholars of National Natural Science Foundation of China (2021), the Excellent Supervisor Award of Chinese Academy of Sciences (2020), the Young Science and Technology Talent Award of China Instrument and Control Society (2016), etc.

He served doctoral tutor of the University of Science and Technology of China, associate editor of "Microsystems & Nanoengineering", member of the MEMS device working group of the National Microelectromechanical Technology Standardization Technical Committee, and member of the Smart Medical Professional Committee of the Chinese Society for Artificial Intelligence, etc.

His research interests include smart nanomaterials, flexible electronics, bionic smart sensing and perception technology, wearable intelligent system, and exploring the innovative applications in smart healthcare, artificial intelligence, human-machine integration, energy and environment and other related fields.

Prof. Yufei Liu
Chongqing University, CHINA

Title:

Ultrabright Fluorescent Silicon Nanomaterials for pH Sensing and Bio-Medical Imaging Applications

Abstract:

Fluorescent materials have been introduced as promising materials in recent years, however, most of these suffer from low photoluminescence (PL) quantum yield (QY). A facile one-step method has been developed for ultrabright silicon nanomaterials (SiNPs) with nearly 100% PLQY. These SiNPs also dementated outstanding pH-sensitivity and shown a linear response from pH 4.0 to 7.0, which has been used to constructed a sensing platform for monitoring pH changes in intracellular and zebrafish with remarkable imaging capability, based on its excellent PLQY, PL stability, biocompatibility, and pH sensitivity. The SiNPs could be potentially employed as multifunctional materials for pH monitoring and in-situ imaging for bio-medical applications.

Biography:

Dr. Yufei Liu is currently a professor in College of OptoElectronic Engineering, Chongqing University. He was awarded the B.S. in Physics, M.Eng. in Microelectronics and Solid State Electronics, and Ph.D. in Electronic Engineering, from Peking University, Shanghai Institute of Microsystem and Information Technology CAS, and Heriot-Watt University, in 2003, 2006 and 2011, respectively. Yufei joint Chongqing University in 2014, after his position as Research Fellow in Swansea University and ERC Research Fellow in Imperial College London. He has been the PI for National Key R&D Program of China (MOST Digital Bio-Medical Equipment call) and the Co-PI of National Key R&D Program of China (MOST China-UK Newton Fund call). His current research interests are Micro/Nano Fabrication & Integration Technology, Intelligent Sensing and Fluorescent Molecular Detection.

Abstract

Micro/Nano Manufacturing and Its Applications - Under One Roof Report - Part VIIII

Cao Xia[1], Jie Song[1,2], Hongxiang Han[1], Song Qu[1], Xin Wang[1], Xu Yang[1], Xin Liu[1], Zhifu Yin[1], Takahito Ono[2], Toshihiro Itoh[3,6], Yuji Suzuki[4], Shimoyama Isao[5], **#Dong F. Wang[1,6*]**, Ryutaro Maeda[6], Masayoshi Esashi[7]

[1] Micro Engineering and Micro Systems Laboratory (JML), Jilin University, Changchun 130025, China
[2] Department of Mechanical Systems and Design, Tohoku University, Sendai 980-8579, Japan
[3] Department of Precision Engineering, The University of Tokyo, Tokyo 113-8656, Japan
[4] Department of Mechanical Engineering, The University of Tokyo, Tokyo 113-8656, Japan
[5] Department of Mechano-Informatics, The University of Tokyo, Tokyo 113-8656, Japan
[6] Research Center for Ubiquitous MEMS and Micro Engineering, AIST, Tsukuba 305-8564, Japan
[7] WPI Advanced Institute for Materials Research, Tohoku University, Sendai 980-8577, Japan
 # Corresponding Author / Email: Prof. Dr. Dong F. Wang / dongfwang@jlu.edu.cn, Tel: +86 (0) 431 8509 4698

ABSTRACT

This abstract is the 2022 report of our group, the Micro Engineering and Micro Systems Laboratory (JLU MEMS LAB), originally established in 2004 in Japan, and continued its international exchange culture value conception - Under One Roof with the world. Some selected research works, such as support-limited quality factor enhancement scheme, passive field conversion-amplification scheme, displacement visualization at flexible interface, low 1/f noise of TMR accelerometer, as well as wings-inspired and ball-impacted nonlinear energy harvesters for low frequency energy are introduced here for further applied research and possible industrial-academic-research cooperation.

Keywords: *Support loss, Resonant current sensors, Displacement visualization, TMR accelerometers, Wings-inspired energy harvester, Ball-impacted energy harvester, Under one roof report*

1. HIGH SENSITIVITY SMART SENSING WITH COUPLED RESONATORS/OSCILLATORS

In terms of internal resonance, the frequency enhancement in coupled resonators have been demonstrated in our previous study. A π-shaped oscillator is proposed in our latest work with analyzing the effects of multiple structural parameters on anchor-limited quality factor [1]. Concerning the synchronized sensing applications with low frequency excitation and high frequency vibration pickup, a structural optimization scheme was proposed to reduce the anchor loss, which can improve the quality factor of low frequency mode and high frequency mode simultaneously. Furthermore, two types of coupled oscillators are designed to explore the effect of the coupling element geometry on the support loss, one of the main energy dissipation mechanisms relevant to quality factor. A support-limited quality factor enhancement scheme is therefore proposed by regulating the parallelogram geometry with both the coupling position and the coupling length [2], as shown in Fig. 1.

2. NON-INVASIVE PASSIVE CURRENT SENSING WITH RESONANT CURRENT SENSORS

Current appliances are used widely in our daily life, with extensive applications of various electronic products. Direct current sensing has been realized in our previous works. In our latest work, a passive field conversion-amplification scheme, is proposed [3], by integrating a magnetic cantilever with a tunnel magnetoresistance (TMR) for current monitoring. In this scheme, a magnetic cantilever with a strong field, is driven and vibrated by the interaction with the weak field of current. The passive movement of the magnetic cantilever physically results in a movement of a strong field. The weak field, is thus converted by the movement and further passively amplified into a strong one and further detected by a TMR, as illustrated in Fig. 2. The sensitivity is thus amplified more than an order of magnitude compared to that with only TMR detection.

3. DISPLACEMENT VISUALIZATION AND A LOW 1/F NOISE OF TMR ACCELEROMETER

In our latest work, we report on the first direct observation of a lateral displacement when normal pressure is applied at a flexible contact interface, using our laboratory's self-developed displacement visualization system [4], as illustrated in Fig. 3(a). A coordinate correction scheme that does not depend on specific sensing nodes or sensing units is proposed for lateral displacement introduced pressure distribution mapping. Potential applications are believed to be found in the fields of robot tactile, object contour recognition, and other applications that require high-accuracy pressure distribution measurements. Also, aiming at minimizing 1/f noise of tunnel magnetoresistance (TMR) accelerometers, a new principle incorporated acceleration sensing and 1/f noise suppression is demonstrated both theoretically and experimentally. A new modulation methodology based on periodically biased magnetic field is proposed and validated to effectively minimize 1/f noise of TMR accelerometers, by integrating a high-frequency resonator with a soft magnetic modulation film [5], as shown in Fig. 3(b). This work clarifies a universally applicable low noise sensing principle not only for TMR accelerometers but also for all elasto-magneto-electric coupling sensors like MR/ME displacement sensors or strain sensors.

4. NON-LINEAR ENERGY HARVESTERS FOR DEVELOPING SELF-POWERED SENSORS

Our group is committed to research about various energy harvesters applicable to self-powered sensing applications. To realize multi-directional vibration energy harvesting, a novel direction self-adaptive piezoelectric energy harvester (DSPEH) is explored by introducing a self-adaptive rotation mechanism into the cantilever beam inspired by mosquito wings to validate the new concept [6], as Fig. 4(a). The average output voltage is 30% higher than that of the conventional PEH. Compared with other multi-directional energy harvesters, the proposed DSPEH also has higher energy harvesting efficiency. Efficient energy harvesting with miniaturized harvesters for both low and random frequency vibrations also remain a large challenge. Hence, a wings-inspired design to implement a parametric coupling mechanism is proposed for widening the frequency bandwidth of a Micro-Electro-Mechanical System (MEMS) energy harvester (PCEH) [7], as Fig. 4(b). Compared to those of non-parametric coupling energy harvesters, bandwidths and harvesting capacity of two wings in PCEH are increased by 55.4% and 73.7%, and by 3.3 and 2.5 times, respectively. The proposed PCEH opens a new way for widening the frequency bandwidth of energy harvesters at micro scale and lays a foundation for self-powered systems. Furthermore, an ultra-low frequency ball-impacted potential-variable nonlinear energy harvester (BPNEH) is proposed [8], as Fig. 4(c). The proposed BPNEH along with the double peak phenomenon is applicable to ultra-low frequency scenes of engineering fields such as wearable devices, structural health monitoring systems, etc.

REFERENCES

[1] R. Wang, Dong F. Wang, C. Xia. et al. Microsyst. Technol. Vol. 28, 2022, pp. 985–993.
[2] R. Wang, Dong F. Wang, C. Xia. et al. Microsyst. Technol. Vol. 28, 2022, pp. 1663–1671.
[3] X. Shang, Dong F. Wang, T. Itoh and R. Maeda. IEEE T. Ind. Electron., Vol. 69, No. 5, 2022, pp. 5295-5303.
[4] H. Cao, Dong F. Wang, Z. Yan, X. Jiang, Y. He, I. Shimoyama. IEEE T. Ind. Electron., vol. 71, 2022, pp. 1-8.
[5] Y. Hou, W. Yuan, Dong F. Wang, T. Itoh, R. Maeda. IEEE T. Ind. Electron., Vol. 71, 2022, pp. 1-11.
[6] M. Han, X. Yang, Dong F. Wang, L. Jiang, W. Song, T. Ono, Appl. Energ., Vol. 315, 2022, 119040.
[7] J. Song, C. Xia, G. Shan, Z. Wang, T. Ono, Dong F. Wang. Energ. Convers. Manage., Vol. 267, 2022, 115924.
[8] C. Li, Dong F. Wang, X. Yang, Y. Suzuki. Mech. Syst. Signal Pr., Vol. 182, 2022, 10958

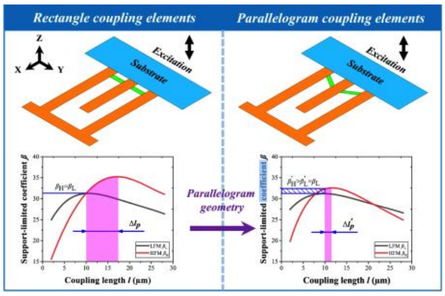

Figure 1. Enhancement scheme of quality factor related to support-loss.

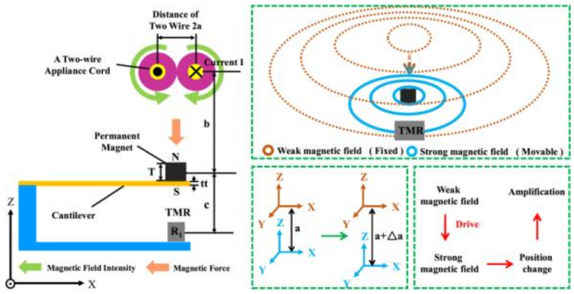

Figure 2. Sensing mechanism of the proposed resonant current sensor.

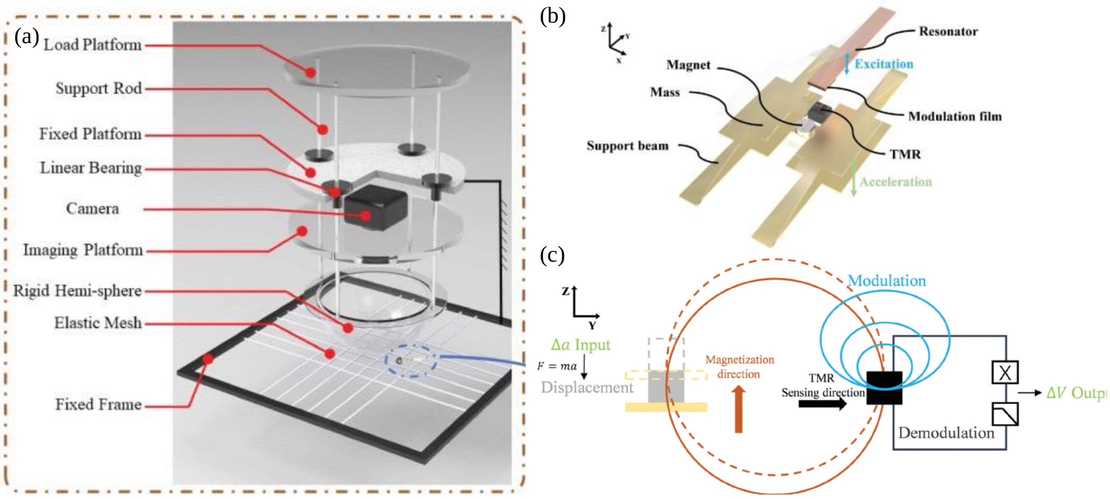

Figure 3. (a) Displacement visualization at flexible interface; (b) Schematic and (c) working principle of the accelerometer structure.

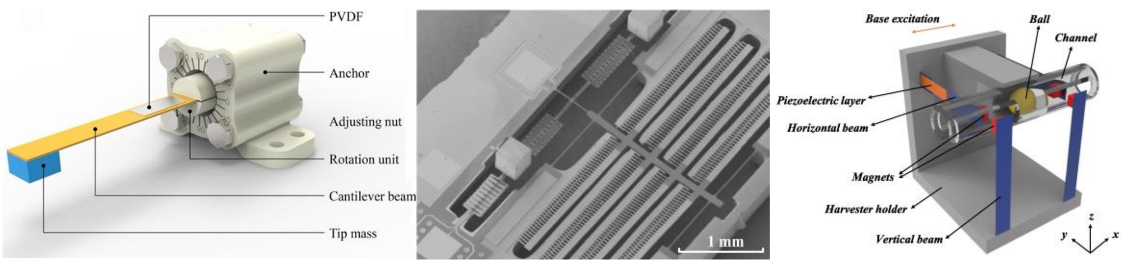

(a) (b) (c)

Figure 4. Energy haverstors for self-powered sensing applications. (a) a direction self-adaptive piezoelectric energy harvester; (b) a wings-inspired MEMS energy harvester; (c) an ultra-low frequency ball-impacted potential-variable nonlinear energy harvester.

Microfabrication of Surface Acoustic Wave Devices with Micro-Patterned AlN Thin Films

Sunao MURAKAMI[1], Kanato KITAMURA[1] and Takahiro ITO[1]

1 Department of Intelligent and Control Systems, Faculty of Computer Science and Systems Engineering, Kyushu Institute of Technology (Kyutech), 680-4, Kawazu, Iizuka, Fukuoka 820-8502, JAPAN
 # Corresponding Author / E-mail: murakami@ics.kyutech.ac.jp

ABSTRACT

In this study, we have fabricated surface acoustic wave (SAW) devices with micro-patterned thin films of aluminum nitride (AlN). Firstly, we deposited AlN thin film on ST-cut quartz (ST-X) substrate using reactive RF-magnetron sputtering with Al metal target in Ar/N_2 gas mixture. After that, nickel (Ni) was deposited as the electrode material and patterned using two sets of combined processes including photolithography and etching. In the first set of the combined processes, micropatterns of Ni thin film were prepared and used as etching masks for the formation of AlN micropatterns. Furthermore, in the second set of the combined processes, the Ni micropatterns were additionally etched to prepare electrodes of SAW devices. The frequency responses have been measured for the SAW devices fabricated on micro-patterned AlN thin film, and have been compared to those of comparable SAW devices fabricated on uniform AlN thin films.

Keywords : surface acoustic wave (SAW) device, aluminum nitride (AlN), quartz, micro-patterned

1. INTRODUCTION

Surface acoustic wave (SAW) devices are one of the piezoelectric microdevices which are widely used as RF filters and resonators, and have received attention as the potential substitutes for physical and chemical sensing [1]. In SAW devices, interdigital transducers (IDTs) work as the micro-transducer between the electrical signals (input and output signals) and the SAW (mechanical vibration wave). It is also known that the acoustic properties including the frequency responses of SAW devices can be controlled by the structure of the substrate and the device element. For example, the peak frequency of SAW devices can be controlled by the design of electrodes in the interdigital region [2]. The controllability of the peak frequency of the SAW propagating through the device substrate is one of the technical advantages of SAW devices. However, it is likely that the control of the frequency characteristics only by the geometry and size in the IDTs does not permit wide ranges of flexibility.

Therefore, we have attempted to increase the flexibility in the control of the frequency characteristics of the propagating wave by the structure of the substrate in SAW devices fabricated on the conventional ST-X substrate. In detail, we have firstly examined the changes in frequency response of SAW devices by combining piezoelectric thin film of aluminum nitride (AlN). The effect of the micro-patterning of the thin film of aluminum nitride (AlN) on the frequency responses also examined for SAW devices with multiple piezoelectric materials.

2. Microfabrication of SAW Devices

We used a Y-rotated, X-propagating ST-cut quartz (ST-X) as a substrate in this study. We have fabricated three-types of SAW devices on ST-X substrates with/without deposited AlN thin films (Fig.1). The first type is a device-(A), in which we have fabricated two IDTs for a SAW device on ST-X substrates (Fig.1(a)). In the others (devices-(B), (C)), the same interdigital micropatterns of metal thin film are fabricated on AlN thin films which are additionally deposited on ST-X substrates (Fig.1(b), (c)). Especially, in the third-type SAW device (device-(C); Fig.1(c)), AlN thin films are micro-patterned and confined to examine the effects of the addition of AlN thin layers on the propagation characteristics of SAW. In this study, we have designed and fabricated SAW devices including IDTs with 50 electrode pairs, and the wavelength (designed values) of the fundamental vibration mode was 20 μm.

The microfabrication procedure of the device-(C) with micro-patterned AlN thin films (Fig. 1(c)) is shown in Fig. 2. The microfabrication started with the formation of AlN thin film (thickness: 500nm) using reactive RF-magnetron

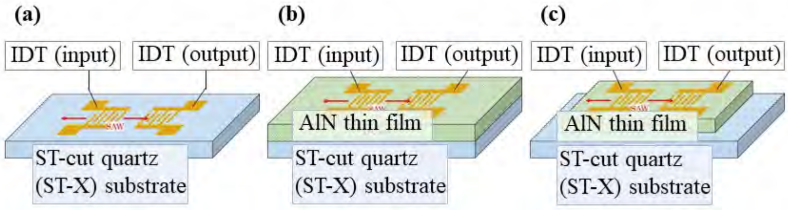

Figure 1 Schematic of three types of SAW devices fabricated on ST-X substrates in this study. (a) device-(A) without AlN thin film, (b) device-(B) with uniform AlN thin film, (c) device-(C) with micro-patterned AlN thin film.

sputtering with Al metal target in Ar/N_2 gas mixture (Fig.2, (ii)). After that, we also deposited Ni thin layer using DC sputtering process immediately (Fig.2, (iii)). Next, micropatterns for the etching masks were drawn on the photoresist layer using photolithography (Fig.2, (iv)) and the micropatterns of AlN thin films were prepared using the consecutive wet etching processes of bi-layered thin films (Fig.2, (v), ((vi)). Finally, additional patterning process of Ni thin film for the preparation of IDTs were performed by using photolithography and wet etching of Ni thin film (Fig.2, (vii), (viii)).

After the microfabrication of those devices, IDTs of each device were observed with optical microscope, and the average distances between adjacent finger electrodes of the IDTs (pitches) were measured in each SAW device. Frequency responses (transmittance properties; S_{21}) were also measured using vector network analyzer.

3. Results

Figure 3 shows optical micrographs of the micro-region including interdigital electrodes of device-(c) fabricated in this study. And the average values of the pitches of the adjacent IDTs are 10.0±0.1 µm (n=20) for three-types of SAW device fabricated in this study (designed value of the pitch: 10 µm). That means that we have been successfully fabricated almost the same micropatterns of the IDT for the three-types of SAW devices.

Furthermore, frequency responses (S_{21}) of each device are shown in Fig. 4. Comparison of the peak frequencies of device (A) and (B) shows that the addition of AlN thin film is effective for the higher SAW velocity (increased peak frequency) as previously reported [3]. It is also known that deposition of AlN thin film on ST-X improve electromechanical coupling coefficient than those of only ST-Q substrate [3]. Meanwhile, the frequency responses (S_{21}) including the peak frequency (f_p) are similar in the device-(B) and device-(C). That means the micropatterns of AlN thin film on ST-X substrate are effective to control the frequency characteristics without significant reflection at the outline of the substrate.

3. CONCLUSION

In this paper, we have fabricated three-types of SAW devices on ST-X substrates with/without deposited AlN thin films. Both uniform and restricted micropatterns of AlN thin film which have been added on ST-X substrates were effective for the control of the frequency properties of the propagating wave of SAW devices.

REFERENCES

1. M.C. Horrillo *et al.*, Detection of volatile organic compounds using surface acoustic wave sensors with different polymer coatings, Thin Solid Film, Vol. 467, pp.234-238, 2004.
2. H. Wohltjen and R. Dessy, Surface acoustic wave probe for chemical analysis. I. Introduction and instrument description, Anal. Chem., Vol. 51, pp.1458-1464, 1979.
3. Wu et al., The structural and acoustic properties of sputtered aluminum nitride on ST-X quartz, J. Mater. Sci. Lett., Vol. 20, pp.1779-1781, 2001.

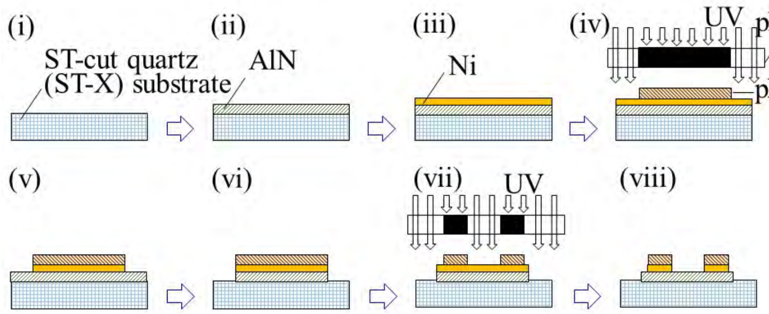

Figure 2 Microfabrication process of SAW device with micro-patterned AlN thin film (device-(C)).

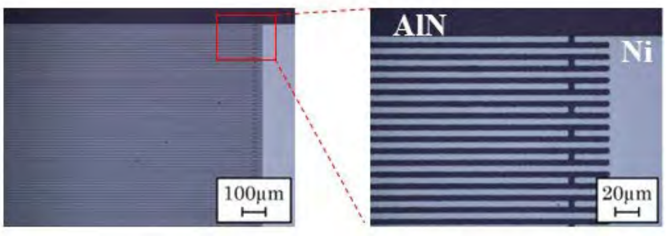

Figure 3 optical micrographs of the region including interdigital electrodes of device-(c).

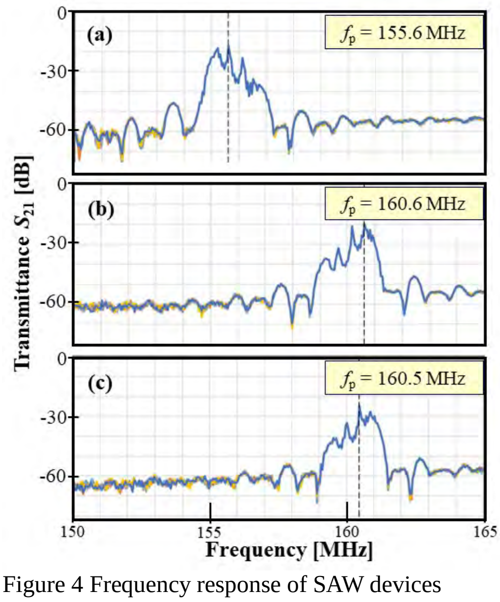

Figure 4 Frequency response of SAW devices ((a) device-(A), (b)device-(B),(c) device-(C)).

Evaluation of humidity-sensing electrode based on conductive carbon resin

#Lan Zhang[1,2] Jian Lu[1] and Sohei Matsumoto[1]

1 Device Technology Research Institute, National Institute of Advanced Industrial Science and Technology (AIST), 1-2-1, Namiki, Tsukuba, Ibaraki 305-8564, JAPAN
2 New-generation Medical Treatment and Diagnosis Research Laboratory, National Institute of Advanced Industrial Science and Technology (AIST), 1-1-1, Higashi, Tsukuba, Ibaraki 305-8566, JAPAN
 # Corresponding Author / E-mail: chou-ran@aist.go.jp, TEL: +86-029-861-2105, FAX: +86-029-861-7225

ABSTRACT
This work is going to develop a thin and flexible humidity sensor electrode using rapid printing technology method. The results demonstrated that the proposed sensor system has a reasonable response in a wide humidity range. The fabricated sensor electrodes with an ultra-thin thickness of only a few tens of microns and completely does not affect the user's comfort. After the relationship between humidity and urine volume was fully understood, the proposed humidity sensor can be used in many application fields, such as, embedding in diapers for urine volume in-situ monitoring, or printing on the mat for urination pattern measurement, etc.

Keywords : Carbon resin, Humidity, Sensor electrode, Urine monitoring, Capacitance

1. INTRODUCTION
In this paper, based on rapid printing technology, the author developed a novel flexure sensor with extended electrodes for humidity measurement. Figure 1(a) shows the photograph of moisture sensor electrode was fabricated on the substrate by the rapid manufacturing system. The contactless print unit of the manufacturing platform is realized by a jet dispenser. The jet dispenser was used to form the sensor electrode, which can stably eject electrode material with a certain distance from the object being processed. The sliding table has a bearing area with 400 × 400 mm, which is large enough to accommodate many kinds of target substrate. The proposed rapid manufacturing system has several incomparable advantages over other traditional manufacturing methods. The most important thing is this, the rapid manufacturing system is not a contact printing method, which means we can print electrodes on uneven surfaces, greatly expanding the range of use. For example, with the increasingly aging society, health detection for the elderly and new-born children has become a very important research topic, the proposed humidity sensor on a diaper can be used to monitor the urine volume [1] for new-born children and measure urination pattern [2] for the elders (see Figure 1(b and inserts)).

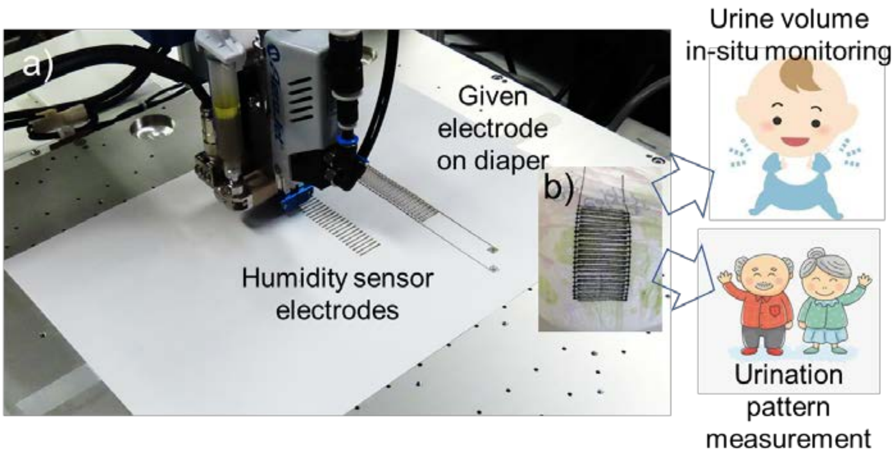

Figure 1 The rapid manufacturing platform of moisture sensor electrode and fabricated typical sensor electrodes on target substrates.

2. EXPERIMENTAL

2.1 Fabrication of carbon-resin based sensor electrode

By the rapid manufacturing system, a typical humidity sensor electrode with size of 50×10 mm^2 was well fabricated. The fabricated sensor pattern was designed and realized with a comb type and two electrodes has an average of 500-um pinch.

2.2 Evaluation of fabricated sensor electrode

In this paper, the series capacitance (Cs) and series resistance (Rs) values of the typical fabricated electrode in different temperature and humidity environment were measured comprehensively. The fabricated sensor electrodes are placed in the test cabinet with well programed and controlled humidity and temperature. The LCR meter is placed outside the chamber by extension wire cable to connecting the electrode and record the output data. We measured the humidity change range from 35 to 95 RH% under the constant temperature of 30, 45 and 60℃, respectively.

Figure 2 shows the comparison of the measured Cs value versus the varying of the relative humidity. Under the same 35% humidity, the Cs values of the typical humidity sensor were measured with the 16.4, 22.68 and 28.88 pF for different temperature of 30, 45 and 60℃, respectively. Figure 3 shows the comparison of the measured Rs value versus the varying of the relative humidity.

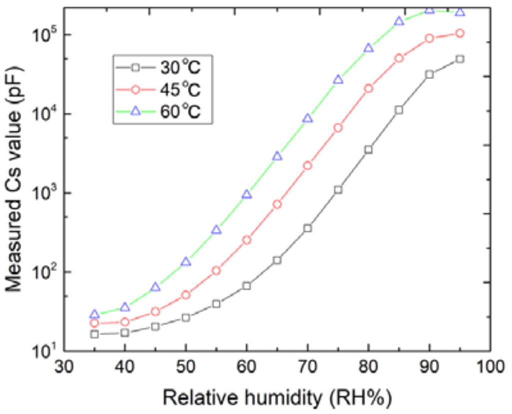

Figure 2 Comparison of the measured Cs value on the relative humidity with different temperature.

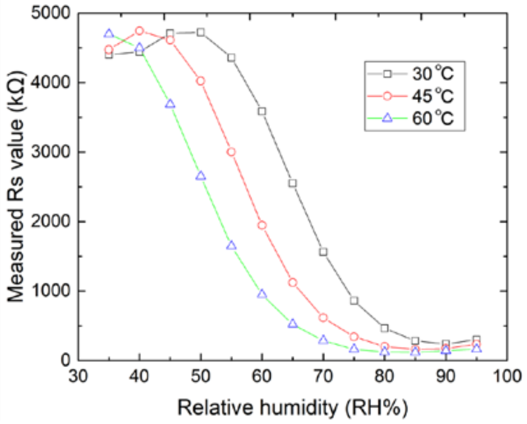

Figure 3 Comparison of the measured Rs value on the relative humidity with different temperature.

3. CONCLUSION

A thin and flexible humidity sensor electrode using rapid printing technology was well developed. The proposed sensor system has a reasonable response in a wide humidity varying range. Moreover, the fabricated sensor electrodes with an ultra-thin thickness of only a few tens of microns and completely does not affect the user's comfort. After the relationship between humidity and urine volume was fully understood, the proposed humidity sensor can be used in many application fields, such as, embedding in diapers for urine volume in-situ monitoring, or printing on the mat for urination pattern measurement, etc.

ACKNOWLEDGEMENT

This research work was supported by New generation Medical Treatment and Diagnosis Research Laboratory, National Institute of Advanced Industrial Science and Technology.

REFERENCES

1. W. Clark, J. Sontrop, J. Macnab, R. Suri, L. Moist, M. Salvadori, A. Garg, Urine Volume and Change in Estimated GFR in a Community-Based Cohort Study, Clinical Journal of the American Society Nephrology, Vol. 6, No. 11, pp. 2634-2641, 2011.

2. Validation and Assessment of Three Methods to Estimate 24-h Urinary Sodium Excretion from Spot Urine Samples in High-Risk Elder Patients of Stroke from the Rural Areas of Shaanxi Province, Environmental Research and Public Health, Vol. 14, No. 10, pp. 1-15, 2017.

High-throughput and label-free cancer stem-like cell assay at a single cell level by microfluidic devices

#Noritada Kaji

Department of Applied Chemistry, Graduate School of Engineering, Kyushu University, Moto-oka 744, Nishi-ku, Fukuoka-shi, Fukuoka 819-0395, JAPAN
 # Corresponding Author / E-mail: kaji@cstf.kyushu-u.ac.jp, TEL: +81-92-802-2883, FAX: +81-92-802-2887

ABSTRACT

The mechanical phenotype of cells is an intrinsic property of individual cells. In fact, this property could serve as a label-free, non-destructive, diagnostic marker of the state of cells owing to its remarkable translational potential. A microfluidic device is a strong candidate for meeting the demand of this translational research as it can be used to diagnose a large population of cells at a single cell level in a high-throughput manner, without the need for off-line pretreatment operations. In this study, we investigated the mechanical phenotype of the human colon adenocarcinoma cell, HT29, which is known to be a heterogeneous cell line with both multipotency and self-renewal abilities. This type of cancer stem-like cells (CSCs) is believed to be the unique originators of all tumor cells and may serve as the leading cause of cancer metastasis and drug resistance. By combining consecutive constriction microchannels with an ionic current sensing system, we found a high heterogeneity of cell deformability in the population of HT29 cells. Moreover, based on the level of aldehyde dehydrogenase (ALDH) activity and the expression level of CD44s, which are biochemical markers that suggest the multipotency of cells, the high heterogeneity of cell deformability was concluded to be a potential mechanical marker of CSCs. The development of label-free and non-destructive identification and collection techniques for CSCs has remarkable potential not only for cancer diagnosis and prognosis, but for the discovery of a new treatment for cancer.

Keywords : Mechanical typing, Single cell analysis, Microfluidic devices, Cancer stem-like cells

1. INTRODUCTION

Induced pluripotent stem cells (iPSCs), which have shown great promise in regenerative medicine, are known to decrease their "deformability" (increase in elastic modulus) as they differentiate[1]. This is true not only for normal cell stem cells, but also for cancer cell populations. It is believed that cancer stem-like cells with high pluripotency exist in the cancer cell population, which may be responsible for cancer recurrence and metastasis. The development of technology to analyze such highly multipotent cancer cells is expected to lead to early detection and early treatment of cancer.

2. EXPERIMENTAL

In this study, we firstly evaluated the pluripotency of HT29 cells and human cervical cancer cells (HeLa cells) by a biochemical approach, ALDH assay. Since HT29 cells are known to be highly pluripotent cancer cells, they are likely to be more pluripotent than HeLa cells. The cell deformabilities were measured by the ionic current changes[2] and the traveling time when the cell passes through the constrictions. This microfluidic device with the two constrictions enabled to measure the cell size and the deformability consecutively.

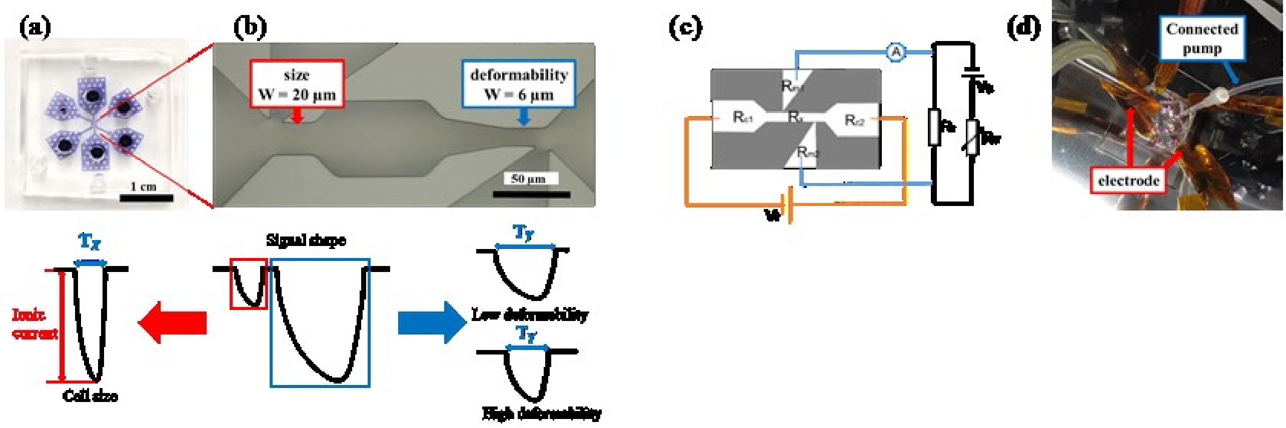

Figure 1: Schematics of ionic current detection system and device (a)Image of device. Bottom left chamber is for introducing sample. Top right one is for connecting pump. (b)Image of ionic current detection system Image of double gap channel. The dimension of detection range for cell size and deformability shown in the figure. The dimension on the channel is 20 µm in height. (c) Circuit diagram of the device (d)Image of ionic current detection system Image of double gap channel. The dimension of

detection range for cell size and deformability shown in the figure. The dimension on the channel is 20 µm in height. (e) Diagram at the center shows signal shape. Left side ionic current signal provides cell size information. Right side one provides cell deformability information. The value of T_Y decreases as cell deformability becomes higher.

3. RESULTS AND DISCUSSION

Figure 2 showed the results of the enzyme activity measurements, ALDH assay, of HT29 and HeLa cells. The x and y axis in the figure shows the side scattering signal and the fluorescence intensity of the ALDH substrate in the cells, respectively. The cells indicated in the right region of the figure are considered to be high ALDH activity corresponding to highly pluripotent cell populations. This result proves that the most of the population of HT29 cells are occupied by highly pluripotent cells than HeLa cells. Moreover, HT29 cells have larger distribution of the fluorescence intensity of the ALDH substrate than the HeLa cells, indicating heterogeneity of the cell population.

Figure 3 showed the results of the ionic current sensing HT29 cells and HeLa cells. The results indicated that HT29 cells had a larger variation in normalized traveling time, and thus had a larger variation in cell deformability than HeLa cells. The results also indicated the heterogeneity in the cell population in HT29 cells. Therefore, our ionic current sensing system demonstrated the ability to discriminate the pluripotency of the cancer cells[3,4].

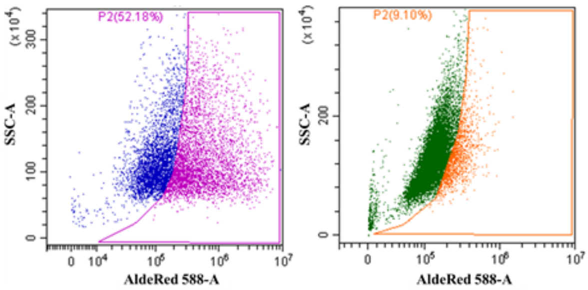

Figure 2: Representative flow cytometry plots for the analysis of ALDH activity in HT29 cells and HeLa cells in the presence of ALDH substrate.(a) Plot of HT29 cells. Highly pluripotent cancer cells contain 52.2 % of the population. The distribution of ALDH substrate fluorescence intensity is large. (b) Plot of HeLa cells. Highly pluripotent cancer cells are present in 9.1% of the population.

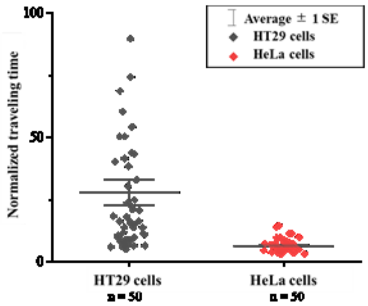

Figure 3: Normalized traveling time (τ) of HT29 cells and HeLa cells. τ is dimensionless number defined uniquely in order to eliminate error. τ is the rate (T_Y/T_X) of first gap traveling time (T_X)and second gap traveling time (T_Y). The smaller value of τ was defined as the higher deformability of the cell.

3. CONCLUSION

If this method can be used not only for cell diagnosis, i.e., single cell analysis, but also for re-collection, it will be possible to apply pre-diagnosed cells to the field of regenerative medicine. To realize this, it is necessary to increase the throughput of the cell diagnosis and re-collection process. We are currently working with Associate Professor Takuya Kubo of Kyoto University to verify whether separation based on cell deformability is possible using chromatography techniques, and we will introduce the results of this work in the presentation.

REFERENCES

1. J. Lv, Y. Liu, F. Cheng, J. Li, Y. Zhou, T. Zhang, N. Zhou, C. Li, Z. Wang, L. Ma, M. Liu, Q. Zhu, X. Liu, K. Tang, J. Ma, H. Zhang, J. Xie, Y. Fang, H. Zhang, N. Wang, Y. Liu, B. Huang: The EMBO Journal, 40, e106123 (2021).
2. H. Yasaki, T. Yasui, T. Yanagida, N. Kaji, M. Kanai, K. Nagashima, T. Kawai, Y. Baba: J. Am. Chem. Soc., 139, 14137-14142 (2017).
3. M. Sano, N. Kaji, A. C. Rowat, H. Yasaki, L. Shao, H. Odaka, T. Yasui, T. Higashiyama, Y. Baba: Anal. Chem., 91, 12890-12899 (2019).
4. M. Terada, S. Ide, T. Naito, N. Kimura, M. Matsusaki, N. Kaji: Anal. Chem., 93, 14409-14416 (2021).

Grating-Based Surface Plasmon Resonance Sensor for Visible Light Employing a Metal/Semiconductor Junction for Electrical Readout

Ryota Kuroki[1], Shinichi Suzuki[1], Shun Yasunaga[2], Masaaki Oshita[1], #Tetsuo Kan[1]

1 Department of Mechanical and Intelligent Systems Engineering, Graduate School of Informatics and Engineering, The University of Electro-Communications, 1-5-1 Chofugaoka, Chofu-city, Tokyo 182-8585, JAPAN.
2 Department of Electrical Engineering and Information Systems, Graduate School of Engineering, The University of Tokyo, 7-3-1, Hongo, Bunkyo-ku, Tokyo 113-8656, JAPAN.
 # Corresponding Author / E-mail: tetsuokan@uec.ac.jp, TEL: +81-42-443-5423

ABSTRACT

We have pursued an electrical readout surface plasmon resonance (SPR) chemical sensor. The proposed SPR sensor has a gold (Au) diffraction grating on an n-type silicon (n-Si) substrate. When the excitation light illuminates the grating, and the SPR happens, the hot electrons are generated by SPR on the grating. The hot electrons are then converted to photocurrent at the Schottky barrier at the Au/n-Si interface. Since the photocurrent provides the refractive index information on the surface of Au, SPR chemical sensing becomes possible with an electrical readout manner. This presentation introduces current research topics regarding the electrical readout SPR sensor and its principle and performance. This technology will contribute to the realization of a thin single-chip label-free chemical sensor.

Keywords: Surface plasmon resonance, Schottky barrier, Electrical readout, Refractive index resolution

1. INTRODUCTION

Surface Plasmon Resonance sensors can detect chemical substances with high sensitivity and are widely used. SPR sensors have been widely applied as taste, gas, and biosensors [1-2]. Conventional SPR sensors are large because they consist of a prism and reflective optics to excite the SPR by total reflection and detect the SPR. In recent years, the miniaturization of the SPR chemical sensing system has been studied[3-4]. In one such study, grating-type SPR sensor devices have been proposed because it does not require an optical prism to couple the SPR onto the sensor. Moreover, semiconductor-based SPR sensors offer electrical sensor readouts in combination with such gratings.

In this study, we propose an electrical readout SPR sensor. Several reports of electrical readout SPR sensors using diffraction gratings detect refractive index changes in the near-infrared light region. However, since the main application of SPR sensors is to detect molecules in an aqueous solution. Since near-infrared light is often absorbed by water, such devices are not necessarily suitable for practical use. Here we report on an electrical readout SPR sensor with a diffraction grating pitch around 500 nm, which can couple visible light.

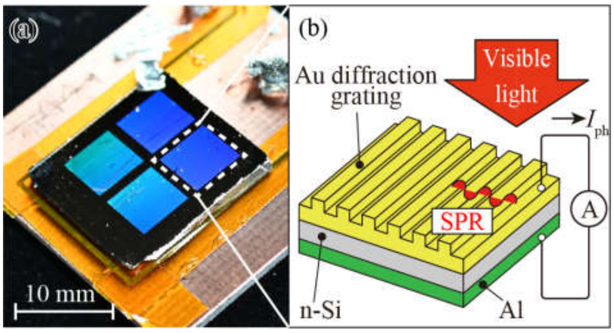

Figure. 1 Surface plasmon resonance sensor, (a) a photograph, and (b) a schematic of the sensor device

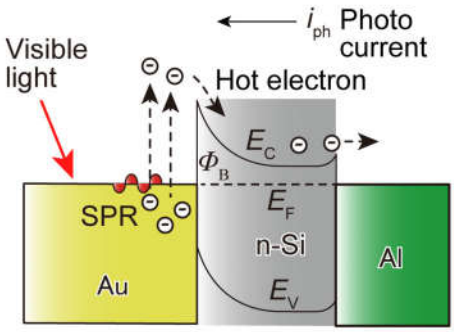

Figure. 2 A principle of the SPR generation and the electrica readout of the SPR singal.

2. FABRICATION AND PRINCIPLE

The prototype device is shown in Figures 1(a) and (b). The diffraction grating geometry was fabricated by electron beam lithography. Using electron beam resist, the grating pattern was formed on an n-Si wafer (ρ = 1-10 Ω·cm). The diffraction grating structure is obtained by patterning an Au film to form stripes by lift-off using the EB resist grating pattern. And finally, 100-nm-thick Au film was deposited on top of the Au stripes. Finally, the Al film was deposited on the entire back surface of the chip to form a cathode electrode for current extraction.

When light is irradiated onto this device from the Au diffraction grating side, the incident light is diffracted by the diffraction grating. When the following Equation (1) conditions are satisfied, the diffracted light induces SPR.

$$\frac{\omega}{c}\sqrt{\varepsilon_{\mathrm{m}}}\sin\theta + \frac{2m\pi}{a} = \frac{\omega}{c}\sqrt{\frac{\varepsilon_{\mathrm{m}}\varepsilon_{\mathrm{Au}}}{\varepsilon_{\mathrm{m}}+\varepsilon_{\mathrm{Au}}}} \quad (1)$$

where ω is the angular frequency of the incident light, c is the speed of light in a vacuum, θ is the angle of incidence on the diffraction grating surface, m is the diffraction order, a is the grating pitch, ε_m is the dielectric constant of the dielectric material facing the grating, and ε_{Au} is the dielectric constant of Au. The energy of the incident light is absorbed by the vibration of free electrons in Au to generate hot electrons. Figure 2 shows the energy band diagram. A Schottky barrier with a typically 0.7—0.8 eV height is formed at the interface between Au and n-Si. When hot electrons overcome the Schottky barrier $q\Phi_B$, they are injected into the n-Si, and the SPR can be detected as a photocurrent i_{ph}. As shown in Equation 1, the wavenumber of the SPR is affected by the dielectric constant of the sample in contact with the Au surface. Since the wavelength or angle of SPR generation changes according to the dielectric constant of the sample, it is possible to measure the chemical amount by monitoring the photocurrent.

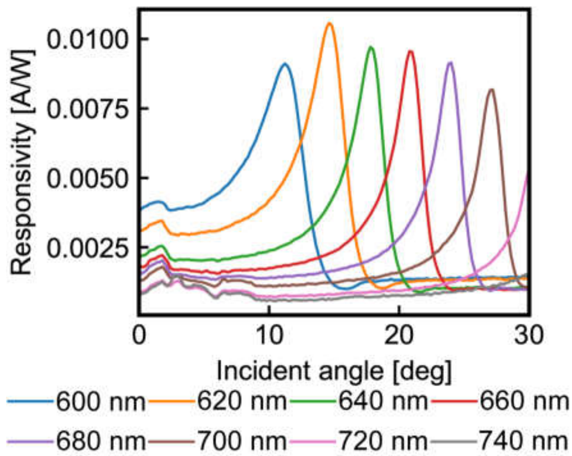

Figure. 3 Electrical responses for the monochromatic light incidence with different visible wavelengths.

3. EXPERIMENT

Experiments were conducted to check the response of the fabricated sensor by irradiating it with visible light. First, as basic characteristics, we measured the angular spectra of current under the condition that the sample on the sensor surface was air. To confirm that the response follows the dispersion relation of SPR, monochromatic light in the wavelength range of 600 - 740 nm was irradiated, the incident angle θ was rotated by 0.2° from 0° to 30°, and the reflectance and current were measured. The monochromatic light was irradiated at eight wavelengths with a wavelength interval of 20 nm. The results of the reflectance measurements at that time are shown in Figure 3. Steep dips were observed at each wavelength, suggesting the occurrence of SPR. Verification using Equation (1) indicates that these SPRs correspond to an order of $m = -1$. The SPR angles are predicted from Eq. (1), and the experimentally obtained angles are consistent with the angular position and shift direction concerning wavelength change. It can be concluded that SPRs are generated on the fabricated device without problems.

4. CONCLUSION

In this study, we report on a grating-type electrical readout SPR sensor that functions under conditions where the surrounding medium is water. Although the data presented in this paper were obtained under air, responses to changes in the refractive index of aqueous solutions have also been obtained. The refractive index resolution in liquid is high enough for a small SPR sensor. It can be concluded that a current-detecting SPR sensor that can be used as a stoichiometric sensor has been realized. The next target is to evaluate the feasibility of deployment for the measurement of substantial bio-molecules by integration with microfluidics.

ACKNOWLEDGEMENT

Electron beam lithography was performed using the University of Tokyo Systems Design Lab (d.lab)'s 8-in. EB writer F5112+VD01, which ADVANTEST Corporation donated. Microfabrication was performed in a clean room of the Division of Advanced Research Facilities (DARF) of the Coordinated Center for UEC Research Facilities of the University of Electro-Communications, Tokyo, Japan. This research was partly funded by JST A-STEP and JSPS KAKENHI (20K20533).

REFERENCES

1. J. Homola, "Present and future of surface plasmon resonance biosensors," Analytical and Bioanalytical Chemistry, vol. 377, no. 3. pp. 528–539, 2003. doi: 10.1007/s00216-003-2101-0.
2. J. Homola, "Surface plasmon resonance sensors for detection of chemical and biological species," Chemical Reviews, vol. 108, no. 2. pp. 462–493, Feb. 2008. doi: 10.1021/cr068107d.
3. Y. Ajiki, T. Kan, K. Matsumoto, and I. Shimoyama, "Electrically detectable surface plasmon resonance sensor by combining a gold grating and a silicon photodiode," Applied Physics Express, vol. 11, no. 2, art. no. 022001, 2018, doi: 10.7567/APEX.11.022001.
4. Y. Saito, Y. Yamamoto, T. Kan, T. Tsukagoshi, K. Noda, and I. Shimoyama, "Electrical detection SPR sensor with grating coupled backside illumination," Optics Express, vol. 27, no. 13, art. no. 17763, 2019, doi: 10.1364/oe.27.017763.

Introduction of the development on vibration-resistant physics package for chip-scale atomic clocks

#Munehisa Takeda, Akihisa Ueno, Isamu Kimura, Takeshi Harada, and Hiroshi Fukumoto

Micromachine Center,
MBR99 Bldg. 6F, 67 Kanda Sakumagashi, Chiyoda-ku, Tokyo 101-0026, JAPAN
 # Corresponding Author / E-mail: m_takeda@mmc.or.jp, TEL: +81-3-5835-1870, FAX: +81-3-5835-1873

ABSTRACT

A vibration-resistant physics package for in-vehicle chip-scale atomic clocks (CSAC) has been developed. The gas cell was fabricated using MEMS technology and was also suspended by thermally isolated support legs. A structure with ribs on the thermally isolated support legs was adopted so as to have vibration resistance. A prototype of the physics package was fabricated. Cs absorption lines were observed, and it was verified that the prototype had basic functions as a physics package for CSAC.

Keywords : Chip-scale atomic clocks, Physics package, MEMS gas cell, Vibration-resistant, Thermally isolated support legs

1. INTRODUCTION

Precise timing is critical for numerous applications such as navigation, communications, surveillance, and synchronization of sensors and systems. Though assured PNT (Positioning, Navigation, and Timing) solutions currently rely on acquiring GPS signals, it is desired to develop a small and highly accurate timing device that can be used even if GPS signals are interrupted. Since the early 2000s, the chip-scale atomic clock (CSAC) has been developed[1)] and commercialized in 2011[2)]. However, commercially available CSAC is expensive, and its vibration resistance and stability are not sufficient for in-vehicle use. A vibration-resistant physics package for in-vehicle CSAC has been developed to solve these problems. In order to improve vibration resistance, we adopted a unique structure in which mass-producible MEMS gas cell is supported by thermally isolated support legs with ribs that have vibration resistance. In this report, we will introduce the structure and operating principle of the vibration-resistant physics package for CSAC, the prototype results, and their basic characteristics.

2. Structure and Operating Principle of Physics Package for CSAC

2.1 Structure

The structure of the physics package for CSAC is shown in Figure 1.

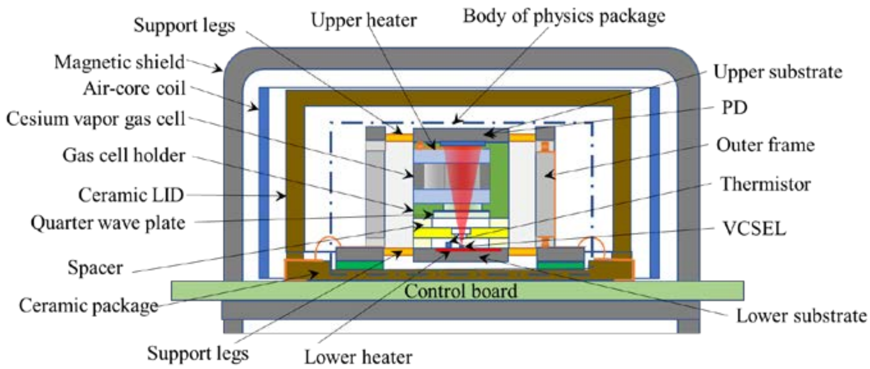

Figure 1. Structure of the physics package

The body of a physics package consists of an upper substrate with a photo diode (PD), a cesium vapor gas cell with an upper heater, a quarter wave plate, and a lower substrate with a vertical cavity surface emitting laser (VCSEL), a thermistor, and a lower heater. The gas cell is fabricated using MEMS technology, is installed in a gas cell holder and suspended by thermally isolated support legs. A structure with ribs on the thermally isolated support legs was adopted so as to have vibration resistance. The body of the physics package is mounted on a ceramic package. The ceramic package is vacuum sealed with a ceramic LID to block the heat that flows from the body of physics package through the air. An air-core coil that applies a magnetic field is arranged on the outer periphery of the ceramic LID, and a magnetic shield that shields an external magnetic field covers the entire circumference including the bottom surface. Finally, the whole physics package is mounted on a control board of a CSAC.

2.2 Operating Principle

Laser light is emitted upward from the VCSEL mounted on the lower substrate. By arranging the gas cell holder containing the quarter wave plate and the MEMS gas cell on the upper part of the VCSEL with the spacer in between, the laser light passes through the quarter wave plate and the gas cell and is detected by the PD mounted on the upper substrate. The lower substrate and the upper substrate are each supported by thermally insulated legs to suppress heat outflow due to heat transfer.

3. Prototype Results of Physics Package

Figure 2 (a), (b), (c) show the lower and upper substrate surfaces and the enlarged SEM (Scanning Electron Microscope) image of the support leg part, respectively. MEMS manufacturing technology was applied to the fabrication. The process consists of rib groove formation on the Si substrate, polyimide film formation on the entire surface of the substrate and polyimide embedding in the rib groove, heater wiring and pad formation, and support leg formation by substrate etching from the back surface.

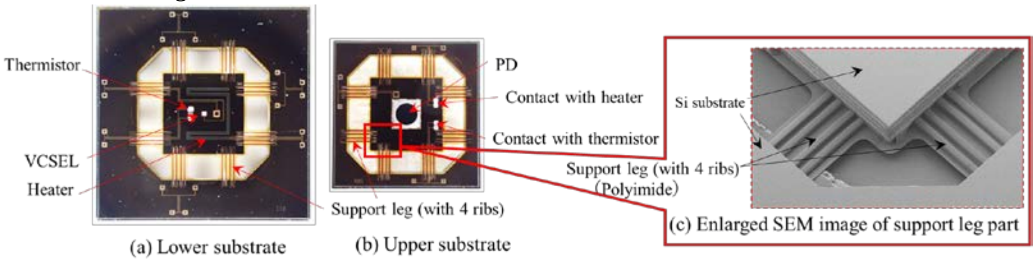

Figure 2. Lower and upper substrate surface

Figure 3 shows the internal structure of the physics package prototype and the observation results of Cs absorption line. It can be confirmed that the MEMS gas cell is incorporated through the transparent outer frame, and the finish is as planned as shown in Figure 1. In addition, Cs absorption lines were also observed in this prototype (Figure 3 (c)). This means that it has a basic function as a physics package for CSAC.

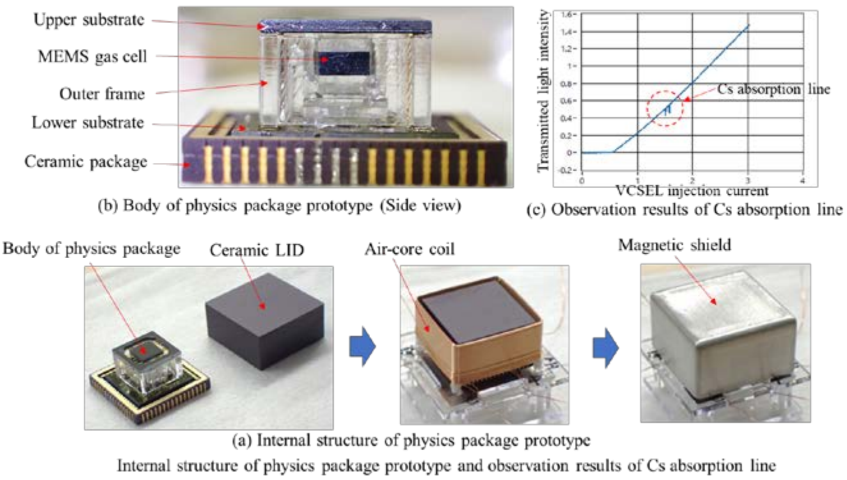

Figure 3. Internal structure of physics package prototype and observation results of Cs absorption line

4. CONCLUSION

A vibration-resistant physics package for CSAC has been developed. In order to improve vibration resistance, we adopted a unique structure in which mass-producible MEMS gas cell is supported by thermally isolated support legs with ribs that have vibration resistance. A prototype of the physics package was fabricated. Cs absorption lines were observed, and it was verified that the prototype had basic functions as a physics package for CSAC.

ACKNOWLEDGEMENT

This study was supported by Innovative Science and Technology Initiative for Security Grant No. JPJ004596, ATLA, Japan.

REFERENCES

1. S. Knappe, V. Shah, P. D. D. Schwindt, L. Hollberg, J. Kitching, L. A. Liew, and J. Moreland, A microfabricated atomic clock, Applied Physics Letters Vol.85, No.9, pp1460–1462, 2004.
2. Symmetricom, Chip-Scale Atomic Clock User’s Guide, Document No.098-00055-000, Rev. 004, 2011

Capsuled edible wireless sensor for gut bacterial monitoring

Ayaka Iami[1], Ken Sakabe[1], Tetsuo Kan[2] and Hiroaki Onoe[1]

1 School of Integrated Design Engineering, Graduate School of Science and Technology, Keio University,
3-14-1 Hiyoshi, Kouhoku, Yokohama, Kanagawa 223-8522, JAPAN
2 Department of Mechanical and Intelligent Systems Engineering, Graduate School of Infromatics and Engineering,
The University of Electro-Communications, 1-5-1 Chofugaoka, Chofu-city, Tokyo, 182-8585, Japan
 # Corresponding Author / E-mail: onoe@mech.keio.ac.jp, TEL: +81-45-566-1507

ABSTRACT

This report describes an ingestible capsule sensor that can wirelessly detect the activity of gut bacteria by irradiating microwaves from outside the body. The proposed sensor is composed of only edible materials: the critical sensing material is a film made of dietary fiber that is decomposed by gut bacteria. We confirmed that the dietary-fiber-made film can be decomposed by gut bacteria, bifidobacteria. For wireless communication, we fabricated an ingestible antenna made from rice paper and gold with a split-ring resonator (SRR), one of the elements of electromagnetic metamaterials. Our sensor fulfills swallowable size and wireless communication requirements for the first time and would be a safety sensor for gastrointestinal (GI) tract monitoring. We believe that our ingestible sensor could be an effective tool for non-invasive biological substances monitoring without retention risk.

Keywords : Edible material, Wireless sensor, Gut bacteria, Monitoring, Electromagnetic Metamaterial

1. INTRODUCTION

Ingestible devices are gathering attention as tools for health management and disease prevention because of the minimally invasive GI biological information acquisition [1]. The feature of the ingestible sensors is small enough to be taken orally, and various types of ingestible sensors have been reported previously [2][3]. However, toxic materials in a typical electronic circuit cause a risk of retention, especially in patients with enteropathies [4]. The approach to solving this problem is fabricating the device with food materials that are completely harmless and safe.

Here in this paper, we propose the ingestible capsule wireless sensor composed entirely of edible materials. Our sensor, whose structure is a passive antenna in the nested inner and outer capsules, can detect gut bacteria for external monitoring.

2. PRINCIPLE

The structure of our passive antenna is a split-ring resonator (SRR), the metallic ring with gaps (Fig. 2(A)), and the SRR can be represented by the simple LC resonator circuit (Fig.2 (B)). Our sensor can measure the resonance characteristics by extracorporeal microwave irradiation. Initially, since the detection target is gut bacteria, our device is delivered to the intestine by an enteric-coating outer capsule to protect the sensor from gastric acid (Fig. 2(C)(i)). When the device reaches the intestine, the outer capsule is dissolved at a pH of the intestine (Fig. 2(C)(ii)), and gut bacteria break down the exposed inner capsule, whose sealing material is a dietary fiber (Fig. 2(C)(iii)). Finally, as the passive antenna interface changes from air to body fluid, the detection signal also changes since the SRR is affected by the dielectric properties of the interface (Fig. 2(C)(iv)). This signal change means proof of the presence of gut bacteria.

We fabricated the antenna by depositing gold on rice paper. The edible antenna was encapsulated in the inner capsule (#0) with a dietary-fiber film and further encapsulated in the enteric-coating outer capsule (#AAA) (Fig. 3).

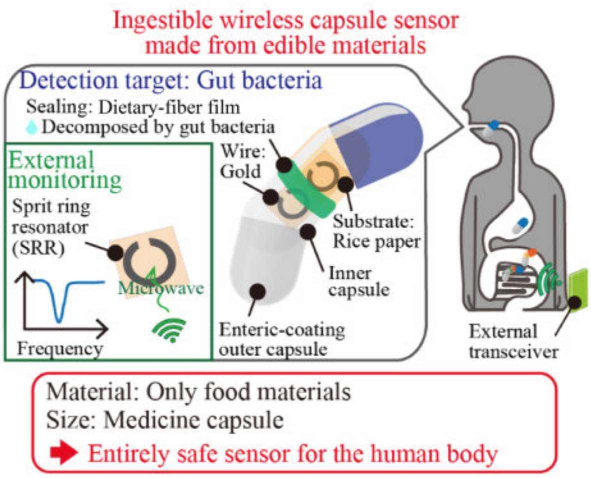

Figure 1: Concept of our ingestible wireless capsule sensor for detection of the biological substances. The sensor is only composed of edible materials without battery for less burden gastrointestinal (GI) examination. Our sensor could detect the activity of gut bacteria wirelessly.

3. EXPERIMENTS

We evaluated the degradation of dietary-fiber films using bifidobacteria. The degradation time of the dietary-fiber film was faster in the solution with bifidobacteria than that in a buffer solution, showing that the dietary-fiber film is an effective substance for detecting bifidobacteria. Wireless measurement of our sensor was tested by irradiating the SRR antenna with microwaves and monitoring the signal strength of S21. The SRR antennas patterned on rice paper resonated at a specific frequency (5.04 GHz). We also confirmed that the transmission characteristics of the electromagnetic waves were different when the SRR antenna was inside (air interface) or outside (water interface) the capsule by simulation. These results indicate that wireless measurement is possible due to the change in the interface caused by the action of the detection target. Furthermore, we demonstrated the degradation of the capsule sealed with the dietary-fiber film. In the solution with bifidobacteria, the dietary-fiber film began to degrade in about 5 minutes, and the capsule disintegrated more quickly than in a buffer solution. These results indicated that our proposed sensor system could be helpful in detecting gut bacteria.

4. CONCLUSION

In this paper, we introduced the ingestible wireless-capsule sensor made from edible materials for gut bacteria monitoring. We confirmed that the proposed dietary-fiber film was significantly degraded by bifidobacteria, a type of intestinal bacteria. In addition, we demonstrated that the edible SRR antenna was activated. Furthermore, we confirmed that the signal strength of the SRR antenna can be changed by using the change in the surrounding environment of the antenna. These results indicated that our proposed sensor system could be helpful in detecting gut bacteria.

ACKNOWLEDGEMENT

This work was partly supported by the Translational Research program; Strategic PRomotion for practical application of INnovative medical Technology (TR-SPRINT) from the Japan Agency for Medical Research and Development (AMED).

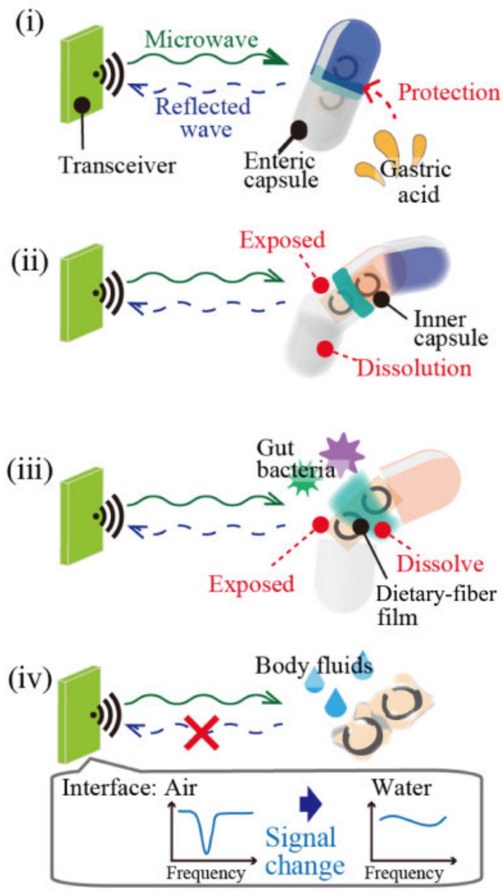

Figure 2: Principle of the wireless detection of gut bacteria.

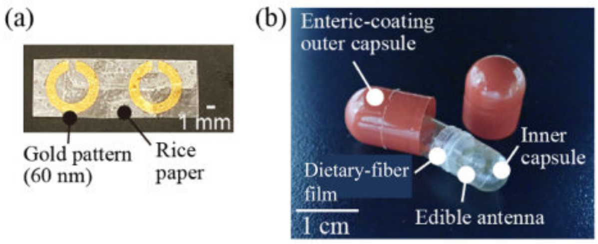

Figure 3: Fabricated device. (a) Image of edible antenna. (b) Image of overall ingestible capsule sensor.

REFERENCES

1. L. A. Beardslee et al., “Ingestible Sensors and Sensing Systems for Minimally Invasive Diagnosis and Monitoring: The Next Frontier in Minimally Invasive Screening,” ACS Sensors, vol. 5, no. 4, pp. 891–910, 2020.
2. M. S. Arefin, J. M. Redoute, and M. R. Yuce, “Integration of Low-Power ASIC and MEMS Sensors for Monitoring Gastrointestinal Tract Using a Wireless Capsule System,” IEEE J. Biomed. Heal. Informatics, vol. 22, no. 1, pp. 87–97, 2018.
3. M. Mimee et al., “An ingestible bacterial-electronic system to monitor gastrointestinal health,” Science, vol. 918, no. May, pp. 915–918, 2018.
4. A. S. Sharova, F. Melloni, G. Lanzani, C. J. Bettinger, and M. Caironi, “Edible Electronics: The Vision and the Challenge,” Adv. Mater. Technol., vol. 6, no. 2, 2021.

Development of Inter-electrode Thin Gaps Filled by Nanofluids for the Investigation of Direct Electrification Mechanism

#Jian Lu[1], Minoru Sakata[2], Lars M. Andersson[2], Lan Zhang[1], Hiroshi Goto[2]

1 Device Technology Research Institute, National Institute of Advanced Industrial Science and Technology (AIST)
1-2-1, Namiki, Tsukuba, Ibaraki 305-8564, JAPAN
2 GCE Institute Inc., Ginza 6-6-1, Chuo-ku, Tokyo, 104-0061, JAPAN
 # Corresponding Author / E-mail: jian-lu@aist.go.jp, TEL: +81-029-8491180

ABSTRACT

This paper presents the design, fabrication, and evaluation of large area thin gaps between metal electrodes with different work functions. Nanofluids with Au particles of 3-5 nm in diameter were then filled into the inter-electrode gaps with the thickness ranging from sub-um to a few um to investigate underlaying physics of direct electrification. The merits, achievements, as well as process difficulties of each design will be presented in detail. Evaluation results demonstrated good repeatability and reliability of the proposed structure, by which an improved device performance was achieved.

Keywords: thin gap, inter-electrode, nanofluid, work function, direct electrification

1. INTRODUCTION

Direct electrification from heat is simpler and less bulky in device design, thus are more flexible for portable and implantable applications in IoT society and coming 6G era [1]. Out previous works have revealed that by filling a nanofluid consisting of dodecanethiol coated Au nanoparticles dispersed in tetradecane into an inter-electrode gap with sub-um to a few um thickness, continues current flow was successfully achieved even at room temperature [2][3]. To investigate the device mechanism and its underlaying physics, various structures were proposed and fabricated using micro-fabrication technologies and low-temperature bonding processes for the pursuit of controllable, repeatable, and solid gaps. The details will be presented in this paper at the conference.

2. Structure Design and Fabrication Processes

Two types of structure with the same surface area were proposed, which have interdigital gap and parallel gap as shown in fig. 1(a) and (b). In the device with interdigital gap, firstly Pt electrode with line width of 3 um was sputtered and etched, followed by W or Al electrode deposition using lift-off, and finally the sealing ring made by UV resin was coated by a dispenser equipped with a robot arm. As shows in fig. 1(c), the device with 3 um gap was achieved successfully. However, the device with 1 um gap had low yields due to process difficulties during lift-off. Thickness of the electrodes were limited too, so as to the effective gap area which is less than 15% of the device with parallel gap shown in fig. 1(d). In the device with parallel gap, glass/Au pillars with diameter of 0.4 mm and pitch of a few mm were used as spacers to control gap thickness as well as to avoid electrical shortage between electrodes. The details have been discussed elsewhere [3]. Fig. 2 shows the evaluation circuits, which uses 1 Mohm as the load resistor and a datalogger with 1 Mohm internal impedance for data acquisition.

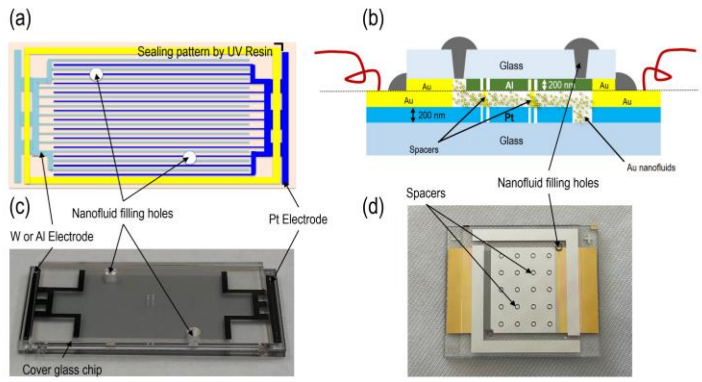

Fig. 1 Structure of the device with interdigital gap (a) and parallel gap (b); and photos of the fabricated devices with interdigital gap (c) and parallel gap (d).

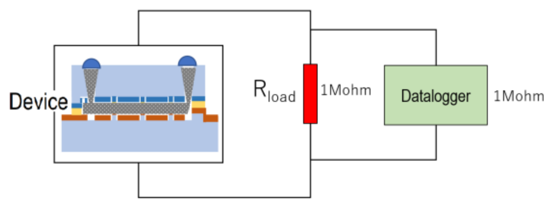

Fig. 2 Circuit for device evaluation using 1Mohm load resistor and a datalogger with 1Mohm internal impedance. The devices were set into a oven at a certain temperature.

3. Experimental Results and Discussions

Fig. 3 shows the measured performances of the device with interdigital gap. The temperature dependency was clearly identified, whereas the output level was much lower than the device with parallel gap [3]. Besides its much smaller effective gap area, nanofluid may not be able to fill the gap effectively due to the wettability as shown in SEM image in inset of fig. 3. Although sub-um gap is difficult to realize by using the device with interdigital gap, fig. 4 clearly shows that the device can be used to monitor the movement of nanoparticles due to its transparent cover glass, which is essentially important to investigating the device mechanism and its underlaying physics.

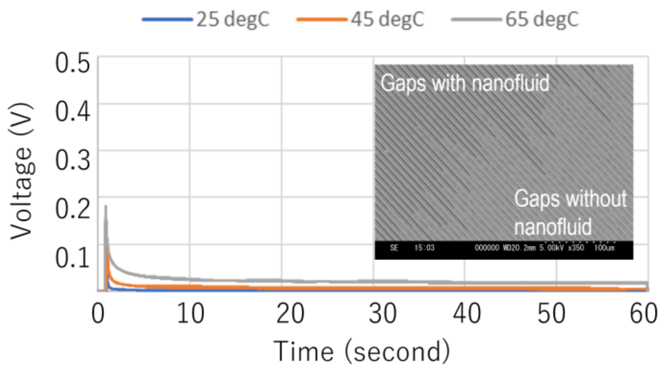

Fig. 3 Measured output of the device with interdigital gap (gap thickness: 3 um; electrode: Pt and W). Inset shows SEM image of the gap after filling nanofluid.

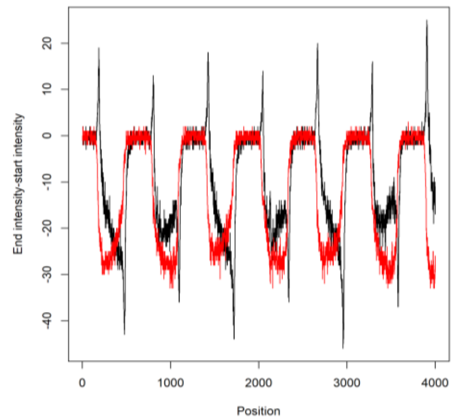

Fig. 4 Nanoparticles movement token by fluorescence-microscope before & after applying electric field to interdigital gap.

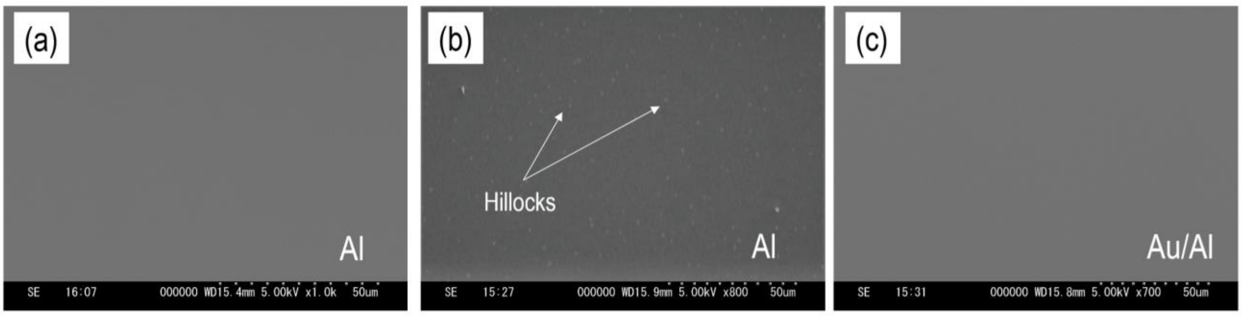

Fig. 5 SEM image of (a) as-deposited Al electrode surface; (b) Al electrode after Ar plasma surface treatment; and (c) Au/Al electrode after Ar plasma surface treatment.

Process of the device with parallel gap is much complicated than the device with interdigital gap, even though controllable, repeatable and solid gaps can be achieved with the thickness ranging from sub-um to a few um. Low temperature bonding using Au thin film is the crucial step to avoid deterioration of the work functions of the electrodes. As shown in fig. 5 (b), Ar plasma treatment prior to bonding resulted in “hillock” on the surface of Al, which frequently lead to short circuit when the gap was 0.5um or less. No “hillock” was found on as-deposited Al or Au covered electrode, as shown in fig. 5(a) and (c). The process needs to be further improved to achieve the gap in nm range.

3. CONCLUSION

The efforts and results in this work may offer practice applicable nanomanufacturing approaches to fabricating submicron gaps for the investigation of direct electrification mechanism as well as for many other potential applications.

REFERENCES

1. D. Champier: Thermoelectric generators: a review of applications, Energy Convers. Manag., Vol. 140, No.15, pp.167-181, 2017.
2. H. M. Nguyẽna, J. Lu, H. Goto, and R. Maeda: Thermionic emission via a nanofluid for direct electrification from low-grade heat energy, Nano Energy, Vol.49, pp. 172-178, 2018.
3. J. Lu, M. Sakata, L. M. Andersson, T. Yasuda, L. Zhang and H. Goto: Mass-producible energy generator with nano gap for direct electrification from low-grade heat, 2022 IEEE 35th International Conference on Micro ElectroMechanical Systems Conference (MEMS), pp. 604-607, 2022.

Mechanical-electrical stimulation integrated culture platform for promoting actuation performance of engineered skeletal muscle

Xiaoxiao Chen[1], Xuefei Chen, Fakang Zhou and #Jianfeng Chen[1]

1 School of Advanced Manufacturing, Nanchang University, Nanchang, Jiangxi 330031, China
 # Corresponding Author / E-mail: cjf@ncu.edu.cn, TEL: +86-17681109005

ABSTRACT

As an indispensable factor in the physiological environment of skeletal muscle, mechanical stimulation played a significant role in regulating skeletal muscle orientation and differentiation. However, mechanical stimulation alone had limited effect on promoting actuation ability of engineered skeletal muscle, which cannot meet the growing demand for actuation capacity of engineered skeletal muscle. Herein, we constructed an integrated mechanical-electrical stimulation culture platform to explore the synergistic effects of multiple factors on the performance of engineered skeletal muscle. The addition of insulin-like growth factor-I (IGF-I) is accompanied by the increasing myotube density and size, and a delayed in the decline of myotube contractility with culture time. Then, under the stimulation of low frequency electrical signals, skeletal muscle can produce regular contractile movements to train their contractility. The combination of uniaxial stretching (US), IGF-I and electrical stimulation training (ES) greatly promoted the proliferation, differentiation and maturation of myotubes, and increased the contraction displacement of myotubes by ~3.2 times. This engineered skeletal muscle with high density myotubes and improved contractility has great potential for biohybrid actuation.

Keywords: Skeletal muscle, hydrogel microfibers, biohybrid actuation, mechanical stimulation, electrical stimulation.

1. INTRODUCTION

Tissue engineered skeletal muscle, as the most potential power source for biohybrid actuators, faces many challenges in biohybrid actuation due to its limited actuation capacity, low output efficiency, and short lifespan[1]. As an indispensable factor in the cellular microenvironment, mechanical stimulation has been widely used to modulate the performance of engineered skeletal muscle[2]. However, the limited contribution of mechanical stimulus to the performance optimization of engineered skeletal muscle remains difficult to accommodate the high demands on biohybrid actuation. The mechanical training has been proven to increase the muscle mass and output force in mammal[3], which is effective in optimizing skeletal muscle output. However, the mechanical training in tissue engineering is mostly based on dynamic mechanical stretching or cyclic magnetic stretching, which requires large space occupation and a complex control system, which will increase the risk of contamination and reduce the efficiency[4, 5]. Therefore, an appropriate training method is highly needed to improve the maturity of skeletal muscle for the application in biohybrid actuation.

Here, we constructed a mechanical-electrical stimulation integrated culture platform to explore the effect of multi-factor synergy on the performance of engineered skeletal muscle (Figure 1A-B). The introduction of mechanical stimulation significantly improved the function of the microfiber skeletal muscle (Figure 2A-C), but its actuation capacity significantly decreased over time in culture (Figure 2I). Then, insulin-like growth factor-I (IGF-I) is added to the uniaxial stretched cell-laden microfiber, significantly improve the density and size of myotubes, and delay the decay of myotube contraction with culture time (Figure 2A-B). Subsequently, low-frequency electrical signal is used to conduct electrical stimulation training on the microfiber skeletal muscles. Under the stimulation of low-frequency electrical signals, skeletal muscles produce significantly enhanced the size (from 33.01±8.82 μm for US group to 58.61±8.82 μm for US+IGF-I+ES group), alignment (about 51%) and contractile capacity of the engineered skeletal muscle (Figure 2F-H). The mechanical-electrical stimulation integrated culture platform reduces device complexity, reduces the risk of cell contamination, and enables in situ observation of skeletal muscle actuation functions. The combination of uniaxial stretching, IGF-I and electrical stimulation training greatly promoted the proliferation of myoblasts and the formation and maturation of myotubes, and the contraction displacement of myotubes increased by ~3.2 times. This microfibrillar skeletal muscle with a high-density myotube sequence and improved actuation capability has great potential for biohybrid actuation.

2. Materials and Methods

2.1 Fabrication of mechanical-electrical stimulation integrated culture platform.

The stretching device with a sample observation window (6 mm in width, 18 mm in length) and two columns of wells was fabricated by 3D printing (Figure 1A). Then, the electrode holder was customized with acrylic sheet to quantify the electrode spacing, and the petri dish lid with two rectangular holes was fabricated using laser cutting to allow the electrodes to be inserted into the culture medium and avoid contamination (Figure 1B). Subsequently, the fixed platinum electrodes were inserted into the petri dish with pillar well-array based stretching device to form an electrical stimulation integrated culture platform (Figure 1C).

2.2 Cell-laden microfiber fabrication and addition of IGF-I.

The cell-laden microfiber was fabricated and stretched as reported previously[6]. Recombinant mouse IGF-I (Sigma, USA) was dissolved in 100 mM glacial acetic acid to prepare a working solution of 10 μg/ml, and placed in a -20°C refrigerator for use. Then, as the density of C2C12 myoblasts on the microfiber skeletal muscle is about 90%, change the growth medium to a differentiation medium containing 50 ng/ml IGF-I, and then culture and differentiate.

2.3 Quantification of electrical responses of microfiber muscle.

The electric field intensities and frequencies of the stimulation wave were 4, 6, 8, 10, 12 V/cm at 1 Hz and 0.5, 1, 2, 3, 4, 5 Hz at 6 V/cm for each sample. The contraction of myotubes were monitored and recorded using CCD camera by phase contrast microscopy at 30 frames per second. The displacement of myotubes were quantified using particle tracking algorithm in Fiji/ImageJ.

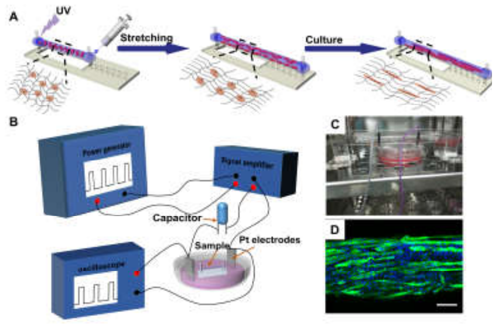

Figure 1. (A) Schematic representation of the stretching device. (B-C) Schematic diagram and image of integrated mechanical-electrical stimulation culture platform. (D) Fluorescence image of myotubes embedded in microfiber.

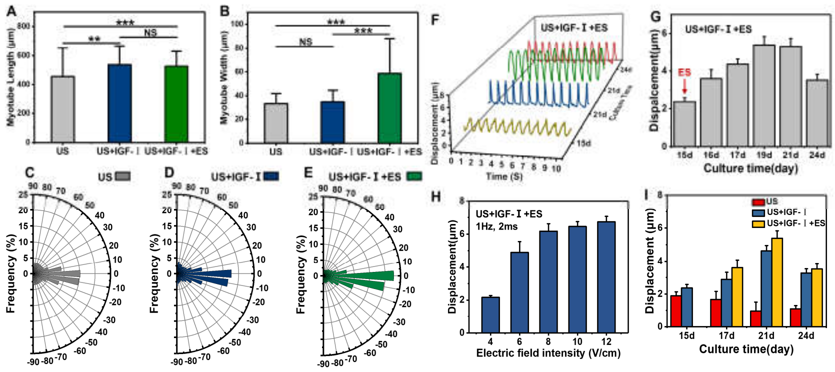

Figure 2. Quantification of length (A), width(B) and alignment (C-E) of myotube in microfiber skeletal muscle under various factors. (F-I) Quantification of contraction displacement of myotube length and width in microfiber skeletal muscle under various factors.

3. CONCLUSION

The mechanical-electrical stimulation integrated culture platform enables the synergy of mechanical, biochemical, and electrical stimulation training factors to significantly promote the optimization of microfiber skeletal muscle actuation performance. The introduction of uniaxial stretching promotes the directional growth and differentiation of myoblasts; the addition of IGF-I has effectively promoted the proliferation of myoblasts, which significantly increase cell density, myotube size and differentiation efficiency; while electrical stimulation training simulates muscle exercise training can promote the hypertrophy and maturation of myotubes. Multiple factors act at different stages of skeletal myogenesis, resulting in microfiber skeletal muscles with well-oriented, densely arranged myotubes, and enhanced actuation capabilities. Besides, attenuation of the actuation ability of microfiber skeletal muscle the with culture time was significantly delayed, enabling it to maintain a stable and high level of actuation capability. The stable and excellent performance of microfiber skeletal muscles optimized for multi-factor-induced performance in actuation and their inherent scalability suggest them potential application in multi-scale biohybrid actuation.

ACKNOWLEDGEMENT

This work is financially supported by the National Natural Science Foundation of China (No. 51905248).

REFERENCES

1. Leonardo Ricotti, Barry Trimmer, Adam W. Feinberg, Ritu Raman, Kevin K. Parker, Rashid Bashir, Metin Sitti, Sylvain Martel, Paolo Dario and A. Menciassi, Biohybrid actuators for robotics: A review of devices actuated by living cells. Science Robotics Vol. 2 No. 12, pp. eaaq049,2017.
2. C. Rinoldi, M. Costantini, E. Kijenska-Gawronska, S. Testa, E. Fornetti, M. Heljak, M. Cwiklinska, R. Buda, J. Baldi, S. Cannata, J. Guzowski, C. Gargioli, A. Khademhosseini and W. Swieszkowski, Tendon Tissue Engineering: Effects of Mechanical and Biochemical Stimulation on Stem Cell Alignment on Cell-Laden Hydrogel Yarns. Adv Healthc Mater, Vol. 8 No. 7, pp. e1801218,2019.
3. D. Park, S. J. Park, S. Cho, Y. Lee, Y. K. Lee, J. J. Min, B. J. Park, S. Y. Ko, J. O. Park and S. Park, Motility analysis of bacteria-based microrobot (bacteriobot) using chemical gradient microchamber. Biotechnol Bioeng, Vol. 111 No. 1, pp. 134-143,2014.
4. G. Zhao, X. Bao, G. Huang, F. Xu and X. Zhang, Differential Effects of Directional Cyclic Stretching on the Functionalities of Engineered Cardiac Tissues. ACS Applied Bio Materials, Vol. 2 No. 8, pp. 3508-3519,2019.
5. Y. Li, G. Huang, B. Gao, M. Li, G. M. Genin, T. J. Lu and F. Xu, Magnetically actuated cell-laden microscale hydrogels for probing strain-induced cell responses in three dimensions. NPG Asia Materials, Vol. 8 No. 1, pp. e238-e238,2016.
6. X. Chen, W. Du, Z. Cai, S. Ji, M. Dwivedi, J. Chen, G. Zhao and J. Chu, Uniaxial Stretching of Cell-Laden Microfibers for Promoting C2C12 Myoblasts Alignment and Myofibers Formation. ACS Appl Mater Interfaces, Vol. 12 No. 2, pp. 2162-2170,2020.

Grasping Force Evaluation of Minimally Invasive Surgical Robotic Forceps

Kazutaka Sato[1], Shuichi Morizane[2], Atsushi Takenaka[2], Masaru Ueki[3], Sang-Seok Lee[4] and #Tadao Matsunaga[4]

1 Department of Engineering, Graduate School of Sustainability Science, Tottori University, Tottori, Japan
2 Division of Urology, Department of Surgery, Faculty of Medicine, Tottori University, Yonago, Japan
3 Division of Medical Education, Department of Medical Education, Faculty of Medicine, Tottori University, Yonago, Japan
4 Electrical Engineering and Computer Science, Faculty of Engineering, Tottori University, Tottori, Japan
 # Corresponding Author / E-mail: matsunaga@tottori-u.ac.jp, TEL: +81-857-31-5104

ABSTRACT

The purpose of this study is to realize the grasping force measurement of forceps for minimally invasive surgical robots. The minimally invasive surgical robots currently in widespread use limit the direct sensation of the surgeon and require a high level of control skills and proficiency to use. The ability to sense the grasping force is in high demand in surgical robotic forceps. However, considering the practical aspects such as miniaturization and tolerant to electromagnetic noise, grasp force sensing in surgical robots remains challenging. To solve those problems, we proposed a novel grasp force sensing system using thin optical displacement sensors and a spring. In this paper, to design a spring for the proposed sensing system, the grasping force of da Vinci surgical system and the traction force of the forceps driving wire has been evaluated.

Keywords : Grasp force, Surgical robot, Robotic forceps, da Vinci

1. INTRODUCTION

Close to 7,000 da Vinci systems are installed worldwide with more than 10 million procedures performed through 2021 [1]. Although the minimal invasive robotic surgery has many advantages, it has also drawbacks. The most important drawback to be improved is the lack of direct force sensation for robotic forceps during operation. To improve this drawback, haptic sensors for surgical robotic forceps have been widely studied. Arata et al. has presented a modular optic force sensor using a Fabry–Perot interferometer that can be used on surgical devices [2]. Due to the involved challenges in sensor design, mass production, and cost, no haptic feedback is yet provided in da Vinci systems [3]. In this study, we propose a new optical force sensor using optical displacement sensors utilizing MEMS fabrication techniques and a designed spring. For this purpose, the grasping force of da Vinci forceps has been measured utilizing st rain gauges and the relationship between the grasping force and the traction force applied to the forceps driving wire has been evaluated.

2. GRASPING FORCE SENSING SYSTEM

Figure 1 shows an overview of the proposed grasping force sensing system. The opening and closing of the robotic forceps is driven by wires. In this system, the elongation of the spring attached to the driving wire is measured with high precision to obtain the grasp force of the robotic forceps [4]. To measure the spring elongation, optical displacement sensors are mounted on both ends of the spring. This optical displacement sensor consists of an optical fiber, of which the diameter is 125 µm, and an optical interference part. The proposed sensing system is suitable for miniaturization and has tolerant to electromagnetic noise.

3. EXPERIMENT AND RESULTS

3.1 Grasping Force Measurement of da Vinci Forceps

To design a spring for the grasp force sensing system, the grasp force of da Vinci forceps was measured. For this grasp force measurement, a strain gauge with a spherical surface was used, as shown in Fig. 2. Note that the spherical shape of the strain gage was formed convex shape to ensure that the grasping force is applied uniformly to the sensing surface of the strain gauge. Three types of da Vinci Xi forceps (Bipolar Forceps, ProGrasp™ Forceps and Needle Driver) were used for measurement. The strain gauge was grasped with the tip of the forceps. During actual surgery, biological tissue is grasped with the tip of the forceps. In the experiment, the strain gauge was grasped in weak grasping and strong grasping.

To convert the output voltage of the strain gauge into a grasping force, a force gauge was used. In addition, to make the touching area of the strain gauge and the force gauge the same, a forceps of the same type as in the grasping force measurement was placed between the strain gage and the force gage.

In the experiment, the correlation between the output voltage of the strain gauge and the grasping force of the da Vinci forceps has been measured and evaluated.

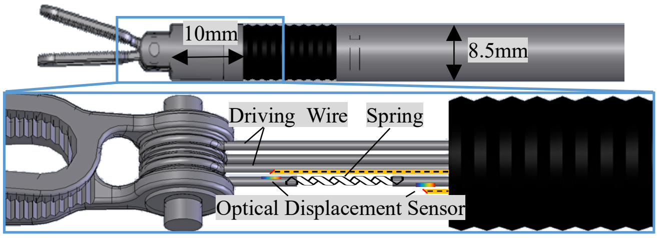

Figure 1 Schematic image of proposed robotic forceps grasping force sensing method.

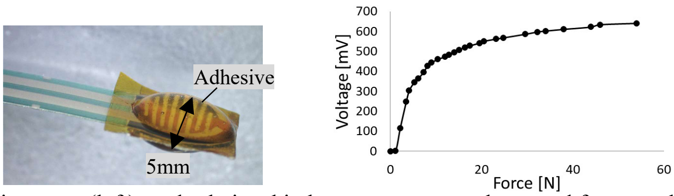

Figure 2 Spherical shaped strain gauge (left), and relationship between output voltage and force applied to strain gauge (right).

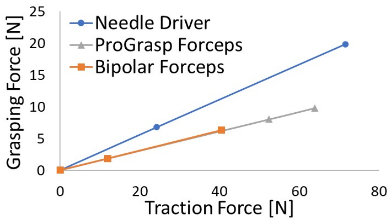

Figure 3 Relationship between grasping force and traction force on driving wire of da Vinci forceps.

3.2 Grasping Force and Traction Force on Driving Wire

A force gauge was used to measure the traction force on the driving wire. The force gauge was fixed on the computer controlled stage, and the wire was pulled by an arbitrary amount of displacement. The measurement results of the traction force and forceps grasping force are shown in Fig. 3.

The results show that the Needle Driver can generate a large grasping force with a small traction force. This is because the Needle Driver is used to grasp the suture needle which is not tissue. The ProGrasp^{TM} forceps have a small range of traction and grasping force, and can switch between the grasping force instantaneously. The Bipolar forceps are used for hemostasis and have a small grasping force. Thus, we confirmed that the grasping force of forceps is controlled according to the purpose.

3.3 Specifications of Spring for Grasping Force Sensing System

The maximum wire traction force of the ProGrasp^{TM} forceps was observed to be 60 N as shown in Fig. 3. In addition, the measurement range of the our developed optical displacement sensor is designed to 2 mm. Therefore, the spring constant should be designed to be 30 N/mm. In the near future, a customized thin spring will be designed and fabricated utilizing the our developed non-planar photofabrication techniques [5].

4. CONCLUSION

In this paper, grasping force was measured by a strain gauge with da Vinci forceps. As a result of evaluating the correlation between the grasping force and the traction force of the driving wire, it was confirmed that the grasping force was controlled according to the purpose of the forceps. In the near future, we will implement the optical displacement sensor and a spring to the surgical robotic forceps and measure the grasping force for tissues.

ACKNOWLEDGEMENT

A part of this study was supported by JSPS KAKENHI Grant Number JP18K12106.

REFERENCES

1. Intuitive Surgical Inc., “Sustainability Report 2021,” [Online]. Available: https://isrg.intuitive.com/
2. J. Arata, et al., “Modular Optic Force Sensor for a Surgical Device using a Fabry-Perot Interferometer”, Applied Sciences, Vol.9(17), 1-11, 2019.
3. A. Saracino, et al., “Haptic feedback in the da Vinci Research Kit (dVRK): A user study based on grasping, palpation, and incision tasks,” Int. J. Med. Robot. Comput. Assist. Surg., vol. 15, no. 4, p. e1999, 2019.
4. M. Yatani, et al., “Study of Grasping Force Measurement of Forceps for Robot-Assisted Surgery,” Microjoining and Assembly Technology in Electronics, pp. 85-88, 2021 (in Japanese).
5. T. Matsunaga, et al., “Multilayered receive coil produced using a non-planar photofabrication process for an intraluminal magnetic resonance imaging,” Sensros and Actuators A, 261, 130-139, 2017.

Development of a Quality Prediction Model for High Pressure Die Casting Process Using Load Cell Sensor

S.-J. Kong[1,2], S.-H. Lee[1], D.-H. Kim[1], #J. Ha[1]

1 Advanced Forming Process R&D Group, Korea Institute of Industrial Technology, Ulsan, 44413, Republic of Korea
2 Department of Digital Anti-Aging Health Care, Inje University, Gyeongsangnam-do, 50834, Republic of Korea
 # Corresponding Author / E-mail: jhjh@kitech.re.kr, TEL: +82-052-980-6006, FAX: +82-980-6099

ABSTRACT

A load cell is used to measure force and torque, which has been applied to various industries to measure the load precisely in manufacturing equipment including hydraulic presses and compact powder metallurgy indenters. The importance of quality monitoring with real-time process data is increasing in high pressure die casting (HPDC) processes. Previously, a hydraulic pressure measuring device has been used to obtain pressure data for quality prediction. As a pressure variable of the quality prediction model, it is difficult to select the features of the hydraulic pressure data. Because there is an accuracy deviation of more than 10% depending on environmental factors and mechanical characteristics such as temperature, humidity, and molten metal filling rate. However, a load cell sensor has a deviation of less than 0.2%. In this study, the load cell sensor was applied to a HPDC machine of the target factory to acquire real-time pressure information. We conducted exploratory data analysis for the load cell data and the hydraulic data. Then an encoder-decoder neural network was employed to predict the quality of parts produced through the casting process using the pressure data. The model was trained according to the principle of minimizing the error between the original data and the reconstructed data. The developed classification model achieved cosine similarity of 0.99 and average mean absolute error of 0.0551 for the load cell sensor data. The proposed neural network-based predictive model with load cell data has a potential in quality prediction of HPDC processes.

Keywords : Load cell, Artificial neural network, High pressure die casting, Quality prediction

1. INTRODUCTION

In general, data for predicting the quality of HPDC products include process data and sensor data. In the case of pressure sensor data, it is measured in a hydraulic system and uses the pressure signal as structured data.[1] To improve quality prediction performance, sensor data with low deviation and time series is required. A load cell sensor was installed in the HPDC facility for this study to obtain pressure data. Through the sensor, detailed information about the pressure can be acquired.

Since the number of the non-defective products is significantly higher than that of the defective products, which leads to the imbalance of the data. Unsupervised learning method was performed using an autoencoder model, one of the encoder-decoder artificial neural networks. The model can distinguish the non-defective and defective at the individual product level through the load cell data for each product.

2. Deep Learning approach for Quality Prediction using a load cell sensor in the HPDC

2.1 Dataset

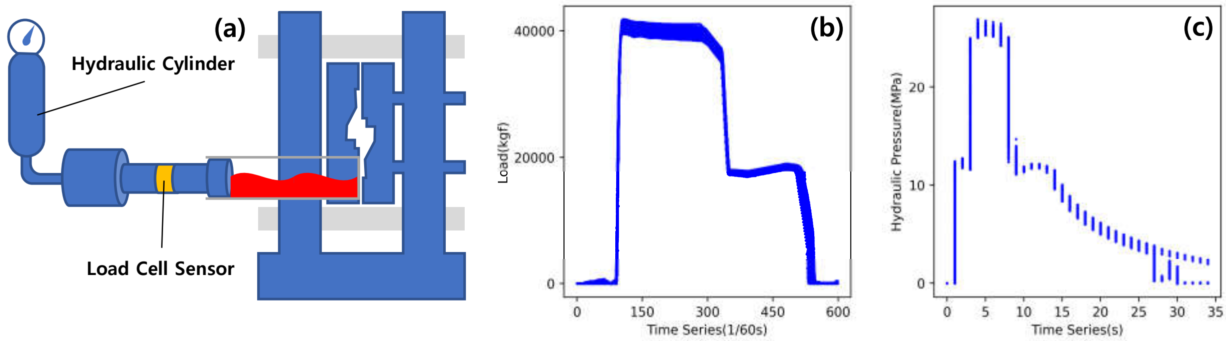

Figure 1 (a) Schematic of the HPDC machine with load cell sensor. (b) Load cell data and (c) and hydraulic pressure data of non-defective products in a cycle time.

We obtained pressure data from the load cell sensor in the HPDC machine. Hydraulic data were also acquired from the same machine for comparison with the load cell data. The dataset consists of a train set for learning, a validation set for evaluation, and a test set. The train set consisted of high-quality product's pressure data with few defects. As shown in Figure 1, time series data were extracted in units of shots. After normalization, it is used for the model training. In one cycle, it was confirmed that the sampling rate of the load cell was 60 times higher and the number of features was about 17 times, showing more detail than the hydraulic data.

2.2 Model Construction

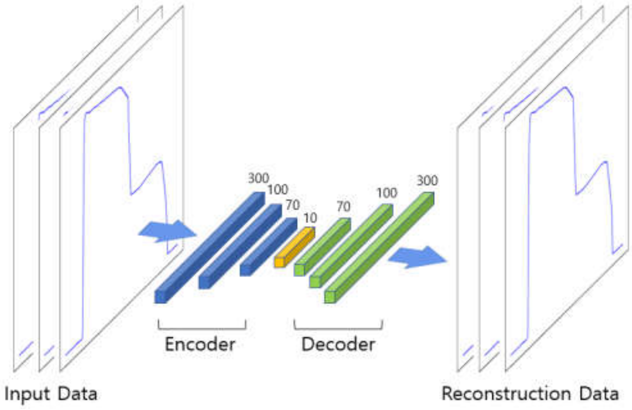

Figure 2 The architecture of the encoder-decoder deep neural network for training of the proposed model.

Encoder-decoder artificial neural network model belongs to unsupervised learning, which can learn without information about labels. The input data is reconstructed into reconstruction data through the encoder and decoder layers as shown in Figure 2. And the learning proceeds according to the principle of reducing the error between the reconstruction data and the input data. The mean absolute error (MAE) function was used as a loss function to calculate the error, and the layer was configured to minimize the MAE value and the hyper-parameters were also tuned. Finally, the model obtained the MAE values of 0.0244 for the load cell train set and 0.0274 for the hydraulic train set.

2.3 Thresholding

In order to determine the quality of HPDC pressure data, it is necessary to set a threshold for the MAE distribution. The validation set enters the input of the trained model to set the threshold. After inference, reconstructed data is created, and every shot has an MAE value calculated by the error between the input data and the reconstructed data. A shot exceeding the threshold is predicted as a shot of defect. Since the MAE distribution follows the standard normal distribution, a sigma value was found through the defective rate and standard normal distribution table. To calculate the threshold, the average and deviation of the MAE distribution were used, and the threshold was set by adding the average to the deviation multiplied by the sigma value.

3. CONCLUSION

We developed an encoder-decoder network model to predict quality using load cell sensor data and hydraulic system data. In this paper, the quantitative performance of the models according to the two data types was compared. Through the exploratory data analysis, it was confirmed that the load cell sensor data had more detail pressure information than the hydraulic system data. When considering the cosine similarity of the predicted result of the test set and the actual number of defects, the similarity of the load cell sensor data was higher. Both types of MAE values for the train set converge, but the MAE values for the test set were lower in the hydraulic system. This indicates that the larger the number of features, the larger the MAE value, but it has a good effect on the prediction performance. Based on the strength of the load cell sensor, it is expected to be utilized as a predictor of a quality prediction in the high pressure die casting process gradually.

Table 1 Quantitative comparison of model performance

Data type	Load cell data	Hydraulic pressure data
Cosine similarity	0.99	0.90
Average MAE	0.0551	0.0301

ACKNOWLEDGEMENT

This study was supported by Ministry of SMEs and Startups (Smart Sensor Leading Project Technology Development Project, No. S3130179) and Ministry of Trade, Industry and Energy (System Industry Base Agency Support Project, No. R0006257).

REFERENCES

1. Jun Kim, Hyoung Seok Kang, Ju Yeon Lee, Development of Intelligence Data Analytics System for Quality Enhancement of Die-Casting Process, J. Korean Soc. Precis. Eng., Vol. 37, No. 4, pp. 247-254, 2020.

Cantilever Type Pyroelectric Device Structure for Compact Non-Contact Temperature Sensor

Yudai Chida[1], Michitaka Yamamoto[1], Toshihiro Takeshita[2],
Takeshi Kobayashi[2], Seiichi Takamatsu[1], and #Toshihiro Itoh[1]

1 Department of Precision Engineering, Graduate School of Engineering, The University of Tokyo, 7-3-1, Hongo Bunkyo-ku, Tokyo 113-8656, JAPAN
2 Hybrid Sensing Device Research Team, Sensing System Research Center, National Institute of Advanced Industrial Science and Technology, 1-2-1, Namiki, Tsukuba, Ibaraki 305-8564, JAPAN
 # Corresponding Author / E-mail: itoh@pe.t.u-tokyo.ac.jp, TEL: +81-3-5841-6491, FAX: +81-3-5841-6485

ABSTRACT

To miniaturize pyroelectric infrared sensors, we focused on a method of mounting a PZT/Si piezoelectric sensor on a polyimide substrate, in which a piezoelectric sensor and a pyroelectric sensor are stacked on a cantilever, and chopping is performed by deformation driven by the piezoelectric sensor. The thickness of the adhesive layer is known to be important for the deformation of this structure, and we investigated the control method and evaluated the deformation. As a result, we were able to control the adhesive layer to less than 10 µm and obtained a large tip displacement of 0.69 mm for a 7.8 mm long cantilever, demonstrating the usefulness of this structure.

Keywords : Pyroelectric, Piezoelectric, Infrared, Cantilever, Chopping, PZT/Si Sensor

1. INTRODUCTION

It is necessary to develop compact, high-sensitivity infrared sensors for monitoring tympanic membrane temperature. Our group has focused on pyroelectric infrared sensors, which have high sensitivity among infrared sensors, and has been conducting research on integrating the chopping mechanism and sensing functions on a cantilever. Simulation analysis has shown that to realize the measurement of tympanic membrane temperature in this structure, it is necessary to use a thin polyimide substrate and integrate a piezoelectric PZT thin film and a pyroelectric PVDF thin film on the polyimide[1].

However, it has been difficult to deposit a PZT thin film on a polyimide substrate because a high-temperature process exceeding 500 °C is generally required to deposit a PZT thin film. In this study, we focus on a recently proposed method[2] in which a PZT thin film is formed on a Si substrate and a PZT/Si sensor is mounted on the target substrate using an adhesive. It has been reported that the thickness of the adhesive layer is important for the deformation of the cantilever in this structure[3], so it is necessary to investigate this effect. Therefore, in this study, we investigated a method to control the thickness of the adhesive layer and evaluated the behavior of the fabricated cantilever when driven.

2. Adhesive layer control and deformation characteristics

2.1 Mounting Method

Fig.1 shows the method of mounting a PZT/Si sensor on a polyimide substrate. A plastic model structure[4] that can detach a PZT/Si sensor is fabricated using MEMS processing technology, and only the PZT/Si sensor part is detached with a multifunctional mounting machine (MRS-850RD/Okuhara Electric Co., Ltd.) (Fig.1(A)). Next, UV curable adhesive (LOCTITE AA 3523/Henkel Japan K.K.) is applied to the polyimide film cut into a cantilever shape by mounting machine, and the cut PZT/Si sensor is mounted on it. Then, to control the thickness of the adhesive layer, a flat plate is pressed at an arbitrary pressure with a load testing machine (FTN1-13A/Iko Engineering Co., Ltd.) (Fig.1(B)). In this case, a sphere is placed between the load testing machine and the flat plate so that the flat plate is pressed at a point. A PTFE sheet is placed between the sensor and the flat plate to prevent adhesion. Finally, the adhesive was cured by UV irradiation, and the lead wires were attached with silver paste.

The thickness of the polyimide substrate used in this study is 5 µm, and the size of the PZT/Si sensor is 1 mm × 6 mm × 5 µm. The amount of applied adhesive was 0.2 mg, and the applied pressure was 10 N and 50 N.

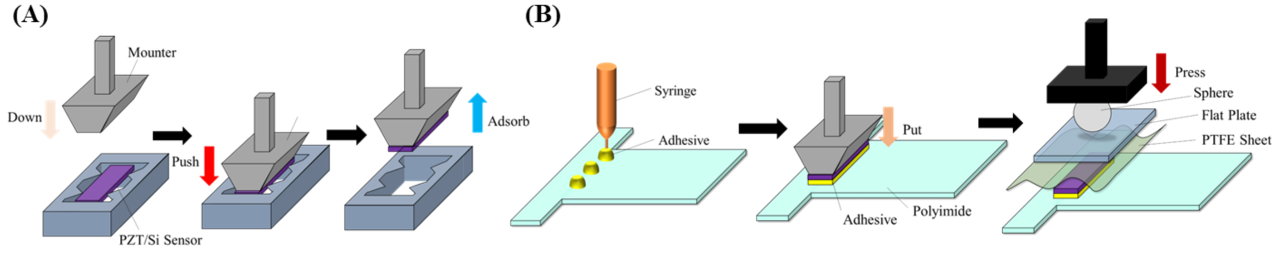

Figure 1. Manufacturing process (A) Separating the sensor from the frame (B) Application of adhesive, mounting of PZT/Si sensor and control of adhesive layer thickness by pressure

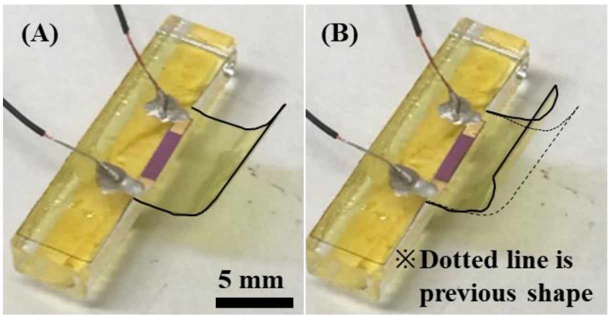

Figure 2. Device deformation (A) before voltage applivation (B) after voltage application

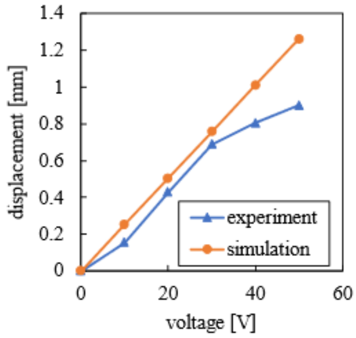

Figure 3. Relationships between applied voltage and cantilever displacement (△) experiment (◯) simulation

2.2 Evaluation method

The thickness and shape of the adhesive layer were measured with a laser microscope (LEXT OLS-5000/Olympus Corporation), and the thickness of the adhesive film was measured by measuring the difference between the steps of the polyimide film and the PZT/Si sensor.

The cantilever behavior was evaluated by applying a voltage and measuring the shape of the cantilever with a measuring microscope (SSTM6-LM-F31-2/Olympus Corporation). The vertical coordinates of both end points on the edge of the cantilever tip were measured while the applied voltage was gradually increased from 10 V. The cantilever was attached to an acrylic base for evaluation of the cantilever characteristics.

2.3. Experimental results

The average thickness of the adhesive layer was 10 μm and 0.3 μm when pressed at 10 N and 50 N, respectively. However, the sensor was damaged when pressed at 50 N. If the thickness of the adhesive layer is less than 10 μm and the angle change is approximately 15° or more, there is a possibility to measure the tympanic membrane temperature[4], and it is possible to achieve the goal by applying a pressing pressure of 10 N or more.

Fig.2 shows the changes in a cantilever with an adhesive layer thickness of 10 μm mounted at a pressure of 10 N before and after the application of voltage. Because of the thinness of the polyimide substrate, the cantilever was already bent before the voltage was applied (Fig.2(A)), but after the voltage was applied (Fig.2(B)), it was further deformed, and its bend was found to increase. Fig.3 shows the results of measuring the average vertical displacement of the cantilever tip by experiment and calculating the amount of change by simulation while gradually increasing the applied voltage. In the range of applied voltage up to 30 V, the displacement increased linearly with increasing voltage, and a large displacement of 0.69 mm was obtained at 30 V. This is the same trend as in the simulation, and the error from the simulation result is about 9%. On the other hand, at applied voltages higher than 30 V, the experimental values gradually began to deviate from the simulation values. This is thought to be because the PZT/Si sensor could not withstand the high voltage and short-circuited.

3. CONCLUSION

In this study, we focused on a method of mounting a PZT/Si sensor on a polyimide substrate to develop a compact pyroelectric infrared temperature sensor integrating a piezoelectric thin film and a pyroelectric sensor on a cantilever, and investigated a method of controlling the thickness of the adhesive layer. As a result, the thickness of the adhesive layer could be controlled to less than 10 μm by pressing a 1 mm × 6 mm PZT/Si sensor placed on the adhesive with a pressure of 10 N or more.

The maximum displacement of 0.69 mm was obtained for the cantilever structure with a length of 7.8 mm. The use of a PZT/Si sensor mounted on a polyimide substrate as a driving source is effective for devices requiring large displacement and for integration with different materials such as PVDF.

REFERENCES

1. Y. Chida, K. Kaiho, S. Takamatsu, and T. Ito: "Study on High Precision Infrared Temperature Sensor Array," 35th Spring Conference of the Japan Institute of Electronics Packaging, 17B1-02, 2021.
2. T. Yamashita, T. Kobayashi, “Smart Table Tennis Racket Using a Rubber Mounted Ultrathin Piezoelectric Sensor Array,” Sensor and Materials, Vol. 33, No.3, pp. 1081-1089, 2021.
3. Y. Chida, K. Kobayashi, S. Takamatsu, and T. Ito: "Study on High Precision Infrared Temperature Sensor Array(II) ―Analysis of Deformation Characteristics during Driving―," 36th Spring Conference of the Japan Institute of Electronics Packaging, 24A1-02, 2022.
4. S. Takamatsu, S. Goto, M. Yamamoto, T. Yamashita, T. Kobayashi, T. Itoh, “Plastic-Scale-Model Assembly of Ultrathin Film MEMS Piezoresistive Strain Sensor with Conventional Vacuum-Suction Sensor Mounter,” Scientific Report, p. 1, 2019.

Development of a Sensor for Simultaneous Measurement of Heart Rate and Contact Load during Husbandry Training

#Takumi Hiejima[1], Hirofumi Nogami[1], Aya Ono[2], Kazuyuki Ban[3], Ryo Takigawa[1], D.S.V. Bandara[1], and Jumpei Arata[1]

1 Kyushu University, 744 Moto-oka, Nishi-ku, Fukuoka, 819-0395, JAPAN
2 Omuta City Zoo, 163 Showa-machi, Omuta, 836-0871, JAPAN
3 Toyohashi zoo and botanical park, 1-238 Oana, Oiwa, Toyohashi, 441-3147, JAPAN
 # Corresponding Author / E-mail: hiejima.takumi.364@s.kyushu-u.ac.jp, TEL: +81-92-802-3241, FAX: +881-92-802-3241

ABSTRACT

Husbandry Training (HT) is recommended from the perspective of an animal welfare. At HT, animals are trained to perform specific behavior for keepers' cue. Keepers are necessary to wander whether animals are under excessive stress during HT by observing. However, it is difficult to determine their stress level only by observation. This causes problems such as overlooking the stress, and increasing the training time. Quantitative stress indicates can help the keeper to make the training efficient.

We have been working to develop a heart rate measurement system without attaching to animals. Heart rate changes indicate stress state changes. Laser Doppler flowmetry (LDF) is used to measure heart rate. Attaching a sensor to animals may give animals extra stress and disturb existing HT. Therefore, it is necessary not to attach the sensor to animals during HT.

The challenge with heart rate measurement during HT is body motion artifacts. Our group has developed an algorithm to eliminate body motion artifacts. This had succeeded in eliminating some body motion artifacts during measurement, but there were still some noises remaining.

In this paper, an effect of contact load changes between a sensor and a measuring point is investigated because it could be one of the causes of remaining noises. It is said that contact load changes disturb LDF signals. In addition, there are no reports of measuring contact load change without attaching a sensor to animals. To clarify the effect of contact load changes on LDF signals, a simultaneous measurement experiment of contact load and heart rate was conducted. As a result, it was found that the LDF signal was disturbed when the contact load change occurred. In the future, based on this result, we would like to develop a heart rate measurement system that can stably measure heart rate during HT.

Keywords: Laser Doppler Flowmetry, Simultaneous Contact Load and Heart Rate Measurement, Husbandry Training, Load Sensor, Body Motion Artifact

1. INTRODUCTION

Husbandry Training (HT) is recommended from the perspective of an animal welfare. HT is the training for animals to perform a specific posture and action when signed by keepers. In zoos, shaping postures and actions by HT enables dental checks, weight measurement, and blood sampling with less stress on the animals.[1)] It is because there is no need for anesthesia and mechanical retention.

However, HT is challenging as learning the specific actions requires keepers' skills and takes a lot of time. When shaping actions, keepers observe the animal and make sure that the animal is not under stress. Keepers must be skilled to grasp the stress state from only observation. If the keeper stresses the animal too much during training and the animal runs away, the keeper has to start the training from the beginning. In addition, some keepers are too cautious and spend too much time.

To make HT more efficient for keepers and animals, it is necessary to quantify the stress state during HT. It is known that heart rate changes under stress. [2)] Therefore, this study aims to develop a heart rate measurement system for HT.

We had conducted heart rate measurement experiments using laser Doppler flowmetry (LDF) on a masked palm civet (*Parguma larvata*) during HT at the Omuta city zoo. The masked palm civet is trained to remain in a specific position while being fed. Since the body of the masked palm civet is not completely immobilized during HT and sensor is not attached to the masked palm civet, the LDF signal is disturbed by body motion artifacts. To solve this problem, our group developed an algorithm to eliminate body motion artifacts. [3)] This algorithm reduced some noise signal intensities. It leads to stabilizing the heart rate measurement during HT.

However, other noises cannot be reduced by the algorithm. It is because the algorithm can reduce only sensor displacement noise due to body motion. It is known that body motion also causes contact load changes. To realize a more stable heart rate measurement, some measures against contact load changes are necessary. However, there are no reports of measuring contact load change without attaching a sensor to animals during HT. Therefore, the purpose of this study is to investigate the contact load change during HT and its effect on the LDF signals. To clarify this, a simultaneous measurement experiment of contact load and heart rate was conducted.

2. EXPERIMENT

2.1 Experimental outline

A simultaneous measurement experiment of contact load and heart rate was conducted on the masked palm civet during HT. The purpose of this experiment was to clarify the contact load change during HT and its effect on the LDF signals. The subject was kept at Omuta city zoo and was the same as the one in the previous study. Since the subject was not fixed to the measurement area, it can move slightly during the experiment. The measurement was performed by LDF (CDF-2000, CyberMed) and a thin load sensor (Fujikura composites) for 1 minute. The sensors are not attached to the subject.

2.2 Result

Fig. 1 is a part of the measurement result. The graph shows the time variation of the blood flow measured by the LDF and contact load measured by the load sensor. In Fig. 1 (a), the contact load changed by about 0.05 N/s, and the blood waves indicate heart rate peaks. It can be said that this degree of contact load changes has no effect on the LDF signal. On the other hand, Fig. 1 (b) shows that when the contact load changed by about 0.4 N/s, the blood flow signals was disturbed and a heart rate peak could not be found (Fig. 1 (b), the area in the box).

There were parts of the signal that were disrupted even though no large contact load change had occurred. This indicates that other factors may be contributing to the noise. In addition, it is found that the load sensor can be used for body motion detection.

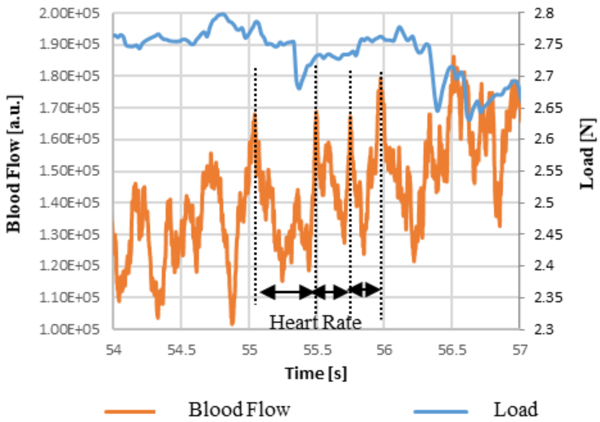

(a) The section where the contact load change is 0.05 N/s and the heart rate can be measured

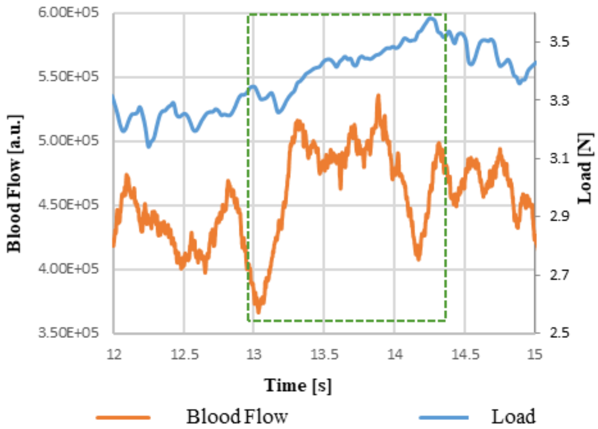

(b) The section where the contact load change is 0.4 N/s and the heart rate cannot be measured

Fig. 1 Some sections of the simultaneous contact load and heart rate measurement experiment result

3. CONCLUSION

In this paper, it was found that changes in contact load have an effect on the blood flow signal. The sensor system used in this study consisted of a commercially available LDF with a load sensor attached. Therefore, the problem remains in the method of transmitting the contact load to the sensor. In addition, the size of the sensor module is around 4 x 2 x 2 mm. It is too large to be applied to various types of HT in the future. Therefore, we are working on the development of a new small optical sensor that can appropriately measure heart rate and contact load simultaneously.

REFERENCES

1. K. Ban, and S. Shiihara, Journal of Japanese society of zoo and wildlife medicine, Vol. 23, No. 3, pp.59-64, 2018.
2. J. F. Thayer, F. Ahs, M. Fredrikson, J. J. Sollers, and T. D. Wager, Neuroscience & Biobehavioral Reviews, Vol. 36, No. 2, pp. 747-756, 2012
3. H. Nogami, S. Ogata, A. Saitou, K. Ban, T. Akiyama, T. Hiejima, R. Takigawa, and T. Hosoya, Japan Journal Apply Physics, Vol. 60, SCCL13, 2021.

Planar spring-supported force plate with an eddy current displacement sensor

Kawasaki Yuta[1] and Takahashi Hidetoshi[1,*]

1 Department of Mechanical Engineering, Faculty of Science and Technology, Keio University, 3-14-1 Hiyoshi, Kouhoku-ku, Yokohama, Kanagawa 223-8522, Japan; yuta.kawa@keio.jp
** Correspondence: htakahashi@mech.keio.ac.jp; Tel.: +81-45-566-1847*

ABSTRACT

This paper reports on a force plate with a planar spring and eddy current displacement sensor to measure a small insect's ground reaction force (GRF) to reveal its motion characteristics. The proposed force plate is composed of an aluminum circular plate, four springs symmetrically connecting to the plate, and eddy current displacement sensor under the plate. When a force is applied to the plate, the plate goes down. Then, an eddy current displacement sensor detects the plate displacement. From the calculation via Fook's law, the applied force can be measured. The proposed force plate has the advantage of fabrication easiness. The diameter and thickness of the fabricated plate were 8 mm and 0.1 mm, respectively. The spring width was 0.3 mm. Then, we evaluated the sensitivity and resonant frequency of the force plate. The experimental result suggested that the proposed force plate had enough performance to measure a small insect's GRF.

Keywords : Force plate, Small insect, Ground reaction force, Eddy current sensor

1. INTRODUCTION

Because tiny insects are less affected by gravity so that they can run at high speed on unstable footholds, GRF measurement and biomechanical evaluation of them are expected to be helpful for designing micro running robots [1][2]. In recent years, MEMS force plates have been developed to clarify the gait mechanism of such insects [3][4]. Previous force plates are sensitive enough to measure GRF. However, they are fragile, and the fabrication procedure is complicated. In addition, previous force plates with displacement meters need a calibration to measure a center of force plate [5].

In this study, we designed and fabricated a force plate with a planar spring and an eddy current displacement sensor to realize simple fabrication procedures, simple calibration, robustness, and high accuracy.

2. Desgin and principle

Figure 1(a) shows a schematic image of the proposed force plate. The proposed force plate is composed of a planar spring and eddy current sensor with the planar coil. When a force is applied, the plate moves down. The eddy current sensor is used to measure the displacement of the plate with non-contact. Then, the force is calculated by the spring constant via Hooke's law. As shown in Figure 1(b), the planar spring is composed of a circular plate and four planar springs. The plane spring's number of turn (n) is designed to be 0.6, and the thickness (d) is 0.1 mm. The spring structures have a width of 0.4 mm and a spacing of 0.6 mm between the adjacent spring structures. As shown in Figure 2, it is made from Aluminum plate by a fiber laser machine.

3. Experiment

As shown in Figure 3, we calibrated the fabricated force plate. A load cell was placed on the piezo stage, and a force was applied to the force plate by moving the piezo stage up and down with a triangle wave with 0.5 Hz. Then, the output of the load cell, the piezo stage and the eddy current displacement sensor were recorded with a low pass filter of 400 Hz. It was found that the output of the eddy current displacement sensor was proportional to the displacement. As shown in

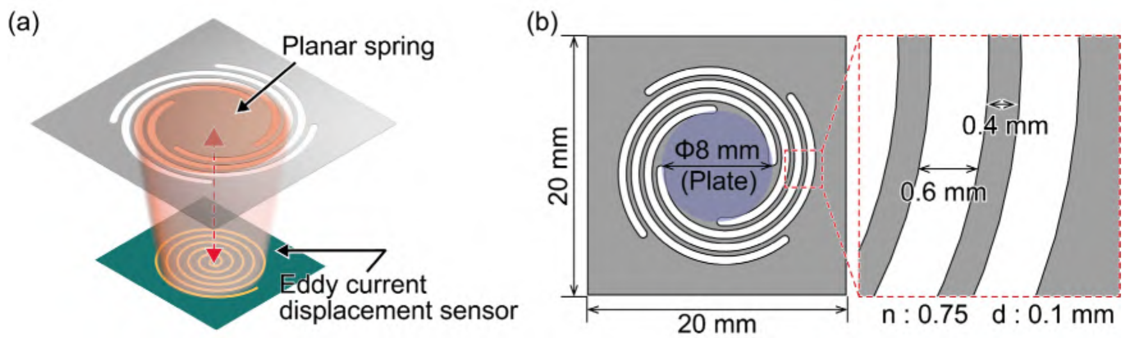

Figure 1 (a) A schematic image of the proposed force plate. (b) Planar spring dimensions.

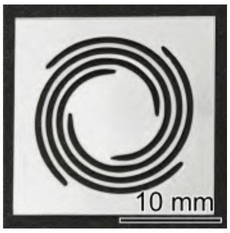

Figure 2 A photograph of the fabricated planar spring.

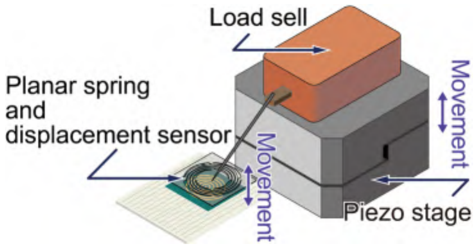

Figure 2 A schematic image of the experiment setup.

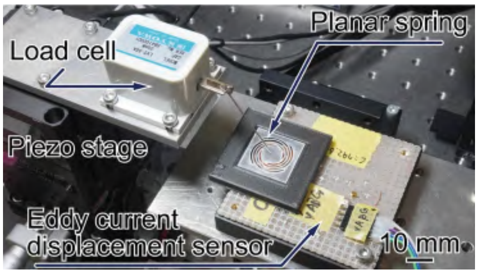

Figure 4 A photograph of the experiment setup.

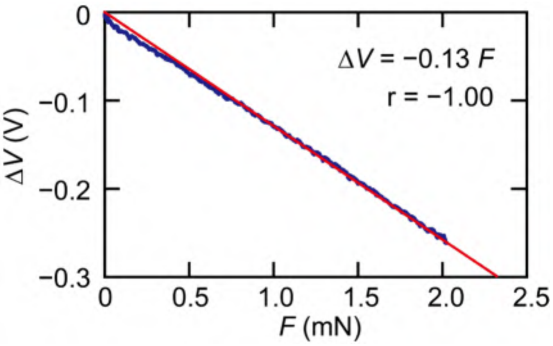

Figure 5 Relationship between F and ΔV.

Figure 4, the tip of needle connected to the load cell was placed at the center of planar spring. The housing for the planar spring and eddy current sensor was fabricated by a 3D printer. The needle was made of metal but did not affect the measurement results.

Figure 5 shows the relationship between applied force F and the eddy current sensor output ΔV. The resolution became 17 μN that was sufficiently high sensitivity. The spring constant of the planar spring was 16 N/m. Additionally, the resonant frequency of the planar spring is 126 Hz.

3. CONCLUSION

In this study, we proposed a force plate composed of an aluminum planar spring and an eddy current displacement sensor. We designed, fabricated, and evaluated the characteristics of the proposed force plate. As the next step, we will evaluate the errors caused by the location of applied force and the eddy current sensors. Then, the proposed force plate can be applied for measurement of GRF of small insects.

ACKNOWLEDGEMENT

This research was supported by JSPS KAKENHI Grant No.20K20984, the Shimadzu Science Foundation. The authors thank Takashi Nakamura for developing the measurement circuit.

REFERENCES

1. K. Y. Ma, et al., Science, Vol. 340, pp. 603-7, 2013 J. Tlusty, S. Smith, C. Zamudia, Operation Planning Based on Cutting Process Model, J. of KSPE, Vol. 39, No. 12, pp. 517-521, 1990.
2. Y. Wu, et al., Science Robotics, Vol. 4, eaax1594, 2019.
3. R. Furuya, et al., Proc. of MEMS2016, pp. 165-168, 2016.
4. Y. Sun, et al., Journal of Micro Electro Mechanical Systems, Vol. 14, No. 1, pp. 4-11, 2005.
5. T. Sugimoto, et al., Measurement Science and Technology, Vol. 13, No. 5, article no. 645, 2022.

Cone-Shaped Air Chamber for the Wearable Scratching-Sound Sensing Device

#Shun Muramatsu[1], Yuki Kohata[1], Emi Hira[2], Yasuyuki Momoi[2], Michitaka Yamamoto[1], Seiichi Takamatsu[1], and Toshihiro Itoh[1]

1 Department of Precision Engineering, The University of Tokyo, 7-3-1, Hongo, Bunkyo-ku, Tokyo, 113-8656, JAPAN
2 Department of Veterinary Medical Sciences, The University of Tokyo, 7-3-1, Hongo, Bunkyo-ku, Tokyo, 113-8656, JAPAN
 # Corresponding Author / E-mail: smuramatsu@g.ecc.u-tokyo.ac.jp, TEL: +81-3-5841-6495, FAX: +81-3-5841-6495

ABSTRACT

A cone-shaped air chamber for an animal collar-type wearable device for wireless scratching-sound sensing was successfully developed. Recently, quantitative monitoring of the number and intensity of scratching behavior in dogs has been required. We have already developed the collar-type wearable device to measure body-conducted scratching-sound. This paper discussed the optimum geometry of the air chamber: a device component for amplifying body-conducted sound. We fabricated the body-conduction microphones with the cone-shaped air chamber and evaluated the amplification ratio of body-conducted sound on each microphone. The results indicated that the cone-shaped air chamber could amplify the body-conducted sound by 4 dB on average. The body-conduction microphone with the air chamber could measure the scratching-sound on the artificially reproduced dog's body surface.

Keywords : Wearable device, Scratching-sound, MEMS microphone, IoT

1. INTRODUCTION

Recently, medical technology for dogs as companion animals has developed remarkably. However, for dermatosis, which has the highest prevalence among canine diseases[1], the evaluation of severity and efficacy of treatment still depends on the subjective judgment of veterinarians and owners[2]. Because the severity of pruritic dermatoses, such as allergic dermatitis, is strongly related to the scratching behavior, quantitative monitoring of the number and intensity of scratching behavior is a valuable technique for veterinary medicine.

The previous studies measuring the scratching behavior of dogs using an accelerometer[3] were difficult to estimate the scratching intensity. The other studies estimating the scratching intensity using the acousto-mechanical sensor[4] were difficult to apply to animals because of the fur.

Therefore, we have already developed an animal collar-type wearable device for wireless scratching-sound sensing (Fig. 1). The body-conduction microphone on this device has two unique structures: the intermedium for attenuating ambient airborne noises and the air chamber for amplifying body-conducted sound, including scratching-sound. This paper discusses the optimum geometry of the air chamber.

2. MATERIALS AND METHODS

The shape of the air chamber is a cone, and the cone's diameter varies from 6 mm to 10 mm. The top of the air chamber is coupled to the hole of a MEMS microphone (Fig. 2 (a)). This body-conduction microphone is fabricated with a MEMS microphone board (BOB-18011, SparkFun Electronics), an acrylic resin, and silicone rubber (KE-1308, Shin-Etsu Silicone) (Fig. 2 (b)).

To evaluate the amplification ratio for the body-conducted sound, sine waves (16 Hz to 500 Hz) were output from a subwoofer and measured using the fabricated microphones. The root-mean-square value of the sound pressure level of measured sine waves was calculated for each frequency and microphone. In addition, the experimental system imitating the body surface of a dog is constructed with silicone rubber and white fox fur. The scratching-sound was measured on this system using fabricated microphones.

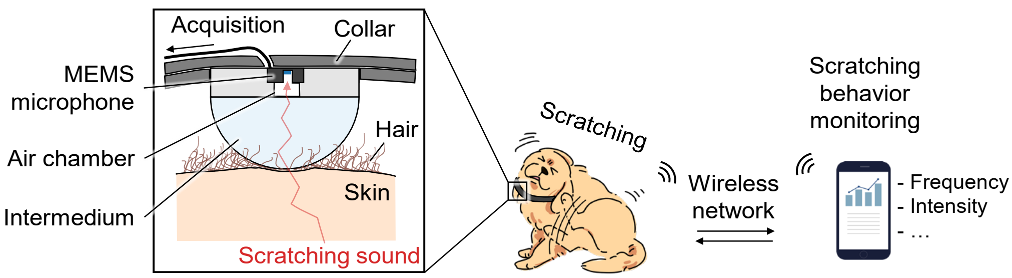

Figure 1 Concept of the animal collar-type wearable device for wireless scratching-sound sensing.

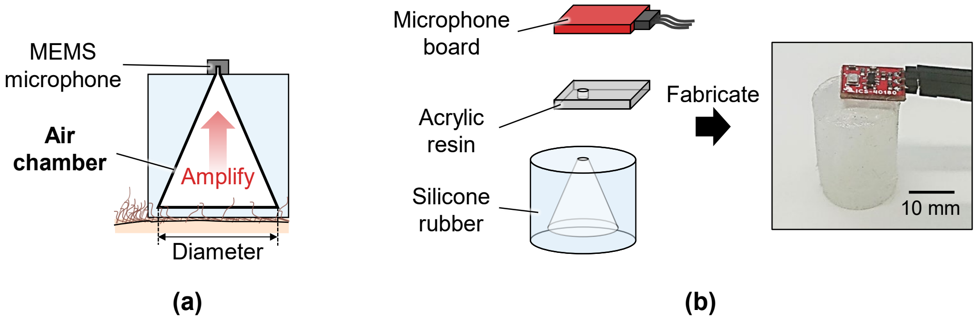

Figure 2 Cone-shaped air chamber. (a) Design of the structure. (b) Fabrication process and the fabricated microphone.

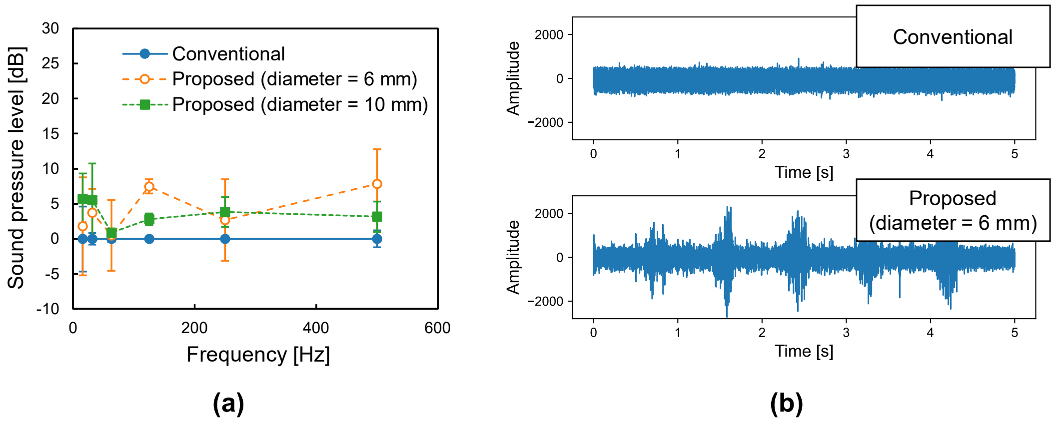

Figure 3 Experimental results. (a) Sound pressure level against frequency of the conventional and the proposed microphones. (b) Scratching-sound measured by the conventional and the proposed microphones.

3. RESULTS AND DISCUSSION

Figure 3 (a) shows the sound pressure level of sine waves measured by fabricated microphones. This result is standardized so that "Conventional" is 0 dB to absorb the sub-woofer's characteristics. The proposed microphones have 4 dB higher amplification ratios on average than the conventional microphone. On the other hand, both the proposed microphones' sound pressure levels are 4 dB on average regardless of the cone's diameter, although a longer diameter is expected to have a higher amplification ratio. This may be because the air chamber had not been sealed well during the fabrication process.

Figure 3 (b) shows the scratching-sound measured by the conventional microphone and the proposed microphone (diameter = 6 mm). The scratching-sound measured by the conventional microphone is buried in the self-noise of the microphone board. On the other hand, the scratching-sound measured by the proposed microphone is visible. This cyclic sound having five peaks in this figure is the scratching-sound on the reproduced dog's body surface.

4. CONCLUSION

This paper discussed the optimum geometry of the air chamber for the animal collar-type wearable device for wireless scratching-sound sensing. The results indicated that the cone-shaped air chamber could amplify the body-conducted sound by 4 dB on average. The proposed microphone could measure the scratching-sound on the artificially reproduced dog's body surface. On the other hand, the influence of the cone's diameter requires further investigation.

ACKNOWLEDGEMENT

This work was supported by JSPS KAKENHI Grant Number JP22K18778.

REFERENCES

1. Anicom Holdings, "White paper on household animals 2021," https://www.anicom-page.com/hakusho/, accessed June 2022.
2. T. Olivry, M. Saridomichelakis, T. Nuttall, E. Bensignor, C. E. Griffin, and P. B. Hill, "Validation of the canine atopic dermatitis extent and severity index (CADESI)-4, a simplified severity scale for assessing skin lesions of atopic dermatitis in dogs," Veterinary Dermatology, vol. 25, issue 2, pp. 77–e25, 2014.
3. R. D. Chambers et al., "Deep learning classification of canine behavior using a single collar-mounted accelerometer: real-world validation," Animals, vol. 11, issue 6, 1549, 2021.
4. K. S. Chun et al., "A skin-conformable wireless sensor to objectively quantify symptoms of pruritus," Science Advances, vol. 7, no. 18, eabf9405, 2021.

Degradation Evaluation by Viscosity Measurement of Low Volume Oil Samples

[#]Kenji Sakamoto[1], Fumikazu Mizutani[2,3], Michio Shimomura[2,3], Tatsuya Fujita[2] and Sang-Seok Lee[2]

1 Department of Intelligent and Control Systems, Kyusyu Institute of Technology,
680-4 Kawazu, Iizuka, Fukuoka 820-8502, JAPAN
2 Graduate School of Engineering, Tottori University, 4-101 Koyama-Minami, Osaka 680-8552, JAPAN
3 Sakuragawa Pump MFG Co., Ltd., 1-2-11 Itsukaichi, Ibaraki, Osaka 567-8525, JAPAN
 # Corresponding Author / E-mail: sakam896@ics.kyutech.ac.jp, TEL: +81-948-29-7537, FAX: +81-948-29-7751

ABSTRACT

In this study, to investigate engine oil degradation, the viscosity of low volume oil samples was evaluated by measuring viscosity using a capillary tube. The viscosity of the oil was evaluated at each usage time, and it was confirmed that the viscosity decreased logarithmically along the usage time.

Keywords : viscosity, high viscosity measurement, capillary flow, oil degradation, Washburn equation

1. INTRODUCTION

There is no established method for evaluating the degradation state of engine oil, and it is difficult to determine when to replace it. Currently, deterioration is determined by empirical rules, such as visual evaluation of oil and replacement based on operating hours. In the visual evaluation of oil, it is known empirically that the viscosity of deteriorated oil decreases, but it is difficult to measure this because it is necessary to collect and measure a high volume of engine oil during operation. For on-site determination, it is desirable to evaluate viscosity in a simple and low volume sample.

As a viscosity measuring device suitable for low volume samples, we are researching a micro viscosity measuring device using a capillary tube[1,2] (measuring device: manufactured by Sibata Scientific Technology Ltd., measuring chip: manufactured by Uchiyama Manufacturing Corp) . This device flows a low volume sample (about 70 μL) in a capillary tube, and the meniscus of the flow is detected by a photo reflector placed close to the capillary tube to measure the flow time. The viscosity of the flow can be derived according to the Washburn equation (1) [3-6].

$$t = \frac{16}{4\sigma cos\alpha + D\Delta P}\frac{\eta}{D}l^2 \quad (1)$$

where each variables are the flow time t, flow distance l, differential pressure ΔP, capillary inner diameter D, and viscosity η (surface tension σ and contact angle α do not contribute to the viscosity by measuring two types of differential pressure[2]). Previous studies[1,2] have focused on low viscosity samples. In this study, we applied it to high-viscosity engine oil and studied the relationship between operating time and viscosity.

2. EXPERIMENT

The sample engine oil was Shell 15W40-DH2. Samples were evaluated at room temperature (28.5°C environment) after approximately 60 to 1570 hours of use with engine V2403-K3A (Kubota Corporation). Figures 1 and 2 show the micro viscosity measuring device and its structural diagram. In the measuring device, approximately 150 μL of sample was introduced into a capillary tube (World Precision Instruments 1B120 4; inner diameter of 0.68 mm, length of 100 mm), and negative pressure was applied to make the sample flow through the capillary tube. Because the sample measured this time was of high viscosity, the negative pressure value for low viscosity could not provide a measurable flow rate. After analyzing the negative pressure values suitable for measuring high viscosity samples, measurements were performed within a flow of approximately 1-5 seconds at negative pressures of 10-35 kPa. To enable measurement of a low volume, positive pressure was applied to the capillary after flow to push the sample back to its initial state. Then,

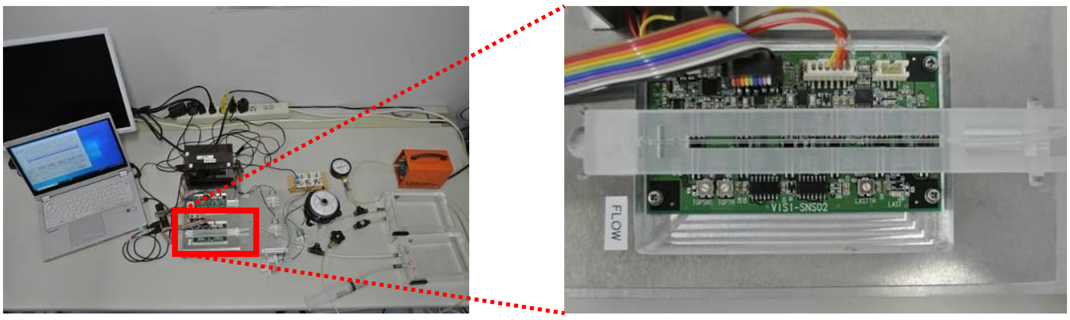

Fig.1 Viscometers and measuring chip

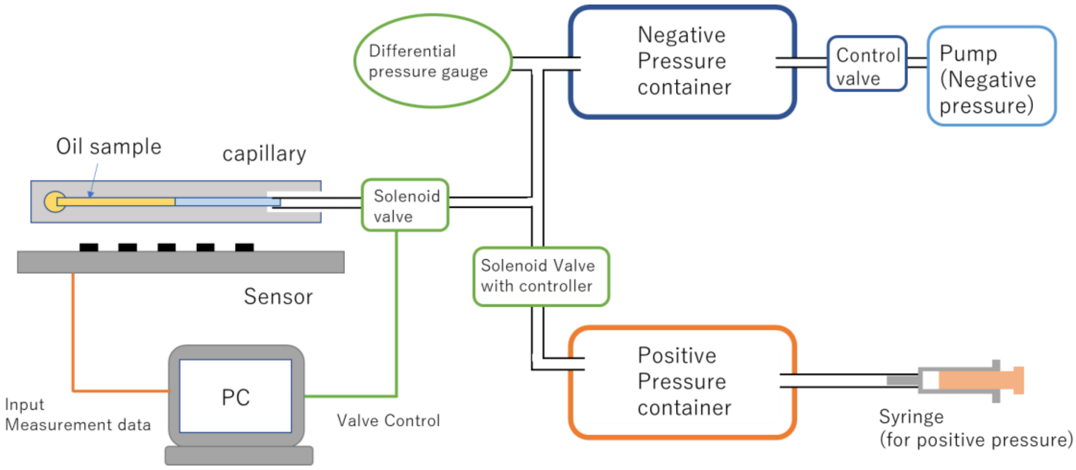

Fig. 2 Structural diagram of measurement system

negative pressure was again applied to flow through the capillary for a total of seven flow measurements at different negative pressure values.

3. RESULTS AND CONCLUSION

Fig. 3 shows a graph of the obtained measurement results of viscosity versus time of use of the sample oil (the viscosity of pure water at the same temperature is used here as the viscosity standard). The measurements show that the viscosity is logarithmically lower. From these results, it was possible to evaluate the operating time and viscosity change with a low volume of oil sample.

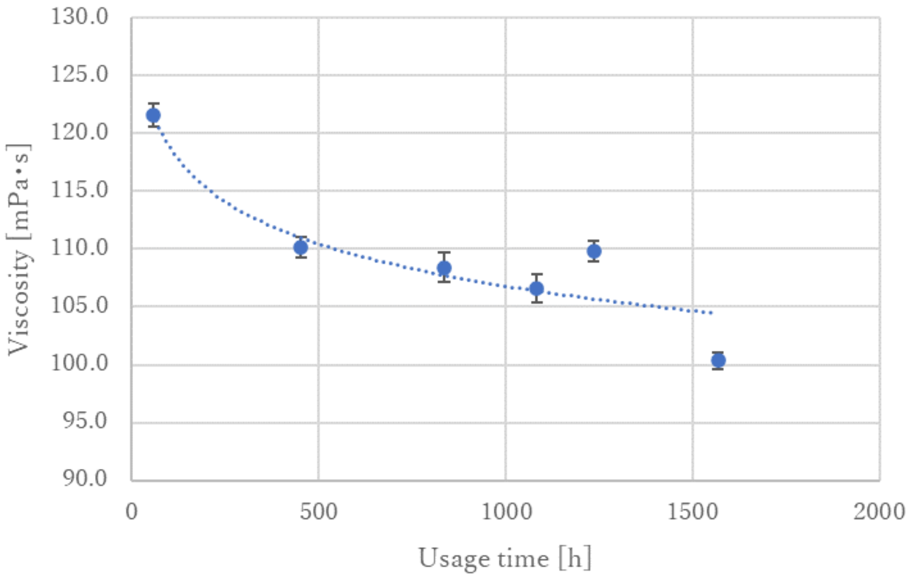

Fig.3 Measurement results of viscosity versus usage time

ACKNOWLEDGEMENT

This study was supported by Uchiyama Manufacturing Corporation and SIBATA Scientific Technology Limited.

REFERENCES

1. K. Sakamoto et al. 2020 Jpn. J. Appl. Phys. 59 107002
2. K. Sakamoto et al 2022 Jpn. J. Appl. Phys. 61 066507
3. R. Lucas, Colloid J. Russ. Acad. Sci. Kolloidnyi Z. 23, 15 (1918).
4. E. W. Washburn, Phys. Rev. 17, 273 (1921).
5. E. K. Rideal, Philos. Mag. 44, 1152 (1922).
6. C. H. Bosanquet, Philos. Mag. 45, 525 (1923).

Facile detection of CD9 based on a non-competitive fluorescence polarization immunoassay using a peptide as a tracer

#Shunsuke Chida[1], Kazuki Takahashi[1], Thanawat Suwatthanarak[2], Mao Fukuyama[3], Masatoshi Maeki[4,5], Akihiko Ishida[4], Hirofumi Tani[4], Takao Yasui[5,6,7], Yoshinobu Baba[6,7,8], Akihide Hibara[3], Mina Okochi[2], Manabu Tokeshi[4,7,8,9]

1 Graduate School of Chemical Sciences and Engineering, Hokkaido University, Kita 13 Nishi 8, Kita-ku, Sapporo 060-8628, Japan
2 Department of Chemical Science & Engineering, Tokyo Institute of Technology, 2-12-2 O-okayama, Meguro-ku, Tokyo 152-8552, Japan
3 Institute of Multidisciplinary Research for Advanced Materials, Tohoku University, 2-1-1 Katahira, Aoba-ku, Sendai 980-8577, Japan
4 Division of Applied Chemistry, Faculty of Engineering, Hokkaido University, Kita 13 Nishi 8, Kita-ku, Sapporo 060-8628, Japan
5 Japan Science and Technology Agency (JST), PRESTO, 4-1-8, Honcho, Kawaguchi, Saitama 332-0012, Japan
6 Department of Biomolecular Engineering, Graduate School of Engineering, Nagoya University, Furo-cho, Chikusa-ku, Nagoya 464-8603, Japan
7 Institute of Nano-Life Systems, Institute of Innovation for Future Society, Nagoya University, Furo-cho, Chikusa-ku, Nagoya 464-8601, Japan
8 Institute for Quantum Life Science, National Institutes for Quantum Science and Technology (QST), 4-9-1, Anagawa, Inage-ku, Chiba 263-0024, Japan
9 Innovative Research Center for Preventive Medical Engineering, Nagoya University, Furo-cho, Chikusa-ku, Nagoya 464-8601, Japan
 # E-mail: shun1221@eis.hokudai.ac.jp

ABSTRACT

We developed a non-competitive fluorescence polarization immunoassay (NC-FPIA) using a peptide as a tracer. The NC-FPIA can easily and quickly quantify the target after simply mixing them together. This feature is desirable for point-of-need applications such as clinical diagnostics, infectious disease screening, on-site analysis for food safety, *etc.* In this study, the NC-FPIA was applied to detect CD9, which is one of the exosome markers. We succeeded in detecting not only CD9 but also CD9 expressing exosomes derived from HeLa cells. This method can be applied to various targets if a tracer for the target can be prepared, and expectations are high for its future uses.

Keywords : Immnoassay, Microfluidic device, Polarization, Exosome

1. INTRODUCTION

Immunosensing makes it possible to selectively measure a target of interest from biological samples having a complex composition by utilizing the specificity of an antibody. In particular, by fusing immunosensing technology with microfluidics, a small amount of sample, rapid analysis and diagnostics, high sensitivity, etc. have been realized. However, most of the devices provide heterogeneous immunoassays, as represented by ELISA, which require antibody immobilization and washing operations that make the analysis operations relatively complicated. On the other hand, homogeneous immunoassays, which can be achieved by simply mixing a sample and reagents in a solution, are not often combined with microfluidics.

We have focused on one of the homogeneous immunoassays, the fluorescence polarization immunoassay (FPIA), which offers ease of operation, and we are working on its applications [1]. The FPIA is a competitive immunoassay for measuring small molecules using the degree of fluorescence polarization (P) as an index. Polarization depends on the speed of rotational motion of the molecules. Therefore, it is difficult in principle to apply large tracer molecules such as proteins for the FPIA. Most recently, we have developed a non-competitive FPIA (NC-FPIA) that can measure large molecules using a fluorescently labeled protein fragment [2] or a fluorescently labeled antibody fragment [3] as a tracer. The NC-FPIA is even simpler than the conventional FPIA. If a tracer that is fluorescently labeled with a substance that has an affinity for the target can be produced, this method can be applied to the detection of various proteins, antibodies, viruses, and so forth.

On the other hand, peptides have been widely studied as drugs for metabolic and tumor related diseases and as valuable tools for diagnostic applications. So far, many peptides with high affinity for targets have been developed for various purposes. Some peptides have a high affinity comparable to antibodies. These peptides have a smaller molecular weight than VHH antibodies and can be expected to be excellent tracers for the NC-FPIA. However, the NC-FPIA using peptides as tracers has not been reported so far, and investigation of its potential, especially in bioapplications, is highly desired.

In this study, we applied the NC-FPIA, which uses a peptide as a tracer, to detect CD9, an exosome marker protein [4]. This is the first report of the NC-FPIA using a peptide tracer. Exosomes are extracellular vesicles secreted by most cell types and are thought to be responsible for cell-to-cell communication. Since exosomes contain biological information about diseases such as cancer, they are expected to be potential cancer biomarkers. Dedicated ELISA kits and equipment have been developed for the detection of tetraspanins, but they have problems such as complicated operations, time-consuming measurements, and high cost. The detection of CD9 by the NC-FPIA that we propose here can detect CD9 quickly without the need for antibody immobilization or washing operations.

2. EXPERIMENTAL

The *P* value depends on the rotational movement of a fluorescently labeled target molecule called a tracer in a solution. When the tracer binds to a macromolecule such as an antibody, the rotational movement of the complex is suppressed and the *P* value changes. The magnitude of the change in *P* value (ΔP) depends on the change in molecular weight of the tracer before and after binding to the antibody. In other words, the smaller the molecular weight of the tracer, the larger the ΔP and the higher the sensitivity of the assay.

In this study, an FITC-labeled CD9 binding peptide (RSHRLRLH) (F-CD9 BP) was used as a tracer [5]. To assess the tracer performance, an AAAA peptide was also labeled with FITC (F-AAAA P) (a negative control). For CD9 measurements, PBS, CD9, F-CD9 BP or F-AAAA P, and 1% BSA-PBS were added to a 0.5 mL microtube with the mixing volume ratio of PBS : CD9 : F-CD9 BP or F-AAAA P : 1% BSA-PBS = 60 : 20 : 10 : 10. The total volume of the final mixed solution was 100 μL. Then, after incubating the mixed solution at 25 °C for 30 min, 20 μL of solution was introduced into the microdevice, and the *P* value was measured with the compact fluorescence polarization apparatus.

3. RESULTS AND DISCUSSION

To optimize the reaction conditions between CD9 and the tracer (F-CD9 BP), the concentration of CD9 was fixed at 8 μM and the F-CD9 BP concentration was changed to measure the degree of fluorescence polarization (*P* value). Fig. 1 shows the F-CD9 BP concentration dependence on ΔP. ΔP is the difference of the *P* value between the maximum value and the blank. From the results of the experiment, we found that the highest ΔP was 2.5 nM. Therefore, we selected 2.5 nM as an optimal tracer concentration for our further experiments on the NC-FPIA of CD9.

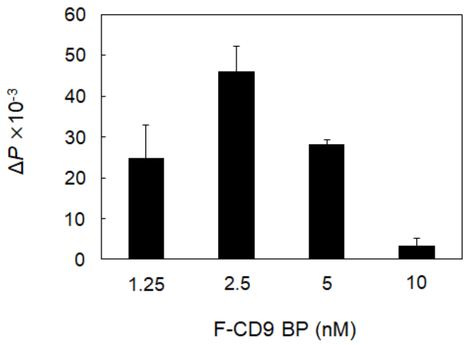

Fig. 1. F-CD9 BP concentration dependence on ΔP. ΔP is the difference of the *P* value between the maximum value and the blank.

We measured the CD9 concentration dependence on ΔP (Fig. 2). ΔP increased with increasing CD9 concentration, indicating that the F-CD9 BP was quantitatively bound to CD9. As clearly seen from the figure, F-AAAA P did not bind to CD9 at all, and F-CD9 BP did selectively bind to CD9. The limit of detection (LOD) of CD9 was evaluated to be 300 nM, considering the average of the blank signal plus three standard deviations. This is the first example of the NC-FPIA using a peptide tracer.

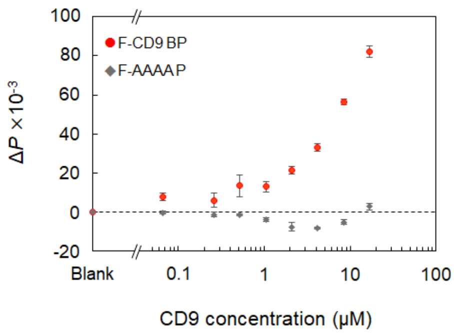

Fig. 2. CD9 concentration dependence on ΔP.

3. CONCLUSION

In this study, we conducted the NC-FPIA using peptides as tracers for the first time and demonstrated the sensing ability of this approach. With the simple operation of mixing the tracer and the sample, we succeeded in detecting CD9 and CD9 expressing exosomes in the samples. In the future, this method can be improved in performance and functionality by developing peptides with higher affinity and peptides that recognize other proteins.

ACKNOWLEDGEMENT

This work was supported by AMED (Grant Number JP22zf0127004), JSPS KAKENHI (Grant Numbers: JP21H01726 and JP21H01960), JST PREST (JPMJPR19H9) and the Cooperative Research Program of "Network Joint Research Centre for Materials and Devices".

REFERENCES

1. A. Nakamura et al., *ACS Food Sci. Technol.*, 2021, **1**, 1623-1628.
2. K. Nishiyama et al., *Sens. Actuators B*, 2020, **316**, 128160.
3. K. Nishiyama et al., *Anal. Bioanal. Chem.*, **413**, 2021, 4619-4623.
4. K. Takahashi et al., *Lab Chip*, in press.
5. T. Suwatthanarak et al., *Chem. Commun.*, 2021, **57**, 4906-4909.

Development of a picoliter-sized incubator array for the cultivation of microorganisms

Yuma Tanaka[1,2], #Tsukuru Minamiki[2] and #Ryoji Kurita[1,2]
1 Department of Materials Science, Faculty of Pure and Applied Sciences, University of Tsukuba, 1-1-1 Tennodai, Tsukuba, Ibaraki 305-8573, Japan
2 Health and Medical Research Institute, National Institute of Advanced Industrial Science and Technology (AIST), 1-1-1 Higashi, Tsukuba, Ibaraki 305-8566, Japan
 # Corresponding Authors / E-mail: t.minamiki@aist.go.jp; r.kurita@aist.go.jp, TEL: +81-29-861-6158, FAX: +81-29-861-6177

ABSTRACT

The development of high-throughput screening methods for microorganisms is desired because microorganisms are useful and sustainable resources to produce valuable substances utilized in various industries. Microarray devices are some of the best candidates for the efficient screening of microorganisms owing to their low consumption of reagents and compact integration. However, the development of the microarray-based incubators for the discovery of valuable microorganisms is still in its early stages. We here developed a picoliter-sized incubator array for the achievement of long-term cultivation and accurate evaluation of microorganisms. As a result, a model microorganism (=*Escherichia coli; E. coli*) was successfully cultured on the array device, and its growth behavior was quantitatively evaluated by the autofluorescence of *E. coli*. The successful demonstration of compartmentation and cultivation of the microorganism could pave the way to the development of efficient cultivation platforms for acquiring useful bioresources.

Keywords: microorganisms, *Escherichia coli*, microarray devices, photolithography,

1. INTRODUCTION

Microorganisms are important resources in the field of green chemistry and sustainable engineering owing to their production ability of valuable substances (=metabolizes). Various culturing apparatus (i.e., flask, jar fermentor, and 96-well microtiter plate) have been applied for the screening of uncultured microorganisms. Although the conventional methods can simultaneously evaluate the growth behavior and metabolic activity of microorganisms, the screening efficiency is insufficient because of their high consumption of reagents and low concurrent-processing ability in the cultivation. Therefore, the proportion of successfully-cultured species to all the microorganisms considered to be currently less than 0.02%. Recently, microdroplet-based cultivation has been attracting attention so as to improve the screening efficiency[1]. Microdroplets can not only reduce the amounts of required reagents in the cultivation, but the screening of microorganisms can be also accomplished due to their mass-producibility of isolated micro-spaces. In the previous research, the separation and cultivation of individual species of microorganisms have been demonstrated[1]. However, the evaluation of metabolic activity for microorganisms in microdroplet-based cultivation is difficult because small molecules such as ions, medium components, and metabolites can easily migrate between the neighbor microdroplets (Fig.1A). Thus, the utilization of microdroplets has been limited to only the evaluation of growth activity. To achieve the high-throughput screening and accurate evaluation of microorgnaisms, the parallelization of complete compartmented micro-spaces is desired. In this presentation, we propose an array device of picoliter-sized incubators composed of a resinous molded by lithographic techniques. The compartmentation and cultivation of a model microorganism (=*E. coli*) on the array were demonstrated.

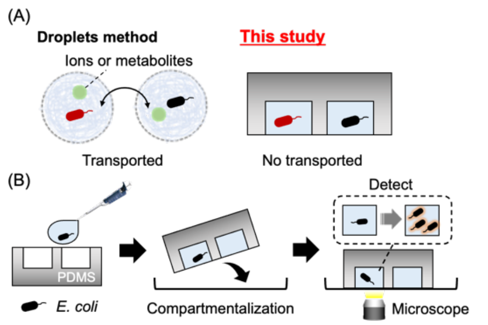

Fig.1. (A) Comparison of microorganism culture and observation with droplets and an array device in this study. (B) Scheme of the growth evaluation of *E. coli*.

2. Evaluation of the Growth Behavior of a Microorganism in a Picoliter-sized Incubator Array

2.1. Experimental

<u>Fabrication of array device</u>: The picoliter-sized incubator array was designed and prepared as follows. A photoresist (ZPN 1150-90, Zeon Corp.) was spin-coated onto a glass substrate. Then, the formed photoresist film was patterned via the standard photolithography process. The patterned residues of the photoresist film (=micropillars) were utilized as a template for the preparation of the picoliter-sized incubators. After that, a polydimethylsiloxane (PDMS) solution (Sylgard 184, Dow Chemical) was spin-coated and cured on the template. Subsequently, the micropattern was transferred from the template to the PDMS substrate. The diameter and height of the transferred microwells were 30 and 5 μm, resulting approximately 3.5 pico-litters of incubator each.

Cultivation and observation of microorganisms: *E. coli* as a model microorganism was cultured for the evaluation of the array device on the growth ability. *E. coli* DH5α was precultured in a medium consisting of 1% (w/v) bacto yeast extract, 2% (w/v) bacto peptone, 5% (w/v) D-glucose, and 1% (w/v) NaCl at 37 °C for 1 day. The optical density of the cell-contained medium solution at the wavelength of 600 nm (OD_{600}) was measured to characterize the cultural state of *E. coli*. The cell solution was diluted with the same medium according to the relationship between the OD_{600} value and the colony forming unit[2]. After that, a single cell of *E. coli* was respectively dispensed to each picoliter-sized incubator on the array device (Fig.1B). Finally, the cell-enclosed incubator array was placed onto the heat stage for the cultivation and observation of the cells. The growth process of the cells was observed by bright field and fluorescence observation on a fluorescence microscope ($\lambda_{Ex}/\lambda_{Em}$=480/520 nm).

2.2. Results and Discussion

First, the isolation state of the picoliter-sized incubators was characterized by the leakage test of an enclosed fluorescence probe (sulforhodamine B). The fluorescence intensity of the probe in each incubator did not change after 24 hr. Thus, the transportation of small chemical substances between each incubator was considered to be prohibited. In preliminary experiments, *E. coli* exhibited high growth-ability and reached a plateau phase after 20 hr of incubation in the flask-based cultivation (Fig.2A). Since the microorganism can autofluorescent derived from flavin adenine dinucleotide inside the cell[3], the quantification of the growth behavior of *E. coli* is available without any labelings on the array. The cultivation state of *E. coli* on the array was determined by comparing the bright field image and fluorescence one (Fig.2B). After 24 hr of incubation, the fluorescence intensity from each incubator increased with the growth of *E. coli*. Here, we confirmed that the probability of encapsulation (=the ratio of compartmentalization) of *E. coli* obeyed the Poisson distribution as intended, meaning that the our array can evaluate the growth behavior starting from a single cell[4]. These results mean that our array device can culture *E. coli* as with the flask-based approach. Furthermore, we concluded that there was no fatal toxicity of the resinous material to *E. coli*. Noteworthy, the change in the autofluorescence signal (i.e., the growth rate of *E. coli*) at each incubator was partly inconstant (Fig.2C, D). The variation might be derived from the fluctuation of the metabolic capacity of *E. coli* and the chemical microenvironment of the incubator.

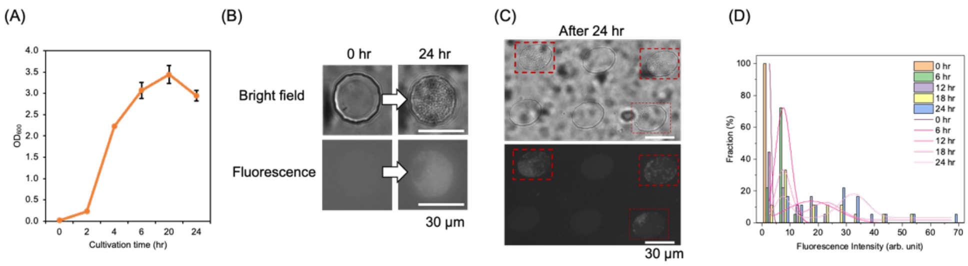

Fig.2. (A) Three cultivations were independently performed in conventional shake-flasks for each mutant. Error bars represent standard deviations. (B) Microscopic observation of *E. coli* in the picoliter-sized incubator at 37°C before and after 24 hr of incubation. (C) The microscopic images of each microwell after 24 hr of incubation. Above: bright field observation. Bottom: fluorescence observation. (D) The transition of the distributions in the growth-related fluorescence intensity on the incubator array at each cultivation time. The data points were fit to the sum of the Gaussian distributions (N=18).

3. CONCLUSION

We successfully compartmented and cultured *E. coli* on the fabricated PDMS-based array. The growth of *E. coli* was evaluated by measuring the autofluorescence of the microorganism. The growth behavior on the array was almost consistent with one in the flask. Whereas, the growth yield of *E. coli* enclosed in the picoliter-sized incubator was partly varied. To further understand the growth behavior of microorganisms in the micro-space, the development of micro-measurement tools combined with the picoliter-sized incubator is underway in our laboratory.

ACKNOWLEDGEMENT

This work was supported by Cabinet Office, Government of Japan, Cross-ministerial Strategic Innovation Promotion Program (SIP), "Technologies for Smart Bio-industry and Agriculture". YT acknowledges the establishment of university fellowships towards the creation of science technology innovation (Grant Number JPMJFS2106) by JST.

REFERENCES

1. E. U. Uzoukwu *et al.*, *Biotechnology Advances*, **2022**, 55, 107903.
2. L. Mazutis e*t al., Nature Protocol,* **2013,** 8, pp. 870–891.
3. N. Billinton and A. W. Knight, *Analytical Biochemistry,* **2001**, 291, pp. 175–197.
4. Y. Obayashi *et al.*, *Analyst,* **2015**, 140, pp. 5065–5073.

Cationic lipid nanoparticles encapsulating positively charged DNA/polyethyleneimine complexes for effective long-chain plasmid DNAs transfection

Shuya Uno[1], Masatoshi Maeki[1,2,3], Yusuke Sato[1], Akihiko Ishida[1], Hideyoshi Harashima[1], and Manabu Tokeshi[1]

1Hokkaido University, JAPAN
2 JST PRESTO, JAPAN
3 High Energy Accelerator Research Organization, JAPAN
 # Corresponding Author / E-mail: likecrepe@eis.hokudai.ac.jp, TEL: +81-080-4392-4312

ABSTRACT

We first report an effective delivery method using lipid nanoparticles (LNPs) and for long-chain plasmid DNAs (15 kbp). Unlike conventional LNP-based pDNA transfection, we found that LNP encapsulating a positively charged complex of cationic polymer and pDNA can achieve three times higher transfection efficiency and lower toxicity than Lipofectamine 3000, a commercially available transfection reagent.

Keywords : Lipid Nanoparticle, Drug Delivery, Long-chain Plasmid DNA Delivery

1. INTRODUCTION

Transfection method of long-chain plasmid DNA (pDNA) (10 kbp~) is a fundamental technology in synthetic biology for artificially creating optimal cells and will significantly contribute to future food, chemicals, and bio-pharmaceuticals. In general, the transfection of long-chain pDNA induces cytotoxicity, and improving transfection efficiency is one of the major challenges. In this study, we developed an efficient and safe long pDNA transfection method using lipid nanoparticles (LNPs) produced by a microfluidic device. We predicted that dynamic membrane fusion between LNPs and endosomal membranes is essential for improving the long chain pDNA transfection efficiency. The addition of polycation to encapsulate negatively charged pDNA into LNPs could allow the dynamic membrane fusion by the surface-enriched ionizable lipids. We verified that cationic complex-loaded LNPs facilitate the endosomal escape of pDNAs (Figure 1).

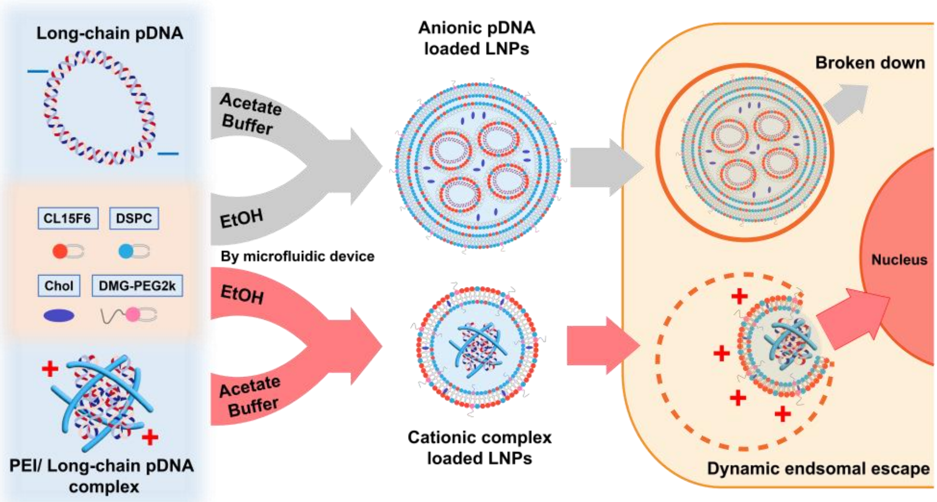

Figure 1. Schematic illustration of the production and intracellular dynamics of the PEI/long-chain pDNA complex-loaded LNPs. CL15F6: pH sensitive cationic lipid, DSPC: helper lipid, Chol: cholesterol, DMG-PEG 2k: PEGylated lipid, and PEI: polyethyleneimine.

2. EXPERIMENTAL

Long-chain pDNA encoding EGFP (15 kbp)-loaded LNPs were produced using a microfluidic device (Figure 2 (a)) [1]. The microfluidic device can produce homogeneous-sized LNPs. Physical properties and in vitro performances of LNPs were evaluated by dynamic light scattering, TEM, small-angle X-ray scattering (SAXS), and flow cytometry.

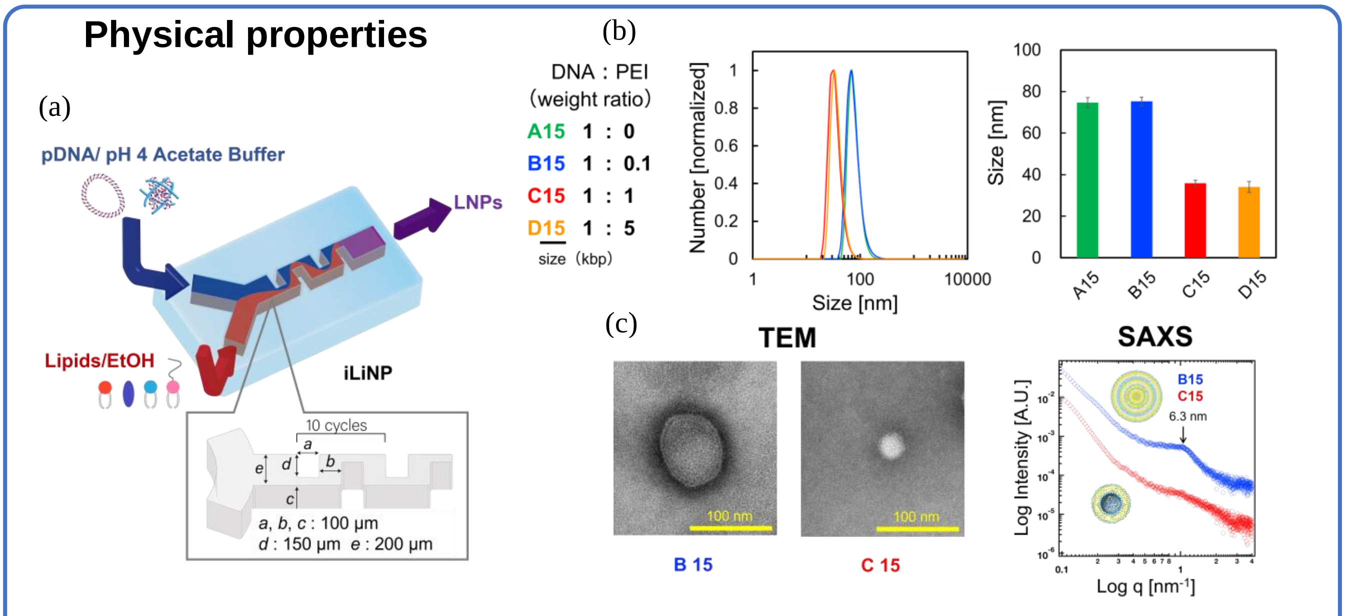

Figure 2. (a) Schematic illustration of LNP praparation using the microfluidic device. (b) Size distribution and the average size of LNPs at four different mixing ratios. (c) Structural characterization of B15 and C15 LNPs by TEM and SAXS.

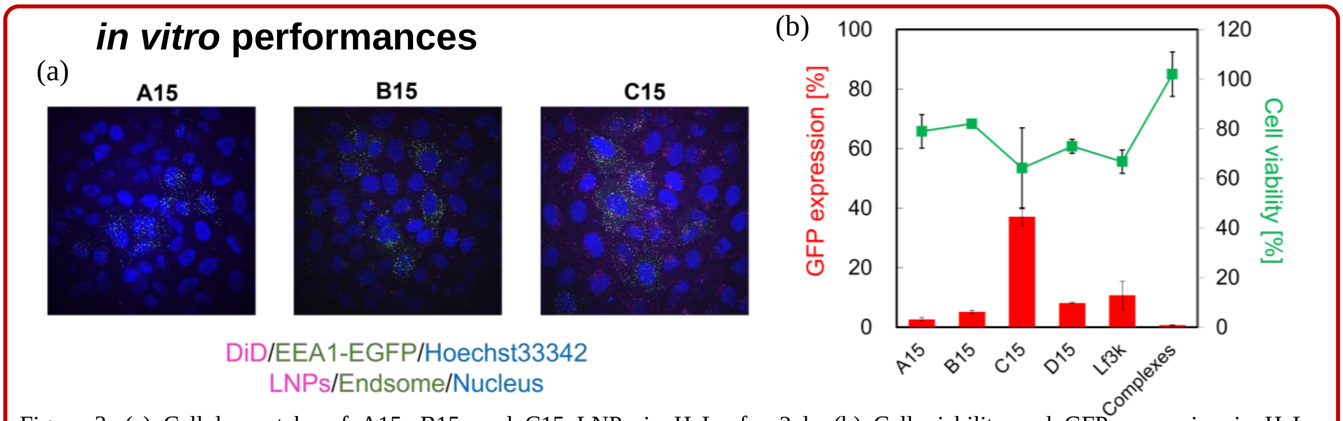

Figure 3. (a) Cellular uptake of A15, B15, and C15 LNPs in HeLa for 2 h. (b) Cell viability and GFP expression in HeLa treated with the LNPs, Lipofectamine 3k (LF3k), and PEI/pDNA complexes at a weight ratio of 1:1 for 24 h.

3. RESULTS AND DISCUSSION

Negatively charged core loaded A15 and B15 LNPs were 75 nm in size. We confirmed that these LNP showed lamellar structure by TEM and SAXS measurements (Figure 2 (b) (c)). In contrast, positively charged core loaded C15 and D15 LNPs were 35 nm in size with liposome-like hollow structure. C15-LNP showed the highest cellular uptake and transfection efficiency of four LNPs, and Lipofectamine 3000, a commercially available transfection reagent. (Figure 3 (a) (b)). In the case of C15-LNP, a large amount of ionizable lipids on the LNP surface accelerated membrane fusion to the endosomal membrane, and the hollow structure also contributed dynamic structural change of the lipid membrane. From these results, the synergistic effects, including small-LNP size, large surface-to-volume ratio, and hollow structure, contributed to the high transfection efficiency.

4. CONCLUSION

In this study, we developed a new strategy for long-chain pDNA transfection using LNPs and the microfluidic device. Small-sized LNPs loaded with positively charged PEI/pDNA complexes exhibited an excellent transfection performance with low toxicity than Lipofectamine 3000, a commercial reagent. Our findings will contribute to various applications in industrial biotechnology and synthetic biology.

REFERENCES

1. N. Kimura et al., Development of the iLiNP Device: Fine Tuning the Lipid Nanoparticle Size within 10 nm for Drug Delivery, ACS Omega, Vol. 39, pp. 5045-5051, 2018.

Development of early lameness detection system for zoo giraffes

#Kenjiro Nakai[1], Hirofumi Nogami[1], Masafumi Kawano[2], D.S.V. Bandara[1], Osamu Takiguchi[3], Shun-ichi Shiihara[2], Haruichi Kanaya[4] and Jumpei Arata[1]

1 Department of Mechanical Engineering, Kyushu University
2 Omuta City Zoo
3 ALSENS Inc
4 Department od Electronics, Kyushu University
 # Corresponding Author / E-mail: nakai.kenjiro.009@s.kyushu-u.ac.jp, 744 Moto-oka, Nishi-ku, Fukuoka, 819-0395, JAPAN,
TEL: +81-92-8023241, FAX: +81-92-8023241

ABSTRACT

Lameness, a common health problem in zoo giraffes, cows and horses, has various negative effects on animal activity. To avoid negative effects such as pain and lack of exercise, early detection and treatment of lameness is necessary. Lameness detection in zoo giraffes is only observation by zookeepers. On the other hand, there are various methods for early lameness detection in cows and horses. To develop early lameness detection system in zoo giraffes, we investigate lameness assessment in cows or horses. These methods are divided into two kinds. One is using cameras, and the other using wearable sensor nodes. The camera-based method often limits the time and place, and lameness can be overlooked. The method using wearable sensor nodes don't cause overlooking, but its recording duration is short, such as a few days. In addition, it requires installation and removal of sensor nodes. To prevent lameness from being overlooked in zoo giraffes, it is necessary to make the measuring duration of wearable sensor nodes longer than one month, or to expand the range of cameras to the entire range of zoo giraffes behavior. In addition, this paper discusses the use of accelerometers to assess lameness in terms of resting time and activity. Previous studies suggest that heat therapy with bandages is effective in preventing lameness in giraffes with osteoarthritis-derived lameness. Therefore, the triaxial acceleration is measured and compared under the two conditions of wearing and not wearing bandages. The results shows that the zoo giraffes sit and rest more frequently during receiving thermotherapy than not receiving it. On the other hand, there is no difference in the amount of activity, excluding rest time, between the heat treatment and no treatment. From these results, it is suggested that measuring sitting time by using accelerometers could be used to detect lameness in zoo giraffes.

Keywords : Lameness, Giraffe, Accelerometer, Thermotherapy, Early Detection

1. INTRODUCTION

Lameness is a common health problem in zoo giraffes. The surgery of lameness requires anesthesia, and the mortality rate from anesthesia is 10%.[1)] If lameness is severe or does not improve with treatment, zookeepers would make the decision to euthanize. Therefore, early detection and preventive medicine are important. However, there is no early lameness detection system for zoo giraffes. To develop early lameness detection system for zoo giraffes, we investigated early studies about cows and horses. In addition, we measured the lying time of zoo giraffes by using triaxial acceleration sensor nodes to assess lameness.

2. Survey of previous studies

The methods of assessing lameness are divided into two kinds. One is using cameras, and the other using wearable sensor nodes. Table 1 shows the experimental conditions for the method using wearable sensor nodes. K. Ito et al. (2010) and Nicola Blackiea et al. (2011) compared lame cows with nonlame cows by monitoring lying time throughout the day.[2) - 3)] Toru Miyamoto et al. (2008) automatically detected acceleration peaks from data obtained from accelerometers attached to the quadrupeds and dorsum of cows, and calculated gait scores from these fluctuations.[4)] This method was effective in detecting lameness, but it had practical problems in that five sensor nodes were mounted on the limbs and back. In addition, these methods had issues with installation and short measurement period, such as four days.

Table 2 shows the experimental conditions using cameras. In these studies, a pressure mat or treadmill was used in combination with cameras to compare gait scores with the ground reaction force and other measurements.[5) –7)] Additionally, there were methods that used infrared cameras to evaluate gait.[8)] In general, these methods guided the target animal to the location where the camera was installed and made the animal walk along a predetermined path. Therefore, it is not possible to evaluate lameness outside the range of the camera.

Table 1 The experimental conditions of Previous study using a sensor[2) - 4)]

Author (Year)	Animal (Number)	Location	Equipments	Sampling Frequency	Recording Duration	Evaluator
K. Ito, et al (2010)	Dairy Cattle (1319)	Farm	Data Loggers (HOBO Pendant Acceleration Data Loggers, Onset Computer Corp)	1/60Hz	5days	Trained Observer
Nicola Blackiea, et al (2011)	Dairy Cattle (59)	Farm	Activity Monitors (IceTag, Ice Robotics Ltd)	8Hz	4days	Observer
Toru Miyamoto, et al (2008)	Dairy Cattle (28)	Farm	Accelerometer (MA3, Micro Stone)	100Hz	(40 m)	None

Table 2 The experimental conditions of Previous study using a wearable camera[5) - 11)]

Author (year)	Animal (number)	Location	Camera	N of camera	Equipments	Evaluator	Angle accuracy
A. Pluk, et al (2012)	Dairy Cattle (70)	Farm	Guppy F-080C 1024×768 pixel, 20 fps	1	Pressure Mat	Trained Observer	—
Kevin G. Keegan, et al (2000)	Horse (10)	—	— 60 fps, 1/1000 s (shutter speed)	2	Treadmill, Reflective Markers	None	0.35°
H.H.F.Buchner, et al (1996)	Horse (11)	—	—	—	Treadmill, Markers	Experienced Veterinarian	≧0.8°
C.B.Gomez Alvarez, et al (2007)	Horse (6)	—	Infrared Camera	6	Treadmill, Reflective Markers	None	—
Tom Van Hertem, et al (2014)	Dairy Cattle (511)	Farm	Microsoft Kinect Xbox 3Dcamera 1920×1080 pixel	1	—	Trained Observer	
F.C.Flower, et al (2006)	Dairy Cattle (48)	Parlor	Panasonic AG-195MP	1	None	Trained Observer	
Tim Van De Gucht, et al (2017)	Dairy Cattle (32)	—	—	—	Pressure Mat	Trained Observer	

3. Experiment and result

The subject of the experiment is a single male giraffe, born in 2005, kept at the Omuta City Zoo. The triaxial acceleration was measured using a self-adhesive bandage (HippoWrap, Cygni), with a wireless 3-axis accelerometer fixed approximately 5 cm above the ball segment of the left forelimb, at 2 second intervals. The wireless sensor was prototyped for giraffes based on previously fabricated sensor nodes for cows[12) - 13)]. The main unit was around 20 x 20 mm and 4.8 g. It is suggested that heat therapy with bandages is effective in preventing lameness in giraffes with osteoarthritis-derived lameness.[14)] Then, triaxial acceleration was measured from February 2 to February14, 2021, under two conditions. As shown in figure 1, one is wearing bandage, and the other not wearing. The conditions were alternated day by day for 6 days each trial. The transportation bunting (EQUITHEME Shipping Boots 1200D, EKKIA) was used for the bunting, which was put on and taken off between 11:30 and 12:30.

The time spent sitting and resting and the amount of activity could be estimated. Figure 2 shows the rest time of giraffe wearing bandage. Figure 3 shows the rest time of giraffe not wearing bandage. Comparing these results, the number of times and the duration the giraffe sat and rested when wearing the vantage was greater than when not wearing the vantage. There was no difference in the hourly average of giraffe activity between the bandage-wearing and unbandaged giraffe.

Figure 1 The position of a sensor node

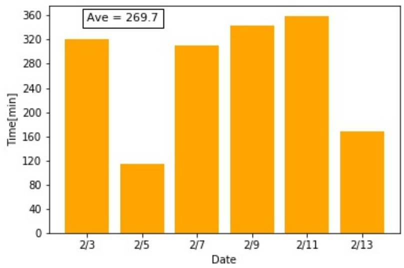

Figure 2 The rest time with bandage

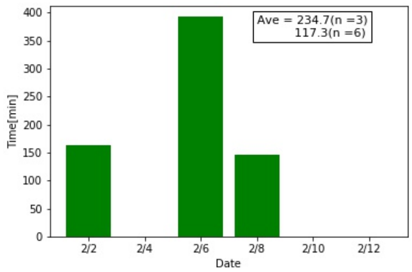

Figure 3 The rest time without bandage

4. CONCLUSION

The camera-based method often limits the time and place, and lameness can be overlooked. On the other hand, when using a wearable sensor, its installation and practicality in the field are issues. To prevent lameness from being overlooked in zoo giraffes, it is necessary to make the recording duration of wearable sensor nodes longer than one month in using wearable sensor nodes, or to expand the range of cameras to the entire range of zoo giraffes behavior in using cameras. In the experiment, it is suggested that measuring sitting time by using accelerometers could be used to detect lameness in zoo giraffes.

REFERENCES

1. Dadone Liza, Zoo Wild Anim. Med, Vol. 9, pp. 623-629, 2018.
2. K. Ito, et al., Journal of Dairy Science, Vol. 93, No. 8, pp. 3553-3560, 2010.
3. Nicola Blackie, et al., Applied Animal Behaviour Science, Vol. 134, No. 3, pp. 85-91, 2011.
4. T. Miyamoto, et al., Bull. Natl. Inst. Anim. Health, No. 114, pp. 51-58, 2008.
5. A. Palk, et al., Journal of Dairy Science, Vol. 95, No. 4, 2012.
6. Kevin G. Keegan, et al., AJVR, Vol. 61, No. 6, pp. 612-619, 2000.
7. H. H. F. Buchner, et al., Equine Veterinary Journal, Vol. 28, No. 1, pp. 63-70, 1996.
8. C. B. Gomez Alvarez, et al., Equine Veterinary Journal, Vol. 39, No. 3, pp. 197-201, 2007.
9. Tom Van Hertem, et al., Biosystems Engineering, Vol.119, pp. 108-116, 2014.
10. F. C. Flower, et al., Journal of Dairy Science, Vol. 89, No. 1, pp. 139-146, 2006.
11. Tim Van De Gucht, et al., Applied Animal Behaviour Science, Vol. 189, pp. 13-22, 2017.
12. R. Miura, et al., Animal Reproduction Science, Vol. 180, pp. 50-57, 2017.
13. H. Nogami, et al., Sensors and Materials, Vol.26, pp. 539-545, 2014.
14. M. Kawano, et al., Animal Behaviour and Management, Vol. 57, No. 4, pp. 146-153, 2021.

Sky-blue microfluidic electrogenerated chemiluminescence device with host-guest solutions

Emiri Kato[1], Jun Mizuno[2] and #Takashi Kasahara[1]

1 Department of Electrical and Electronic Engineering, Faculty of Science and Engineering, Hosei University, 3-7-2 Kajinocho, Koganei-shi, Tokyo 184-8584, JAPAN
2 Academy of Innovative Semiconductor and Sustinable Manufacturering, National Cheng Kung University, No. 1, Daxue Road, East District, Tainan City 70101, TAIWAN
 # Corresponding Author / E-mail: t.kasahara@hosei.ac.jp, TEL: +81-42-387-6219

ABSTRACT

We prepared two kinds of host-guest solutions and evaluated their electrogenerated chemiluminescence (ECL) characteristics using electro-microfluidic devices. 9,9'-10,10'-Tetraphenyl-2-2'-bianthracene (TPBA) and 1-4-di-[4-(*N*,*N*-diphenyl)amino]styryl-benzene (DSA-Ph) were used as sky-blue guests and dissolved in an organic solvent with a host molecule. An anthracene derivative, 2-*tert*-butyl-9,10-di(naphth-2-yl)anthracene (TBADN), was used as the host. The ECL intensities were found to be significantly enhanced by using host-guest systems.

Keywords : Microfluidic, Electrogenerated chemiluminescence, host-guest solution

1. INTRODUCTION

Recently, the solution-based ECL cells have attracted attention for potential applications in lightings and unique displays.[1)] Conventional ECL cells have a simple structure of the ECL solution sandwiched between a pair of electrode-coated glass substrates. In general, the solutions have been prepared by dissolving a single luminescent material such as fluorescent acene derivatives and ruthenium complexes in an organic solvent. When the voltage is applied to the cell, the excited luminescent material, which can emit light, is produced by the electron-transfer reaction between its radical anion and radical cation. However, the electrochemically bipolar molecules, which can be used as the ECL materials, have been limited.

Our research group have been investigating the host-guest solutions in order to develop various color ECL cells.[2-5)] In 2014, the red ECL solution was prepared by using 5,6,11,12-tetraphenyltetracene (rubrene), which is a well-known yellow fluorescent material, as the host.[2)] In 2021, the bright green ECL cell was developed by using an anthracene derivative (TBADN) as the host and a quinacridone derivative as the guest.[4)] In 2022, we also developed the sky-blue ECL cell using an anthracene derivative (TPBA) as the guest.[5)]

In this study, we prepared two sky-blue ECL solutions using TBADN which can emit deep-blue light as the host. Here, DSA-Ph, which has been widely used as a guest material in organic light-emitting diodes (OLEDs), was also chosen as the ECL guest. The ECL characteristics of the prepared solutions were evaluated with the electro-microfluidic device which was developed in our previous work.[6)]

2. EXPERIMENTS

Figure 1(a) shows the chemical structure of TBADN (host), TPBA (guest), and DSA-Ph (guest) and the design of the electro-microfluidic device. The ECL solutions were prepared by dissolving host and guest materials in a mixture of 1,2-dichlorobenzene and acetonitrile (2:1 (v/v)). The concentration of the TBADN host was fixed at 7 mM, while TPBA and DSA-Ph were dissolved in the solution at 1 mM and 2 mM, respectively. In addition, 1,2-diphenoxyethane (180 mM) was also added to the solutions as an ion conductive assistant dopant.[7)] The microfluidic device consists of the 5-μm-thick microchannels sandwiched between two transparent electrodes. An indium tin oxide (ITO)-coated polyethylene terephthalate (PET) film was used as an anode substrate, while a fluorine doped tin oxide (FTO)-coated glass was used as a cathode substrate. The device was fabricated by microelectromechanical systems (MEMS) processes and a heterogeneous bonding technique.[6)]

3. RESULTS AND DISCUSSION

As shown in Fig. 1(b), a photoluminescence (PL) spectrum of TBADN was found to be well overlapped with absorption spectra of both the guests. In our previous work, we have reported that the ECL intensity of TPBA can be enhanced by using the host-guest solution (see Fig. 1(c)).[5)] Thus, the excited DSA-Ph molecule is also expected to be produced by the energy transfer from the host.

As shown in Fig. 1(d), sky-blue ECL emission was clearly observed from the microfluidic device with the DSA-Ph-doped TBADN solution. On the other hand, when the TBADN host was absent from the solution, ECL emission was not observed, indicating that the radical anion and radical cation of DSA-Ph were unbalanced. As shown in Fig. 1(e), cyclic voltammetry (CV) measurements suggest that DSA-Ph is not easily reduced, but is easily oxidized.

4. CONCLUSION

Novel sky-blue ECL cell was developed by doping the DSA-Ph molecules into the TBADN host solution. We expect that our host-guest ECL solutions will contribute to future highly luminescent solution-based self-emissive display and lighting applications.

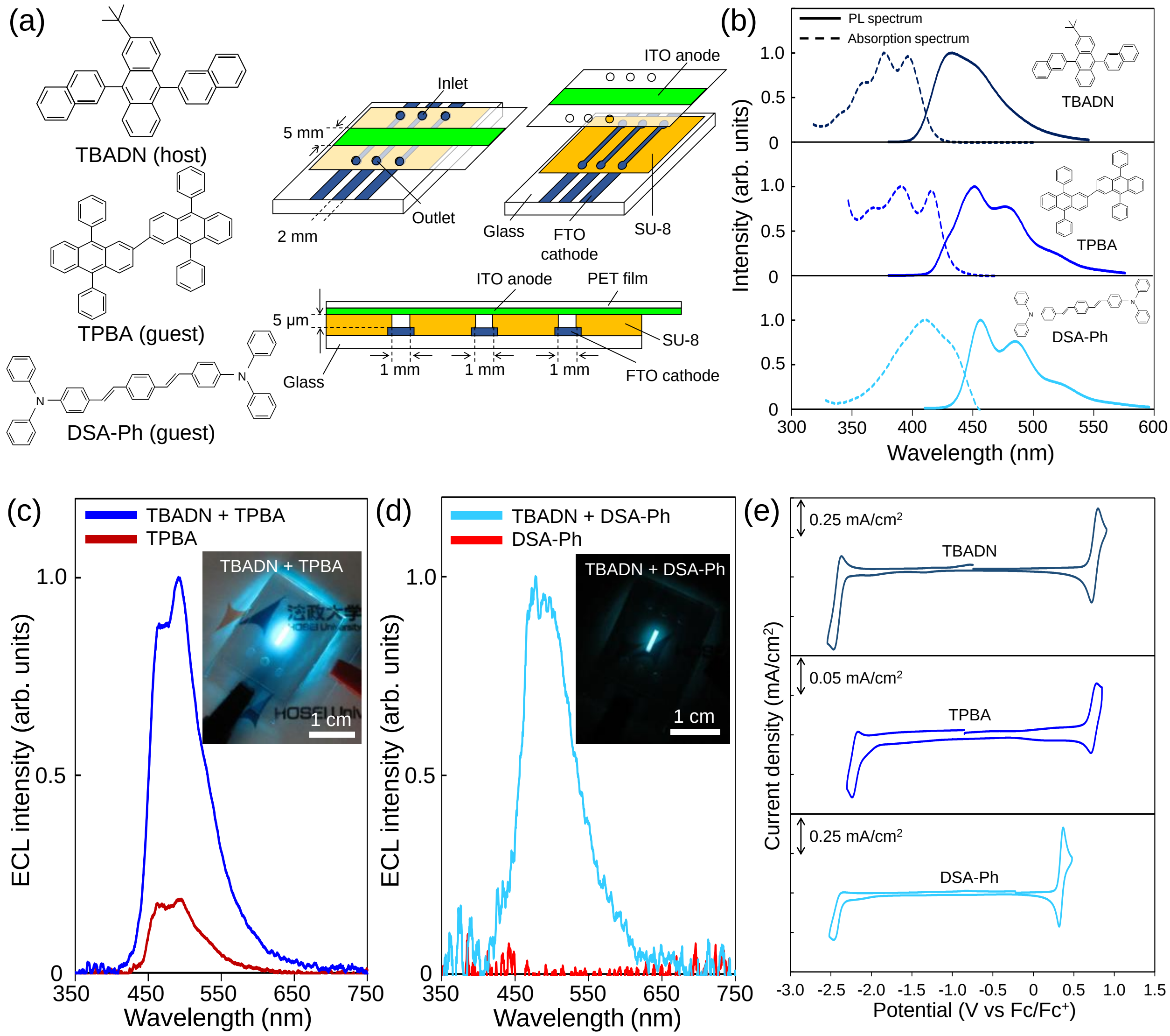

Figure 1(a) Chemical structure of the employed materials and the design of the microfluidic device. (b) PL and absorption spectra. (c) ECL spectra of TPBA with and without the host. (d) ECL spectra of DSA-Ph with and without the host. (e) CV characteristics.

ACKNOWLEDGEMENT

The authors would like to acknowledge Dr. Ryoichi Ishimatsu (Kyushu University) for fruitful discussions. This research was partially supported by JSPS KAKENHI Grant Number JP21K14170.

REFERENCES

1. S.H. Kong, J.I. Lee, S. Kim, M.S. Kang, ACS Photon. 5, 267 (2018).
2. T. Kasahara, S. Matsunami, T. Edura, R. Ishimatsu, J. Oshima, M. Tsuwaki, T. Imato, S. Shoji, C. Adachi, J. Mizuno, Sens. Actuators A 214, 225 (2014).
3. Y. Koinuma, R. Ishimatsu, H. Kuwae, K. Okada, J. Mizuno, T. Kasahara, Sens. Actuators A 306, 111966 (2020).
4. Y. Koinuma, R. Ishimatsu, E. Kato, J. Mizuno, T. Kasahara, Electrochem. Commun. 127, 107047 (2021).
5. E. Kato, R. Ishimatsu, Y. Koinuma, J. Mizuno, T. Kasahara Jpn. J. Appl. Phys. 61 060903 (2022).
6. K. Okada, R. Ishimatsu, J. Mizuno, T. Kasahara, Sens. Actuators A 334, 113329 (2022).
7. K. Nishimura, Y. Hamada, T. Tsujioka, S. Matsuta, K. Shibata, T. Fuyuki, Jpn. J. Appl. Phys. 40, L1323 (2001).

Optofluidic device with Gold- nanofève -based-SERS active nanostructure

Shunya Saegusa[1], Taku Tanaka, Masayuki Naya, Takao Fukuoka, Sho Amano, Yuichi Utsumi and Akinobu Yamaguchi

1 Laboratory of Advanced Science and Technology for Industry, University of Hyogo, 3-1-2, Koto, Kamigori, Ako-gun, Hyogo, 678-1205, JAPAN
 # Corresponding Author / E-mail: saesae54@lasti.u-hyogo.ac.jp, TEL: +81-791-58-0245, FAX: +81-791-58-0245

ABSTRACT

Rapid and sensitive chemical sensing using microfluidic device equipped with gold nanofève (GNF) nanostructure was demonstrated. The GNF nanostructure was fabricated by magnetron sputtering process. We installed the GNF based surface enhanced Raman scattering (SERS) active structure onto the desired microfluidic channel by lithography technique. Our device showed detection of further enhanced spectrum of 10µM 4,4'-Bipyridine (4bpy) was accomplished in flow measurement. This microfluidic device sheds light on the rapid label-free chemical analysis for environment and bioanalysis.

Keywords : Surface-enhanced Raman scattering, Microfluidic devices, Sensing, Nano structures

1. INTRODUCTION

Surface-enhanced Raman scattering (SERS) is a spectroscopic technique that enhances the weak Raman signal by localized surface plasmon resonance (LSPR) and enables the detection of a single molecule (1-5). SERS has a high sensitivity, label-free measurement, and less influence on light fading compared to fluorescence methods. Thus, it is suitable for long-term monitoring for bioanalysis and environmental analysis (2,3). In this study, we have focused on a method to easily fabricate SERS-active structures of gold nanofève (GNFs) using the boehmite structure, a hydroxide of aluminum, because of its advantage of easy fabrication on a wide range of substrates such as glass (4,5). In this paper, in order to realize long-term measurements for bioanalysis and environmental analysis, SERS structures fabricated by the above method were implemented in a microfluidic device, and the changes in detection intensity with time and concentration were evaluated.

2. Experiment and Discussion

2.1 Fabrication of SERS device

First, an Al layer of 84 nm is formed on a glass slide using magnetron sputtering. After that, the glass substrate is heated in water at 100°C for 10 minutes to progress the Al hydroxylation reaction. To build the SERS structure on top of the boehmite made in a series of processes, the boehmite substrate is tilted 10 degrees and sputtered about 60 nm of Au. The flow channel structure was fabricated by pouring polydimethylsiloxane (PDMS) into a mold master fabricated by a 3D printer and heating at 110°C for 30 minutes to solidify it. Finally, the surface of boehmite substrate and channel structure were plasma treated and bonded. The SERS device shown in Figure U was fabricated from the above process.

2.2 Fluid Measurement

SERS measurement was demonstrated using the fabricated SERS device. A schematic measurement system is shown in Figure 1. The measurement method was to mix 4,4'-Bipyridine (4bpy) and pure water using a syringe while pumping the liquid, and then irradiate it with a laser using the Raman spectroscopy module to perform SERS measurements. In this experiment, 4bpy (20µM) and pure water were each pumped at a flow rate of 0.1mL/min for 40 minutes. The measured Raman spectra are shown in Figure A. It can be seen that the intensity of the Raman spectrum increases with time. Figure 4 shows the change in peak intensity at 1618 cm^{-1}. This graph indicates that it saturates after about 15 minutes. This may be because 4bpy adhered to all the enhanced portions of the SERS structure and reached the detection limit. In other words, this intensity change indicates that the sample molecules accumulate on the SERS substrate. Therefore, if the sample molecule is adsorbable on the SERS substrate, it can be detected at any low concentration by keeping the fluid flowing for an extended period of time. In addition, The SERS structure can be applied to long-term experiments because the Raman intensity was maintained even after fluid flow for more than 40min. Based on the above, we believe that it is possible to develop analytical devices for long-term bioanalysis and environmental analysis by examining the relationship between the change in saturation intensity with flow rate and the time to reach saturation intensity with concentration.

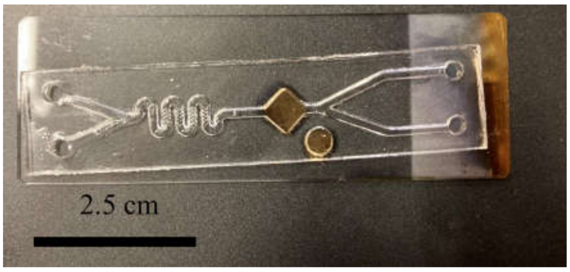

Figure 1 SERS device.

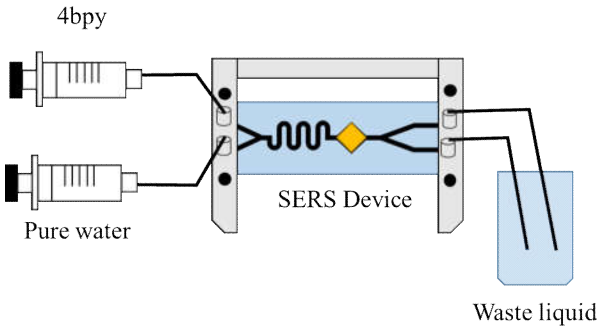

Figure 2 A schematic of the experimental setup for SERS measurement.

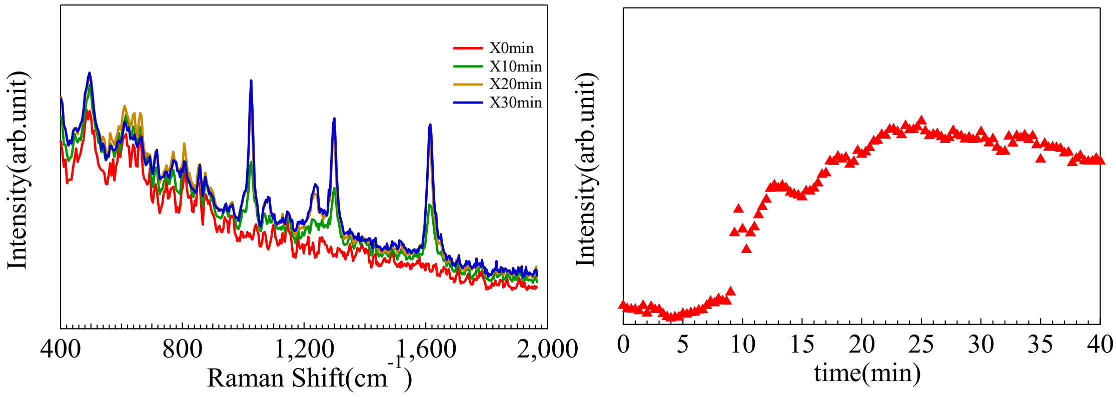

Figure 3 Changes in the intensity of Raman spectra with time.
(a) Raman spectra of 4bpy, (b) Peak intensity at 1618 cm^{-1}.

3. CONCLUSION

In this study, we implemented GNF-SERS with a Boehmite substrate in a microfluidic device and attempted to measure the SERS of fluids. As a result, we succeeded in measuring a fluid of 4bpy at 10 μM. It was found that the intensity saturates as the sample molecules accumulate and become more numerous than in the electric field enhancement section when the fluid continues to flow for a long time. Our GNF-SERS-active microfluidic device can provide a cutting-edge platform for application to real-time molecular imaging in vitro bio-analysis and enviro nmental analysis.

ACKNOWLEDGEMENT

The research and development was supported by the Tokyo Ohka Foundation for Science and Technology Promotion and the Hyogo Science and Technology Association.

REFERENCES

1. K. Kneipp, Y. Wang, H. Kneipp, L. T. Perelman, I. Itzkan, R. R. Dasari, and M. S. Feld, Single Molecule Detection Using Surface-Enhanced Raman Scattering (SERS), Phys. Rev. Lett., 78, 1667, 1997.
2. C. Zong, M. Xu, L. Xu, T. Wei, X. Ma, X. Zheng, R. Hu, and B. Ren, Surface-Enhanced Raman Spectroscopy for Bioanalysis: Reliability and challenges, Chem. Rev. , 118, 4946–4980, 2018.
3. H. Wei, S. M. H. Abtahi, and P. J. Vikesland, Plasmonic colorimetric and SERS sensors for environmental analysis, Environ. Sci.: Nano, 2, 120, 2015.
4. S. Yamazoe, M. Naya, M. Shiota, T. Morikawa, A. Kubo, T. Tani, T. Hishiki, T. Horiuchi, M. Suematsu, and M. Kajimura, Large-Area Surface-Enhanced Raman Spectroscopy Imaging of Brain Ischemia by Gold Nanoparticles Grown on Random Nanoarrays of Transparent Boehmite, ACS Nano, 8, 6, 5622–5632, 2014.
5. M. Shiota , M. Naya, T. Yamamoto , T. Hishiki , T. Tani, H. Takahashi, A. Kubo, D. Koike, M. Itoh, M. Ohmura, Y. Kabe, Y. Sugiura, N. Hiraoka , T. Morikawa, K. Takubo, K. Suina, H. Nagashima, O. Sampetrean, O. Nagano, H. Saya, S. Yamazoe, H. Watanabe and M. Suematsu, Gold-nanofève surface-enhanced Raman spectroscopy visualizes hypotaurine as a robust anti-oxidant consumed in cancer survival , Nature communications, 9, 1561, (2018)

Development of gel micromachining technique for tissue formation with multiple types of cells

#Keito Sonoda[1], Haruhiko Takemoto[1], Yoichi Saito[2], Yoshitaka Nakanishi[2,3], Yuta Nakashima[2,3,4,5]

1 Graduate school of Science and Technology, Kumamoto University, Japan; 211d8466@st.kumamoto-u.ac.jp
2 Faculty of Advanced Science and Technology, Kumamoto University, Japan
3 Institute of Industrial Nanomaterials, Kumamoto University, Japan
4 International Research Organization for Advanced Science ＆ Technology, Kumamoto University, Japan
5 Japan Science and Technology Agency, Fusion Oriented Research for Disruptive Science and Technology, Japan
#Corresponding Author / E-mail: 211d8466@st.kumamoto-u.ac.jp, TEL:+81-96-342-3743

ABSTRACT

Tissue formation technology consisting of multiple types of cells similar to those *in vivo* is required for the development of new drugs and artificial organ formation. This paper presents a gel patterning technique to culture multiple types of cells on the same device. Alginate gel micropattern was formed on a glass plate by photolithography, wet etching, lift-off, or laser processing. Cell micropatterns were formed along the gel micropattern on the glass plate by cell adhesion inhibition effect of alginate gel. This technique permits the creation of cell micropatterns with arbitrary geometry because hydrogel materials promoting or inhibiting cell adhesion can be patterned precisely. Also, this technique can be processed the culture surface during cultivation because the gel materials can be removed by non-cytotoxicic solution such as ethylen diamine tetraacetate. We developed a gel patterning method using laser processing to achieve maskless microfabrication of gel materials. Moreover, we demonstrate that this technique can be used to form three kinds of cell co-culture patterns.

Keywords : Photolithography, Co-culture, Alginate gel, Laser processing

1. INTRODUCTION

The number of organ transplant recipients and the demand for organ transplants is increasing every year. However, the number of organ donors is predominantly insufficient, and the supply of organs is not keeping up with the demand for transplants. In order to solve this problem, it is necessary to develop new drugs for each disease and artificially tissue models that mimic organs *in vitro*. In Japan, technology to regenerate and transplant cartilage tissue, which is difficult to heal spontaneously, by culturing the patient's own cells [1] has been put to practical use. However, these transplantable cellular tissues are limited to those composed of a single type of cell, and those composed of multiple types of cells have not been put to practical use. We had developed the gel micromachining technique for creating cell micropattern by applying to the photolithography technique [2]. This research objective is to create a co-culture pattern consists of three types of cells using gel micromachining process. In addition, we investigated laser processing as a processing method that can be used in combination with photolithography.

2. MATERIAL AND METHOD

2.1 Gel micromachining technique

Multiple-type cell co-culture patterns were fabricated using gel micromachining technique. The cell co-culture device consists of the two types of cells were fabricated by following process (Fig.1). Photoresist was coated by spin-coating (a) and patterned using the desired micropatterned photomask (b, c). The micropatterned substrate was spin-coated with sodium alginate solution and immersed in calcium chloride solution for gelation of the sodium alginate (d). Then alginate gel was lift-offed by removing the photoresist using developer, and the alginate gel pattern that consists of cell adhesion and non-adhesion surface was created (e). The first type of cell was seeded on the fabricated substrate. Cells are only adhered to glass surface by cell non-adhesion property of alginate gel. In this case, cell pattern is formed on the fabricated substrate (f). Then the alginate gel was removed by injecting EDTA to the culture medium during incubation (g). The second type of cells was then seeded to form a two types of cell co-culture pattern (h). In addition, a gel patterning method using multiple exposures of photoresist was developed to form three types of cell co-culture patterns. The first and second types of cells were previously fluorescently stained with different fluorescent dye and observed using an inverted fluorescence microscope.

2.2 Laser processing

The laser processing was used as gel material processing method that can be combined with photolithography. Glass substrate was coated with sodium alginate solution by spin-coating and immersed in calcium chloride solution for gelation. The coated alginate gel was etched by a laser processing. After laser processing, the thin alginate gel remaining on the surface was etched by immersion in a PBS solution containing alginate lyase. Then the gel micropattern was created without the photomask.

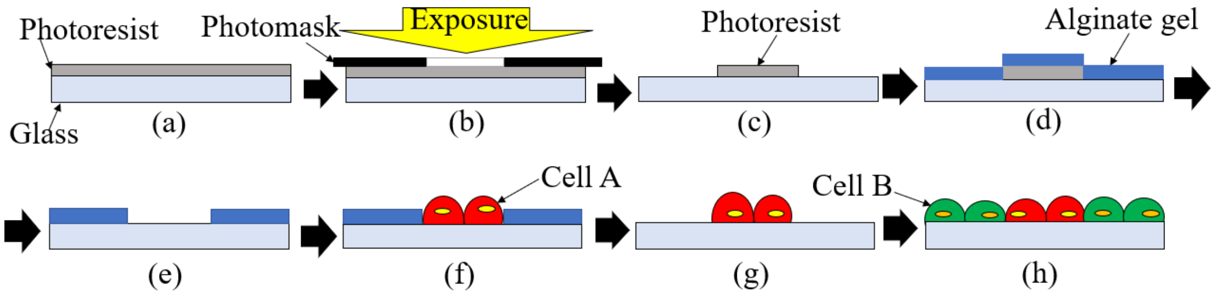

Fig.1 Procedure of two types of cells co-culture pattern formation.

3. RESULT AND DISCUSSION

Figure 2 shows two types of cell co-culture pattern fabricated using photolithography. Cells were adhered to the entire surface, and it could not be confirmed that two types of cell patterns were formed in the phase contrast image (a). In the fluorescence image (b), no cells were observed in the center area. These two photographs were taken at same area, demonstrating that the two types of cells were patterned and co-cultured on the same substrate. In other words, only the second type of cells that seeded after removing the alginate gel pattern were adhered to the center area. Figure 3 shows the cell micropatterns on the gel pattern fabricated by the laser processing. The dashed line in the figure indicates the boundary between the alginate gel and the laser processed area. Cells were not adhered to the alginate gel and adhered to the glass surface exposed by the laser processing. Fabricated alginate gel micropattern was measured by the inverted microscope. The creatable minimum size of alginate gel pattern by the laser processing is approximately 150 µm, and the error of the fabricated micropattern size was approximately 50-80 µm.

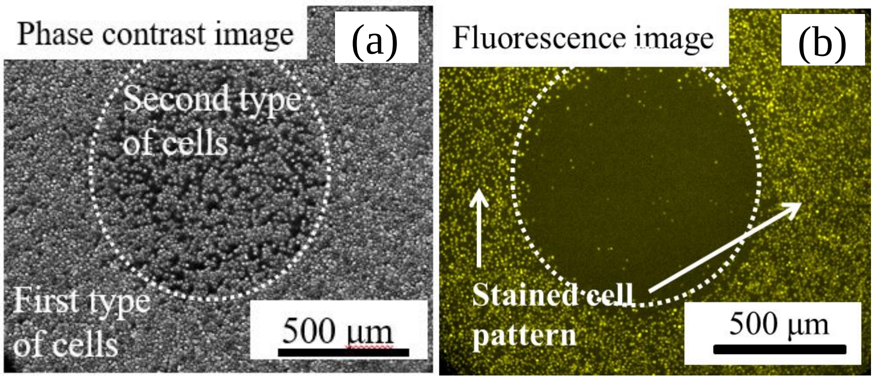

Fig.2 Photographs of created cell micropattern consisting of two types of cells. (a) Phase contrast image. (b) Fluorescence image.

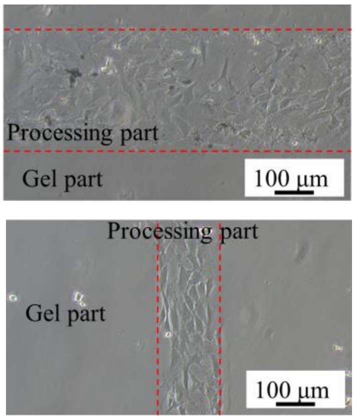

Fig.3 Cell micropattern along the alginate gel fabricated by the laser processing.

4. CONCLUSION

In this study, cell patterning technique for multi type of cell co-culture were developed by photolithography and laser processing. Two types of cells were successfully patterned to desired shape along the gel micropattern using this technique. Photolithography and laser processing errors were approximately 5-20 µm and 50-80 µm, respectively. The cell micropatterning technique and co-culture technique will be achieve the fabricating various tissue model and disease models.

REFERENCES

[1] K. Hoshi, Y. Fujihara, Y. Asawa, S. Nishizawa, S. Kanazawa, T. Sakamoto, M. Watanabe, T. Ogasawara, H. Saijo, Y. Mori, T. Takato T, “Recent trends in cartilage regenerative medicine and its application to oral and maxillofacial surgery”, Oral Science International, Vol. 10 (2013), pp. 15-18.

[2] Y. Nakashima, Y. Yamamoto, Y. Hikichi, Y. Nakanishi, Creation of cell micropatterns using a newly developed gel micromachining technique. Biofabrication,2016 Jul 26:8(3):035006

Development of shock wave focusing device for needle-free electrically induced microbubbles injector

Yibo Ma[1], Keita Ichikawa[1], Yoko Yamanishi[1,#]

1 Faculty of Engineering, Kyushu University, Fukuoka, Nishi Ward, 744 Motooka, 819-0382, Japan
 # Corresponding Author / E-mail: yoko@mech.kyushu-u.ac.jp, TEL: +81 92-802-3156

ABSTRACT

We developed a needle-free injector based on electrically induced microbubble injection. In this work, a shock wave focusing device was developed to improve the electrically induced microbubble injector perform. First, we evaluated microbubble injector reagent injection depth. Then we fabricated an elliptical hemispherical reflector to focus the shock waves from the microbubbles and thus amplify the shock and expansion waves. We realized the amplification of the shock and expansion waves by the fabricated reflector

Keywords : Electrically induced microbubble, Drug delivery, Needle free injector, Shock wave focusing

1. INTRODUCTION

Currently, the metal needle injector has been widely used. However, the pain and the infectious due to metal needle injector using have been worldwide problems. To solve the problems, drug delivery systems were developed worldwide such as skin permeation and implantable drug delivery devices(1) and biomimetic needle-free injection systems(2). Although the needle-free injector has been developed, its high-pressure water jet may cause bruising or bruises and pain during injection(3). Therefore, the pain resulting from injections and the stress they cause have not yet been resolved.

Unlike the gas-pressure type needle-free injection systems, our new needle-free injection system uses microbubbles to perforate the skin and introduce the reagent. In this study, we propose a mechanism for drug introduction using microbubbles and describe the results of reagent introduction. The fluorescent reagent introduction, creation of reflectors to generate shock waves and expansion waves for microbubble injector perform improvement, results of pressure measurements are reported in this article.

2. CONCEPTS OF SKIN PERFORATION AND DRUG DELIVERY

We develop a bubble injector that can generate microbubbles (electrically induced microbubbles) in an electrolyte solution. Fig. 1(a) shows an overall view of the bubble injector. The FEM simulation of the electric field generated when 1000 V is applied to the device shown in Fig. 1(b). A high electric field of 10^6~10^7 V concentrated at the peak of the device is shown in Fig. 1(b). The high electrical field induced the microbubble generation. Fig. 1(c) shows how electrically induced bubbles are generated and ejected by bubble injector. The high-pressure jet(shock wave) generating from the microbubble has enough perforating power to locally perforate metal. Therefore, this study proposes a new needle-free system using a bubble injector to realize skin perforation, as shown in Fig. 1(d).

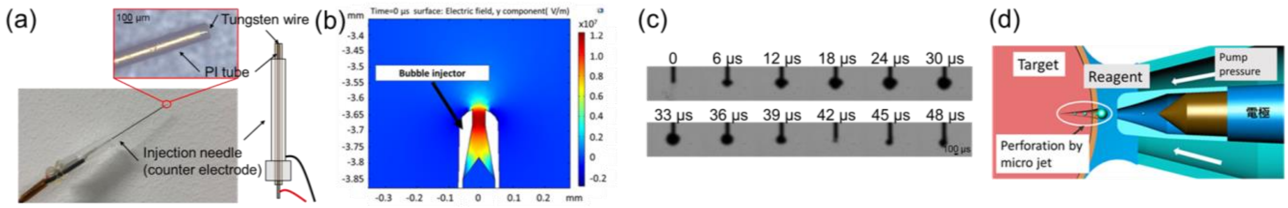

Fig.1 (a) The overall and magnified view of the bubble injector; (b) Electric field at the tip by FEM analysis (Applied voltage is 1 kV); (c) Sequential photograph capturing the state of bubble generation; (d) The concept of reagent introduction

3. INTRODUCTION EXPERIMENT USING FLUORESCENT REAGENT

First, an experiment was conducted to evaluate the bubble injector drug introduction ability. Fig. 2(a) shows the experiment setup diagram. The target of introduction was chicken breast fillet. The reagent was a mixture of fluorescent beads with a diameter of 2.1 μm in 0.9% NaCl solution. The delivery results were observed by a stereoscopic zoom microscope. Fig. 2(b) shows the reagent introduction depth at each voltage application. Reagent was introduced to about 400 μm depth by the bubble injector. Generally, for the injection of influenza vaccination it is necessary to introduce the reagent to depth of at least 1 mm. It is necessary to improve the piercing force of bubble injector.

4. SHOCK WAVE APPLICATION TO IMPROVE REAGENT INTRODUCTION CAPABILITY

4.1 The reflector for shock wave and expansion wave generation

In this section, we propose a method to amplify the pressure by reflecting the shock wave that diffuses to the surrounding area and focusing it to a single point. Fig. 2(c) shows the concept of shock wave focusing device. The shape of the reflector is elliptical. The tip of the bubble injector, the point of shock wave generation, is placed at the elliptical focus. The generated shock wave was reflected by reflector and focused to other focus point where target would be placed. There are two type reflectors were made, Tin and PDMS. PDMS reflector can generate the expansion wave, covering Tin reflector on PDMS reflector can generate shock wave. The fabricated reflector is showed in fig.2(d).

4.2 Shock wave and expansion wave convergence pressure measurement

Fig. 3(a) shows the diagram of the pressure measurement experiment. A Muller Plate Needle Probe was used for shock wave pressure measurement. A platform made of PDMS was used between the reflector and the hydrophone. After constructing the experimental setup, the inside of the reflector was filled with saline solution. A microbubble injector was inserted from the top of the reflector, and the tip of the bubble injector was moved to the focal point on the reflector side using a fine manipulator and fixed. First, the pressure of the expansion wave was measured using a PDMS reflector. Then a tin reflector was attached to the PDMS reflector, and the pressure of the shock wave was measured. Non-focusing shock wave pressure without the reflector was also measured to compare the focusing effect.

Fig. 3(b) showed the pressure of shock without focusing. The pressure peak is 0.5 Mpa. Fig. 3(c) shows the expansion wave pressure measurement results. A negative pressure of -1.5 MPa was measured. The pressure using PDMS reflector is approximately 3 times of pressure without PDMS reflector. As a result, a negative pressure was generated using the fabricated device. The obtained negative pressure demonstrates that the concept of converting shock waves into expansion waves by reflection between PDMS and air has been achieved. Fig. 3(d) shows the shock wave pressure measurement results. A positive pressure of 2 MPa was measured. This confirms that the tin reflector is effective to amplify the pressure (approximately 4 times).

5. CONCLUSION

In this research, we aimed to develop a needle-free injection system using electrically induced bubbles. We evaluated the reagent introduction capability and created reflectors to utilize shock waves to improve the applicability of the bubble injector. As a result, it was confirmed that the current bubble injector has a reagent introduction capacity of approximately 400 μm in the depth direction, which is insufficient for general injections. To improve the microbubble injector perform, we made PDMS/Tin reflectors to focusing the shock wave. The fabricated reflector can generate shock wave or expansion wave by switching the reflector. And the result showed that the pressure using PDMS reflector is approximately 3 times of pressure and using Tin reflector is approximately 4 times. However, in the case of Tin reflector, there is negative pressure. This may be due to a positioning error when aligning the reflector focal point and the bubble injector tip. In the future, we would solve the problem identified in experiment and use the reflector to improve the reagent introduction depth. Also, introduction perform of the expansion wave and shock wave would be evaluated. Furthermore, we will further study the switching between shock wave and expansion wave, which was confirmed in this method, and apply it to various research fields as a device that can switch between positive and negative pressure.

ACKNOWLEDGEMENT

This work was supported by JSPS KAKENHI Grant Number JP19H02113, JP21J13114, JP22H00198 and JP22K17783. We would also like to thanks to Associate Professor Tokitada Hashimoto of Saga University for his knowledge of shock waves and experimental advice in conducting this research.

REFERENCES

1. K. Kawa, Drug Delivery System, Vol. 27, No.3, pp.164-175 (2012) .
2. K. Oka, S. Aoyagi et al., Sensors and Actuators A, Vol.97-98, pp.478-485 (2002).
3. N. Petrovsky, Y. Honda-Okada et al., Trials in Vaccinology, Vol.2, pp.39-44 (2013).

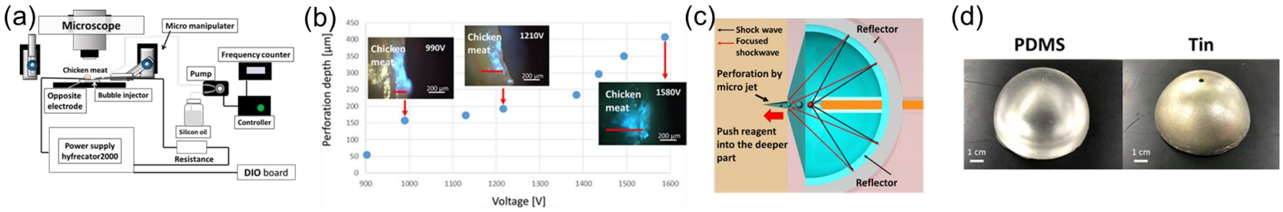

Figure.2 (a) Experiment setup for measuring the depth of injected reagent; (b) The result of measuring depth experiment; (c) The concept of applying shock wave; (d) Reflector made with each material

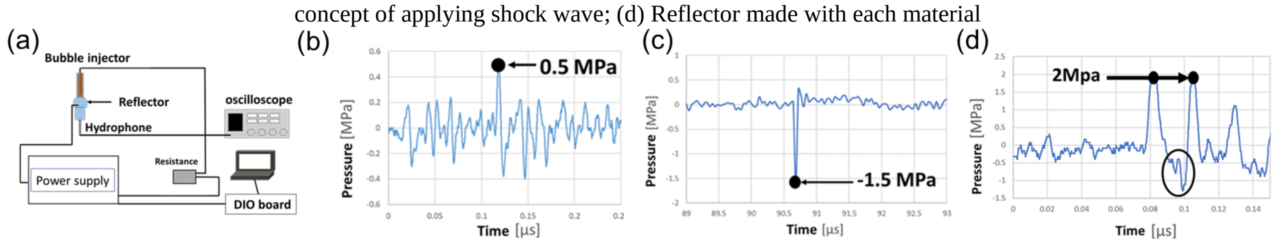

Figure.3 (a) Experimental setup for measuring the pressure of focused shock and expansion wave; (b) The pressure of shock; (c) The pressure of focused expansion wave; (d) The pressure of focused shock wave

Flow Control in Paper Channels Using Thermo-responsive Valve

#Masaya Nagano[1,2], Wataru Iwasaki[2], Nobutomo Morita[2], Taisei Motomura[2], Kenshin Takemura[2], Yoshitaka Nakanishi[3,4] and Yuta Nakashima[3,4,5,6]

1 Graduate School of Science and Technology, Kumamoto University, Japan
2 Sensing System Research Center, National Institute of Advanced Industrial Science and Technology, Japan
3 Faculty of Advanced Science and Technology, Kumamoto University, Japan
4 Institute of Industrial Nanomaterials, Kumamoto University, Japan
5 International Research Organization for Advanced Science & Technology, Kumamoto University, Japan
6 Japan Science and Technology Agency, Fusion Oriented Research for disruptive Science and Technology, Japan
#Corresponding Author / E-mail: 226d8479@st.kumamoto-u.ac.jp TEL: +81-96-342-3743

ABSTRACT

Analysis using multiple reagents, such as enzyme-linked immunosorbent assay (ELISA) in microfluidic paper-based analytical devices (μPADs), requires fluid control in the paper channel. In this study, a valve mechanism using thermo-responsive polymer was developed as a fluid control technology applicable to μPADs. To clarify the performance of the developed valve, permeability tests were conducted using colored liquid, and it was confirmed that the valve could open and close in response to temperature. Furthermore, it was confirmed that the heating and cooling can be reversibly and repeatedly opened and closed the valve. These results indicate that the developed valve is expected to make ELISA with μPADs possible.

Keywords : Microfluidic paper-based analytical devices, Thermo-responsive polymer, Poly(N-isopropylacrylamide), Valve, Plasma-induced graft polymerization

1. INTRODUCTION

Microfluidic paper-based analytical devices (μPADs) can flow reagents by the capillary force of paper [1], making analysis inexpensive and easy without the use of a pump. To perform analysis using multiple reagents such as enzyme-linked immunosorbent assay (ELISA) with μPADs, it is necessary to set the reagents multiple channels and flow them in sequence. However, due to the difficulty of fluid control on paper [2], analysis accuracy is reduced because of backflow and mixing of reagents in the flow path. Therefore, we developed a valve mechanism using thermo-responsive polymer as a fluid control technology applicable to μPADs. A hydrophilic PVDF porous membrane was used as the base material of the valve, and poly(N-isopropylacrylamide) (PNIPAAm) was used as the thermo-responsive polymer. Because PNIPAAm has the property of changing hydrophilic and hydrophobic properties at 32°C, polymerization on PVDF porous membranes causes it to swell and close pores or shrink and open pores (Fig. 1). We have previously confirmed that the developed thermo-responsive valve performs an open/close function in response to temperature [3]. However, we have not investigated the performance of the thermo-responsive valve, such as its permeability and whether it can be used repeatedly. Therefore, the purpose of this study was to clarify the performance of the thermo-responsive valve.

2 MATERIALS AND METHODS

A plasma-induced graft polymerization method was used to polymerize NIPAAm on PVDF porous membrane. When PVDF porous membrane is irradiated with argon plasma, radicals are generated on the PVDF porous membrane. NIPAAm was polymerized on The PVDF porous membrane by immersing in NIPAAm solution and incubating it at 30°C for 5 hours. The polymerization of NIPAAm was inhibited when exposed to air because the radicals react with oxygen and other substance. Therefore, we have assembled a plasma-induced graft polymerization system in which all processes can be performed continuously without exposure to the air. The purified NIPAAm monomer was dissolved in

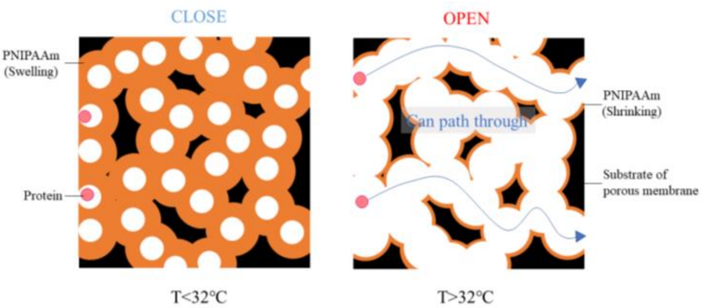

Figure 1 Schematic of the thermo-responsive valve. Below 32°C, PNIPAAm swells and the pores close; above 32°C, PNIPAAm shrinks and the pores open.

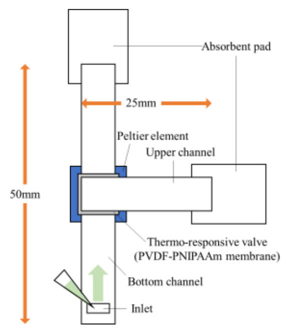

Figure 2 Evaluation system of valve operation.

a 50/50 vol% of methanol/water solution at a 2.5 wt% concentration. N,N'-methylenebisacrylamide and ammonium peroxodisulfate were dissolved in the NIPAAm solution to give a molar ratio of 0.5% and 1% to the NIPAAm monomer, respectively.

3 RESULTS AND DISCUSSIONS

To confirm the performance of thermo-responsive valve, a valve permeability test was performed using the system shown in Fig. 2. Thermo-responsive valve was placed between two nitrocellulose membrane, and they are stacked in T-shape. Colored liquid injected from the inlet flows through the bottom channel. If the valve is closed, it flows only in the vertical direction; if the valve is open, it flows in the upper channel. The temperature of the valve was controlled by the Peltier element. After injecting the green colored liquid through the inlet, the valve membrane was heated to 37°C using the Peltier element and then cooled to lower than 32°C by stopping heated the Peltier element. The heating and cooling operations were repeated at 60, 250, 315, 495, 555, and 765 seconds from the start of heating. The behavior of the liquid during the switching between heating and cooling is shown in Fig. 3. It was confirmed that the colored liquid moved when the thermo-responsive valve was heated, while the colored liquid hardly moved when the valve was cooled. Furthermore, despite repeated cycles of heating and cooling, the behavior of the liquid showed similar results.

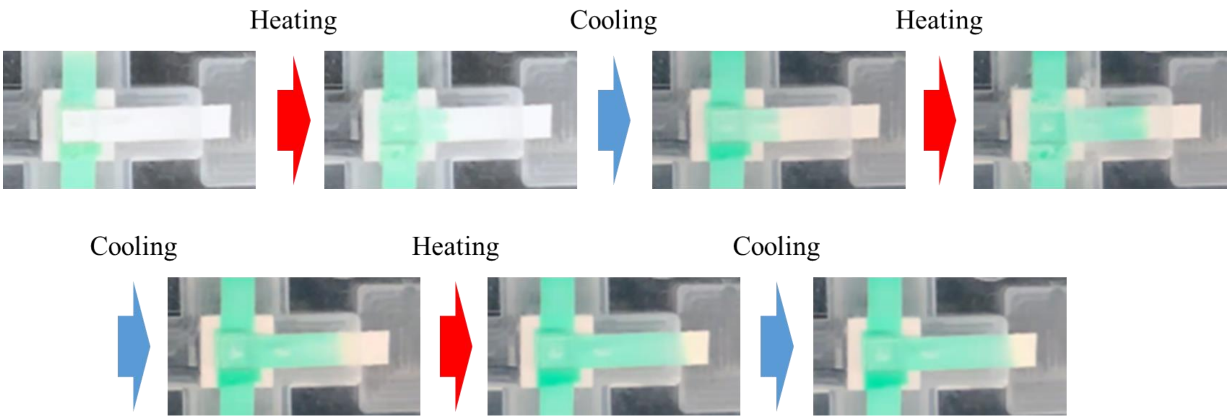

Figure 3 Flow behavior when the thermo-responsive valve is repeatedly opened and closed. The wetted surface of green colored liquid in the upper channel was photographed during switching between heating and cooling.

4. CONCLUSION

In this study, valve permeability tests were conducted using green colored liquid to clarify the permeability function of the thermo-responsive valve. The results showed that the liquid moved when the valve was heated, but hardly moved when it was cooled. Furthermore, by repeating the heating and cooling cycles, the valve was able to open and close reversibly and repeatedly. These results indicate that the valve has open/close capability and can be used continuously. In the future, we plan to demonstrate the usefulness of the valve by conducting ELISA.

ACKNOWLEDGEMENT

This work was supported by the Japan Society for the Promotion of Science (JSPS) KAKENHI Grant #20H02123.

REFERENCES

[1] A.W. Martinez, et al. Chem., Int Ed. 2007, 46, 1318-1320.
[2] Bowei Li, et al. Anal. Chem. 2017, 89, 11, 5707-5712.
[3] Wataru Iwasaki, et al., Microfluid. Nanofluidics, 2022, 26, 47.

Fundamental evaluation of biosensing microdevice based on immune response

#Yusuke Ide[1], Soichiro Fukuyama[1], Koki Yamasaki[1], Yoichi Saito[2], Yukio Fujiwara[3], Yoshitaka Nakanishi[2,4] and Yuta Nakashima[2,4,5,6]

1 Graduate school of Science and Technology, Kumamoto University, Japan,
2 Faculty of Advanced Science and Technology, Kumamoto University, Japan
3 Faculty of Life Science, Kumamoto University, Japan
4 Institute of Industrial Nanomaterials, Kumamoto University, Japan
5 International Research Organization for Advanced Science & Technology, Kumamoto University, Japan
6 Japan Science and Technology Agency, Fusion Oriented Research for disruptive Science and Technology, Japan
 # Corresponding Author / E-mail: 224d8452@st.kumamoto-u.ac.jp

ABSTRACT

This paper presents the fundamental evaluation of a biosensing microdevice for cancer diagnosis based on the immune response. The biosensing microdevice consists of a meandering channel and quartz crystal microbalance (QCM). The immune cells are cultured in the meandering channel. When the cancer cell cultured supernatant is injected into the meandering channel, the immune cells respond to the supernatant and produce immune response substances. The produced immune response substances were evaluated by QCM in real-time. In the experiment result of immune cell culture in the meandering channel, the cells were successfully cultured and the amount of TNF-α produced by immune cells was able to be evaluated by ELISA. In this case, evaluation time was reduced to less than half of the general experiment time using a microplate. These results indicated sufficient quantities of cells were able to be cultured in the channel to evaluate the immune response. Furthermore, the concentration is 10 ng/ml of recombinant TNF-α was evaluated in real-time by QCM. Thus, the fabricated biosensing microdevice can high-speed detection of minute amounts of immune response substances compared with typical methods.

Keywords : Microdevice, Biosensing, Immune cell, Immune response, QCM

1. INTRODUCTION

The main methods of cancer screening are imaging such as CT and MRI and biopsy. These methods are physical and mental burdens to recipients. Because of this, liquid biopsy shows promise for diagnosis methods of cancer. The liquid biopsy can reduce the burdens of recipients by using biological fluid. For example, cancer can be diagnosed by detecting CTCs (circulating tumor cells) in the blood[1] or by evaluating cancer-derived scents in urine using nematodes[2]. These technologies can easily and unburden detect the present/absent cancer. On the other hand, one of the challenges is the impossibility to detect the cancer site. This research objective is to fabricate a biosensing microdevice for the detection of the cancer primary tumor based on immune response (Fig. 1). This paper presents the evaluation of the fundamental characteristics of an immune response detection microdevice.

2. MATERIAL AND METHOD

A microdevice having a meandering shape microchannel was fabricate by photolithography of SU-8 3050 (Nippon Kayaku Corp.) and PDMS (Polydimethylsiloxane) molding. The meandering microchannel was designed for sufficient quantity of immune cells could be cultured to measure the immune response. The cell cultured area of the fabricated meandering microchannel is 1.2 cm^2. This area is three times larger than the culture area of the 96 well microplate and can culture 1×10^5 cells of immune cells. The width and height of the meandering channel were 500 µm and 200 µm, respectively.

Human monocyte-derived macrophages (HMDMs) isolated from the peripheral blood of healthy donors were used as the immune cell. Human ovarian carcinoma cell (RMG-1) was used as cancer cell. HMDMs were seeded into the meandering channel after improving the cell adhesion by fibronectin coating. When the RMG-1 supernatant was injected into the microchannel using a microsyringe pump, HMDMs received the stimulation by supernatant and produced the immune response substance. This solution including immune response substance was collected and evaluated to the amount of TNF-α by ELISA (Enzyme-linked immunosorbent assay). The injecting condition was 5 µl/min for 200 min at 37 ℃ on a hotplate. RMG-1 culture supernatant used in this experiment was collected from the RMG-1 culture dish at 1 day culture. The negative control was a liquid collected by injecting a normal medium into the device under the same condition.

The amount of recombinant TNF-α (rTNF-α) was measured by a flow-type QCM for demonstrating the real-time detection of immune response substance. The sandwich method of antigen-antibody reaction with the capture and detection antibody was used for detecting the rTNF-α. The capture antibody was immobilized on the electrode of the

QCM substrate and the detection antibody was modified with biotin at the terminal. Also, HRP (Horseradish Peroxidase) that modified with streptavidin at the terminal was used amplification in order to improve the detection sensitivity. The concentration of rTNF-α was prepared to 10 ng/ml. The sample and reagents were pumped at 10 μl/min for 20 min using a peristaltic pump.

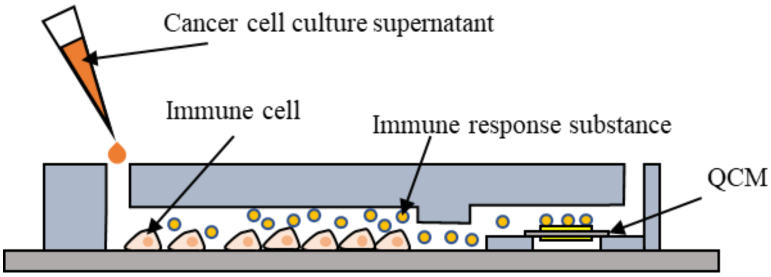

Fig.1 Schematic of a proposed microdevice.

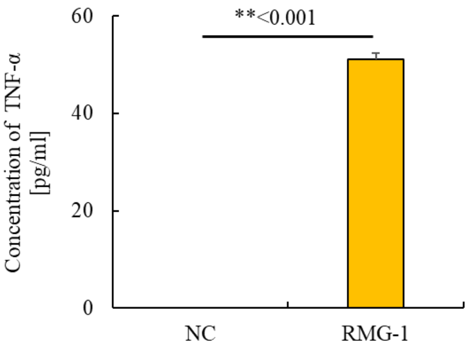

Fig.2 Evaluation of TNF-α production from HMDMs by ELISA.

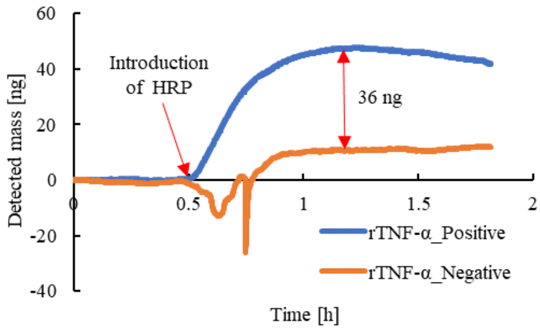

Fig.3 Measurement of rTNF-α by QCM.

3. RESULTS AND DISCUSSION

HMDMs produced TNF-α when RMG-1 culture supernatants were injected into the meandering microchannel (Fig. 2). On the other hand, a normal medium was injected into the meandering microdevice, HMDMs did not produce TNF-α. This result was statistically significant with a p-value of 0.001. This result indicates that HMDMs produced immune response substances by detecting cancer cell produced substances. From the results of negative control, the meandering microchannel did not stimulate immune cells and did not induce the immune response due to their shape. Consequently, the fabricated microdevice was effective as the microdevice for measuring immune response. Additionally, experimental results were the similar trend and evaluation time was reduced to less than half comparing with using a microplate.

Figure 3 shows the evaluation result of rTNF-α detection by QCM. The mass change resulted from 48 ng for rTNF-α positive and 12 ng for rTNF-α negative by a flow-type QCM. The mass difference of 36 ng was obtained in the presence and absence of rTNF-α. This result suggests that real-time detection of immune response substances by flow type QCM is possible by mass amplification with HRP.

4. CONCLUSION

The fabricated microdevice can culture a sufficient number of immune cells in the microchannel. Furthermore, the significant immune response was obtained in the short evaluation time. Besides, real-time detection of rTNF-α was achieved by flow-type QCM. These results indicate the biosensing microdevice based on immune response can be achieved. In the near future, we will evaluate the repeatability, detection accuracy, limitation, and etc. of the fabricated microdevice.

ACKNOWLEDGEMENT

This work was partly supported by a fund from the Japan Society for the Promotion of Science (JSPS) KAKENHI via a Grant-in-Aid for Scientific Research (B) (grant no. 19H04489), and the Japan Science and Technology Agency (JST) via a FOREST program (grant no. 21470036).

REFERENCES

1. B. Franken, et al, Circulating tumor cells, disease recurrence and survival in newly diagnosed breast cancer, Breast Cancer Research, Vol. 14, No. 5, R133, 2012
2. T. Hirotsu, et al, A Highly Accurate Inclusive Cancer Screening Test Using Caenorhabditis elegans Scent Detection, PLos one, Vol. 10, No. 3, e0118699, 2015

Characterization of Polyether Sulfone Membranes for Renal Replacement Therapy Devices

#Rei Kono[1] Takashi Ota[1] Yoshihiko Kanno[2] and Norihisa Miki[1]

1 Department of Mechanical Engineering, Keio University, 3-14-1 Hiyoshi, Kohoku-ku, Yokohama, Kanagawa 223-8522, Japan
2 the Department of Nephrology, Tokyo Medical University, Shinjuku Japan
 # Corresponding Author / E-mail: miki@mech.keio.ac.jp, TEL: +81-45-566-1430, rei.kono@keio.jp , TEL: +81-80-5544-2678

ABSTRACT

This paper reports characterization of nano-porous polyether sulfone (PES) membranes to design the dialysis devices for renal replacement therapy (RRT). In this work, we particularly highlight the thickness of the PES membranes. The PES membranes have a nano-porous skin layer and a micro-porous support layer. It is formed by the liquid-inversion method and the thickness can be determined by the spin-coating process of the PES casting solution. The PES membranes with various thickness are formed and optically investigated and the diffusion capacity is obtained via *in vitro* experiments. It was revealed that the thickness of the skin layer is almost constant and the micro-porous support layer changes with the total thickness. Interestingly, too thick micro-porous layers were found to have little diffusion capacity, which may originate from the collapse of the micro-porous layer during the formation process.

Keywords : hemofiltration, diffusion, polyether sulfone, nano porous, skin layer, renal replacement therapy

1. INTRODUCTION

The kidneys play an important role in removing waste and toxic substances from the blood and regulating electrolyte levels such as sodium and potassium. However, when patients suffer from acute kidney injury or multiorgan failure complicated by kidney damage or chronic kidney diseases, they need to be treated by renal replacement therapy (RRT).

Our group has been developing the implantable hemofiltration device (IHFD) for next generation RRT [1]. Nano porous polyether sulfone (PES) membranes are used for the dialysis membranes, which need to fulfil the requirements in both diffusion capacity and mechanical strength. In this research, we investigated the thickness of the PES membranes with respect to the diffusion capacity. First, we optically investigate the composition of the nano-porous skin layer and the micro-porous support layer by SEM. Then, in vitro diffusion experiments are conducted to deduce the diffusion capacity.

2. FABRICATION

2.1 Device design

This RRT device utilizes the principle of hemodialysis, in which small molecular-sized waste products are removed from the blood to the dialysate through the dialysis membrane. The device is a multi-layered microfilter composed of blood microchannels 300 μm in height and dialysate flow microchannels 300 μm in height which are separated with PES membranes. PES membranes have a bilayer structure, consisting of a skin layer with nanoscale holes on the surface and a porous layer with microscale holes inside.

2.2 Fabrication process

Figure 1 is the fabrication process of the device. The liquid inversion method is used to form the PES membrane. First, PES casting solution is spin coated on a substrate, where the spin speed determines the resulting thickness of the PES membrane. The substrate is carefully immersed into the curing solution and the PES membranes are formed after 24 h. Next, the blood channels and membranes are attached each other with a UV-cured adhesive resin. Finally, the dialysate flow channels and blood channels with PES membranes are piled up to achieve the target diffusion.

3. EXPERIMENT

3.1 Evaluation of PES membranes

We fabricated PES membranes with thicknesses of 100, 150, 200, 250, and 300 μm and observed the cross-sectional views using environmental scanning electron microscope (ESEM). The ratio of skin layer thickness to total thickness was then calculated from each image.

The results are as shown in Fig. 2. Results showed that the whole thickness of the PES membranes is not proportional to the thickness of the skin layer, and that the porous layer was further divided into two parts when the thickness of the PES membrane exceeded 150 μm (see Fig. 2).

3.2 Measurement of clearnace

We conducted *in vitro* experiments using hemodialysis devices fabricated with 80-μm and 160-μm-thick PES membranes. The experimental circuit was designed based on JIS T 3250. The simulated blood was saline mixed with albumin and creatinine, and the dialysate was saline solution. The creatinine concentration changes were measured over a 6-hour period with these circuits. In addition, the total clearance (K_t) was calculated using the creatinine concentration(C_B [mg/dL]) and the simulated blood flow rate (Q_B [mL/min]) based on the general clearance parameter [2]. Clearance was calculated as follows.

$$K_t = \frac{\left(C_{B(t)} - C_{B(t-1)}\right)}{C_{B(0)}} \times Q_B \tag{1}$$

The results are as shown in Fig. 3. The device with 80 μm PES membrane reached a concentration equilibrium after 6 hours of dialysis, whereas the device with 160 μm membrane showed a severe decrease in clearance.

4. CONCLUSION

The thickness of the dialysis membrane was found to have a significant effect on the diffusion of small molecules in the blood. We also found that the thickness of the skin layer of the PES membrane is not affected by that of the total thickness of the membrane. Therefore, the dialysis performance is considered to depend on the thickness and composition of the porous layer[3].

REFERENCES

1. Y. Gu and N. Miki, Multilayered microfilter using a nanoporous PES membrane and applicable as the dialyzer of a wearable artificial kidney, J. Micromechanics Microengineering, Vol. 19, No. 6, 2009.
2. M. Fukuda, Performance Evaluation Equation for Dialyzers, The Japanese Journal of Clinical Dialysis, Vol. 26 No.4, pp.399-405, 2010
3. B. Tüzün-Antepli, L. Yılmaz, H. Kalıpçılar, Investigating the State of Skin Layer of Asymmetric Polyethersulfone (PES)-Zeolitic Imidazole Framework-8 (ZIF-8) Mixed Matrix Gas Separation Membranes and Its Effect on Gas Separation Performance, ChemistrySelect 2022, e202200014.

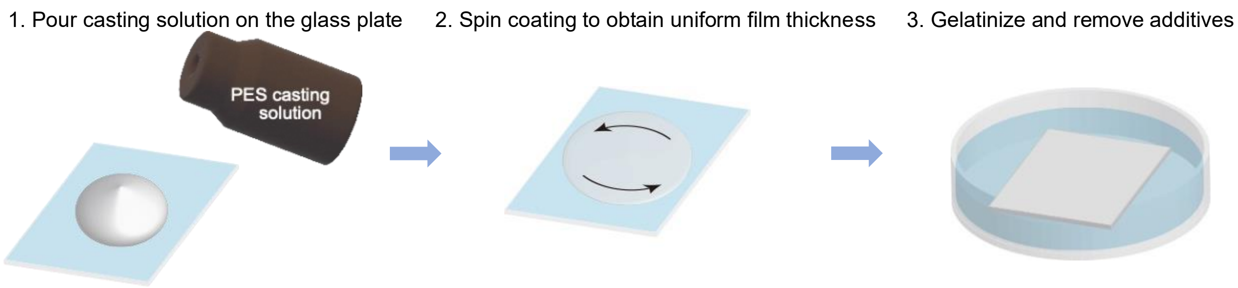

Figure 1 Fabrication process of PES membrane

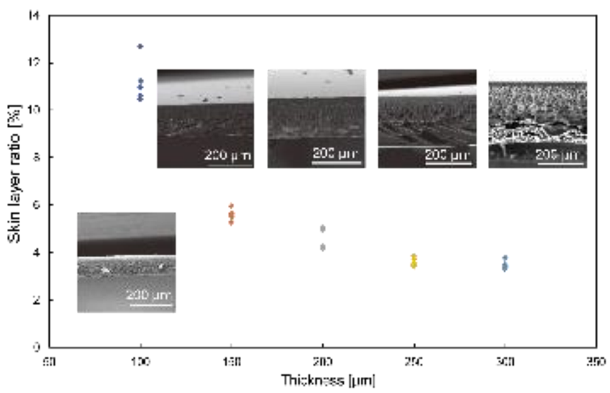

Figure 2 The ratio of skin layer to total thickness and the cross-sectional image of the PES membranes with different thickness

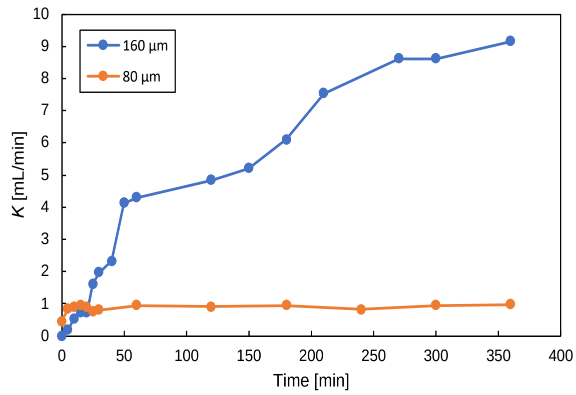

Figure 3 Diffusion capacity as a function of the time

Optimization of Electrode Structure for Rumen Bacteria Fuel Cell

Yusuke Yashiro[1] Yoshihiro Muneta[2], Hiroshi Sawada[2], Michitaka Yamamoto[1], Seiichi Takamatsu[1] Shozo Arai[2] and #Toshihiro Itoh[1]

1 Department of Precision Engineering, Graduate School of Engineering, The University of Tokyo,7-3-1,Hongo Bunkyo-ku, Tokyo 113-8654, JAPAN
2 National Institute of Animal Health, National Agriculture and Food Research Organization, 3-1-5 Kannondai,, Tsukuba, Ibaraki 305-0856, JAPAN
 # Corresponding Author / E-mail: itoh@pe.t.u-tokyo.ac.jp, TEL: +81-3-5841-6491, FAX: +81-3-5841-6485

ABSTRACT

Recently, a method of power generation using rumen (first stomach of cattle) bacteria has been discovered, and it is necessary to design an electrode structure to ensure a stable amount of power to drive a sensor to measure rumen status for health. To design the electrode structure, we evaluated the power generation parameters and the power performance of the current rumen bacteria fuel cell. In the experiment, the electrode area, electrode thickness, and electrode-to-electrode thickness were changed as parameters, and the open circuit voltage (OCV) and maximum power point (MPP) were obtained by creating polarization curves. The results showed that the OCV was constant around 0.4 V regardless of the parameters, while the MPP tended to increase nonlinearly as the electrode area increased. The lower electrode resistance could be caused by some biological mechanism in addition to an increase in the number of bacteria connecting with the electrode. The maximum power was 0.627 mW/m^2, which is smaller than other microbial fuel cells, but further improvement can be expected by using electrodes with low resistance and large surface area.

Keywords : Cattle, Bacteria fuel cell, Rumen bacteria, Bamboo charcoal electrode, Power supply.

1. INTRODUCTION

Recently, a method of generating power using rumen bacteria living in the rumen (first stomach) of cattle has been discovered[1]. In this method, an electrode made of bamboo charcoal is inserted into the rumen, and rumen bacteria settle on the electrode, then the bacteria produce electrons through fermentation under anaerobic conditions and generating voltage. If the rumen bacteria fuel cell can generate practical electricity and function well, it is expected to be used as a battery for wireless sensor to monitor cattle health by measuring pH in the rumen[2]. However, the current performance of generating power by rumen bacteria has not been evaluated in detail, and the bacteria and the electrode parameters involved in generating power have not been clarified. To utilize the power supply of rumen bacteria fuel cell that can drive a sensor, it is necessary to improve the power supply by devising an electrode structure. The objective of this study is to design an optimal electrode structure to ensure practical power supply of rumen bacteria fuel cell.

2. EXPERIMENT METHODS

From healthy cows, rumen contents were taken and 3 parameters for generating power (electrode area *S*, electrode thickness *t*, and inter-electrode thickness *T*) were set, and several rumen bacteria fuel cells (70 × 120 × T mm) were fabricated (Figure. 1-a). The fabricated fuel cells had the standard as *S*:67 cm^2, *t* :5 mm, and *T* :45 mm, respectively, and each parameter was varied by 49, 67, 94, and 139 cm^2 for *S*, 3.5, 5, 7, and 9 mm for *t*, and 10, 30, 45, and 60 mm for *T*. For each cell left for two weeks, the voltage was measured while varying the additional resistance between 50.9 and 462920 Ω. And polarization curve was generated (Figure. 1-b). From the polarization curve, open circuit voltage (OCV), which is the voltage when the resistor is not connected and the maximum power point (MPP), which is the maximum value of power approximated by a quadratic curve, ware read and the relationship between these parameters was investigated.

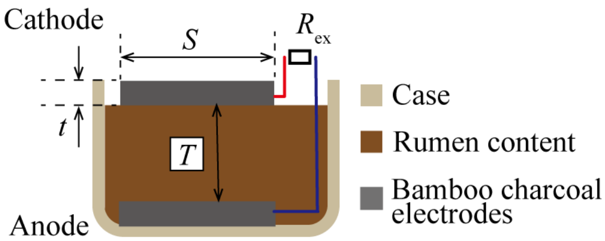

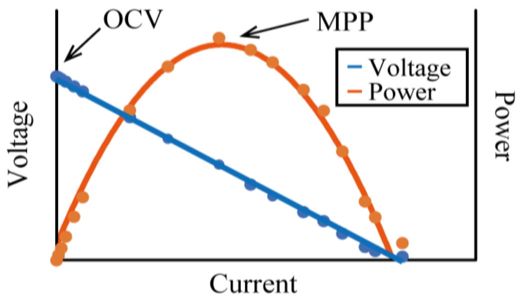

Figure.1 a. Experimental rumen bacteria fuel cell and parameters. b. polarization curve

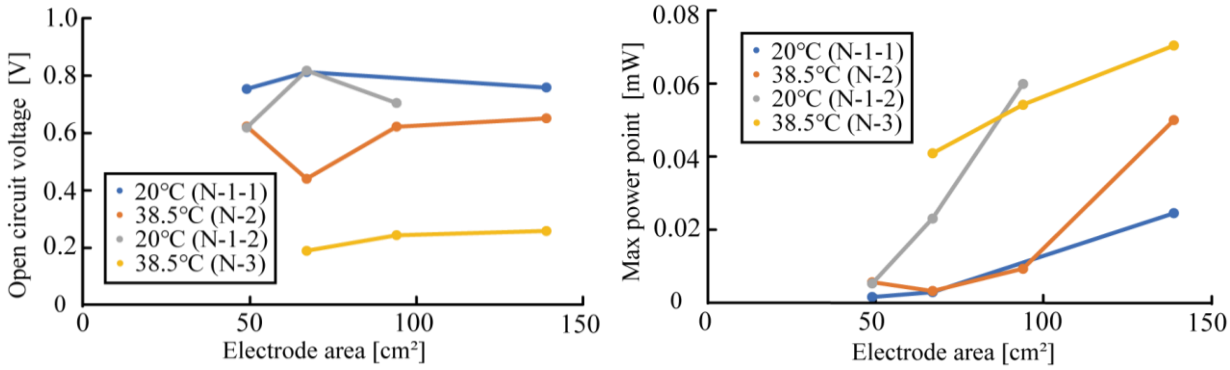

Figure.2 Relationship between electrode area: *S* and OCV or MPP. (plots are color-coded according to storage temperature and number of experiments)

3. RESULTS

Of the results obtained, only the results for the electrode area are shown in Figure.2. The OCV showed a constant voltage value of about 0.4 V regardless of the electrode area, electrode thickness, and electrode-to-electrode thickness. The results suggest that voltage in the fuel cell may be determined only by the activity of the bacteria in the rumen. Also, no correlation was observed between MPP and electrode thickness or inter-electrode thickness. But for the electrode area, MPP increased as the electrode area increased, and a maximum power of 0.07 mW was obtained. This is thought to be due to an increase in the number of bacteria and electrons which contact with the electrode as the electrode area increased, resulting in an increase in current. However, between electrode area and MPP, a linear relationship could not be confirmed, and there was a tendency for the power to increase rapidly with an increase in electrode area. The high resistivity of the bamboo charcoal electrode body (286 Ω-m) may have limited the current, but biological mechanisms such as the formation of bacterial colonies on the electrode surface may have influenced a rapid decrease in electrode resistance. The maximum power of the current fuel cell is 0.627 mW/m^2, which is considerably smaller than the 124.6 mW/m^2 of the fuel cell using bacteria in industrial wastewater[3].

4. CONCLUSION

Measurements of the power performance of rumen bacteria fuel cell revealed that a maximum power is 0.627 mW/m^2, which is about 200 times as small as that of other bacteria fuel cell. On the other hand, the voltage was not affected by any of the parameters set in the experiment and was around 0.4 V. However, the power increased nonlinearly as the electrode area increased. The reason for this could be an increase in the number of bacteria and electrons connecting with the electrodes in addition to a influence of biological mechanisms. The above results indicate that the fabrication of electrodes with low resistance and large surface area is required to realize a high-power rumen bacteria fuel cell. For example, the use of bolus metals is expected to enable the fabrication of electrodes with improved power performance, while maintaining a small size.

ACKNOWLEDGEMENT

This work was supported by Cabinet Office, Government of Japan, Cross-ministerial Moonshot Agriculture, Forestry and Fisheries Research and Development Program, "Technologies for Smart Bio-industry and Agriculture" (funding agency: Bio-oriented Technology Research Advancement Institution) (JPJ009237).

REFERENCES

1. Yoshihiro Muneta, Hiroshi Sawada, Chihiro Shimodan, Hirotaka Okada, Toshihiro Itoh and Shozo Arai, "Establishment of Basic Technology for Rumen Content (Bacterial Flora) Generation (RuMie-E-E)," *164th Annual Meeting of the Japan Veterinary Medical Association*, online, Sep, 2021.
2. Lan Zhang, Jian Lu, Hirotaka Okada, Hironao Nogami, Toshihiro Itoh, and Shozo Arai, "Low-Power highly sensitive pH sensor with μ dots protective structures for monitoring rumen in cows in real-time," *IEEE Sensors*, vol. 17, no. 22, pp. 7281–7289, 2017.
3. Pepe Sciarria Tommy, Tenca Alberto, D'Epifanio A, Mecheri Barbara, Merlino Giuseppe, Barbato Marta, Borin Sara, Licoccia Silvia, Garavaglia Virgilio and Adani Fabrizio, "Using olive mill wastewater to improve performance in producing electricity from domestic wastewater by using single-chamber microbial fuel cell," *Bioresource technology*, vol. 147, pp.246-253, 2013.

Fabrication of $LiTaO_3$/SiC hybrid wafer using surface activated bonding method

Seigo Murakami and Ryo Takigawa

Kyushu University, 744 Moto-oka, Nishi-ku, Fukuoka 819-0395, Japan
E-mail: murakami.seigo.015@s.kyushu-u.ac.jp

ABSTRACT

We investigated the applicabilty of the SAB method to direct bonding of $LiTaO_3$ and SiC wafers. As a results, the $LiTaO_3$/SiC hybrid wafer could be successfully fabricated, and the strong bond strength was demonstrated at room temperature. This $LiTaO_3$/SiC structure can be used to realize surface acoustic wave (SAW) filters which can satisfy both efficient temperature compensation and heat dissipation in high frequency band and high-power applications.

Keywords : $LiTaO_3$/SiC, Surface activated bonding method, SAW filter

1. INTRODUCTION

Advanced communication applications, such as Multiple-Input Multiple-Output (MIMO), Internet of Things (IoT), and Cognitive Radio (CR), require radio frequency (RF) front ends with higher operating frequencies [1]. Surface acousitic wave (SAW) filter is one of the key components in this RF front ends. Typicaly, LiTaO3 crystal-based SAW filter has been used in the common mobile phone. In future SAW filter that meets the requirement of next-gen RF front ends, the temperature stability and heat dissipation are important because of the tighter spectrum filtering in the high-frequency band and high power applications [2]. However, conventional $LiTaO_3$ bulk based-SAW filters have difficulty in meeting these requierments owing to its large coefficient of thermal expansion (CTE) and low thermal conductivity. One solution is direct bonding of $LiTaO_3$ crsytal and a support substrate with high Young's modulus, low CTE, and high thermal conductivity [3]. Therefore, we focus on a SiC crystal as a a support substrate, and direct bonding method of $LiTaO_3$ and SiC has been developed.

Application of typcal bonding method with annealing process is difficult to bond these materials owing to the serious CTE mismatch (CTE of $LiTaO_3$: $16.1 \times 10^{-6}[/K]$), CTE of SiC: $4 \times 10^{-6}[/K]$)). For example, plasma-activated bonding method requires high-temperature annealing at 200°C or higher [4], which causes serious thermal stress. On the other hand, surface activated bonding (SAB) method is one of the promising room temperature bonding method [5]. It is interesting to apply this method to bonding of these meterials.

In this presenation, we report the applicability of SAB method with Ar fast atom beam (FAB) irradiation to direct bonding of $LiTaO_3$ and SiC wafers.

2. RESULT

Figure 1 shows a schematic diagram of the SAB method with Ar FAB irradiation. In this SAB method, $LiTaO_3$ and SiC wafers were set in the bonding chamber firstly. Under ultra-high vacuum conditions, each wafer surface was irradiated with Ar FAB for 60 seconds for the surface activation. Immediately after that, the both activated surfaces were brought into direct contact with a press load at room temperature. As a result, the $LiTaO_3$/SiC hybrid wafer was successfully fabricated using SAB method, Figure 2 shows a cross-sectional scanning electron microscope (SEM) image of the bonded $LiTaO_3$/SiC interface, indicating a successful bonding at the micron scale. Next, the bond strength was evaluated by two-type tests: the blade test and the dicing test. By measuring the length of the crack propagated when the blade is inserted into the bond interface, the surface energy showing the bond strength can be calculated [6]. Generally, the surface energy of 1 [J/m^2] or higher indicates a sufficient bond strength for a practical use. Figure 3 shows the photograph of the propagated crack after blade insertion into the bonded $LiTaO_3$/SiC interface at room temperature. The estimated surface energy of the bonded $LiTaO_3$/SiC wafer was approximately 1.3 [J/m^2]. Next, the bond strength of $LiTaO_3$/SiC was evaluated by the dicing test. In the dicing test, the bonded wafer was cut into 8 mm x 8 mm dies and then cut into 0.5 mm x 0.5 mm dies with a dicing blade. Figure 4 shows a photograph of a succesful 0.5 mm x 0.5 mm dicing without debonding of the bond interface. The results of these tests indicates the successful formation of the strong bond $LiTaO_3$/SiC interface using SAB method.

3. CONCLUSION

The effectiveness of SAB method was demosntrated for room temperature direct bonding of $LiTaO_3$ and SiC wafers. The $LiTaO_3$/SiC hybrid structure could be successfully fabricated in a wafer-level. The blade test and dicing test showed the strong bond strength of $LiTaO_3$/SiC for the practical use. This $LiTaO_3$/SiC structure is expected to be used for temperature compensation and heat dissipation of conventional $LiTaO_3$-based SAW filter. Future research will focus on fabricating $LiTaO_3$-based SAW filter structures mounted on SiC substrates.

ACKNOWLEDGEMENT

Part of this work was financially supported by the Kakenhi Grants-in-Aid (JP20H02207, JP21K18729) from JSPS and JST CREST (JPMJCR210).

REFERENCES

1. L. Zhang *et al.*, High Frequency, Low Loss and Low TCF Acoustic Devices on $LiTaO_3$-on-SiC Substrate, 2021 IEEE International Ultrasonics Symposium (IUS), pp. 1-4, 2021
2. J. Shen *et al.*, SAW Filters With Excellent Temperature Stability and High Power Handling Using $LiTaO_3$/SiC Bonded Wafers, Journal of Microelectromechanical Systems, vol. 31, no. 2, pp. 186-193, April 2022
3. R. Takigawa, and J. Utsumi. Direct bonding of $LiNbO_3$ and SiC wafers at room temperature, Scripta Materialia, Vol. 174, pp. 58-61, 2020
4. D. Pasquariello and K. Hjort, Plasma-Assisted InP-to-Si Low Temperature Wafer Bonding, IEEE J. Sel. Top. Quant. Electron., Vol.8, No. 1, pp. 118, 2002
5. H. Takagi, R. Maeda and T. Suga, Room-temperature wafer bonding of Si to $LiNbO_3$, $LiTaO_3$ and $Gd_3Ga_3O_{12}$ by Ar-beam surface activation, J. Micromech. Microeng., Vol.11, No.4, pp. 348, 2001
6. M. P. Maszara, G. Goetz, A. Cavigila, and J. B. McKitteruck, Bonding of silicon wafers for silicon-oninsulator, J. Appl. Phys., Vol. 64, No. 10, pp. 4943, 1988

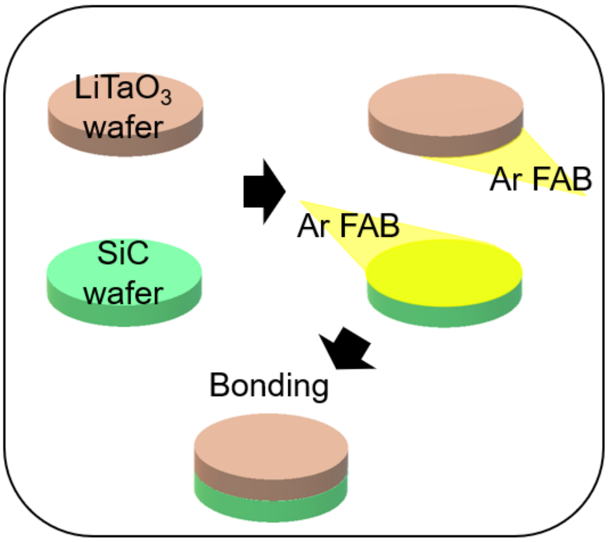

Figure 1 Schematic diagram of the SAB method

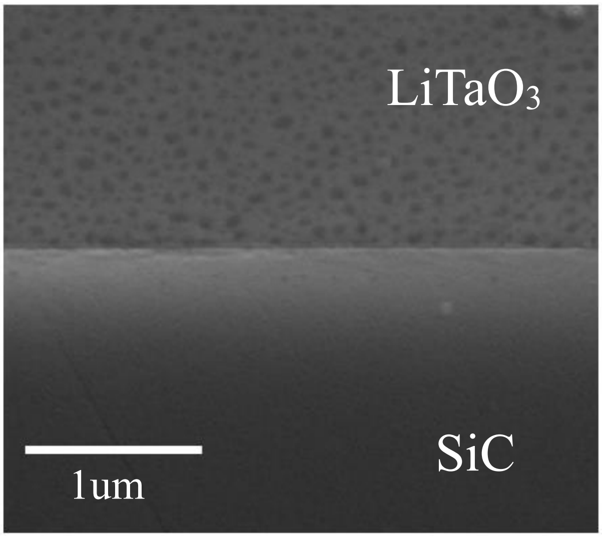

Figure 2 Cross sectional SEM image of the bond $LiTaO_3$/SiC interface at room temperature.

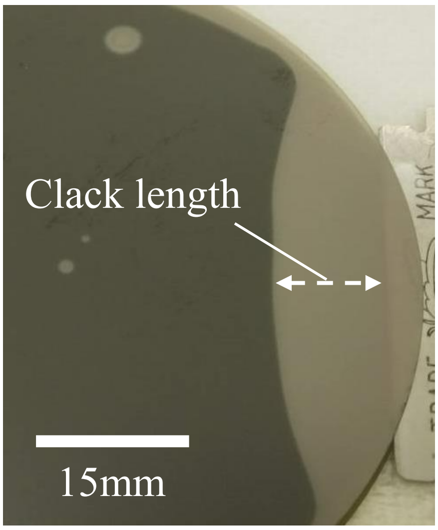

Figure 3 Photograph of the bonded wafer after blade insertion

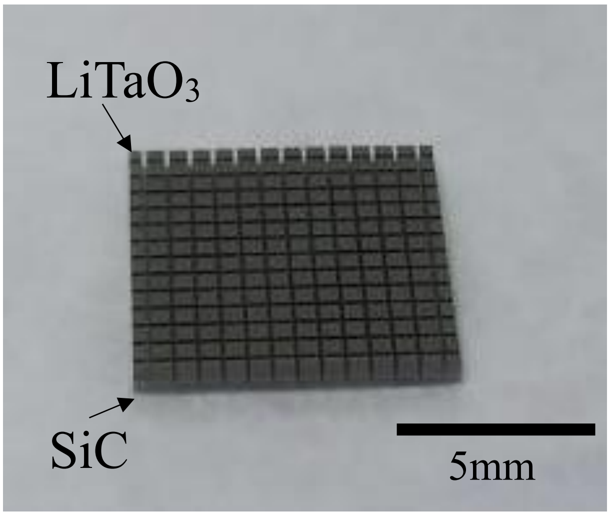

Figure 4 Photograph of the diced 0.5 mm x 0.5 mm dies

A Basic Study of Texture Classification by Active Sensing Using a MEMS-LSI Integrated Tactile Sensor

Takao Saitou[1], Shuji Tanaka[2] and #Masanori Muroyama[1,2]

1 Department of Electrical and Electronic Engineering, Tohoku Institute of Technology,
35-1 Yagiyama, Kasumicho, Taihaku-ku, Sendai, Miyagi 982-8577, JAPAN
2 Department of Robotics, Tohoku University,
6-6-01, Aramaki aza Aoba, Aoba-ku, Sendai, Miyagi 980-8579, JAPAN
 # Corresponding Author / E-mail: m-muroyama@tohtech.ac.jp, TEL: +81-22-305-3226, FAX: +81-22-305-3202

ABSTRACT

In this paper, we demonstrated a texture classification example based on 3-axis force sensor data from a MEMS-LSI integrated tactile sensor with active sensor device movement. Since the tactile sensor device can sense not only Z-axis force, but also X-axis and Y-axis shear forces, the active sensing system can acquire detailed surface characteristics of target objects. With the obtained sensing data and deep learning algorithm, in this paper, we tested the possibility of texture classification with 5 different target objects and proved texture classification with high accuracy.

1. INTRODUCTION

Human like tactile sensation for robots will realize human-robot coexisting society. Object surface texture recognition of the robots may help comfortable and safe human support. So far, we developed a small sized MEMS-LSI integrated tactile sensor device which can sense 3-axis force and temperature [1]. The force sensor has the following characteristics: 10mN force resolution, 5N dynamic range, and less than 10% sensing hysteresis for full scale range. The sensor device includes our original sensor platform LSI which has a unique sensing control method and parameter configurability of sensing type, sensing accuracy, sensing data transmission ways [2].

2. Sensing System Development and Experimental Results

2.1 Active Sensing System Development

We constructed an active sensing system (Fig. 1) which includes a robot finger equipped with the tactile sensor device and linear actuators for X, Y, Z and rotation (θ) movement of the robot finger. The actuator control and sensing system was developed with LabView (National Instruments Corp.). After contacting the sensing target object, we moved the finger for one direction and return direction. The moving distance was 50mm and its speed was 5 mm per sec.

2.2 Texture Classification Environment and Experimental Results

By using the developed active sensing system, we acquired the force sensing data. The following five type objects were used for experiments as texture classification: polyester (PES), acrylic, MDF, insulation board, and melamine (Fig. 2). For each object, we acquired 30 data sets. Each data set contained time series data of 200-time steps.

Two patterns of sensing data were used for training: (CASE A) six single capacitive force data of triaxial force sensor data (x+, x-, y+, y-, z+, and z-), and (CASE B) three differential capacitive force data (x-axis, y-axis, and z-axis) with removing abnormal sensing data. LSTM (Long-Short Term Memory), a type of RNN (Recurrent Neural Network), was used as the deep learning network model. The activation function for the hidden layer was LeakyReLu, and the activation function for the output layer was Softmax (5 type classification). The learning rate was 0.1. The optimization algorithm was Adam. The output was a multi-class classification, and the evaluation criteria were accuracy, precision and recall. The training environment were as follows: Ubuntu 20.04LTS, Keras/TensorFlow 2.7.0, and Python 3.8.2 programming.

Figure 3 shows learning phase results. Compared with CASE A, CASE B noise reduction method improved the learning efficiency enough. With the trained deep neural networks of CASE A and B, we tested those performance. CASE A and B both showed 100% accurate classification results. Figure 4 shows Confusion Matrix of the five classification results.

3. CONCLUSION

In this paper, we showed basic research results of texture classification by using a developed active sensing system with a MEMS-LSI integrated 3-axis tactile sensor device. The system demonstrated high-accurate classification performance for small number of sensing data. In the future, we will try large number of sensing data for verifying our sensing system performance as a texture classification system.

ACKNOWLEDGEMENT

This work was supported by JSPS KAKENHI Grant Number JP18K04256.

REFERENCES

1. S. Asano, M. Muroyama, T. Nakayama, Y. Hata, S. Tanaka, CMOS-on-LTCC Integrated Fingertip Sensor with 3-

axis Tactile and Thermal Sensation for Robots, Transducers 2017, pp. 516-519, 2017.
2. M. Muroyama, T. Nakayama, Y. Hata, S. Tanaka, Multi-Sensor Platform LSI Enabling Different Sensors to Be Event-driven and Connected to Common Differential Bus Line, Transducers 2017, pp. 1156-1159, 2017.

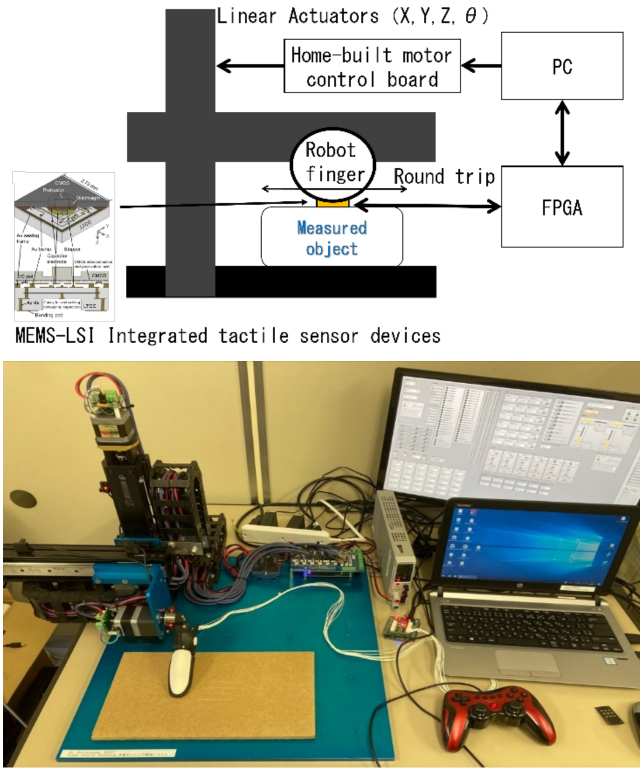

Figure 1 Developed Active Sensing System. (Upper side: System Block Diagram. Lower side: Photograph of the System.)

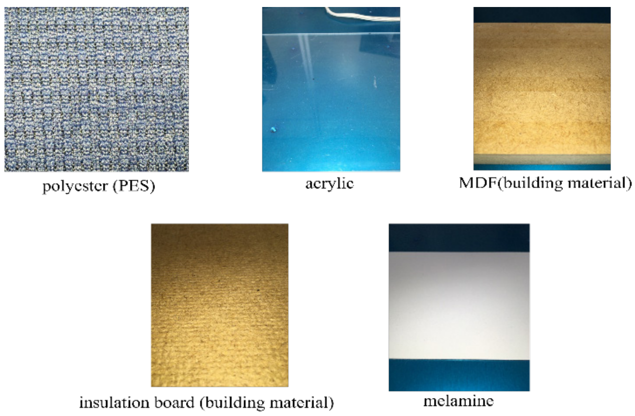

Figure 2 Target Objects for Texture Classification.

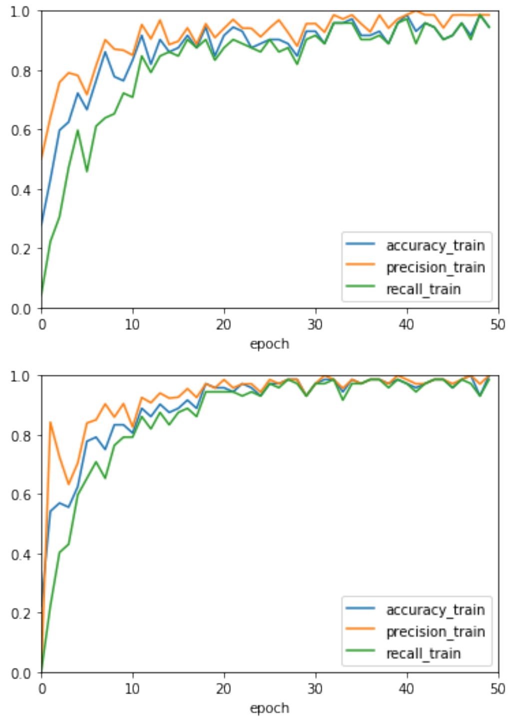

Figure 3 Learning Chart. (Upper side: CASE A, and Lower side: CASE B.)

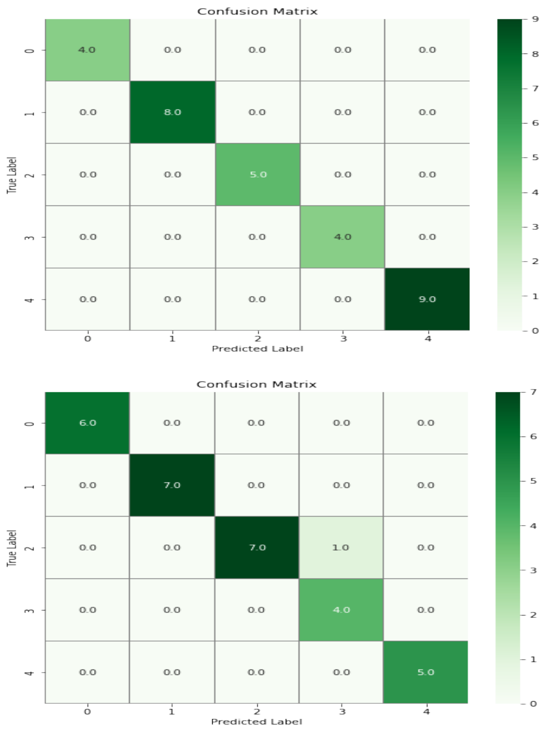

Figure 4 Confusion Matrix (Classification results for 5 type objects). (Upper side: CASE A, and Lower side: CASE B.)

Fabrication of LNOI/Si optical modulator using room temperature wafer bonding method

#Kaname Watanabe and Ryo Takigawa

Graduate School of Information Science and Electrical Engineering, Kyushu University, 7-3-1 Motooka, Nishi-ku, Fukuoka 819-0395, Japan
 # Corresponding Author / E-mail:watanabe.kaname.446@s.kyushu-u.ac.jp, TEL: 092-802-3721

ABSTRACT

This research aims to fabricate a 4-inch wafer-level LNOI/Si optical modulator arrays using room-temperature bonding method with activated Si atomic layer. The realization of LNOI/Si optical modulator arrays fabricated on wafer scale at room temperature will open up the possibility of heterogeneous integration of LNOI photonics on Si platform implementing MEMS, LSI, and Si photonics.

Keywords: room temperature bonding, wafer bonding, surface activated bonding, lithium niobate, optical modulator

1. INTRODUCTION

Lithium niobate ($LiNbO_3$, LN) is a promising electro-optic (EO) crystal for ultrafast optical modulators. The LNOI, a structure in which LN is bonded with a low refractive index material such as SiO_2, is expected to further reduce the drive voltage and overall device size compared to conventional bulk LN optical modulators due to the strong optical confinement[1,2)]. In additions, LNOI/Si structure will enable heterogeneous integration with MEMS, LSI, and Si photonics. To realize this LNOI/Si structure, a direct wafer-level bonding method between LN and thermally oxidized Si is required. Wafer-level bonding between LN and Si has been considered difficult due to the stress caused by the large difference in coefficient of thermal expansion (CTE). Surface activated bonding (SAB) is a bonding method in which bonding is performed by surface activation in a vacuum[3)]. SAB can overcome the stress because it is performed at room temperature. However, SAB is difficult to bond oxide material substrates. Therefore, we have proposed a room-temperature bonding method with activated Si atomic layer which is capable of a good transparency at optical communication wavelength[4)]. In this study, 4-inch wafer-level LNOI/Si electro-optical modulator arrays are demonstrated using this room temperature bonding method.

2. RESULTS

LNOI/Si hybrid wafers were fabricated using 4-inch LN wafer (X-cut) and 4-inch thermally oxidized Si wafer. No visible level voids or cracks were observed at the bonding interface. Figure 1 shows the comparison of the bond strength of bonded wafers using SAB and this bonding methods. Blade test[5)] was performed to estimate the bond strength. The bond strength of wafer bonded using this bonding method was 1.1 J/m^2 (Figure 1(b)). This result shows a dramatic improvement in bond strength compared to SAB (0.3 J/m^2, Figure 1(a)). Figure 2 shows a cross-sectional observation of the bonding interface by scanning electron microscopy (SEM). SEM observation results showed no micro-level voids or cracks at the interface in wafers bonded by this bonding method, confirming micro-level adhesion at the bonding interface. Next, LN was thinned to approximately 3 um and LNOI/Si optical modulator arrays were fabricated. Figure 3(a) shows a 4-inch wafer-level LNOI/Si optical modulator arrays. This wafer-level optical modulator was cut into chips, and the ridge waveguide edge-facing process was performed using dicing saw(Figure 3(b)). No peeling or cracking of the LN thin film was observed during dicing process, confirming that the bonding strength is strong enough to withstand micro-fabrication even after LN thinning. In addition, the operational characteristic results of the fabricated modulators demonstrated EO modulation characteristics.

3. CONCLUSION

In this study, for the realization of future ultrafast optical modulators, LNOI/Si optical modulator arrays were successfully fabricated at wafer-level using the room temperature bonding method with activated Si atomic layer and the EO modulation characteristics were demonstrated. It was also confirmed that this bonding method is strong enough to realize LN thin films of approximately 3 um. These results are expected to contribute to the development of high-speed optical communication systems after 6G.

ACKNOWLEDGEMENT

This research was partially supported by JST CREST (JPMJCR210) JSPS Grants-in-Aid for Scientific Research (JP20H02207).

REFERENCES

1. G. Poberaj, D. Rezzonico, R, Degl'Innocenti, and P. Gunter, Electro-optically tunable microring resonators in lithium niobate, Nature photonics, Vol. 1, pp. 407-410, 2007.
2. A. Boes, B. Corcoran, L. Chang, J. Bowers and A. Mitchell, Status and Potential of Lithium Niobate on Insulator (LNOI) for Photonic Integrated Circuit, Laser Photonics Rev., Vol. 12, Issue 4, pp. 1700256, 2018.
3. H. Takagi, R. Maeda, T. R. Chung and T. Suga, Low-temperature direct bonding of silicon and silicon dioxide by the surface activation method, Sens. Actuators A: Physical, Vol. 70, Issues 1-2, pp. 164-170, 1998.
4. R. Takigawa and T. Asano, Thin-film lithium niobate-on-insulator waveguides fabricated on silicon wafer by room-temperature bonding method with silicon nanoadhesive layer, Opt. Express, Vol. 26, Issue 19, pp. 24413-24421, 2018.
5. W. P. Maszara, G. Goetz, A. Caviglia, and J. B. McKitterick, Bonding of silicon wafers for silicon-on-insulators, Journal of Applied Physics, Vol. 64, Issue 10, pp. 4943, 1988.

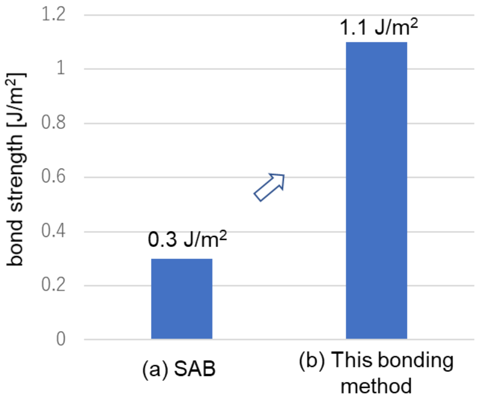

Figure 1. Comparison of bond strength (a) SAB (b) This bonding method

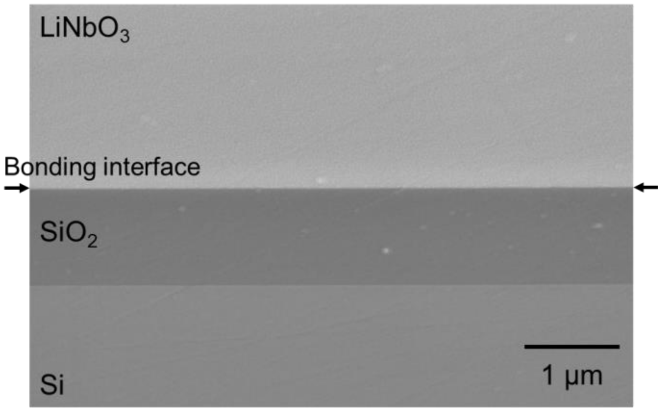

Figure 2. Cross-sectional SEM of LNOI/Si hybrid wafer

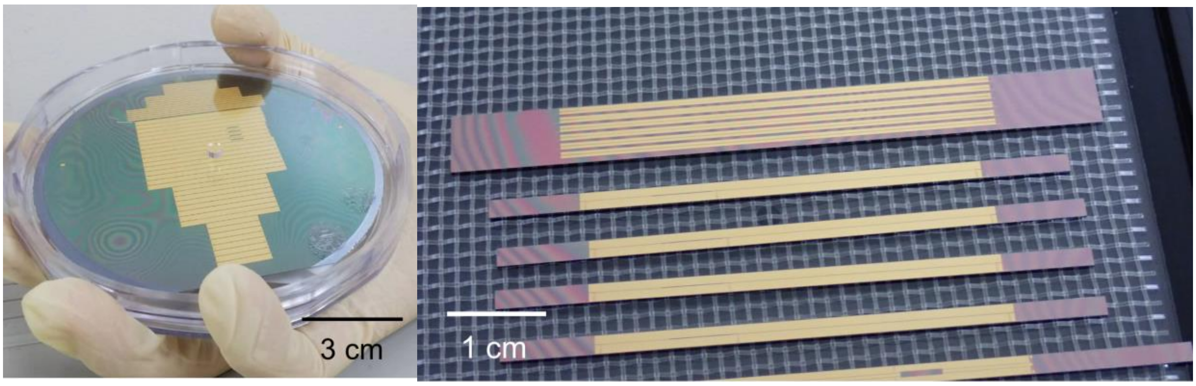

(a) (b)

Figure 3. LNOI/Si optical modulator arrays fabricated by room temperature bonding method with activated Si atomic layer (a) 4-inch wafer level and (b) after dicing and end-facing

A Microbial Fuel Cell Using Microbes in the Mud

Yuki Sano[1], Keisuke Abe[1], Tomoaki Kageyama[1], Hiroko Yamada[2,3], Tadao Matsunaga[1] and #Sang-Seok Lee[1]

1 Faculty of Engineering, Tottori University,
4-101, Koyama-Minami, Tottori, Tottori 680-8552, JAPAN
2 Symbiotic Environmental Technology Laboratory Co., Ltd., 1-7-16 Yabuta-Minami, Gifu, Gifu 500-8384, JAPAN
3 Graduate School of Engineering, Tohoku University, 6-6-1, Aoba, Aramaki, Aoba-ku, Sendai, Miyagi 980-8579, JAPAN
 # Corresponding Author / E-mail: sslee@tottori-u.ac.jp, TEL: +81-857-31-5961

ABSTRACT

In this study, we propose a microbial fuel cell using microbes in the mud. In the natural mud near lake or river, microbes are abundant, and there are electric current producing microbes among them. To obtain current efficiently and constantly from the current producing microbes, a device of microbial fuel cell is necessary. Here, we report the small sized microbial fuel cell prototype fabricated by 3D printing technique. In the fabricated prototype of microbial fuel cell, a commercial carbon felt was used as electrodes. Moreover, the microbes were used included in the mud collected from the lake. The prototyped microbial fuel cell was modified to obtain more stable generated current. We show how the microbial fuel cell structures were modified to improve the generated current characteristics. As a result, using the prototyped microbial fuel cell, we could obtain a constant current generation for 26 hours during measurement for 70 hours.

Keywords : Microbial Fuel Cell, Current Producing Microbe, 3D Printing, Current Generation

1. INTRODUCTION

In nature, there are a lot of various microbes. Among them, we pay attention to microbes which can create electric current such as *Shewanella* [1] and *Geobacter* [2] because those microbes can be considered as one of sustainable, clean and biological energy sources in future. To use them as a bio-energy source, there are two approaches. One is using themselves as an energy source that is using electric current created by microbes. Another approach is applying their electric current creation mechanism occurring inside the microbes to a new electric current generation method. In this study, first of all, we focus on the first approach and we investigate the availability of microbes' electric current creation capability. To obtain and use electric current created from the electric current producing microbials, a microbial fuel cell (MFC) device is necessary. We fabricated the device of MFC using 3D printing technique, and we investigated electric current creation capability of the MFC. Moreover, the MFC was improves to obtain more stable constant current. We report fabrication results and generated electric current characteristics by the MFC in following sections.

2. EXPERIMENTS

2.1 Fabrication of Microbial Fuel Cell

We fabricated the MFC to investigate characteristics of created electric current from electric current creation microbes. In Fig. 1, schematic diagram of the fabricated MFC is shown with brief electric current generation mechanism. The MFC was fabricated by 3D printing technique for rapid prototyping. Electric current producing microbes used in the MFC was cultivated by MudWatt [3]. Mud was initially collected near lake Koyama. The collected mud was put into MudWatt and culture medium was supplied to grow electric current producing microbes. After confriming the existence of current producing microbes in MudWatt by checking current values between electrodes built in MudWatt, the cultivation was stopped. Then, the current producing microbes are collected from the electrode of the MudWatt and they will be moved onto the electrode of MFC.

In the fabricated MFC, carbon felts are used as electrodes and we attached cultivated current producing microbes onto cathode electrode. Electrons created by microbes' metabolism are released to electrode, which are used as an electrical energy. Specifically, the current producing microbes are attached on the cathod carbon felt as postive electrode (anode). If organic culture medium is input onto positive electode, then the organic culture medium is decomposed by microbes, and hydorgen ions and electrons are created. The created electrons are moved to negative electrode (cathode) of anode carbon felt through an external circuit. On the other hand, hydrogen ions are also moved to negative electrode through an internal membrane. Near negative electrode, hydrogen ions and electrons are combined. Then, they reacted with oxygens of air and water is expelled. In this process, we can take out eletrical energy from the external circuit between anode and cathode electrodes. In the experiment, we measured the time change of the electric current with supplying the organic culture medium.

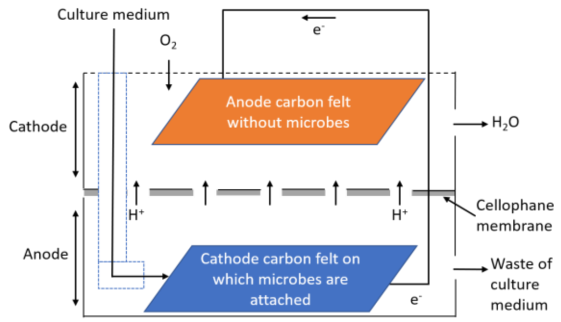

Figure 1 Schematic diagram of fabricated microbial fuel cell

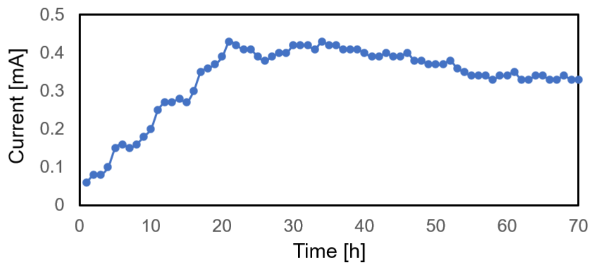

Figure 2 Generated current from fabricated MFC for 70 hours

2.2 Experiment

To clarify electric current generation capability of the fabricated MFC, we measured current characteristics over time. The generated current measurement was performed continuously for 70 hours. During the measurement, the culture medium was supplied regularly. In Fig. 2, generated electric currents from the MFC for 70 hours are shown. The generated electric current increased from the initial measurement stage until 20 hours later. After 20 hours until 46 hours from the measurement begins, the currnet was kept consistently as 0.4 mA. After that the current decreased gradually and became below 0.4 mA until the end of measurement. To obtain these characteristics, we improved the MFC structure several times. Specifically, we modifed MFC structure so as not to overflow H_2O which was created by reaction. Moreover, we also condidered the MFC structure not to move microbes from negative electrode to positive electrode, which becomes a resistence and generated current degradation.

3. CONCLUSION

As one of promising sustainable energy sources, we focused on electric current producing microbes such as *shewanella* and *Geobacter*, which can be obtainable easily in nature. To obtain current efficiently and constantly from the current producing microbes, we proposed an MFC device. The proposed MFC was fabricated by 3D printing technique for rapid prototyping. We measured generated electric current characteristics of the MFC to clarify its electric current generation capability. In the experiment, electric current producing microbes for the MFC were cultivated from mud near the lake. The fabricated MFC structure was modified to obtain more stable generated current. As a result, we could achieve a consistent generated current of 0.4 mA for 26 hours within total measurement times of 70 hours.

The fabricated MFC should be improved to obtain higher and more consistent electric current for sufficiently long periods. To do so, we are considering modification of material or structure of negative electrode. For instance, to enlarge adsorption quantity of electric current producing microbes, we consider that nano-structural material on the negative electrode can be helpful.

REFERENCES

1. G. Newton, S. Mori, R. Nakamura, K. Hashimoto, K. Watanabe, Analyses of Current-Generating Mechanisms of *Shewanella loihica* PV-4 and *Shewanella oneidensis* MR-1 in Microbial Fuel Cells, Appl. and Environ. Microbio., 75, pp. 7674-7681, 2009.
2. J. Wei, P. Laing, X. Cao, X. Huang, A New Insight into Potential Regulation on Growth and Power Generation of *Geobacter sulfurreducens* in Microbial Fuel Cells Based on Energy Viewpoint, Environ. Sci. Technol., 44, pp. 3187-3191, 2010.
3. Magical Microbes, https://www.magicalmicrobes.com/products/mudwatt-clean-energy-from-mud (Accessed August) 2022.

A Passive Wireless Vibration Sensing Method in Harsh Environment

Ziqi Zhao[1], Michitaka Yamamoto[1], Seiichi Takamatsu[1] and #Toshihiro Itoh[1]

1 Department of Precision Engineering, Graduate School of Engineering, The University of Tokyo, 7-3-1, Hongo, Bunkyo-ku, Tokyo 113-8656, JAPAN
 # Corresponding Author / Email: itoh@pe.t.u-tokyo.ac.jp, TEL: +81-3-5841-6491, FAX: +81-3-5841-6485

ABSTRACT

With the advent of the Internet of Things (IoT), industrial health monitoring is also becoming wireless and passive gradually. In this research, a passive wireless vibration sensing method is proposed for harsh environment applications. By using RFID backscattering technique, the vibration of a tag antenna could be transferred to the return loss variation of the RFID system. After background subtraction, the return loss variation of the tag antenna could be extracted, which has a relationship with the measured vibration amplitude. Experimental results show that the peak-to-peak value of the measured return loss is basically positively correlated to the vibration amplitude. The sensitivity of the proposed method can reach a maximum of 5.89 dB/mm, while the average sensitivity is about 3.80 dB/mm. Since the tag antenna could endure a harsh environment and has a good sensitivity, this method is believed to be applicable in a harsh environment.

Keywords : Harsh environment, Internet of Things, Passive, RFID backscattering, Vibration sensing, Wireless Sensor Network.

1. INTRODUCTION

In the recent years, Wireless Sensor Network (WSN) is gaining interest in machine health monitoring and structural health monitoring. Just like the human pulse could reflect the health of the human body, mechanical parameters such as vibration could reflect the health of machines and structures [1]. For an accurate measurement, sometimes the sensor needs to be embedded or installed on some hard-to-reach positions, so the read-out of the data and the regular maintenance will be difficult. Moreover, the monitored machine and structure may work in harsh environment for some applications [2][3]. To monitor the health condition of a working device or a structure in such an environment, the vibration sensor needs to be wireless, passive, and harsh-environment resistant.

2. METHODOLOGY

2.1 Sensing Mechanism

In this research, RFID backscattering technique is used, as shown in Fig. 1. When a tag antenna is placed in the read range of a reader antenna, it will passively and wirelessly receive the RFID signal from the reader antenna and then send a modulated backscattered signal to the reader antenna. Such modulation depends on the coupling of the reader antenna and the tag antenna. So, when the tag antenna is vibrating, the received power and the reflected power of the tag antenna will both change, building a relationship between the return loss of the tag antenna and the measured vibration. As a result, the measurement is achieved in a wireless and passive way.

2.2 Evaluation

The experimental system is shown in Fig. 1. The reader antenna is connected to a network analyzer, to receive power supply and transmit the antenna characteristics. The tag antenna is packaged and connected to a vibration exciter by a fixture. For the evaluation of the proposed method, different sine vibrations are applied on the packaged tag antenna, with the same vibration frequency but different vibration amplitude. The input vibration is measured by the vibration meter, while the output return loss is obtained wirelessly by the network analyzer.

The experimental results are shown in Fig. 2 and Fig. 3. Since the measured return loss includes the contribution of the reader antenna, the tag antenna and the surrounding environment, background subtraction method [4] is needed to get solely the contribution of the tag antenna. After background subtraction, the maximum return loss in the frequency domain under each vibration is measured respectively, as shown in Fig. 2. In Fig. 2, it is shown that the return loss will have an obvious shift in the frequency domain when the vibration amplitude is changing. And there is a relationship between return loss variation and vibration amplitude.

Similarly, the return loss at the center frequency is also recorded in the time domain, as shown in Fig. 3(a). In Fig. 3 (a), it is shown that the return loss signals of the tag antenna under different vibrations are periodic signals with different peaks and valleys. The peak-to-peak value of the measured return loss is basically positively correlated to the vibration amplitude. To show it more clearly, the relationship between the return loss variation and the vibration amplitude is shown in Fig. 3(b), which is also the characteristic curve of the tested device. As a result, the sensitivity of the proposed method can reach a maximum of 5.89 dB/mm, while the average sensitivity is about 3.80 dB/mm.

Figure 1. The experimental system.

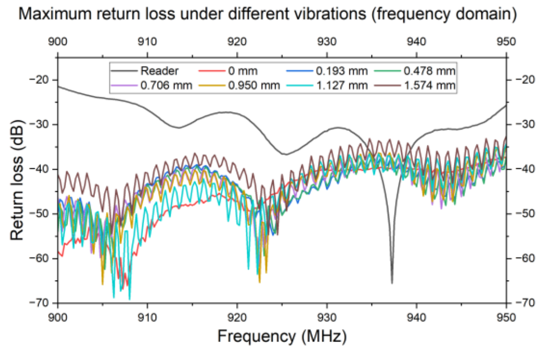

Figure 2. Return loss after background subtraction.

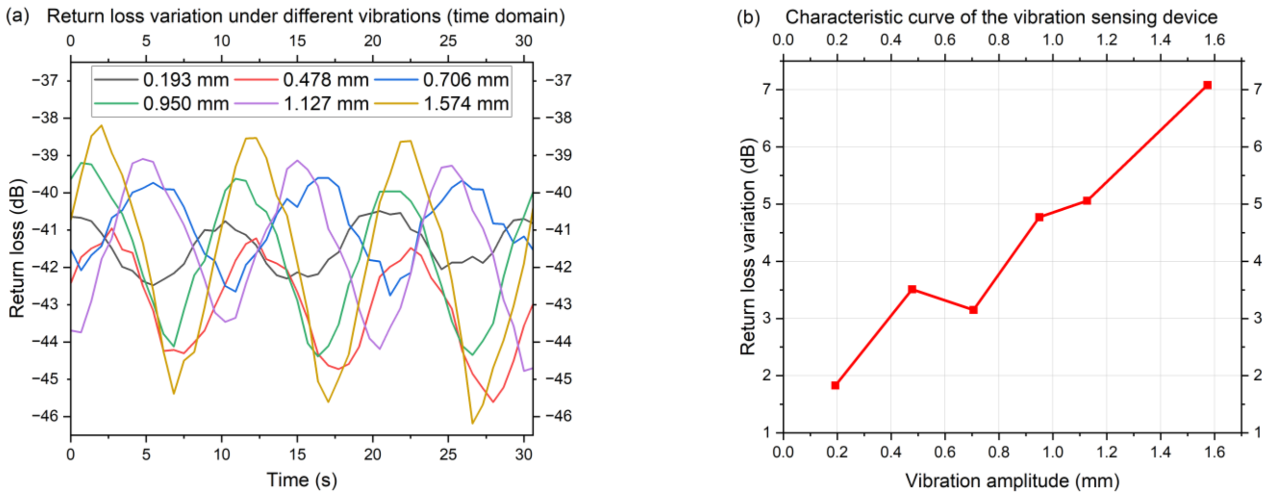

Figure 3. (a) Return loss in time domain. (b) The characteristic curve of the vibration sensing device

3. CONCLUSION

In this research, a vibration sensing method is proposed for passive wireless measurement in harsh environment. The feasibility of the proposed method is proved experimentally. As a result, the sensitivity of this method can reach a maximum of 5.89 dB/mm, while the average sensitivity is about 3.80 dB/mm. Since the tag antenna is actually a thin film of aluminum on PET substrate, which could endure cryogenic conditions, the proposed method is believed to be applicable to harsh environment applications. In the future, cryogenic experiments will be conducted to prove the feasibility of the sensor in harsh environments. Also, temperature sensing experiments and strain sensing experiments will be conducted, to explore the possibility of multi-parameter sensing. In addition, the decoupling of the backscattered signal will also be explored, to obtain different measured parameters from a single return loss signal.

ACKNOWLEDGEMENT

This work was supported by NEDO (Grant Number: JPNP18016). Author Ziqi Zhao would like to show special thanks to the China Scholarship Council (CSC No. 202106170012) for their support to his living expenses.

REFERENCES

1. Zhao, Z., Wang, D. F., Hou, Y., Itoh, T., & Maeda, R. Noninvasive Passive Measurement of Multiphase Currents in IoT. IEEE Transactions on Industrial Electronics, Vol. 68, No. 12, pp. 12860-12870, 2020.
2. Chen, Tong, et al. Self-heated all-fiber sensing system for cryogenic environments. Measurement Science and Technology, Vol. 21, No. 9, 094036, 2010.
3. Wilson, William C., and Gary M. Atkinson. Passive wireless sensor applications for NASA's extreme aeronautical environments. IEEE Sensors Journal, Vol. 14, No. 11, pp. 3745-3753, 2014.
4. Babaeian, F., & Karmakar, N. C. Time and frequency domains analysis of chipless RFID back-scattered tag reflection. IoT, Vol. 1, No. 1, pp. 109-127, 2020.

Microscopic Dynamic Diffusion Behavior of W/Ni/SiC Ohmic Contact at High Temperatures

Chen Wu[1,2], #Xudong Fang[1,2], Qiang Kang[1,2], Ryutaro Maeda[1,2,3], and Zhuangde Jiang[1,2]

1 State Key Laboratory for Manufacturing Systems Engineering, International Joint Laboratory for Micro/Nano Manufacturing and Measurement Technologies, Xi'an Jiaotong University, No.28, West Xianning Road, Xi'an, Shaanxi, 710049,P.R. CHINA

2 School of Mechanical Engineering, Xi'an Jiaotong University, No.28, West Xianning Road, Xi'an, Shaanxi, 710049,P.R. CHINA

3 Research Center for Ubiquitous MEMS and Micro Engineering, National Institute of Advanced Industrial Science and Technology, 1-2-1, Namiki, Tsukuba, Ibaraki 305-8564, JAPAN

 # Corresponding Author / E-mail: dongfangshuo30@xjtu.edu.cn, TEL: +86-17795832955

ABSTRACT

Failure of the electrical ohmic contact is one of the main factors affecting the operating performance of SiC-based high-temperature sensors and directly determines the sensor lifetime. The existing research method is to process and analyze the experimental samples, and pre-experimental mechanism prediction and calculation are lacking. In this paper, a three-dimensional model of the W/Ni/4H-SiC ohmic contact system was developed using the large-scale atomic/molecular parallel simulator (LAMMPS) and high-temperature molecular dynamics simulations were carried out. Results indicate that the atomic activity increases at high temperatures and the interdiffusion between the atoms of different layers will occur, and the higher the temperature the more significant this phenomenon is. In addition, when the temperature exceeds 900 ℃, the higher the temperature of the system, the more amorphization will occur in the SiC substrate. The above conclusions implied that molecular dynamics simulations can predict the microscopic changes of the system at high temperatures and that ohmic contact failure at high temperatures mainly comes from inter-atomic diffusion and amorphization of the substrate. This inspires us to use metals with weaker diffusion phenomena, which will be beneficial to enhance the high-temperature performance of SiC ohmic contacts.

Keywords : Silicon Carbide, Metals, Microdynamics, Diffusion, Ohmic Contact.

1. INTRODUCTION

Silicon carbide (SiC), as a third-generation semiconductor material with high breakdown voltage, high mechanical strength, high-temperature stability, can work stably in high-temperature harsh environments up to 1200 ℃, making it the preferred alternative material to Si for MEMS applications in extreme environments[1,2]. Therefore, it is important to carry out research related to the theoretical design, manufacturing process, packaging and testing of pressure sensors for all-SiC MEMS high-temperature devices. Existing studies show that 40% of the failures in high temperature SiC devices come from the disappearance of electrical signals [3], which shows that electrical ohmic contact failure is one of the main factors affecting the working performance of high temperature sensors, and the performance of ohmic contact directly determines the lifetime of sensors, which is a key challenge limiting the research of SiC-based MEMS electronic devices. Only by completely solving the high-temperature applicability problem of SiC-based ohmic contact can we give full play to the breakthrough application of SiC in the field of micro and nanoelectronic devices.

In contrast to Si, SiC ohmic contacts are more difficult to form due to the large work function [4]. On the one hand, the existing studies show that there are few types of metals that can contact with SiC and form linear ohmic properties, mainly represented by Ni and Ti [5]. On the other hand, SiC ohmic contacts are very prone to failure at high temperatures, and electrically stable SiC ohmic contact technology at high temperatures is still a major research challenge. In fact, the diffusion between layers at high temperature has been obtained only by post-processing analysis of failed samples, and it is not possible to predict the diffusion behavior at high temperature by analysis before the ohmic contact sample fabrication, so that metal species with less diffusion can be preferentially selected, which is of great significance for studying the high-temperature stability of SiC ohmic contacts. In this work, the contact m icroscopic dynamic model between the ohmic contact layer metal W/Ni and the 4H-SiC substrate was developed. The microscopic atomic-level diffusion mechanism and substrate damage behavior of the W/Ni/4H-SiC system at different high temperatures were obtained by using Lammps calculation software.

2. Methods and Results

2.1 Methods

Figure 1 shows the three-dimensional molecular dynamics simulation model of a silicon carbide substrate with metal (tungsten and nickel) atomic layers. The model consists of three parts: the uppermost layer is the tungsten (W) atomic layer, the middle layer is the nickel (Ni) atomic layer, and the lowermost layer is the silicon carbide atomic layer. The spacing between each atomic layer is 4 Å. Table 1 shows the structural dimensions of the model and the simulation parameters. The X and Y directions of the target material are set as periodic boundary conditions to reduce the simulation scale effect and to avoid lattice damage and loss of atoms in the workpieces. The integration time step is set to 1 fs. The simulation is divided into two phases: the chirality phase and the warming phase. The chilling phase keeps the simulation at a constant temperature of 293 K in the micro-regular system synthesis, with the aim of keeping the whole model in a steady state. The model can be considered as a stable equilibrium when the temperature of the simulated system is the initial set point and remains constant or when the pressure fluctuation range of the system is equal to or close to 0 bar. Considering the class of atoms and the form of interaction in the model, C-C, Si-Si and Si-C were calculated using Tersoff-type three-body potential functions. EAM.aloy-type potential functions were used to describe the W-W, Ni-Ni and W-Ni interactions.

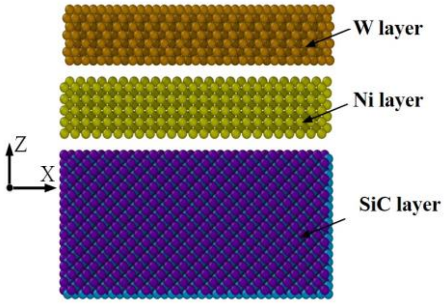

Figure 1. The three-dimensional model of W/Ni/4H-SiC ohmic contact system.

Table 1. Dimensional parameters for atomic diffusion modeling.

Materials	Tungsten	Nickel	SiC
Atomic Types	W	Ni	C和Si
Dimensions	90 Å×60 Å×20 Å	90 Å×60 Å×20 Å	90 Å×60 Å×50 Å
Number of Atoms	5236	4750	18144
Potential Function	EAM	EAM	Tersoff
Initial Temperature	293 K		
Time Step	1 fs		

2.2 Results

Figure 2a shows the vector diagrams of four different types of atomic displacements of the three atomic layers at high temperature (800 degrees C). At high temperatures, the activity of the atoms increases, the volume of the atomic layers diffuses, the interatomic spacing becomes larger, and the atoms at the demarcation of the atomic layers gain a certain amount of energy due to the increase in temperature will penetrate through the adjacent atomic layers into the adjacent lattice. Specifically, the left part of the nickel layer diffuses into the tungsten layer, while the right part diffuses into the silicon carbide layer. Figure 2b shows a three dimensional schematic of the atomic diffusion model at different temperatures. Below the temperature of 500 ℃, the model changes insignificantly. When the temperature of the system is kept above 1100 ℃, the volume of the atomic layers increases to fill the gaps between the atomic layers, and the atomic diffusion effect appears in the middle of the gaps between the atomic layers. When the temperature exceeds 1300 ℃, the atomic interlayer interdiffusion effect intensifies with the temperature change, which indicates that the phenomenon of atomic escape in devices operating at high temperature conditions leads to a significant reduction in the structural strength performance of the device.

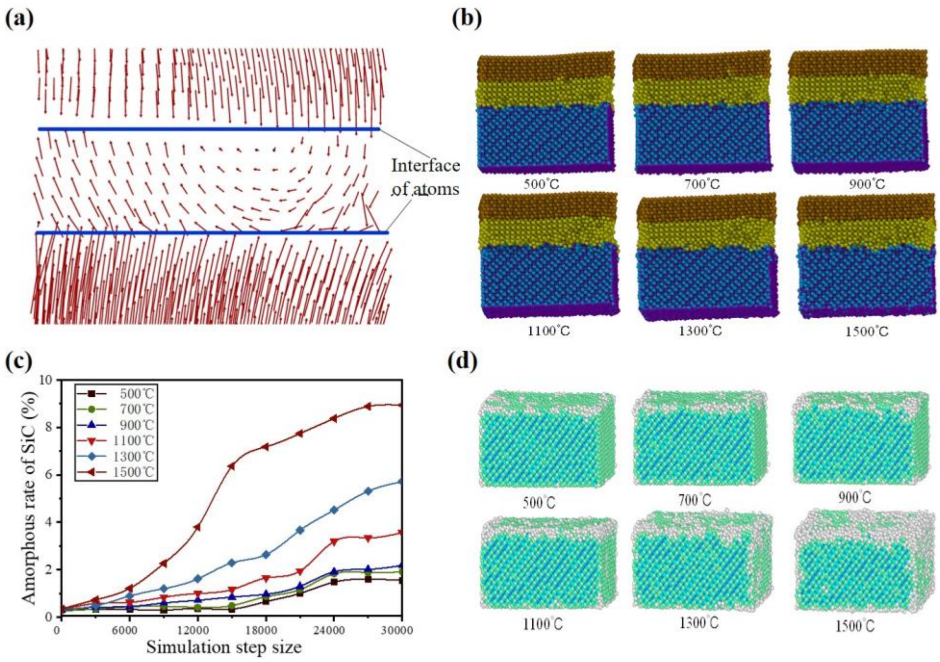

Figure 2. Calculation results. (a) Diffusion vector diagram of atoms at the atomic layer partition interface.(b) Schematic diagram of

the diffusion of atoms at different temperatures. (c) Variation of SiC atomic amorphization rate with simulation step. (d) Schematic diagram of the damage of SiC atoms at different temperatures.

Figure 2c shows the graph of the variation of the atomic damage rate of the SiC layer on the model with the simulation step. In the low temperature region (temperature less than 900 ℃), the atomic change of amorphization is small. Whereas, when the temperature exceeds 900 ℃, the higher the temperature of the system, the larger the increase in the number of amorphized atoms. Figure 2d shows snapshots of the atomic damage at different temperatures after the system is in the steady state, and the damaged atoms are mainly concentrated in the edge region of the model. Since in the edge region, the covalent bond formed is not a stable structure, the atoms in this region lack the covalent bonds that make up the stable structure, while each C and Si atom in the interior forms a stable structure with four covalent bonds in the cubic structure. The thermal conductivity of metal atoms is much higher than that of non-metal atoms, and the layer of metal atoms will somewhat accelerate the damage to the silicon carbide atoms.

3. CONCLUSION

As an important component of SiC electronic devices, the high-temperature stability of ohmic contacts deserves to be noticed and studied. In this work, the behavior of W/Ni metal combination with 4H-SiC substrate system at high temperature is investigated from a microscopic point of view. This is different from the previous way of obtaining the cause of failure by microscopic analysis of experimental samples, and this method can predict the diffusion characteristics of SiC ohmic contacts at high temperature without experiments, which can provide an effective research reference for experimental studies and mechanism analysis.

ACKNOWLEDGEMENT

The authors would like to thank the support from National Natural Science Foundation of China (No. 52175517, 51720105016), Zhejiang Lab (2022MG0AB03), China Postdoctoral Science Foundation (No.2017M610634), The Recruitment Program of Global Experts (Grant No. WQ2017610445).

REFERENCES

1. Fraga M A, Pessoa R S, Massi M, et al. Silicon Carbide as Base Material for MEMS Sensors of Aerospace Use: An Overview. Matéria (Rio de Janeiro). vol. 19, no. 3, pp. 274-290, 2014.
2. Chien-Hung Wu, Christian A. Zorman, Mehran Mehregany. Fabrication and testing of bulk micromachined silicon carbide piezoresistive pressure sensors for high temperature applications. IEEE Sensors Journal, 2006, 6(2):316-324.
3. Kim S, Kim H K, Lim M, et al. Ohmic Contact Mechanism for Ni/C-Faced 4H-n-SiC Substrate. Journal of Nanomaterials. vol. 2019, pp. 1-5, Jan. 2019.
4. Evans L J, Okojie R S, Lukco D. Development of an Extreme High Temperature n-Type Ohmic Contact to Silicon Carbide. Materials science forum. vol. 717-720, no.2, pp.841-844, Sep. 2012.
5. Cole M W, Joshi P C, Hubbard C W, et al. Improved Ni based composite Ohmic contact to n-SiC for high temperature and high power device applications. Journal of Applied Physics., vol. 88, no.5, pp. 2652-2657, Sep. 2000.

Research on output performance of different PVDF thicknesses and adhesives

Zhenxuan Fei [1,2], Lu Wang [1,2,#], Qian Wang [1,2], Libo Zhao [1,2], Maeda Ryutaro [1,2]

1 State Key Laboratory for Manufacturing Systems Engineering, International Joint Laboratory for Micro/Nano Manufacturing and Measurement Technologies, Collaborative Innovation Center of Suzhou Nano Science and Technology, Xi'an Jiaotong University, Xi'an 710049, China
2 School of Mechanical Engineering, Xi'an Jiaotong University, Xi'an 710049, China
 # Corresponding Author / E-mail: wang.lu@xjtu.edu.cn, TEL: +86-82668616, FAX: +86-82668616

ABSTRACT

To realize high sensitivity vibration energy harvesting at different frequencies by stiffness and damping design, output performance of different PVDF thicknesses and adhesives has been researched. Three kinds of piezoelectric cantilever beams with thickness of 28 μm, 52 μm and 110 μm and three kinds of adhesives used in piezoelectric cantilever beams are fabricated. After the experimental test and analysis, PVDF gets the best performance when its thickness is 110 μm. And the piezoelectric cantilever beam with Ergo 5800 glue has the largest rigidity and the highest output voltage. The cantilever beam bonding Ergo 5800 glue with 110 μm thickness PVDF can get the best performance.

Keywords : Energy harvesting, PVDF, piezoelectric, adhesives bonding

1. INTRODUCTION

There are a lot of vibration energy in the equipment vibration, which can be collected during the device operating. The piezoelectric effect can be used to harvest vibration energy, which was found in the first generation of piezoelectric crystals [1]. Polyvinylidene fluoride (PVDF) is a flexible organic polymer piezoelectric material. Some researchers have studied its performance in different occasions. Li .et al [2] used 0.7mm thickness PVDF in the energy harvester, but its rigidity is extremely high. Cao .et al [3] bond PVDF and PET substrate with double faced adhesive, resulting in its relatively low performance. Thus, this study research the output performance of different PVDF thicknesses and adhesives to improve its performance.

2. Device design and analysis

2.1 Output performance of different thickness of PVDF

Three kinds of piezoelectric cantilever beams with thickness of 28 μm, 52 μm and 110 μm are fabricated. As shown in Fig. 1.1 (a), 0.3 mm PET is selected as the cantilever beam base, transparent acrylic is selected as the mass and fixed support, and Ergo 5800 glue screen printing process is adopted for the adhesion between PVDF and the base. After adhesion, the electric charge generated by PVDF is led out through the nickel cloth wire, and the nickel cloth is bonded to the PVDF on the fixed support. Its output performance is not disturbed by the nickel cloth. After the three prototypes are manufactured, the experimental platform is built, as shown in Fig. 1.1 (b), and the frequency domain response and power curve are analyzed.

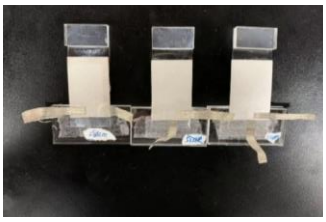

(a) Three kinds of piezoelectric cantilever beams

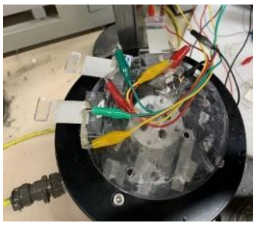

(b) Experimental platform

Fig.1.1 Three kinds of piezoelectric cantilever beam and experimental platform

The frequency response curve of PVDF with three different thicknesses is obtained as shown in Fig. 1.2.

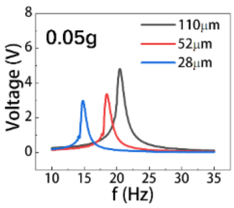

(a)0.05g

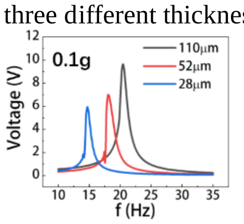

(b) 0.1g

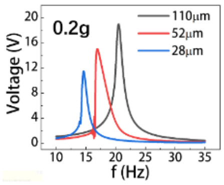

(c) 0.2g

Fig. 1.2 Frequency sweep curves of PVDF with three different thicknesses

Fig. 1.2 (a), (b) and (c) are frequency sweep curves of PVDF with three thicknesses under acceleration excitation of 0.05 g, 0.1 g and 0.2 g respectively. It can be seen that with the increase of PVDF thickness, the output voltage of PVDF piezoelectric thin film increases. According to the piezoelectric energy equation of d_{31} power generation mode, when the length and width of PVDF single crystal piezoelectric thin film are constant, its piezoelectric volume V increases with the increase of thickness, and the integral $\int \sigma 2dV$ of the square of stress in the whole piezoelectric volume increases, thus its piezoelectric energy is improved.

2.2 Output performance of different adhesives

The adhesion mode between PVDF and the substrate also has an important impact on the output of the piezoelectric power generation unit. Therefore, it is necessary to study the influence of different bonding methods on the system stiffness and output voltage. Three kinds of piezoelectric cantilever beams with a thickness of 110μm are fabricated. The bonding methods of PVDF and piezoelectric cantilever beam are 3M tape, Ergo 5800 glue screen printing, and Ergo 9900 AB glue screen printing. The three glues are as shown in Fig.2.1 (a). Screen printing can ensure the uniform thickness. After bonding, the charges generated by PVDF are led out through the nickel cloth wire, and the nickel cloth is bonded to the PVDF on the fixed support, Its output performance is not interfered by the nickel cloth. The cantilever beams of three kinds of piezoelectric sheets after bonding are shown in Fig. 2.1 (b).

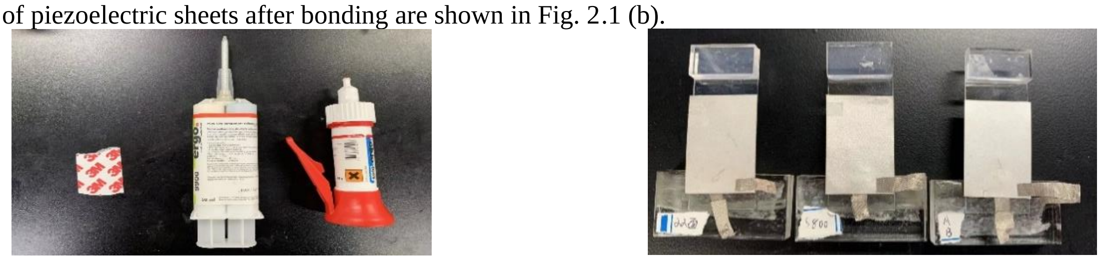

(a) Three adhesives (b) Three kinds of piezoelectric cantilever beams

Fig. 2.1 Three kinds of adhesive glue used and three piezoelectric cantilever beams after bonding

The frequency response curve of the piezoelectric cantilever beam with three different adhesives is shown in Fig. 2.2.

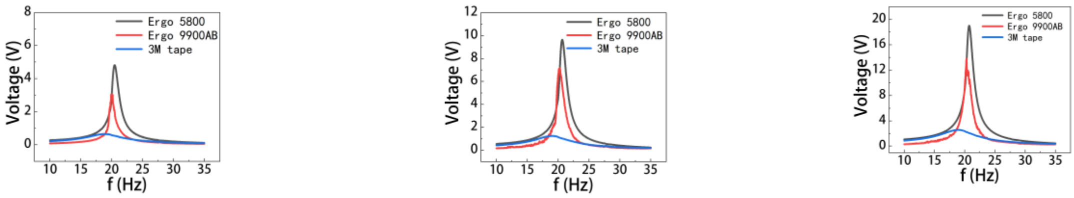

(a)0.05g (b) 0.1g (c) 0.2g

Fig. 2.2 Sweep frequency curves of PVDF using three different adhesives

We can see from the curve that with the increase of acceleration excitation, the output voltage of the three bonding methods has been improved; The piezoelectric cantilever beam with Ergo 5800 glue has the largest rigidity and the highest output voltage.

3. CONCLUSION

In this study, we research output performance of different PVDF thicknesses and adhesives. After the experimental test and analysis, PVDF gets the best performance when its thickness is 110 μm due to its larger volume. And the piezoelectric cantilever beam with Ergo 5800 glue has the largest rigidity and the highest output voltage. Among the liquid adhesives, Ergo 5800 glue has the lowest damping. The cantilever beam rigidity of the piezoelectric sheet after bonding is the largest. Therefore, the cantilever beam bonding Ergo 5800 glue with 110 μm thickness PVDF can get the best performance.

ACKNOWLEDGEMENT

This work was supported in part by the Shaanxi Youth Fund (2022JQ-315), and the China National Postdoctoral Program for Innovative Talents (BX2021237), and the Recruitment Program of Global Experts (Grant No. WQ2017610445)

REFERENCES

1. M. Gao, J. Cong, J. Xiao, Q. He, S. Li, Y. Wang, Y. Yao, R. Chen, P. Wang, Dynamic modeling and experimental investigation of self-powered sensor nodes for freight rail transport, Appl. Energy 257 (2020), 113969
2. [2] Y. Li. RESEARCH ON PIEZOELECTRIC AND ELECTROMAGNETIC COMPOUND VIBRATION ENERGY HARVESTING BASED ON PVDF [D]. Harbin Institute of Technology,2020.
3. W. Cao. Characterization and construction of the PVDF energy harvester on human walking pressure energy [D]. Donghua University,2018.

Bidirectional Vibration Energy Harvesting of L-shaped Mass Piezoelectric Beams Adapting to Multiple Scenarios

Congsheng Duan [1,2], Lu Wang [1,2,#], Libo Zhao [1,2], Maeda Ryutaro [1,2]

1 State Key Laboratory for Manufacturing Systems Engineering, International Joint Laboratory for Micro/Nano Manufacturing and Measurement Technologies, Collaborative Innovation Center of Suzhou Nano Science and Technology, Xi'an Jiaotong University, Xi'an 710049, China
2 School of Mechanical Engineering, Xi'an Jiaotong University, Xi'an 710049, China
 # Corresponding Author / E-mail: wang.lu@xjtu.edu.cn, TEL: +86-82668616, FAX: +86-82668616

ABSTRACT

In the Internet of Things era, in order to collect vibration energy in different environments, piezoelectric devices with different resonance frequencies need to be made. In addition, environmental bidirectional excitation is very common, such as human motion, generator vibration, pump vibration, etc. Therefore, we designed a PVEH structure using L-shaped tungsten mass block thickness to adjust the resonant frequency for these three scenarios, and obtained three prototypes with resonant frequencies of 48 Hz, 28 Hz, and 18 Hz, and tested their bi-directional vibration power output in vertical and lateral arrangements at 0.05 g, 0.1 g, and 0.15 g, respectively, to obtain the output power of the three prototypes. The prototypes can collect the vibration energy of specific scenes to power the wireless sensor nodes.

Keywords: adjustable frequency, small volume, high power, magnetic force

1. INTRODUCTION

With the development of embedded system, MEMS, wireless communication network technology and sensor technology, the Internet of Things (IoT) technology, which is one of the main technical innovation directions in the future, is also developing vigorously. The Internet of Things technology obtains all kinds of information through many wireless nodes distributed in the environment. However, there are many problems in the power supply of wireless sensor nodes, such as difficulty in long-distance distribution of power lines, difficulty in replacing batteries, environmental pollution caused by batteries, etc. Therefore, it is very important to explore the vibration energy collection technology in special scenes[1].

Aiming at the scenes with multi-directional vibration characteristics, such as human motion, motor vibration, engine vibration, etc., the current PVEH resonance frequency point is narrow and fixed, which can't effectively collect energy. Therefore, a PVEH structure is proposed in this paper, which can adjust the resonance frequency and collect the energy of two-way vibration by superimposing mass blocks, and different prototypes satisfying the resonance frequency of the above actual working conditions are obtained, which can be applied to the energy collection in the case of engine vibration, etc.

2. DEVICE DESIGN AND ANALYSIS

2.1 Structural design of vibration energy harvesting device

In order to realize the vibration energy collector with high power output, a linear vibration energy collector as shown in Figure 2.1 is prepared. The upper and lower PZT-5H piezoelectric plates are connected in series, and an L-shaped tungsten mass is added at the free end to ensure compact and high input mechanical power. Control the thickness ratio of large and small masses to optimize the output power and stress, and control the length of small masses to optimize the bonding length. The length of the small mass plus the length of the piezoelectric sheet is the length of the copper substrate. When it is excited by an acceleration of 0.1 g, polarized charges appear on the upper and lower surfaces of the piezoelectric sheet, which converts mechanical energy. Piezoelectric energy collectors with different resonant frequencies can be obtained by adjusting the number of L-shaped mass blocks. Adjusting the arrangement of energy collectors can collect vibration energy from different directions. As shown in Figure 2.1(a), it is arranged vertically, and Figure 2.1(b) is arranged horizontally.

(a) Vertical arrangement (b) Horizontal arrangement (c) PVEH with two and three mass blocks

figure 2.1 Structure and arrangement of piezoelectric energy harvester

Under the excitation of 0.05 g, 0.1 g, 0.15 g acceleration, the frequency sweep test of the vertical layout prototype with different numbers of mass blocks was carried out by using the direct digital frequency synthesis (DDS) signal generator and power amplifier, and the resonant frequencies were obtained as 48 Hz, 28 Hz and 18 Hz, respectively. Table 2.1 shows its open circuit voltage and resonant frequency.

Table 2.1 Open circuit voltage and resonant frequency of different energy harvesting collector

	Resonant frequency	OCV under 0.05g	OCV under 0.1g	OCV under 0.15g
PVEH with one mass block	48Hz	0.67V	5.5V	8.43V
PVEH with two mass blocks	28Hz	1.41V	10.47V	14.3V
PVEH with three mass blocks	18Hz	2.13V	14.31V	17.73V

2.2 Comparison of power output in different arrangement modes

The output power of PVEH with two mass blocks under the excitation of 0.1 g acceleration in vertical and horizontal arrangement was tested and analyzed. It can be found that both vertical and horizontal arrangements have obtained larger output voltage and power. Among them, the open-circuit voltage of vertical arrangement is 10.47 V, the optimal load is 500 KΩ, and the maximum output power is 40.7 μW W. The transverse open-circuit voltage is 9.71 V, the optimal load is 500 KΩ, and the maximum output power is 32.1 μW W. The output power of vertical arrangement is 1.26 times that of horizontal arrangement.

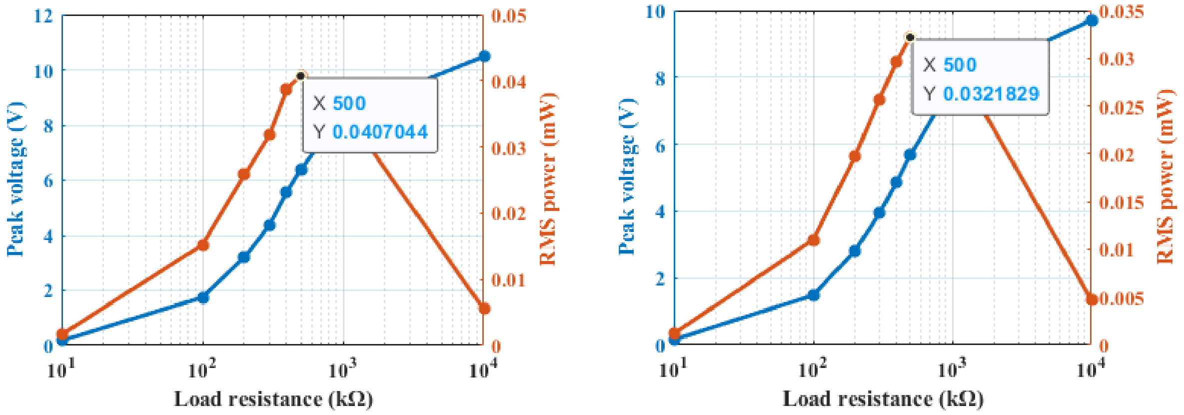

(a) Vertical arrangement (b) Horizontal arrangement

figure 2.2 Output power with different load

2.3 Bidirectional limiter design

The biggest disadvantage of the piezoelectric material PZT used in this design is that it is brittle and can only bear a small amount of strain. The PZT piezoelectric structure works in a resonant state, and cracks or even breaks will occur at the position where the stress at the root of the metal substrate of the energy harvester is high after a long period of cyclic vibration. Therefore, in order to ensure the normal and stable operation of the energy trap in a certain vibration frequency range and prolong its service life, it is necessary to design a limiting structure for the energy trap and control the amplitude of the cantilever beam, so as to reduce the stress of the metal substrate when the energy trap works[2].

3. CONCLUSION

In this research, we put forward PVEH structure with L-shaped tungsten mass thickness to adjust the resonant frequency, and obtained three prototypes with resonant frequencies of 48 Hz, 28 Hz and 18 Hz. Under the excitation of 0.1 g acceleration, vertical layout prototype has the maximum power output, which makes it possible for wireless sensor nodes to supply power.

ACKNOWLEDGEMENT

This work was supported in part by the Shaanxi Youth Fund (2022JQ-315), and the China National Postdoctoral Program for Innovative Talents (BX2021237), and the Recruitment Program of Global Experts (Grant No. WQ2017610445).

REFERENCES

[1] Chongfeng Wei and Xingjian Jing. A comprehensive review on vibration energy harvesting: Modelling and realization[J]. Renewable and Sustainable Energy Reviews, 2017, 74 : 1-18.

[2] Xiang Wang et al. A frequency and bandwidth tunable piezoelectric vibration energy harvester using multiple nonlinear techniques[J]. Applied Energy, 2017, 190 : 368-375.

Design, Fabrication, and Test of 4H-SiC Accelerometer

Yu Yang, #You Zhao, Lukang Wang and Yulong Zhao

State Key Laboratory for Manufacturing Systems Engineering, Xi'an Jiaotong University, Xi'an, 710049, China
#Corresponding author. E-mail: zhaoyou628@xjtu.edu.cn.

ABSTRACT

Silicon carbide (SiC) is a promising material to fabricate MEMS accelerometers used in extreme environments. Due to the difficulties of processing bulk SiC materials and the complex structure of accelerometers, the studies on SiC accelerometers are still insufficient. In this study, we designed a single beam accelerometer based on 4H-SiC. The traditional MEMS process is used to fabricate the piezoresistors and electrodes. And the femtosecond laser etching is used to thin the sensitive beam and release the proof mass. The static test shows that the resistance change is stable under constant acceleration and has a good signal-to-noise ratio. Under different accelerations, the resistance change has good linearity. The measured sensitivity of resistance change of the sensor under acceleration is 0.02‰ /g.

Keywords: Silicon carbide, accelerometer, laser fabrication

1. INTRODUCTION

As a third-generation semiconductor material, SiC has excellent electrical and mechanical properties. The wide band gap (3.2 eV for 4H-SiC), and the high thermal conductivity (4.9 W/cm/K) enable SiC to withstand higher operating temperatures. The young's modulus of SiC is about 480 GPa, which is three times that of silicon, making it withstand higher impact. Moreover, SiC still has a good piezoresistive effect at high temperatures [1]. The above characteristics make SiC a good application prospect in the field of high temperature sensing. It could be a substitute for Si material. A large number of studies have proved the feasibility of SiC piezoresistive pressure sensors[2]. Due to the difficulties of processing bulk SiC materials and the complex structure of accelerometers, the studies on SiC accelerometers are still insufficient. NASA designed a SiC accelerometer with a sensitivity of only 343 nV/g[3]. Shi et al. designed an accelerometer with a symmetric quad-beam structure and thinned the sensitive beam by nanosecond laser etching. The designed sensor can be used for high-g measurement[4]. In combination with mechanical thinning and deep etching, Zhang et al. designed an accelerometer with four beams. The sensitivity is as high as 0.21 mV/ g, but its fabrication processes are complex[5].

In this paper, we design a single beam accelerometer. The simulation results show that the stress caused by acceleration is mainly concentrated on the sensitive beam. The traditional MEMS process is used to fabricate the piezoresistors and electrodes. Given the difficulty of deep etching of bulk SiC, femtosecond laser etching is used to thin the sensitive beam and release the proof mass. The test results show that the designed sensor has good sensitivity and linearity.

2. DESIGN AND FABRICATION

Figure 1(a) shows the designed accelerometer schematic. The sensor consists of a large proof mass and a sensitive beam. The piezoresistor is arranged on the sensitive beam, which can convert the acceleration signal into a measurable electrical signal. The change of the resistance can reflect the magnitude of acceleration. The finite element analysis result, as shown in Figure 2(b), demonstrates the stress and voltage distribution of the accelerometer under the 20 g (1g ≈ 9.8 m/s^2) acceleration. The stress is mainly distributed on the sensitive beam, on which the piezoresistor can obtain the maximum sensitivity.

The fabrication process of the accelerometer is shown in Figure 2. The sensor is made of an N-type 4H SiC wafer with a doping concentration of 10^{19} cm^{-3} and a thickness of 1 μm. Firstly, the piezoresistor was fabricated by ICP etching under the cover of the metal mask, the etch depth was 1.5 μm to ensure that the N-type resistor was completely isolated from the substrate [Figure 2(b)]. Then a 300 nm thick SiO_2 layer was deposited on the epitaxial layer by plasma enhanced chemical vapor deposition (PECVD) method, followed by etching the contact holes by the buffered oxide etch solution (BOE solution, 49% HF: 40% NH_4F =1:6) [Figure 2(c)]. Then Ni/Ti/Au was sputtered on the substrate, followed by the rapid thermal annealing process (RTP) to form a good ohmic contact with metal leads and pads [Figure 2(d)]. The femtosecond laser etching with the laser center wavelength of 1032 nm and the spot diameter of 30 um was carried out to reduce the thickness of the sensitive beam and release the proof mass of the sensor [Figure 2(e) and Figure 2(f)]. Finally, single chips were cut off from the wafer by laser.

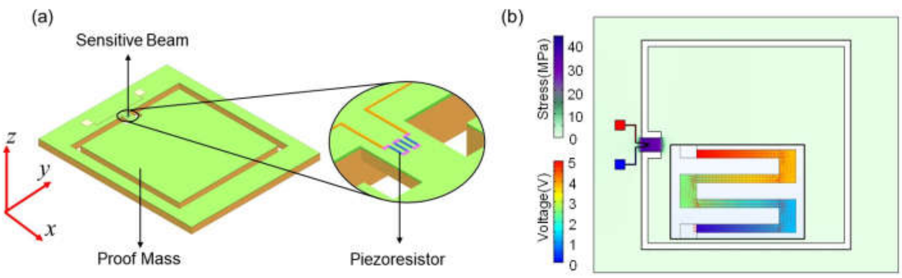

Figure 1 (a) Schematic diagram of the accelerometer. (b) Finite element analysis of stress and voltage distribution of the accelerometer. Insert: Current density along the piezoresistor.

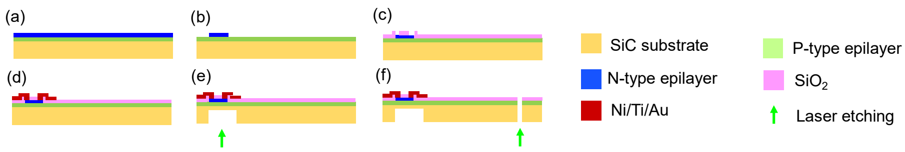

Figure 2 Fabrication process of the accelerometer

3. RESULTS AND DISCUSSION

The designed sensor is tested under static acceleration. Figure 3(a) shows the recorded real-time change of resistance under different accelerations. Figure 3(a) shows the resistance change rate under different accelerations. It can be seen that under constant acceleration, the resistance changes stably and has a good signal-to-noise ratio. The resistance decreases with the increase of acceleration. The resistance change rate is linear with the acceleration change, and the sensitivity of the resistance change of the designed sensor is calculated as about 0.02 ‰ /g.

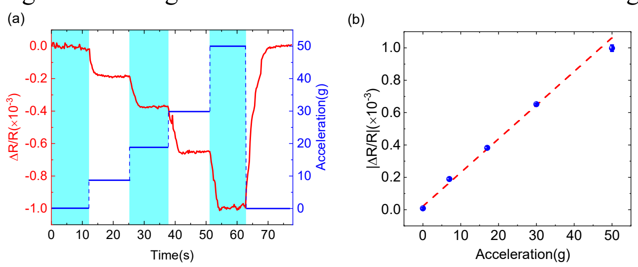

Figure 3 (a) Real-time measurement of resistance change at varying acceleration. (b) Linear resistance changes upon the acceleration

4. CONCLUSION

In this paper, we designed a single beam structure bulk SiC accelerometer, solved the problem of SiC deep etching by femtosecond laser etching, and carried out the static test on the designed sensor. The test results show that the change of the sensing resistance is stable under constant acceleration and has a good signal-to-noise ratio. Under different accelerations, the resistance has good linearity. The sensitivity of resistance change of the sensor under acceleration is measured to be 0.02 ‰ /g. This study demonstrates the feasibility of SiC material for acceleration measurement.

ACKNOWLEDGEMENT

This work was supported by Key Research and Development Project of Shaanxi Province (Grant No. 2020ZDLGY14-10), Postdoctoral Foundation of Shaanxi Province (Grant No. 2018BSHYDZZ06), and National Key Research and Development Program (Grant No.2018YFB2002901).

REFERENCES

1. R. S. Okojie, D. Lukco, V. Nguyen, and E. Savrun, 4H-SiC Piezoresistive Pressure Sensors at 800 °C With Observed Sensitivity Recovery, IEEE Electron Device Letters, Vol. 36, No.2, pp. 174-176, 2015.
2. L. Wang, Y. Zhao, Y. Yang, X. Pang, L. Hao, Y. Zhao, and J. Liu, Development of Laser-Micromachined 4H-SiC MEMS Piezoresistive Pressure Sensors for Corrosive Environments, IEEE Transactions on Electron Devices, Vol. 69, No.4, pp. 2009-2014, 2022.
3. A. R. Atwell, R. S. Okojie, K. T. Kornegay, S. L. Roberson, and A. Beliveau, Simulation, fabrication and testing of bulk micromachined 6H-SiC high-g piezoresistive accelerometers, Sensors and actuators. A. Physical., Vol. 104, No.1, pp. 11-18, 2003.
4. Y. Shi, Y. Sun, J. Liu, J. Tang, J. Li, Z. Ma, H. Cao, R. Zhao, Z. Kou, K. Huang, J. Gao, and T. Hou, UV nanosecond laser machining and characterization for SiC MEMS sensor application, Sensors and Actuators A: Physical, Vol. 276, pp. 196-204, 2018.
5. Y. Zhai, H. Li, Z. Tao, X. Cao, C. Yang, Z. Che, and T. Xu, Design, fabrication and test of a bulk SiC MEMS accelerometer, Microelectronic Engineering, Vol. 260, p. 111793, 2022.

Flexible strain sensor based on magnetron-sputtered MoS_2 film

Xing Pang, #Qi Zhang Xiaoya Liang and #Yulong Zhao

State Key Laboratory for Manufacturing Systems Engineering, Xi'an Jiaotong University,

No.28, West Xianning Road, Xi'an, Shaanxi, 710049,P.R. CHINA

E-mail: zhq0919@xjtu.edu.cn, TEL: +86-15929899087 (Q. Zhang)

E-mail: zhaoyulong@xjtu.edu.cn, TEL: +86-029-83395073 (Y. Zhao).

ABSTRACT

Magnetron-sputtered MoS_2 can be used for piezoresistive functional materials research due to its unique nanostructure. In this work, we report the piezoresistive impact of growing MoS_2 films with vertical nanosheet layer shape on polyimide substrates over a large area by magnetron sputtering for the first time. The microstructure shows that MoS_2 nanosheets with vertical lamellar shape spacing change underneath strain, leading to original modifications in resistance, therefore exhibiting excellent piezoresistive properties. Here, we explored the electrical and piezoresistive properties of sputtered MoS_2 with the defects of sulfur vacancy,thus investigated their conductivity mechanisms. The perpendicular nanosheet MoS_2 with super-rich S vacancies exhibits high electrical conductivity and piezoresistive effects. We also report that it is due to the electron channels which provided nanosheets in contact with each other and the formation of unsaturated electrons induced through the vacancy of sulfur atoms, which will increase the conductivity and the carrier concentration of the film and improve its sensitivity as a sensitive element of the sensor. The Gauger factor of the device exhibited the high GF of 2.66 and 23.22 with the tensile and compressive strain of < 0.29%. The dynamic response of the strain presents good repeatability. The results of the fabricated flexible thin-film sensors show that the sensors can be used to capture weak strains in human skin and for bionic film applications.

Keywords : Magnetron-sputtered, MoS_2, Piezoresistance, Flexible, Sensor

1. INTRODUCTION

Flexible electronic devices offer unlimited potential for wearable devices, electronic skin and bionic films [1] [2]. As the core component of external signal acquisition, flexible strain sensor is considered as an indispensable part of flexible integrated electronic system. Usually, flexible strain sensors are based on the piezoresistive mechanism of sensitive materials, to achieve conductive structure resistance change by various sensitive materials and structural designs. As a classical transition-metal dichalcogenide, MoS_2 possesses excellent mechanical properties in addition to its excellent electrical, optical and chemical stability [3] [4]. In recent years, MoS_2 has received attention as a strain-sensitive material in piezoresistive strain sensors [5] [6].

In this work, the structure of vertical nanosheet for MoS_2 grown with Magnetron Sputtering had a piezoresistive effect, which was discovered for the first time. We report a simple and effective physical vapor deposition method to regulate the concentration of carriers in MoS_2, which is based on creating S vacancies that leave Mo atoms with unsaturated electrons. The vertical lamellar nanosheets of MoS_2 were stretching or compressing lead to the increase or decrease of these distances, resulting in a regular change in resistance. Therefore, it exhibits excellent piezoresistive performance. It showed that the MoS_2 with vertical nanosheet, which has more carriers, can be prepared uniformly over large areas by the Magnetron sputtering method. It could be mass achieved flexible sensors with high sensitivity to strain, such as flexible sensors for human skin health monitoring and bionic film, which agrees with theoretical studies.

2. Piezoresistive Properties of Magnetron-sputtered MoS_2

2.1 Experiment

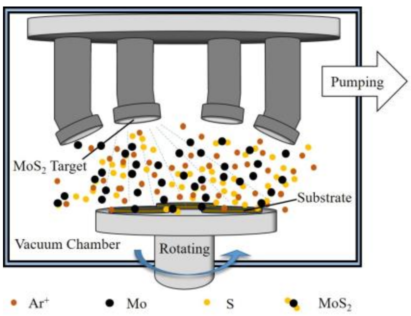

Figure 1 Schematic diagram of magnetron sputtering MoS_2 process

MoS_2 Film Deposition: MoS_2 was deposited used a target (99.99%, ZhongNuo Advanced Material Technology Co., Ltd, China) on flexible PI substrates of 100 μm thickness. First, the PI substrates were cleaned with ethyl alcohol and deionized water. The substrates were then heated to 80°C for 30 min to remove the residual solvent and water. The DISCOVERY635 Discovery Magnetron Sputtering system, produced by American DENTON, was used to deposite the

MoS_2 films in this experiment. Prior to the subsequent MoS_2 deposition, high-purity Ar gas was introduced into the chamber at a flow rate of 30 mL/min when the vacuum was less than 0.3×10−6 Pa, resulting in a final working pressure of 0.5 Pa. Then, the MoS_2 target was ignited and maintained at 400 W for 3600 s. The substrate was rotated at a velocity of 20 rpm during deposition to improve the uniformity of the MoS_2 film.

Piezoresistance Analysis of the MoS_2 Films: For the strain tests, a linear stage (TSA50-A, Zolix) was used to apply the strain, while the output signals were collected by a high precision multimeter (8846A, Fluke). The strain of the MoS_2 film was controlled by varying the displacement of both ends of the flexible sensor and the relationship between the strain and output was analyzed. The bending strain was calculated using the following formulas:

$$R = \frac{l}{2\pi\sqrt{\frac{\Delta l}{l} - \frac{\pi^2 t^2}{12 l^2}}} \qquad (1)$$

$$\varepsilon = \frac{t}{2R} \qquad (2)$$

where R is the curvature radius, l is the substrate length, △l is the compression distance, and t is the substrate thickness.

2.2 Applications of the Ultrathin Flexible Sensors

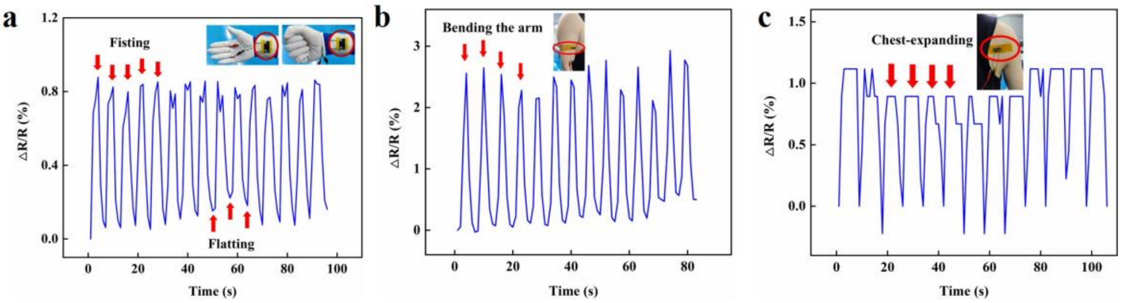

Figure 2 The MoS_2 flexible film sensor for human motion monitoring of different body parts.

The excellent GF and sufficient flexibility also make the developed sensor promising for the monitoring of weak strain signals on curved surfaces, such as the human body. The real-time monitoring of these signals is valuable for flexible wearable electronics, muscle movement monitoring, and exercise guidance. In this study, attachment of the developed ultrathin MoS2 film sensor to various parts of the body allowed different muscle movements to be distinguished. As shown in Figures 2a–c, the sensor was affixed to the skin covering the palmaris longus muscle of the wrist, the bicipital muscle of the upper arm, and the infraspinatus muscle of the shoulder to test three types of human motion, namely, fist clenching, arm bending, and chest expansion, respectively. According to the sensor signal, arm bending led to more significant deformation of the corresponding skin than the other two motions. The relative change in resistance was close to 3% for arm bending, whereas it was approximately 1% for fist clenching and chest expansion. Thus, the sensor signal can be used to detect the muscle expansion and contraction forces occurring in the human body during exercise, as well as the frequency of such motions, which is expected to prove useful for applications in human health.

3. CONCLUSION

In summary, MoS_2 films composed of vertical nanosheets rich in sulfur vacancies were successfully prepared and used to fabricate piezoresistive sensors with good GF values and high stability during film deformation. Notably, the deposition temperature could be used to tune the sulfur vacancy concentration to increase the carrier concentration in the films, demonstrating the feasibility of constructing high-performance nanosheet-structured MoS_2 thin-film sensors with considerable potential in future wearable electronic and bionic devices. The fabricated devices exhibited high GF values of 2.66 and 23.22 under weak tensile and compressive strain of ≤0.29%. The present work is expected to provide valuable insights for the optimization of devices based on MoS_2 films and their applications.

ACKNOWLEDGEMENT

The authors are grateful to the National Natural Science Foundation of China (Grant No. U20A201293), the Ningbo Major Special Project “Science and Technology Innovation 2025” (Grant No. 2020Z023), and the National Key Research and Development Program (2021YFB3201100).

REFERENCES

1. Q. Zhang, X. Liu, L. J. Duan, G. H. Gao, Chemical Engineering Journal 2019, 365, 10.
2. M. Amjadi, K. U. Kyung, I. Park, M. Sitti, Advanced Functional Materials 2016, 26, 1678.
4. Q. H. Wang, K. Kalantar-Zadeh, A. Kis, J. N. Coleman, M. S. Strano, Nature Nanotechnology 2012, 7, 699.
5. M. M. Furchi, D. K. Polyushkin, A. Pospischil, T. Mueller, Nano Lett 2014, 14, 6165.
7. M. Park, Y. J. Park, X. Chen, Y. K. Park, M. S. Kim, J. H. Ahn, Advanced Materials 2016, 28, 2556.
8. D. X. Qiu, Y. C. Chu, H. X. Zeng, H. H. Xu, G. Dan, Acs Applied Materials & Interfaces 2019, 11, 37035.

NEMS Force Sensors Based on Suspended Graphene Membranes

Xiaoya Liang, # Qi Zhang, Xing Pang, # Yulong Zhao
State Key Laboratory for Manufacturing Systems Engineering, Xi'an Jiaotong University,
No.28, West Xianning Road, Xi'an, Shaanxi, 710049,P.R. CHINA
E-mail: zhq0919@xjtu.edu.cn, TEL: +86-15929899087 (Q. Zhang)
E-mail: zhaoyulong@xjtu.edu.cn, TEL: +86-029-83395073 (Y. Zhao).

ABSTRACT

Graphene is an atomically thin material that has been widely used into nanoelectromechanical systems (NEMS). Here, we report on a force sensor. The suspended double-layer graphene ribbons with attached silicon proof masses can be used as combined spring–mass. Through dry etching processes, PECVD deposition and other processes, the silicon dioxide substrate is used to microfabricate the suspended proof masses. The piezoresistive effect of suspended graphene was studied by applying external force to the proof mass. Since the four corners of the graphene membranes are usually cracked due to stress concentration in the process of transfer, so we propose a cross-beam clamping model to evaluate the mechanical properties, such as Young' s modulus and built-in stress. Since the size of a single graphene sensor is at least two orders of magnitude smaller than that of a traditional silicon sensor, the device has high sensitivity. The fabrication of graphene force sensors will contribute to the development and research of NEMS device.

Keywords : Graphene piezoresistive sensor, Suspended graphene, Force sensor, NEMS

1. INTRODUCTION

Graphene, as an extremely interesting functional material, is used for nanoelectromechanical system(NEMS) devices[1-4]. Suspended atomically thin graphene structures that include resonating beams[1], and pressure sensor membranes[4] have been extensively studied. However, the research of suspended membranes utilized in force sensors are still poor due to its little loading force. We fabricated suspending silicon proof masses on double-layer graphene membranes to achieve sufficient response. The ultra-small spring–mass systems that include doubly clamped graphene beams[2], fully clamped graphene membranes[3] have been studied. However, the four corners of the graphene membranes are usually cracked due to stress concentration in the process of transfer, so we propose a cross-beam clamping model to better explain the mechanical properties of suspended graphene force sensors, which can be used in photodetectors and other NEMS devices.

2. Results and Discussion

2.1 The Mechanical Properties of Suspended Graphene Force Sensors

To characterize the static mechanical properties of our graphene structures, we performed force-displacement measurements using AFM tip indentation at the center of a suspended proof mass of a structure with 5µm wide trenches and a proof mass size of 28µm × 28µm× 19.2µm. As the graphene membrane ruptured at the four corners as shown in Figure 1, we simplified the model as a center loaded cross beam clamping structure. We used doubly clamped ribbon to analyze the model to extract the Young' s modulus and built-in stress. During consecutive loading cycles with same AFM indentation forces for each cycle, the Young' s modulus to the measured AFM deflection–force data slightly float, around 1.73698TPa, and the built-in stress is about 238MPa (Figure 2) within the force range of 0~4µN.

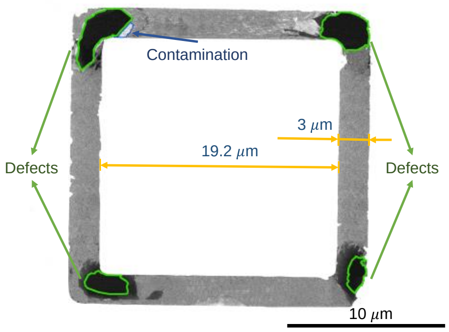

Figure 1 The SEM of measured device

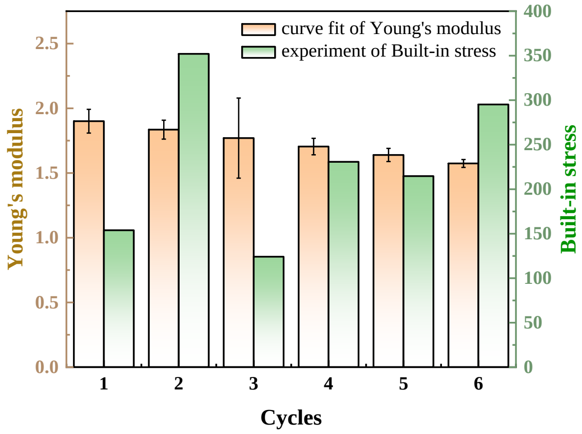

Figure 2 Mechanical properties on the deflection–force data

2.2 The Fabrication of Suspended Graphene Force Sensors

In our experiments, four inch silicon substrates, covered with 300nm SiO_2 and 200nm SiN_x on the backside and 300nm SiO_2 on the frontside, were successively deposited 40 nm Cr and 80 nm Au. A square back cavity area was defined via UV lithography on the back side, after that the SiO_2 and the SiN_x were etched away to expose the underlying silicon. Next, alkaline corrosion wet etching processes were employed, the thickness of the silicon diaphragm was kept at 19.2µm approximately. 500nm silicon dioxide thin films were deposited by PECVD to form the support layer. Finally, the silicon proof mass is formed by ICP etching, followed by transfer of double-layer graphene to substrate and release of the proof mass by sacrificially removing the supporting layer using dry etching.

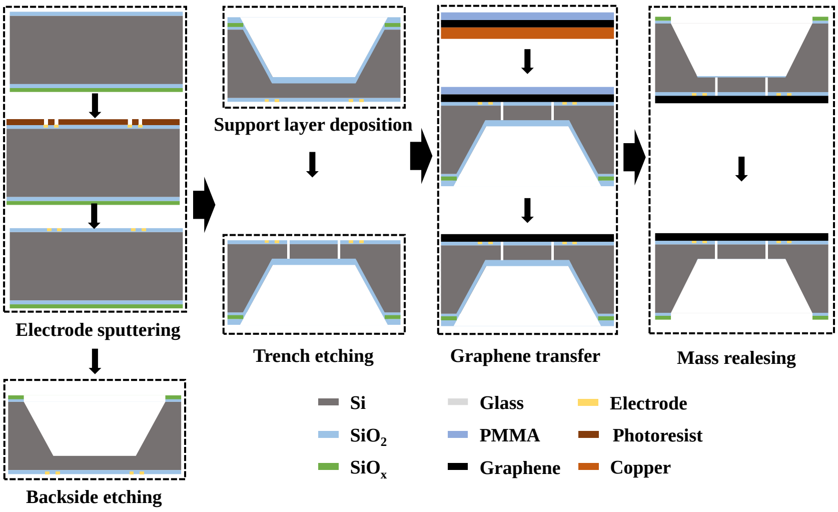

Figure 3 The schematic diagram of double graphene NEMS force sensor

2.2 The Output of Suspended Graphene Force Sensors

To further clarify the piezoresistive behavior of the force sensors, we choose the suspended proof mass of a structure with 10μm wide trenches and a proof mass size of 35μm × 35μm× 19.2μm sensor. During loading process, as shown in Figure 4, the force sensor showed a high sensitivity of 0.2869Ω/μN within the force range of 0~590μN, and the nonlinearities of the loading curves were 3.51% full scale(FS)

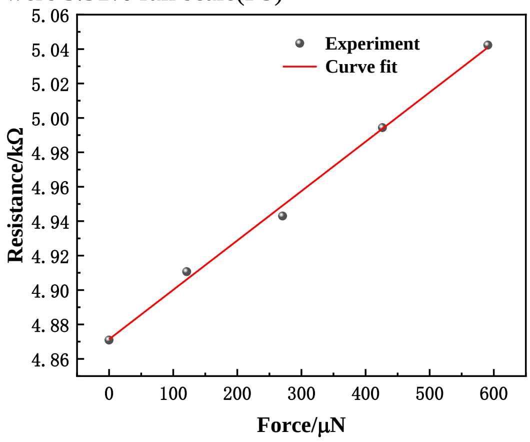

Figure 4 The output signals of double graphene NEMS force sensor

3. CONCLUSION

The suspended graphene ribbons with attached silicon masses was fabricated with MEMS silicon process. We propose a cross-beam clamping model to evaluate the mechanical properties of suspended graphene force sensors. The Young's modulus to the measured AFM deflection–force data slightly floated, around 1.73698TPa, and the built-in stress is about 238MPa. The force sensor showed a high sensitivity of 0.2869Ω/μN, which demonstrated the promising application prospect of graphene membrane in NEMS device.

ACKNOWLEDGEMENT

The authors are grateful to the National Key Research and Development Program (2021YFB3201100), the National Natural Science Foundation of China (Grant No. U20A201293) and the Ningbo Major Special Project "Science and Technology Innovation 2025" (Grant No. 2020Z023).

REFERENCES

1. R. J. Dolleman, D. Chakraborty, D. R. Ladiges, H. S. J. van der Zant, J. E. Sader, and P. G. Steeneken, Squeeze-Film Effect on Atomically Thin Resonators in the High-Pressure Limit, Nano Letters, vol. 21, no. 18, pp. 7617-7624, 2021.
2. X. G. Fan, F. Forsberg, A. D. Smith, S. Schroder, S. Wagner, M. Ostling, M. C. Lemme, and F. Niklaus, Suspended Graphene Membranes with Attached Silicon Proof Masses as Piezoresistive Nanoelectromechanical Systems Accelerometers, Nano Letters, vol. 19, no. 10, pp. 6788-6799, 2019.
3. X. G. Fan, F. Forsberg, A. D. Smith, S. Schroder, S. Wagner, H. Rodjegard, A. C. Fischer, M. Ostling, M. C. Lemme, and F. Niklaus, Graphene ribbons with suspended masses as transducers in ultra-small nanoelectromechanical accelerometers, Nature Electronics, vol. 2, no. 9, pp. 394-404, 2019.
4. D. Smith, F. Niklaus, A. Paussa, S. Schroder, A. C. Fischer, M. Sterner, S. Wagner, S. Vaziri, F. Forsberg, D. Esseni, M. Ostling, and M. C. Lemme, Piezoresistive Properties of Suspended Graphene Membranes under Uniaxial and Biaxial Strain in Nanoelectromechanical Pressure Sensors, Acs Nano, vol. 10, no. 11, pp. 9879-9886, 2016.

Operation of 4H-SiC Piezoresistive Pressure Sensor for extreme environments

Lukang Wang, #Yulong Zhao, You Zhao and Yu Yang

State Key Laboratory for Manufacturing Systems Engineering, Xi'an Jiaotong University, Xi'an 710049, China
 # Corresponding Author / E-mail: zhaoyulong@xjtu.edu.cn, TEL: +86-029-83395073

ABSTRACT

The widespread application of bulk silicon carbide in pressure sensing has been largely limited by the slow etching rate of traditional micromachining processes. This paper proposes the operation of a 4H-SiC piezoresistive pressure sensor with diaphragm which has controllable thickness realized by femtosecond laser. A modified stress model was established by finite element analysis to fit the SiC circular diaphragm prepared by laser micromachining. The test results proved that the fabricated sensor with diaphragm thickness of 60 μm had sensitivity of 1.42 mV/V/MPa under the applied pressure of up to 5 MPa at room temperature. Small hysterisis error of 0.17 %/FSO and nonlinearity of 0.20 %/FSO was achieved. The sensor was able to work in a broad temperature range with the temperature coefficient of sensitivity of -0.23% FSO/°C at -50 °C and -0.10% FSO/°C at 300 °C. The research demonstrates the prospect of employing the femtosecond laser technology to prepare bulk SiC pressure sensors for extreme temperature environment.

Keywords : Silicon carbide, pressure sensor, femtosecond laser, extreme temperature

1. INTRODUCTION

For a long time, pressure sensors based on MEMS technique have been deemed as the most significant and universal sensing devices [1]. The piezoresistive effect caused by the strain-induced change in the electrical resistance of materials has been viewed as a prime sensing mechanism for strain/stress sensor sensors. In the past four decades, silicon-based mechanical sensors dominated the market due to its wide usability and mature micromachining [2]. However, the degradations of mechanical properties and piezoresistive effect of silicon under extreme environment limited its application. Silicon carbide (SiC) has long been regarded as a superior candidate suitable for application requirement in hostile environment thanks to its attractive electrical characteristics, robust mechanical properties and chemical inertness [3]. Nevertheless, SiC pressure sensors are not yet accessible as standard products on the market despite these advantageous characteristics. The reason for the lack of deep involvement in market is that SiC substrates are hard to bulk-micromachine due to its robust covalent bonds between the Si and C atoms [5].

2. Results and Discussion

2.1 Design and simulation

A circular diaphragm would be released through a deep cavity machined by femtosecond laser etching. A Wheatstone full bridge with constant voltage input (U_i) is set on the front surface of the diaphragm, which is composed of four piezoresistors of equal resistance (R) in series, as shown in Fig. 1(a). The applied pressure would deform the diaphragm and cause stress in the piezoresistors. Due to the piezoresistive effect of 4H-SiC crystal, the pressure-induced stress would change the electrical resistance, which would break the bridge balance and cause the output voltage (U_o) to change. The output voltage of the bridge circuit can be expressed as:

$$U_o = \frac{\Delta R}{R} U_i = \left(\pi_l \sigma_r + \pi_t \sigma_\tau\right) U_i$$

where σ_r and σ_τ are the pressure-induced radial stress and tangential stress of circular diaphragm, π_l and π_t are the piezoresistive coefficients along the longitudinal and transverse directions. As shown in Fig. 3(a), the stresses induced by an applied pressure of 5 MPa into a 4H-SiC sensor diaphragm with typical dimentions (radius = 600 μm, thickness = 60 μm) was estimated based on finite element analysis using COMSOL Multiphysics. Fig. 3(b) plots the estimated output voltage and potential distribution of the full bridge.

2.2 Experiment

The sensor chips were prepared from a 4H-SiC wafer by combining MEMS processing and laser micromachining. As shown in Fig. 2. All test results for the output voltages of sensors were obtained at an input voltage of 5 V. To validate the static performance of the sensors at room temperature, the variation of output voltage with applied pressure was real-time recorded, as shown in Fig. 3(a), showing the good stability and repeatability. Low hysteresis error of 0.17 %/FSO and nonlinearity of 0.20 %/FSO were achieved through three successive pressure cycle tests in Fig. 3(b), which is compared favorably with the SiC piezoresistive sensors fabricated by other methods. To describe the ability of the developed pressure sensor in extreme temperature environment, the sensor performance was characterized in a temperature range from -50 °C to 300 °C. The temperature effect on the static calibration of the sensor is depicted in Fig.

3(c). Each test temperature point was maintained for 2 hours to ensure that the collected sensor output voltage was stable. The full-scale output (FSO) at 300 °C was 25.66 mV, indicated a 27.8 % drop from its room-temperature value of 35.58 mV. The temperature coefficient of sensitivity (TCS) was found to be -0.23% FSO/°C at -50 °C and -0.10% FSO/°C at 300 °C. The decrease in output sensitivity with rising temperature is clearly exhibited in Fig. 12(b). The sensitivity of 1.42 mV/V/MPa was obtained at 25 °C, marginally enhanced to 1.63 mV/V/MPa at -50 °C and dropped to 1.04 mV/V/MPa at 300 °C.

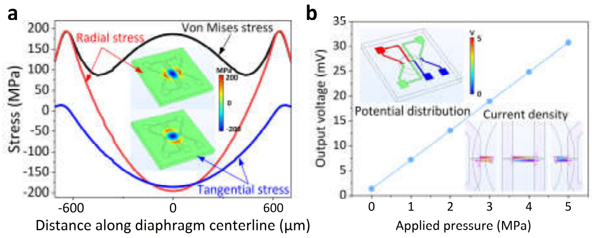

Figure 1 Finite element analysis results of the pressure sensor: (a) Stress distribution on the top surface of the sensor diaphragm under an applied pressure of 5 MPa; (b) Electrical signal output of the sensor.

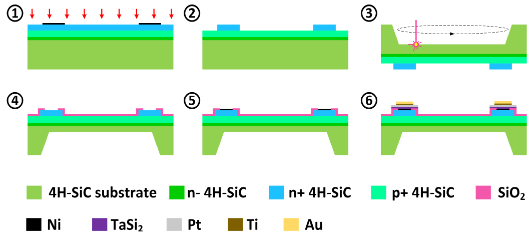

Figure 2 Flow diagram of the 4H-SiC sensor chip preparation combining MEMS processing and laser micromachining.

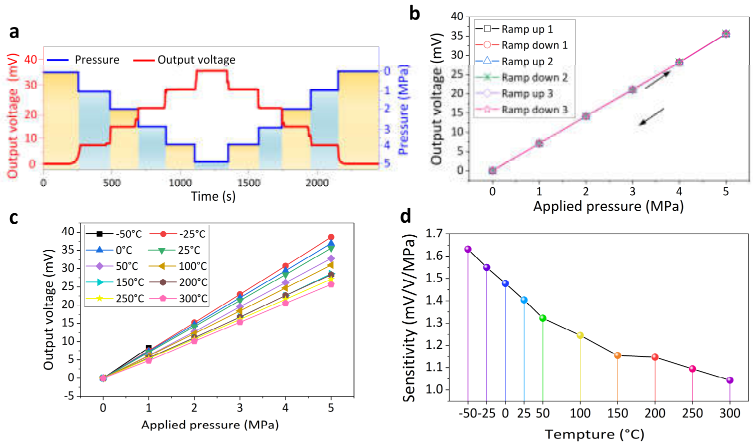

Figure 3 (a) The response of the SiC pressure sensor in applied pressure ranges of 0–5 MPa; (b) The calibration characteristics of the sensor under three cycles of loading and unloading; (c) The output characteristics of the sensor at various temperatures of -50–300 °C under the pressure of 0–5 MPa; (d) The temperature characteristic of the sensor sensitivity.

3. CONCLUSION

To summarize, we reported the operation of 4H-SiC pressure sensor with diaphragm realized by femtosecond laser. The sensitivity of 1.42 mV/V/MPa was obtained. Slight hysteresis error of 0.17 %/FSO and nonlinearity of 0.20 %/FSO were realized. Temperature test results show that the temperature coefficient of sensitivity of -0.23% FSO/°C at -50 °C and -0.10% FSO/°C at 300 °C.

REFERENCES

1. P. Song, Z. Ma, J. Ma et al., Recent progress of miniature MEMS pressure sensors, Micromachines, vol. 11, no. 1, pp. 56, 2020.
2. H.-P. Phan, D. V. Dao, K. Nakamura et al., The piezoresistive effect of SiC for MEMS sensors at high temperatures: A review," Journal of Microelectromechanical systems, vol. 24, no. 6, pp. 1663-1677, 2015.
3. R. S. Okojie, D. Lukco, V. Nguyen et al., 4H-SiC piezoresistive pressure sensors at 800 °C with observed sensitivity recovery, IEEE Electron Device Letters, vol. 36, no. 2, pp. 174-176, 2014.
4. D. G. Senesky, B. Jamshidi, K. B. Cheng et al., "Harsh environment silicon carbide sensors for health and performance monitoring of aerospace systems: A review," IEEE Sensors Journal, vol. 9, no. 11, pp. 1472-1478, 2009.

Multi frequency piezoelectric vibration energy harvesters powered sen sing in power grid transformer

Qian Wang[1,2], Lu Wang[1,2,#], Libo Zhao[1,2], Maeda Ryutaro [1,2]

1 State Key Laboratory for Manufacturing Systems Engineering, International Joint Laboratory for Micro/Nano Manufacturing and Measur ement Technologies, Collaborative Innovation Center of Suzhou Nano Science and Technology, Xi'an Jiaotong University, Xi'an 710049, China

2 School of Mechanical Engineering, Xi'an Jiaotong University, Xi'an 710049, China

 # Corresponding Author / E-mail: wang.lu@xjtu.edu.cn, TEL: +86-82668616, FAX: +86-82668616

ABSTRACT

In order to obtain a vibration energy harvester with small volume and high power, a piezoelectric vibration energy harvester based on piezoelectric bimorph was developed. Thick piezoelectric blocks and L-shaped tungs ten blocks are introduced . L-shaped tungsten blocks function as adjusting the resonant frequency of the cantil ever beam. PVEH of 100 Hz, 200 Hz and 300 Hz are designed with array structure, and the piezoelectric an d vibration characteristics are analyzed in COMSOL MULTIPHYSICS to check the stress. When the accelerati on is 0.1g, three PVEHs power are greater than 0.1mW.

Keywords : small volume, high power, array

1. INTRODUCTION

In the Internet of things era, many wireless sensors are used in smart grids [1]. Vibration energy harvester i s an ideal solution for self power supply of wireless sensor nodes in transformer [2]. Because multi frequency resonance can harvest more energy, the 100Hz, 200Hz and 300Hz PVEH are designed and fabricated to match transformer vibration resonance.

2. DEVICE DESIGN AND ANALYSIS

In order to realize high-power output vibration energy harvester, a linear vibration energy harvester array a s shown in Figure 1 is prepared. The upper and lower PZT-5H piezoelectric plates are connected in series, an d double L-shaped tungsten large mass blocks are added at the free end to ensure compact high input mecha nical power.The thickness ratio of large and small mass blocks is controlled to optimize output power and str ess,and the length of small mass blocks is controlled to optimize bonding length .The length of small mass pl using the length of piezoelectric sheet is the length of copper substrate. When it is excited by 0.1g acceleratio n,polarization charges appear on the upper and lower surfaces of the piezoelectric sheet, converting mechanical energy..

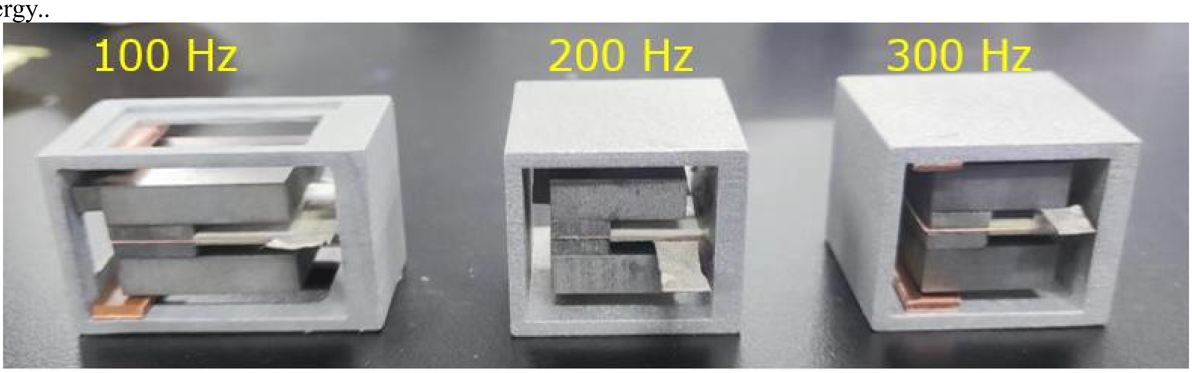

Figure 1 High power linear piezoelectric energy array of 100 Hz、200 Hz、300 Hz

By using the vibration controller to test the open circuit and short circuit frequency response curves of 100 Hz, 200 Hz and 300 Hz PVEH at 0.1g acceleration, and under the standard 100 Hz, 200 Hz and 300 Hz frequency points test the power and voltage curve at different loads, then identify system parameters. Fi gure 2 shows the frequency response characteristics and the open circuit voltage and output power under dif ferent loads.

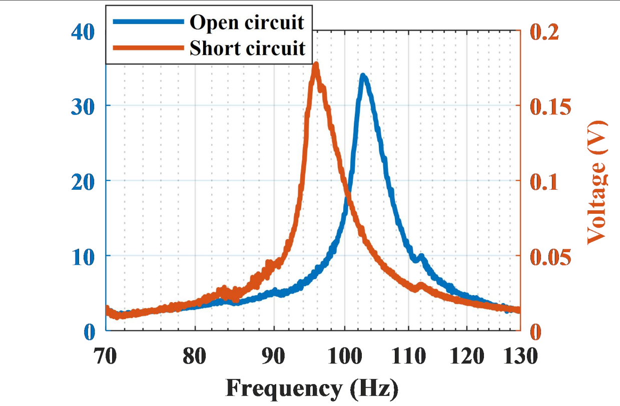

(a)100Hz PVEH peak voltage frequency response curves

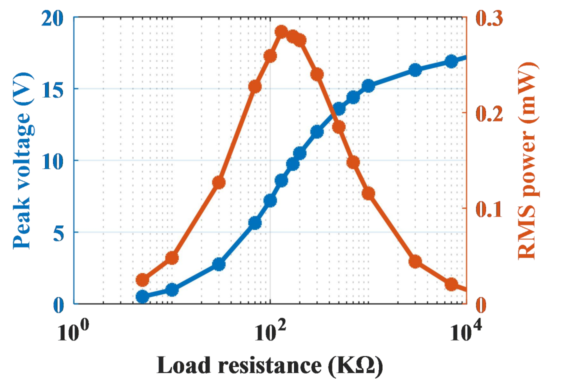

(b)peak voltage and RMS power in different load resistance at 100 Hz

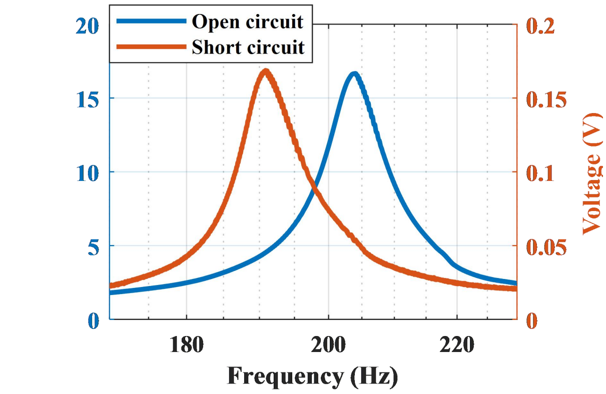

(c)200Hz PVEH peak voltage frequency response curves

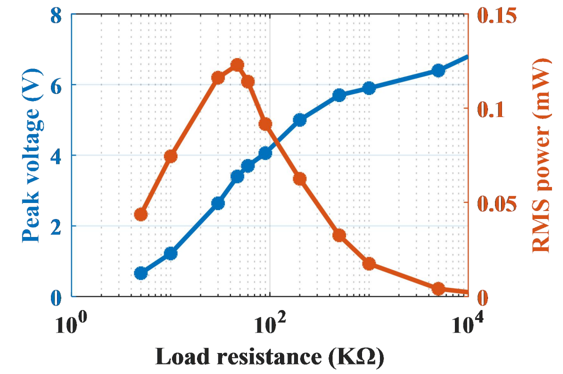

(d)peak voltage and RMS power in different load resistance at 200 Hz

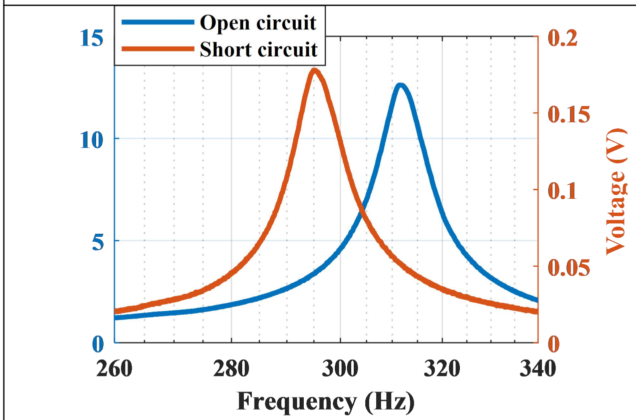

(e)300Hz PVEH peak voltage frequency response curves

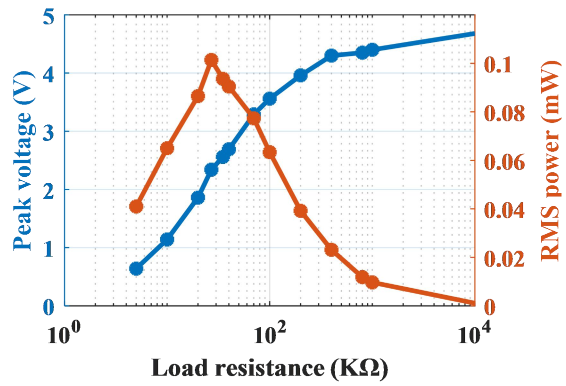

(f)peak voltage and RMS power in different load resistance at 300 Hz

Figure 2 PVEH frequency modulation result by load impedance

3. CONCLUSION

In this study, we propose an array type high output power PVEH. The L-shaped tungsten block is used to adjust the resonance frequency. Output power of 100 Hz, 200 Hz and 300 Hz PVEH is 0.2904 mW, 0.1218 mW and 0.1014 mW when the acceleration excitation is 0.1g.It can meet the power supply demand of the wireless sensing nodes.

ACKNOWLEDGEMENT

This work was supported in part by the Shaanxi Youth Fund (2022JQ-315).

REFERENCES

[1] ERTURK A , HOFFMANN J , INRMAND . A piezomagnetoelastic structure for broadband vibration energy harvesting[J] . Applied Physics Letters , 2009 , 94(25) : 254102 .

[2] Liya Zhao,Yaowen Yang.An impact-based broadband aeroelastic energy harvester for concurrent wind and base vibration energy harvesting[J].Applied Energy,2018,212:233-243.

Triboelectric Nanogenerator Based on Solid-Liquid electrification Interface and Top Electrode Structure

Yahui Li[1,2], Zhuoqing Yang[1#]

1 National Key Laboratory of Science and Technology on Micro/Nano Fabrication, Shanghai Jiao Tong University, Shanghai 200240, China
2 Department of Micro/Nano Electronics, School of Electronic Information and Electrical Engineering, Shanghai Jiao Tong University, Shanghai 200240, China
 # Corresponding Author / E-mail: yzhuoqing@sjtu.edu.cn, TEL: 86-21-34206687, FAX: 86-755-26033504

ABSTRACT

The working principle of triboelectric nanogenerator (TENG), contact electrification and electrostatic induction, has been used to harvest raindrop energy in recent years. However, the existing research is mainly concentrated on solid-liquid electrification, and adopts the traditional electrostatic induction (TEI) for output. Fortunately, the output of liquid TENG is greatly improved based on the proposal of top electrode structure on the electret charging surface. Here we introduce switch effect based on electric double layer capacitor (EDLC), and establish an equivalent circuit model to understand its working mechanism. Without pre-charging, a single droplet could generate high voltage over 100 V and the output is directly improved by 2-orders of magnitude compared with TEI, which is precisely utilizing the interfacial effect. This work provides insightful perspective and lays solid foundation for DEG applications in large scale.

Keywords: Droplet electricity generator, Equivalent circuit model, Electric double layer capacitor, Interfacial effect

1. INTRODUCTION

With the depletion of fossil energy and the deterioration of environment, there is an urgent need to develop green and sustainable energy to satisfy the rapid development of the world today [1-4]. Up to now, energy sources in the form of solar, wind, and biological energy have been widely applied in many fields. Existing energy harvesting systems mainly target on regular and large-scale energy sources, however, there are various scattered and irregular energy sources in natural environment [5]. Recently, the mechanism of solid-liquid electrification has been explored, and theories such as electric double layer model and Wang's hybrid layer model have also been proposed to expand its applications [6]. However, these researches are mainly concentrated on the solid-liquid electrification process, while there is little research on the output process for electricity. As a result, most droplet electricity generators (DEG) still utilize the traditional electrostatic induction (TEI) for output, and the performance is severely constrained. In this work, the electric double layer capacitor (EDLC) formed at the solid-liquid electrification interface is introduced into circuit model, and the equivalent circuit models corresponding to the different characteristics of a droplet is established. Without pretreatment of the solid surface (corona charging or ion injection, etc.), a single droplet could generate high voltage over 100 V only utilizing the interfacial effect in EDLC. Compared with the traditional electrostatic induction electricity generation, the output is directly improved by 2 orders of magnitude. In addition, combined with the equivalent circuit models, the output mechanism and physicochemical characteristics of the switch-effected droplet electricity generator (SEDEG) have been deeply investigated. Furthermore, based on this model, the verification on several solid-liquid interfaces is carried out, showing the strategy has universality and applicability. More importantly, these systematic results and analysis will provide an insightful perspective and lay a solid foundation for harvesting droplet energy in large scale.

2. RESULT AND DISCUSSION

2.1 Experiment

Figure 1a is the current characteristic of the switched effect droplet electricity generator (SEDEG), which is based on the solid-liquid electrification interface. A droplet falls and spreads on the FEP surface, before it contacts Al strip, there is almost no current (i). Then, when the spreading droplet contacts with Al, a significant current peak is instantly generated, which is mainly attributable to the discharge of $C_{D/F}$ formed by the droplet and FEP in the loop (ii). It is worth noting that this current signal is not the traditional electrostatic induction current, but the directional movement of the positively separated charges caused by the loop. The contact area between droplet and FEP, and the contact area between droplet and Al change constantly, resulting in a change in the values of $C_{D/F}$, $C_{F/C}$, and $C_{D/A}$. Therefore, each capacitor in the loop will charge and discharge back and forth within a short period of time. That is, the current in the loop will generate positive and negative fluctuations after the peak value, however, this fluctuation is gradually attenuated owing to the resistance of R_D and R_L (iii). After the droplet leaves the FEP surface, switch $S_{D/F}$ is opened, and $C_{D/F}$, $C_{F/C}$ disappears. That is, the loop also disappears, accordingly, charges' movement caused by charging and discharging between capacitors in the loop also disappears (iv). Figure 1b is a voltage signal diagram of a single droplet, the revealed relationship between signal and the droplet motion characteristics is highly consistent with that of the current signal.

To further verify the importance of switch effect in this circuit model, four structural modes were designed to examine the electrical output, and the schematic and equivalent circuit diagrams are illustrated in Figure 1c. That is, the droplet only impinges and flows through the pure FEP (case 1), the droplet impinges the FEP film, contacts the Al, and flows through the Al strip (case 2), the droplet impinges Al, contacts the FEP film, and flows through the FEP film (case 3), and the droplet only impinges and flows through the pure Al electrode (case 4). The case 1 is actual the traditional electrostatic induction. After the droplet contacts FEP, the droplet is positively charged, and the FEP is negatively charged. During the shrinking process, the negative charges on the FEP surface that cannot be neutralized increase gradually. To achieve electrostatic equilibrium, the conductive cloth induces positive charges that is opposite to the electrical polarity remaining on the FEP and causes the migration of free electrons. However, this process is not instantaneous, charges are continuously induced and transferred, therefore, the induced current in the circuit is very weak. As for the case 2, this is the SEDEG model we proposed in this work. When the droplet contacts Al electrode, the switch $S_{D/A}$ is closed, meanwhile, a loop is formed. The positive charges accumulated in $C_{D/F}$ is instantly released, forming a large current and voltage peak. The principle of case 3 is similar with that of case 2, the difference lies in the capacitors in the circuit model. In addition, due to the electricity between the droplet and Al is much smaller than the droplet and FEP, the charges stored in $C_{D/A}$ are also less, resulting in a smaller current and voltage peak. The output principle of case 4 is similar with case 1, the droplet contacts Al to accumulate negative charges, and positive charges are formed on the surface of Al. As the droplet shrinks, the negative charges on the Al surface that cannot be neutralized increase gradually. To achieve electrostatic equilibrium, the conductive cloth induces negative charges that is opposite to the electrical polarity remaining on the Al and causes the migration of free electrons. However, the charges are induced and transferred continuously, therefore, the induced current in the circuit is also very weak. As shown in Figure 1d-f, the electrical output and comparison of the four modes shows that the output has been greatly improved in our proposed SEDEG.

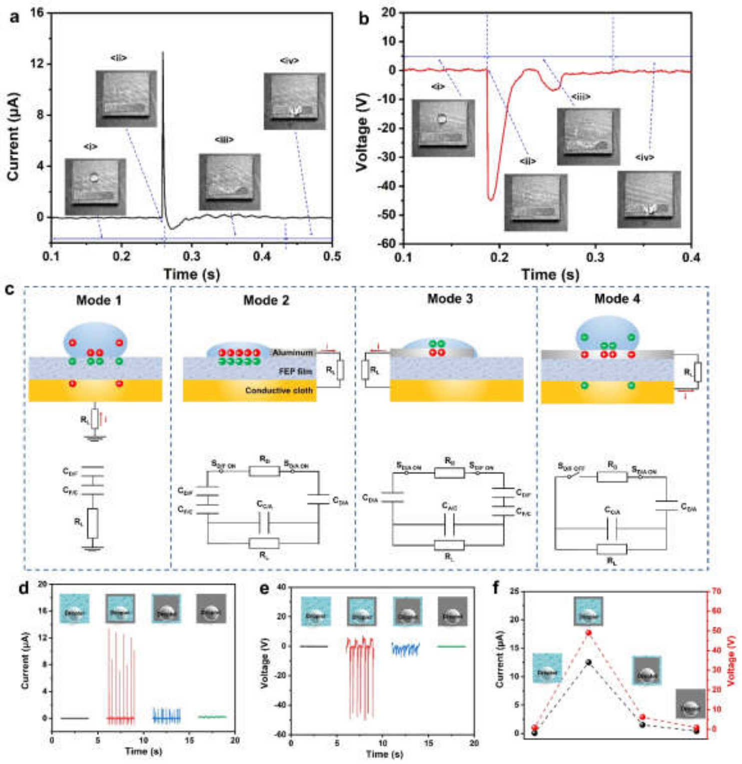

Figure 1 Verification on the universality of the SEDEG. a) The current signal characteristics of a single droplet based on SEDEG. b) The voltage signal characteristics of a single droplet based on SEDEG. c) The schematic diagram and equivalent circuit model of the designed four structural electricity generator. d) The current signal of four modes designed in this work. e) The voltage signal of four modes designed in this work. f) Comparison of electrical output of four modes designed in this work.

3. CONCLUSION

In summary, we have recognized the importance of interfacial effect and output strategies in solid-liquid contact electrification. Specifically, inspired by the working principle of field effect transistor (FET), we have introduced an electric double layer capacitor (EDLC) formed at the solid-liquid electrification interface into the circuit, and established an equivalent circuit model of switch-effected droplet electricity generator (SEDEG). Without pretreatment of the solid surface (corona charging or ion injection, etc.), a single droplet could generate a high voltage over 100 V only utilizing the stored charges in EDLC. Compared with the traditional electrostatic induction electricity generation method, the output is directly improved by 2 orders of magnitude. Additionally, we should also clearly realize that the output strategy used in solid-solid electrification cannot be mechanically applied to solid-liquid electrification, which is determined by the physical characteristics of the two different interfaces. Furthermore, based on the analysis of equivalent circuit equations, the output behavior and the physicochemical characteristics of SEDEG, a systematic and in-depth perspective is provided for researchers to understand the working mechanism of the SEDEG. Finally, this work also brings meaningful guidance for the future development of droplet electricity generator and lays solid foundation for harvesting droplet energy on large scale.

ACKNOWLEDGEMENT

This work was supported in part by the National Key Research and Development Program of China (2020YFB2008503), and the National Natural Science Foundation of China (No.61974088).

REFERENCES

1. L. Gu, J. Liu, N. Cui, Q. Xu, T. Du, L. Zhang, Z. Wang, C. Long, Y. Qin, Nat. Commun. 2020, 11, 1030.
2. W. He, W. Liu, J. Chen, Z. Wang, Y. Liu, X. Pu, H. Yang, Q. Tang, H. Yang, H. Guo, C. Hu, Nat. Commun. 2020, 11, 4277.
3. Y. Li, Q. Zhang, Y. Liu, P. Zhang, C. Ren, H. Zhang, H. Cai, G. Ding, Z. Yang, C. Zhang, Nano Energy 2021, 89, 106390.
4. H. Yang, Y. Pang, T. Bu, W. Liu, J. Luo, D. Jiang, C. Zhang, Z. L. Wang, Nat. Commun. 2019, 10, 2309.
5. Z. L. Wang, Mater. Today 2017, 20, 74-82.
6. F. Zhan, A. C. Wang, L. Xu, S. Lin, J. Shao, X. Chen, Z. L. Wang, ACS Nano 2020, 14, 17565-17573.
7. S. Lin, L. Xu, A. Chi Wang, Z. L. Wang, Nat. Commun. 2020, 11, 399.

On chip organic synthesis by microwave heating in a micro-channel coupled with post-wall waveguide

#Kaito Fujitani[1], Mitsuyoshi Kishihara[2], Ryota Tanaka[1], Tomoyuki Nakano[1], Akinobu Yamaguchi[1], and Yuichi Utsumi[1]

1 Laboratory and Advanced Science and Technology, University. of Hyogo; 3-1-2 Koto, Kamigori-cho, Ako-gun, Hyogo, Japan
2 Okayama Prefectural University; 111 Kuboki, Soja-shi, Okayama, Japan
 # Corresponding Author / E-mail: kit1129@lasti.u-hyogo.ac.jp, TEL: +86-029-82668616, FAX: +86-029-82668616

ABSTRACT

We have developed a micro-chemical chip coupled with post-wall waveguide in a microchannel for microwave heating at 24.125 GHz. This system can provide microwave selective heating for the locally heating in the microchannel and monitor the chemical reaction during microwave heating. We have investigated on-chip synthesis of Ag nanoparticles and Ru complex using this system. As the result of dynamic scattering measurement, we found that Ag nanoparticles with about 22 nm were produced by 10 minutes microwave heating. In addition, we have succeeded the fast synthesis of ruthenium complex by 2 minutes microwave heating. These results show this micro-chemical chip is effective for organic synthesis using microwave heating.

Keywords : microwave, post-wall waveguide, nanoparticles, metal complex, on-chip synthesis

1. INTRODUCTION

Chemical synthesis using microwave heating has been widely investigated and applied in various fields, such as chemistry, drug synthesis, and materials because of its high reaction rates and yields [1]. However, it is difficult to monitor the reaction during microwave heating and obtain combinatorial syntheses with a small amount of source reagents, because the reaction fields must be isolated by metal cavities. One of the candidates is the application of a lab-on-a-chip and microreactor system. However, there are no reports which can achieve monitoring the reaction during microwave heating and efficiently using the microreactors consisting of microwave heating combined with microfluidics[2]. In this study, we demonstrate that on-chip synthesis of Ag nanoparticles and metal complex achieved by a microwave-induced reaction in a microchannel embedded in a post-wall waveguide design to confine 24.125 GHz microwave radiation. In addition, this device's characteristics were investigated [3].

2. EXPERIMENT

To create the microsystem which can monitor the reaction during microwave irradiation and archive highly efficient microwave heating, fluorinated ethylene propylene (FEP) is used as a structural material because of its high thermal property, low dielectric loss, and high chemical stability. We also explored the adaption of poly-dimethylpolysiloxane (PDMS) for combination with other unit chemical operations. These systems were prototyped by machining and molding. To demonstrate organic synthesis using this microchip, we have investigated on-chip synthesis of Ag nanoparticles and ruthenium complex by microwave-induced reaction using this system. We prepared a mixed solution of Polyvinylpyrrolidone, 0.1mM of $AgNO_3$, and ethanol for the synthesis of Ag nanoparticles. Similarly, to synthesize Ru complex, we prepared a mixed solution of ruthenium (III) chloride, bipyridine, and ethylene glycol.

3. RESULTS AND DISCUSSION

Figure 1 shows the diagram of a microchip with microchannel combined with post-wall waveguide. The microchannel and the post-wall waveguide are formed on two sheets of FEP and PDMS (Fig. 1(a)). It is sandwiched between two pieces of glass, on which an ITO film of 3 mm thickness was formed. According to the simulation result, the thermal energy locally heats the inside of the microchannel (Fig. 1(b)). Figure 1(c) shows the experimental setup for microwave irradiation with an input power of 4.0 W. The microwave emitted from the 24.125 GHz transmitter is amplified by a power amplifier and emitted to the microchip with an output of 4 W. As a result of water temperature measurement using a fiber-optic thermometer, the temperature rose to more than 80°C.

We used this chip to synthesize ruthenium complex by microwave heating. Figure 2(a) shows the absorbance spectrum of ruthenium complex irradiated with microwaves of 4.0 W input power for the arbitrary time. The absorbance peak of the ruthenium complex can be observed when microwaves are irradiated for 2 minutes. It was possible to monitor the formation process during the microwave irradiation (Fig. 2(b)).

Similarly, we synthesized Ag nanoparticles using this device. Figure 3(a) shows the absorbance spectrum of Ag nanoparticles irradiated with microwaves of 4.0 W input power for 10 minutes. It was observed that the absorbance peak of Ag nanoparticles at 406 nm. This result shows the range of particle size is 20 nm ± 10 nm. In addition, as the result of dynamic light scattering (DLS), there is a peak in the scattering intensity at a particle size of 22 nm (Fig. 3(b)). These results shows this microwave chemical synthesis system allows us to achieve automatic, fast chemical synthesis and fast selective synthesis of nanoparticles.

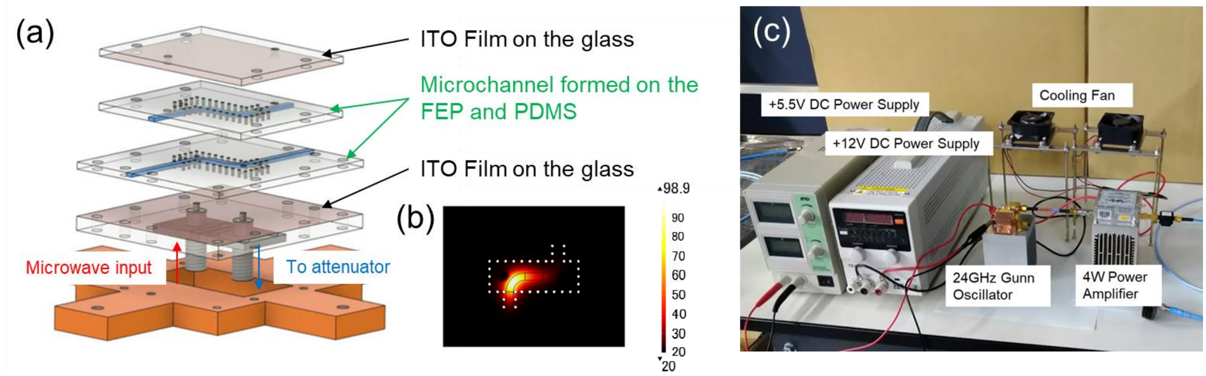

Figure 1 (a) A diagram of designed structure of microchannel coupled with the post-wall waveguide. (b) Temperature distribution of water during microwave irradiation simulated using COMSOL Multiphysics. (c) Photograph of experimental setup for the organic synthesis using a microchip.

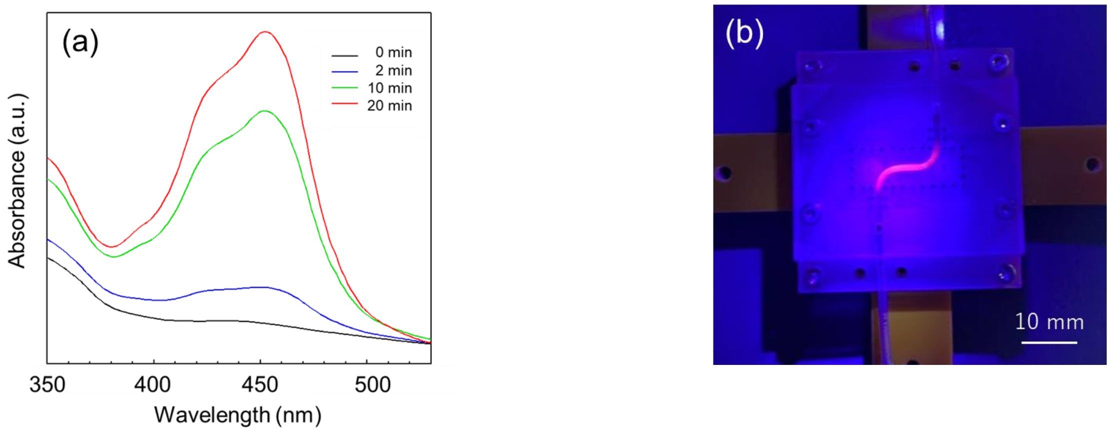

Figure 2 (a) Absorbance spectra and (b) photograph of ruthenium complex in a microchannel synthesized by microwave heating.

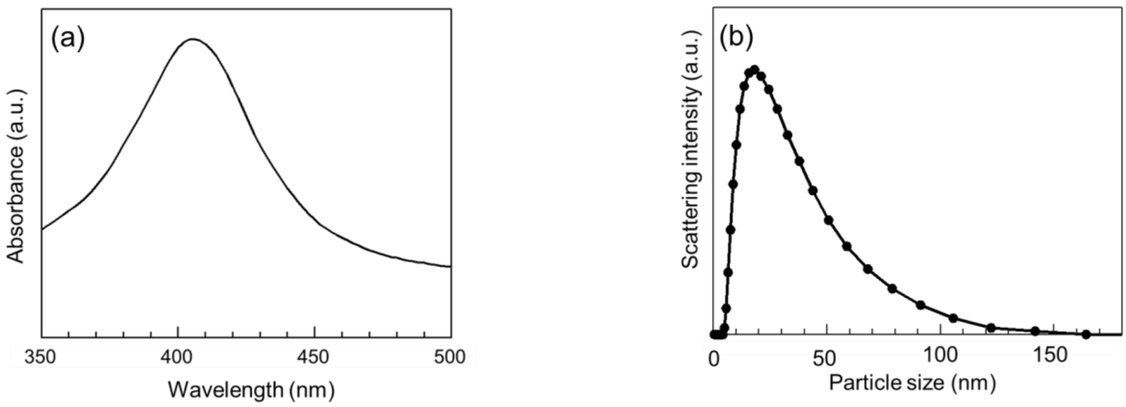

Figure 3 (a) Absorbance spectra and (b) dynamic light scattering measurement for Ag colloid solution synthesized by a mixed solution of Polyvinylpyrrolidone, 0.1mM of AgNO3, and ethanol.

ACKNOWLEDGEMENT

This work was supported in part by JSPS Grants-in-Aid for Scientific Research (No. 22J22928 and No. 19K05142).

REFERENCES

1. C. O. Kappe, “Controlled microwave heating in modern organic synthesis” Angew. Chem. Int. Ed. 43 (2004) 6250.
2. L. Jasińska, and K. Malecha, “Microfluidic modules integ-rated with microwave components overview of applications from the perspective of different manufacturing technologies” sensors., 21 (2021)1710.
3. K. Fujitani, M. Kishihara, T. Nakano, R. Tanaka, A. Yamaguchi, and Y. Utsumi. Development of Microfluidic Device Coupled with Post-wall Waveguide for Microwave Heating at 24.125 GHz, Sens. Maters., 33 (2021) 4399

Internal Resonance in Coupled Oscillators and Its Sensing Applications

Cao Xia[1], #Dong F. Wang[1,2*], Takahito Ono[3], Toshihiro Itoh[2,4], Ryutaro Maeda[2], Masayoshi Esashi[5]

[1] *Micro Engineering and Micro Systems Laboratory (JML), Jilin University, Changchun 130025, China*
[2] *Research Center for Ubiquitous MEMS and Micro Engineering, AIST, Tsukuba 305-8564, Japan*
[3] *Department of Mechanical Systems and Design, Tohoku University, Sendai 980-8579, Japan*
[4] *Department of Precision Engineering, The University of Tokyo, Tokyo 113-8656, Japan*
[5] *WPI Advanced Institute for Materials Research, Tohoku University, Sendai 980-8577, Japan*
 # Corresponding Author / Email: Prof. Dr. Dong F. Wang / dongfwang@jlu.edu.cn, Tel: +86 (0) 431 8509 4698

ABSTRACT

In the past decade, there has been a growing interest in exploiting rich nonlinear dynamic features of resonant-based sensors to enhance their functionality. In this paper, we review our research efforts to investigate the nonlinear modal interaction in mechanically and magnetically coupled cantilevers, focusing especially on internal resonance phenomena. Complex nonlinear dynamics caused by energy transfer between modes with an integral frequency ratio, such as amplitude stability, frequency multiplication and differential amplification, have been theoretically and experimentally explored in T-shaped, Π-shaped, and orthogonally coupled oscillators. Based on the above characteristics, scale-free smart sensing schemes for a single trace or multiple traces with high linearity, high stability, and high sensitivity have been further proposed and demonstrated, opening a new avenue for traces sensing.

Keywords: *internal resonance, energy transfer, modal interaction, coupled oscillators, trace(s) sensor*

1. AUTOPARAMETRIC INTERNAL RESONANCE IN COUPLED OSCILLATOR: AN EXCITATION AMPLITUDE INSENSITIVE MASS SENSING SCHEME WITH A ROOF TILTING

To overcome the effect of slowly changing excitation amplitude caused by temperature drift etc. on sensing performance, a slope-based working mechanism is exploited in autoparametric internal resonance systems in our latest work. Through increasing modal damping, energy transfer between coupled modes is observed to be decreased, and the depressed cave on the amplitude response curve transits to a flat roof that is independent of both excitation amplitude and excitation frequency [1], as Fig. 1(a). A theoretical expression is established to characterize the flat roof, which tends to tilt when applying mass perturbations. The slope of the flat roof is found to be independent of the excitation amplitude but a function of the applied mass perturbations, while the frequency range of which broadens or narrows with the increase or decrease of the excitation amplitude respectively. Further concerning on the slopes under different excitation amplitudes, results from numerical study is also basically consistent with those from the theoretical prediction, apart a maximum relative deviation about 8%. An excitation insensitive mass sensing scheme via flat roof tilting is thus proposed, as Fig. 1(b). With applying different mass perturbations, the proposed scheme is mutually confirmed by both theoretical and numerical results, featured with a high linearity in a certain mass range. Compared to conventional frequency shift based or amplitude change based one, the proposed sensing scheme is insensitive to slow change of excitation amplitude and is believed to have great potential in engineering scenarios with varying environmental temperature.

2. INTERNAL RESONANCE IN ORTHOGONALLY COUPLED OSCILLATORS: A DOUBLE AMPLIFICATION MASS SENSING SCHEME WITHOUT DUFFING NONLINEARITY

To further improve the mass sensitivity to break through the mass sensing limit, we further report a double amplification scheme for mass sensitivity, via a differential phenomenon in various non-Duffing internal resonance systems with even power nonlinearities and coupling [2], as illustrated in Fig. 2. Both frequency sum and amplitude difference of the two symmetrical peaks, in response amplitude of the basic mode, are capable of differentially amplifying the sensitivity as well as greatly suppressing the effect of noise caused by driving amplitude fluctuation. Combining frequency up-conversion to further amplify the sensitivity, double amplified mass sensitivity is thus achieved via frequency shift, as Fig. 2(b). Magnetically coupled orthogonal beams with a frequency ratio of two to one, is adopted as an example for both theoretical and experimental demonstration, as Fig. 2(a). Experimental results show effect of driving voltage fluctuating in the range of 200mV to 600mV is reduced by 360%, as well as the sensitivity for mass perturbation in the range of 0g to 10g is 332% amplified. Lower driving threshold and wider sensing range are further obtained through adjusting modal damping. Compared to those based on synchronization or internal resonance under the same frequency ratios, the proposed amplification scheme, not only enhances the mass sensitivity up to about 166%, but also suppresses the effect of driving amplitude fluctuation down to about 27.8%, indicating a potential possibility to break through the sensing limit. Furthermore, that magnetically coupled orthogonal beams can also be applied for the synchronously sensing of mass perturbation and driving force, when the driving force is large enough for Duffing oscillation [3].

3. SYNCHRONOUS IDENTIFICATION AND SUCCESSIVE DETECTION OF MULTIPLE TRACES WITH TUNABLE COUPLING OSCILLATORS

Trace identification and detection of toxic, flammable, explosive substances, pollen allergens, as well as biological viruses is crucial for public health and safety, chemic production, and scientific research, etc. A single trace is detectable via various nonlinear resonance phenomena, while quantitative detection of two traces is physically limited by the trace ratio even with localized oscillators. We have discovered that, in internal resonance systems, response amplitude of any coupled mode physically reflects multi-modal features [4]. In case of multi-mode coupled duffing oscillators, peaks and jumps in response amplitudes show great potential in synchronous identification and successive detection for multiple traces. With tunable magnetically coupled duffing oscillators, a multiple traces sensing scheme is thus proposed and verified, as illustrated in Fig. 3(a). Two traces are both experimentally and theoretically demonstrated to be synchronously identified and successively detected with multiplied frequency shifts. Measurement ranges and manufacturing errors are adjustable or compensable respectively only through turning the coupling strength. The proposed scheme is also applicable to multiple traces through the internal resonance among multi-mode coupled duffing oscillators, as Fig. 3(b). This work not only opens a new avenue in applications of nonlinear resonators, but also provides a new metrological scheme for synchronous identification and successive detection of multiple traces.

REFERENCES

[1] C. Xia, D.F. Wang, T. Ono, et al., IEEE Sens. J., Vol. 22, 2021, pp. 1998 - 2005.

[2] C. Xia, D.F. Wang, T. Ono, et al., Mech. Syst. Signal Pr., Vol. 159, 2021, 107886.

[3] C. Xia, D.F. Wang, T. Ono, et al., Mech. Syst. Signal Pr., Vol. 160, 2021, 107887.

[4] C. Xia, D.F. Wang, J. Song, et al., Mech. Syst. Signal Pr., Vol. 166, 2022, 108395.

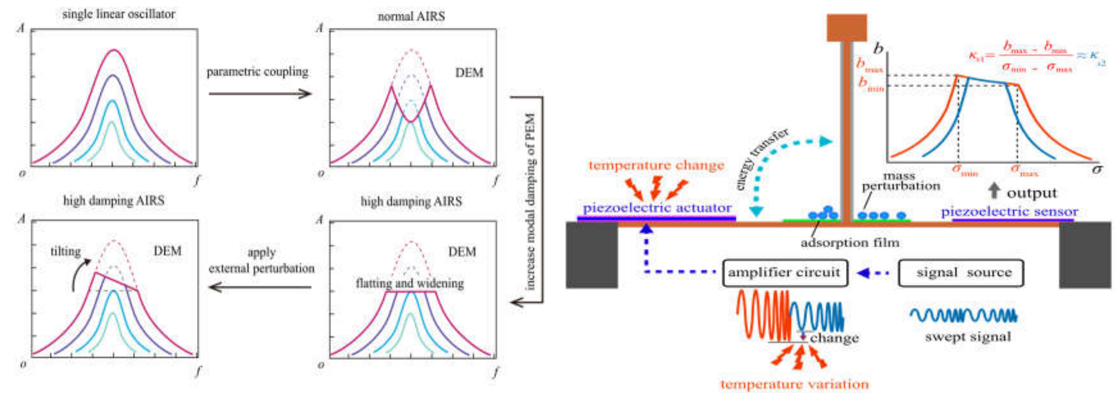

Figure 1. (a) Illustration of the tilting of the flat roof on the amplitude response curve and its sensing potential; (b) Illustration of the excitation amplitude insensitive mass sensing scheme.

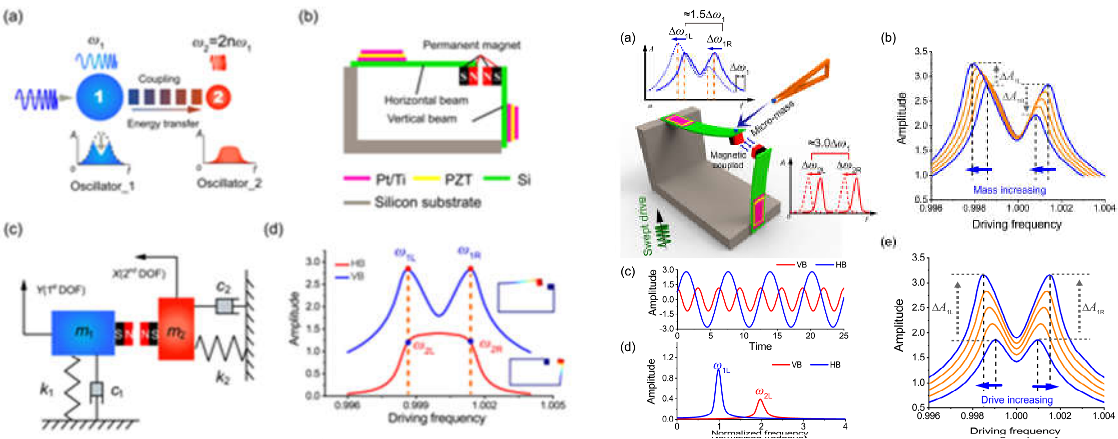

Figure 2. (a) Illustration of the physical mode; (b) Illustration of the double amplification scheme for mass sensitivity.

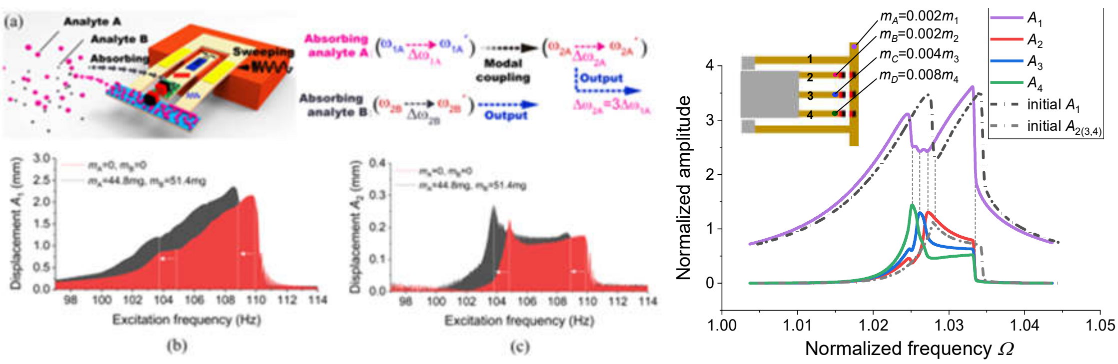

Figure 3. (a) Schematic diagram of the proposed synchronous identification and successive detection scheme for two traces scheme; (b) Response amplitude of the four magnetically coupled oscillators after absorbing analytes with different mass perturbations.

Design and Fabrication of pH-ISFET Sensor Using MEMS Technology

Hoang Ba Cuong[1], Michio Shimomura[2], Tran Duy Hoai[1], Nguyen Thanh Phuong[1], Nguyen Chi Cuong[1], Trinh Xuan Thang[1], Ngo Vo Ke Thanh[1], Tadao Matsunaga[2] and Sang-Seok Lee[2*]

[1] *The Research Laboratories of Saigon high Tech Park, Lot I3, N2 Street, Saigon High Tech Park, Thu Duc city, Ho Chi Minh city 70000, Vietnam.*
[2] *Graduate School of Engineering, Tottori University, 4-101 Koyama-Minami, Tottori 680-8552, Japan*
* Corresponding author/ Email: sslee@tottori-u.ac.jp.
Presenter/Email: cuong.hoangba@shtplabs.org; Tel. (+84)28 3736 0889; Fax: (+84) 28 3736 0890.

ABSTRACT

This work presents the development of pH based on ion-sensitive field-effect-transistor (pH-ISFET) using MEMS technology. ISFET is an integrated device that similar to MOSFET except the gate was covered by SiN_x acting as a pH sensing membrane during pH measurement. The SiN_x/SiO_2 sensing membrane of ISFET and reference electrode were both exposed to the solution to execute the IV curves in order to identify the sensitivity and other characteristics of pH-ISFET. The results show that the pH-ISFET is stable and the achieved sensitivity is about 22.7 mV/pH.

Keywords : pH-ISFET, PECVD, MEMS, SiN_x/SiO_2 sensing membrane

1. INTRODUCTION

ISFET based pH sensor is gained a lot of attractions as it plays an important role in almost all fields of science and technology including engineering, medical, industrial control, aerospace, food and beverage production, security and defense and environmental applications [1, 2]. ISFET was first introduced in 1972 [3, 4], which combined electrochemical parameters with microelectronic technology to be used as a chemical and/or biochemical sensor. In recent years, many researchers have investigated the characteristics of ISFET based on MOSFET technology due to its small, short response time, low output impedance, solid state nature and able for mass production. In this study, silicon nitride (SiN_x) acts as the sensing layer because of its hydrogen ion sensing capability, chemically stable and has low leakage current. The overall process has 7 mask levels and the electrical test, both exposed membrane of ISFET and reference electrode were immersed in different pH solutions to measure I_{ds}-V_{ds} (drain current-drain voltage) and I_{ds}-V_{gs} (drain current-gate voltage) characteristics in order to identify the ISFET behavior.

2. EXPERIMENT

2.1 Device Fabrication

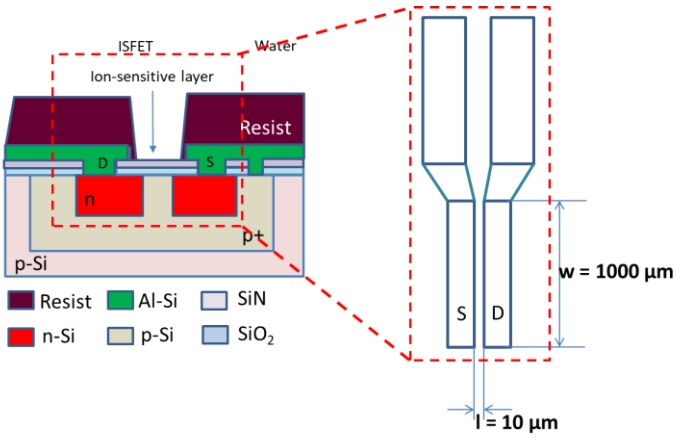

Figure 1 Schematic diagram of designed ISFET

ISFET were fabricated using MEMS technology based on standard MOSFET fabrication process with silicon nitride as sensing layer in clean room environment. The ISFET structure is shown in Fig. 1. P-type silicon wafer with 100 crystal orientation was used to fabricate the pH-ISFET devices. There are seven total masks that been used, the silicon nitride layer around 50 nm was deposited over a buffer SiO_2 layer by PECVD as sensing membrane for ISFET. The channel width and length of ISFET are 1000 and 10 µm, respectively.

2.2 Current-Voltage Measurement

The current voltage measurement setup is shown in Fig. 2. The ISFET packaged sensor and the reference electrode

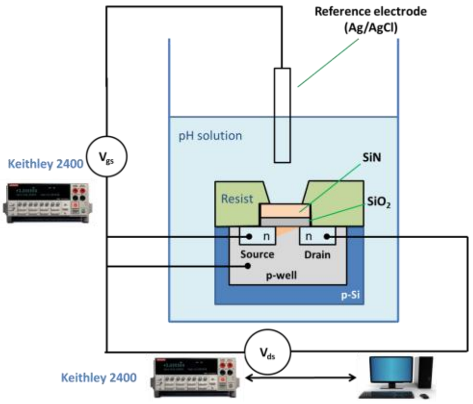

Figure 2 Measurement setup for IV characteristics

were immersed in one type of buffer solution at a time. The pH ISFET sensor and reference electrode were connected to the source measure unit and semiconductor device analyzer. The gate voltage was swept from 2 to 4 V.

3. RESULTS AND DISCUSSION

The output characteristics of the pH-ISFET device were tested. As shown in Fig. 3(a), the applied voltage ranged from 2 to 4 V with a step size of 0.1 V. The source-drain current changes as the source-drain voltage was varied from 0 to 1 V. It is revealed that the large applied gate voltages can results in large corresponding source-drain currents. The source-drain current can be enhanced with increase in gate voltage, after the source-drain voltage reaches a certain value, and the source-drain current can saturate, which is consistent with the theory. Fig. 3(b) represents the transfer characteristics of the device, which clearly indicates the gate voltage's ability to regulate source and drain current. As the source-drain voltage was fixed at 200 mV, the output gate voltage can be varied with the pH change and the sensitivity was about 22.7mV/pH.

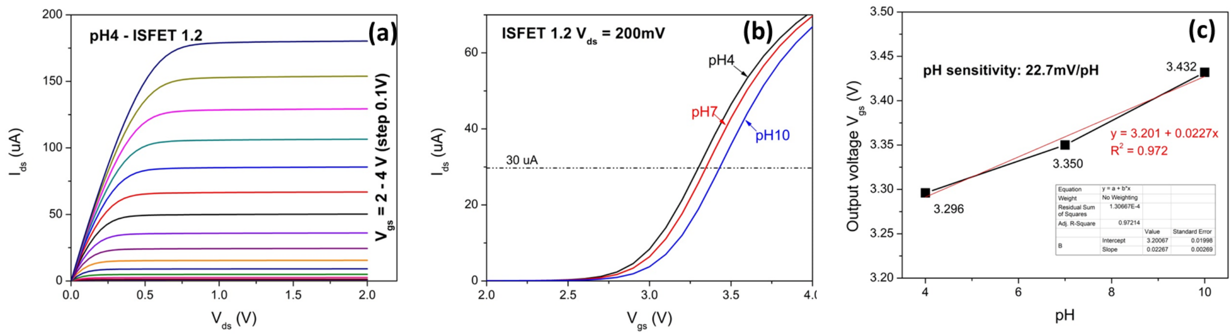

Figure 3 I-V characteristics of pH-ISFET sensor

3. CONCLUSION

The pH-ISFET device was successfully fabricated using MEMS technology, and by analyzing the ISFET characteristics the pH-ISFET sensitivity was about 22.7mV/pH. We propose a pH-ISFET sensor can be used to measure the pH of solution and other environmental monitoring applications.

ACKNOWLEDGEMENT

This research was supported by the Department of Science and Technology in Ho Chi Minh city, the grant contract No. 119/2019/HĐ-SKHCN.

REFERENCES

1. W. Dang, L. Manjakkal, W. T. Navaraj, L. Lorenzelli, V. Vinciguerra, R. Dahiya, Stretchable wireless system for sweat pH monitoring, Biosensors and Bioelectronics, 107 (2018) 192-202.
2. T. Guinovart, G. Valdés-Ramírez, J. R. Windmiller, F. J. Andrade, J. Wang, Bandage-based wearable potentiometric sensor for monitoring wound pH, Electroanalysis, 26 (2014) 1345-1353.
3. C. Toumazou, P. Georgiou, Piet Bergveld, 40 years of ISFET technology: From neuronal sensing to DNA sequencing, Electronics Letters, 47 (2011) S7-S12.
4. P. Bergveld, Development of an ion-sensitive solid-state device for neurophysiological measurements, IEEE Transactions on Biomedical Engineering, (1970) 70-71.

S!J Super Inkjet printer
SIJTechnology

Solution Provider
KYODO
INTERNATIONAL INC.

SUMITOMO PRECISION PRODUCTS CO., LTD.

HEIDELBERG INSTRUMENTS
The power of direct writing

微纳制造与测试技术国际合作联合实验室
INTERNATIONAL JOINT LABORATORY FOR MICRO/NANO MANUFACTURING AND MEASUREMENT TECHNOLOGY

Fine Polish TDC

SANMEI GROUP IDENTITY
sanmei